



Max-Planck-Institut für Kolloid- und Grenzflächenforschung



Chemical Vapor Deposition of Carbon-based Thin Films: from Binary to Ternary Systems

Dissertation

zur Erlangung des akademischen Grades
Doktor der Naturwissenschaften (Dr. rer. nat.)
In der Wissenschaftsdisziplin „Polymerchemie“
eingereicht an der

**Mathematisch-Naturwissenschaftlichen Fakultät
der Universität Potsdam**

von

Paolo Giusto

Geboren am 02.05.1989 in Imperia, Italien

Table of contents

Table of contents	i
General background and perspective	1
Chapter I	7
1. Introduction.....	7
1.1. Basic concepts of carbon-based materials: from bulk to thin films	7
1.2. Graphitic carbon nitride: preparation and properties	10
1.3. Boron carbon nitride materials: preparation and properties	14
1.4. Chemical vapor deposition for thin film technology	17
1.5. Optical properties of materials	22
Chapter II	25
2. Graphitic carbon nitride thin films	25
2.1. Background and state of the art.....	25
2.2. Chemical vapor deposition of g-C ₃ N ₄ from melamine precursor	30
2.3. Optical properties of g-C ₃ N ₄ thin films.....	42
2.4. Summary of chapter 2 and perspectives	54
Chapter III	59
3. Boron carbon nitride thin films	59
3.1. Background and state of the art.....	59
3.2. Chemical vapor deposition of BCN thin films from melamine-boric acid adduct precursor	62
3.3. Optical properties of BCN thin films.....	71
3.4. Summary of chapter 3 and perspectives	80
Chapter IV	83
4. Low temperature carbon.....	83
4.1. Low temperature carbons from carbon suboxide precursor	83
4.2. Low temperature carbon synthesis from C ₃ O ₂ method	87
4.2.1. Preparation of low temperature carbon	89

Table of contents

4.2.2. Thin films deposition of low temperature carbon.....	96
4.3. Low temperature carbon from malonic acid acetic anhydride precursors.....	98
4.3.1. Synthesis of low temperature carbon from acetic anhydride and malonic acid precursors	99
4.4. Summary of chapter 4 and perspectives.....	103
Chapter V.....	107
5. Conclusion, final remarks and perspectives.....	107
Appendix	113
A. Materials	113
B. Synthesis procedures	113
C. Supporting information.....	120
D. Characterization methods	142
E. Abbreviation list	149
F. Publication list.....	152
G. Acknowledgements.....	153
H. Declaration	155
I. Bibliography	157

To my family

Frustra fit per plura quod potest fieri per pauciora
(Summa totius logicae, William of Ockham)

General background and perspective

Challenge. Semiconductors are nowadays among one of the most important materials in research and industrial applications. They are widely used in electronic, optoelectronic and optical devices, such as transistors, diodes and solar cells. Despite recent developments, semiconductors are still dominated by inorganic materials, for example silicon, gallium arsenide and indium phosphide. In a world with exponential growth of computing power and miniaturization, inorganic semiconductors like silicon are expected to reach their physical limits and issues in processability. This, however, bears several other disadvantages:

- Materials for inorganic semiconductors are difficult to retrieve, for example through mining (gallium, indium, rare earths)
- Elements and intermediate products can be toxic (arsenic, lead, cadmium)
- Processing requires high energies (silicon)

Moreover, future applications such as wearables will require compatibility with biological systems as well as flexibility, stretchability and mechanical softness which, however, cannot be met by the current inorganic-based semiconductor devices.

A promising class of materials with high potential to overcome the abovementioned problems is the organic semiconductors. In this regard, the *challenge* is to develop new and improve existing organic materials in order to create next generation devices which are smaller, more efficient, flexible and disposal more environmentally acceptable. To fulfill this task, it is necessary to:

- Develop methods to create high quality thin films of organic semiconductors
- Tune material composition and properties required for the final application

With regard to the synthesis of organic semiconductors, the discovery of semiconducting and metallic polymers, awarded with the Nobel Prize to Alan J. Heeger, Alan MacDiarmid and Hideki Shirakawa, paved the way for what was defined first by Bengt Rånby as “*the fourth generation of polymeric materials*”.^[1] “Conducting polymers offer the promise of achieving a new generation of polymers: materials that exhibit the electrical and optical properties of metals or semiconductors

and that retain the attractive mechanical properties and processing advantages of polymers” said Alan J. Heeger in his Nobel lecture.^[1] This highly important finding triggered further investigations of organic semiconductors both, from the synthetic and application point of view. Eventually, additional organic semiconductors were further developed in the past years, two of which will be center of this work, i.e. carbon nitride and boron carbon nitride.

Economy. The semiconductor technology is growing extremely fast. The impact of improvement can be seen in our daily lives: communication is easier all over the world, data processing is faster, cars are more interactive and our screens have better resolution every day. This trend is reflected in the increasing market size of semiconductors, with a compound annual growth rate of about 6 % per year, a trend which is also true for optical semiconductors with a market size that is foreseen to be about 35 billion \$ in 2019.

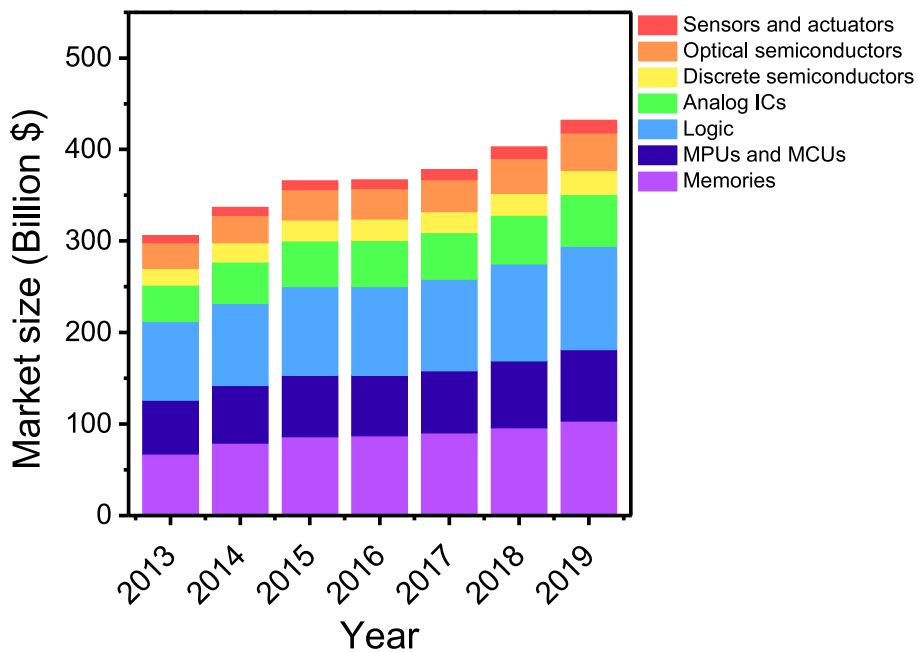


Figure 1. Semiconductors sales worldwide grouped by application.

These numbers for semiconductors visualize the large market demand for high performing semiconductor-based devices, which is due to the fact that these devices improve our life quality and safety. Additionally, in May 2013, the European commission announced an initiative for 10 billion € for public and private fundings in the period 2014-2020 for research and development in the semiconductor area to increase the industrial investments in manufacturing. In this scenario, organic

electronics have a key role with a market size expected to grow from 16.67 billion \$ in 2017 to 59.26 billion \$ by 2023 at a compound annual growth rate of 23.6%. Moreover, Germany as a world leading industrial country is present on the organic electronics market with companies such as BASF SE, Bayer MaterialScience AG, Merck KGaA, Novaled GmbH and Evonik Industries, showing the high importance of this material class.

Organic semiconductors and thin films. As mentioned above, organic semiconductors can overcome the limits of inorganic semiconductors and the discovery of conductivity in polymers is a milestone in polymer science. Organic semiconductors are constituted by alternating π -bonds that improve electrical conductivity. This, however, is also affecting optical properties such as the refractive index, which makes the latter an important property of organic semiconductors. As they are constituted of carbon-based materials, the introduction of heteroatoms (such as B, N, S and more) allows to further tune electronic and optical properties.

The refractive index is a key parameter when it comes to light management in optical and photonic devices: indeed, the precise tuning of materials at the molecular level allows for the possibility to create novel super-high refractive index materials that can open new ways for high quality devices. Moreover, the size of such devices can be significantly reduced: for instance, a simple optical device, such as a lens, can be reduced in thickness up to 60% by raising refractive index of the material from 1.5 to 1.7. The ability to control material properties and structure at the molecular level is nowadays a fundamental interdisciplinary field of high importance called nanoscience. At the nanoscale, classical phenomena descriptions are not applicable anymore and material surface properties gain more and more relevance. The *art of nanoshaping* is extremely important in different fields such as catalysis, optics, membranes, energy storage and so on. However, most of the times syntheses are focused on the creation new bulk materials, requiring further processing steps, when possible, for the application in optics and photonics. Here, also control of the geometrical shape on the macroscale requires one dimension to be in the sub-micron range, i.e. the thin films. In general, the thickness of thin films ranges from the micrometer to the nanometer size. The ability to control also this parameter at the nanoscale provides even wider opportunities for technological applications, where nanometer-sized layers are required, e.g. for light management, free-standing

membranes or in devices with materials stacks of planar heterojunction, such as light emitting diodes (LED), photovoltaic cells and transistors.

Carbon: the sixth element. “*Humankind has seen the Stone Age, the Golden Age, and the Iron Age. Some would argue the 20th century should be called the Silicon Age. Based on the events of its first 10 years, the 21st century may very well become known as the Carbon Age*”- said Aaron Feaver, CTO of the company EnerG2, in 2010. Carbon is the sixth element of the periodic table and one of the fundamental elements for living beings. Between the many reasons why carbon is so fundamental for life, it is the four electrons of the carbon atom, which are available for covalent bonds allowing for a large variety of strong but reversible bonds. The electronic configuration of carbon allows to create countless numbers of compounds, from small molecules over polymers to macroscopic bulk materials. The versatility of carbon is also reflected in the large number of allotropes found to date: diamond, lonsdaleite, graphene, fullerenes, carbon nanotubes, amorphous and glassy carbon, and many other predicted structures like D-, M-, bcc-, bct- carbon, just to name few. In many cases, carbon materials can be described as molecules with high molecular mass, which structure comprises multiple repetitions of units with relatively low molecular mass, which is also the definition for polymer materials.

Carbon materials allow for a wide range of tunability in terms of composition, e.g. by the introduction of heteroatoms, in terms of nanostructure, e.g. layers, nanotubes or fullerenes and in terms of macroscopic processing, e.g. bulk materials or thin films. The extensive amount of opportunities to combine carbon with other elements opens an endless exciting amount of possibilities. In this way, by properly choosing precursors and conditions, scientists may have found the *old solution to new problems* for addressing present and future challenges in material science.

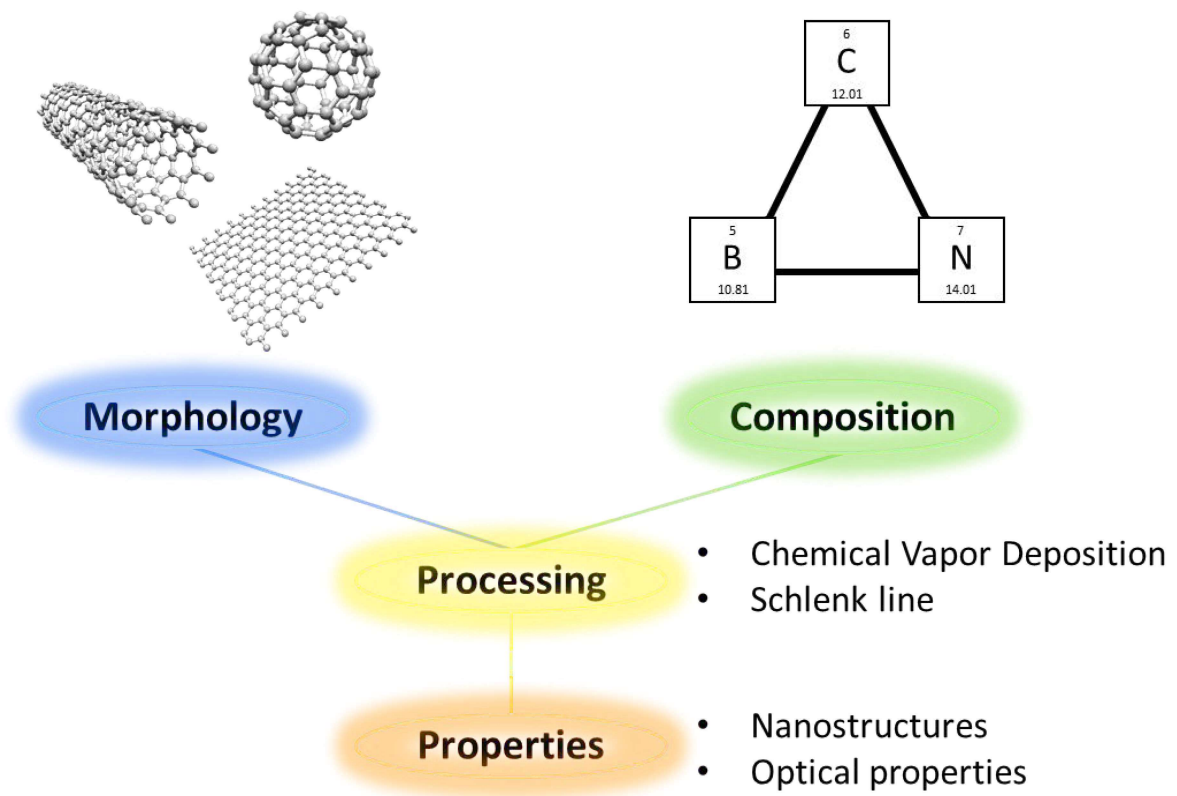


Figure 2. Overview of topics and approaches within this thesis.

Overview. In the present work, approaches towards the synthesis of carbon-based semiconductor thin films via chemical vapor deposition will be introduced. The main focus is based on tuning the thin film thickness, as well as the influence of the composition on the optical properties.

Chapter 1 will introduce carbon-based materials in bulk, which are of interest in this work giving an overview on the syntheses, properties and applications. It will be briefly described the technique used for the preparation of thin films, i.e. chemical vapor deposition, with a summary of the main parameters important for the deposition. Furthermore, optical properties will be introduced with a focus on the refractive index and extinction coefficient parameters, as main important parameters for light management.

Chapter 2 will focus on the synthesis of high-quality thin films of graphitic carbon nitride ($g\text{-C}_3\text{N}_4$) via chemical vapor deposition from the solid precursor melamine. The latter is a convenient safe powder precursor which sublimates at relatively low temperature and can thus be used as single-source precursor of C and N. The successful deposition of high-quality $g\text{-C}_3\text{N}_4$ thin films with tunable nano-sized

thickness will be described. The structure, composition and optical properties of the material obtained will be discussed with perspectives for future applications in optics.

In **chapter 3**, a method for the synthesis of boron carbon nitride (BCN) thin films from a solid single-source precursor will be introduced. Also in this case, a non-hazardous solid precursor has been chosen, but differently from the method described in chapter 2, in this case the precursor does not sublime but the thin film deposition occurs via thermal decomposition of the solid and followed by further polymerization of the volatile by-products on the substrate. Chapters 2 and 3 present methods for deposition of carbon-based thin films on various substrates using a chemical vapor deposition setup. Characterization of structural, composition and optical properties will be described and compared between different synthetic conditions.

Chapter 4 is dedicated to the controlled synthesis and characterization of carbons. Here, carbon suboxide has been prepared according to the method proposed by Diels in 1907 and further used as highly reactive synthon to obtain carbons at very low temperature (200°C). In addition, another synthesis method from very common precursors and very mild conditions is presented. The proposed methods are of high interest because they open ways for the alternative for synthesis of nano-engineered carbon materials both in bulk but, since carbon suboxide is gaseous, also in thin film technology for chemical vapor deposition.

Chapter I

1. Introduction

1.1. Basic concepts of carbon-based materials: from bulk to thin films

Carbon materials have been known since ancient times mainly in form as charcoal, soot, graphite and diamond. However, the name carbon was given from Antoine-Laurent de Lavoisier who took the name from the latin “*carbo*” i.e. coal. Lavoisier in 1772 proved that diamond is formed of carbon since it decomposes only in carbon dioxide upon combustion, as theorized from Sir Isaac Newton in 1704.^[1] Carl Wilhelm Scheele, in 1779, did a similar experiment on graphite that led to similar conclusion; until that time graphite had been thought to be a lead-based material.^[2] Just then it was clear that both diamond and graphite were different form of the same element. Almost 100 years later Friedrich Wöhler, with his famous experiment on conversion of ammonium cyanate to urea, paved the way for the current field of organic chemistry.^[3] These discoveries have been the fundamental milestones for the modern carbon chemistry: using the fact that by using the same element can be created materials which reveal very different properties depending on e.g. molecular structure, morphology and spatial arrangement. From the 20th century, with the development of modern analytical techniques carbon chemistry attracted more and more attention. Further improvements have been made with vacuum and high-pressure technology syntheses. From the 1960s on many different carbon allotropes have been prepared and studied with different degrees of hybridization (sp , sp^2 and sp^3) from HOPG (highly oriented pyrolytic graphite) fullerenes, carbon nanotubes, glassy carbons and last but not least isolated graphene (2004), which attracted much interest especially regards exceptional electronic, mechanical and thermal properties.^[4] With growing interest in carbon materials, a further way to control properties caught the attention in recent research: the introduction of heteroatoms into the carbon structure.

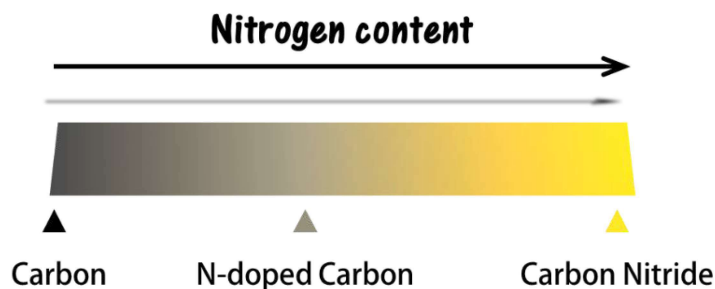


Figure 1.1. Tuning carbon properties by N content, from conductors to semiconductors.

In this regard, substitutional doping of heteroatoms into various carbon materials have been reported in the last decades, including graphene, graphite, porous carbon, carbon nanotubes, and fullerenes, in which C was substituted with other non-metallic elements such as B, N, P and S, with many reports in which also co-doping was achieved.^{[5] [6]} In such cases the C substitution, achieved by adding the abovementioned elements in a pool of sp^2 -bonded graphitic carbon atoms, can occur at the surface or as structural substitution. In the first case, the heteroatom mostly changes only the chemical properties, whereas structural substitution, by incorporation of heteroatoms in the graphitic sheets, deeply modifies physical properties of the material.^[6] Special attention has been given to N doping, which was proven to highly improve electrical conductivity by modification of the electronic structure.^{[7] [8]} With appropriate N insertion in the carbon structure the electron density at the Fermi level can be increased, the valence band lowered (more positive respect to standard hydrogen electrode), so making the material more stable upon oxidation.^[9] Therefore, proper introduction of structural N (or S and O) with aromatization and aromatic packing can further stabilize the material structure giving rise to what are nowadays called “noble carbons”.^[10] Strategies to obtain “noble carbons” rely on the choice of appropriate precursor, with HOMO level being highly positive (respect to standard electrode potential). Assuming for simplicity that upon carbonization the main released by-products are CO, CO₂ and NH₃, if they have less positive electrochemical potential, this pushes the material to reduce the internal energy which is reflected in an electrochemical increase of the HOMO level (figure 1.2). As introduced before, diamond and graphite have been proven to be made of carbon upon oxidation: in this way noble carbons have very different electronic properties with respect to their progenitors (diamond and graphite), however showing

structural and chemical common motifs (as aromatic structure and graphitic stacking).

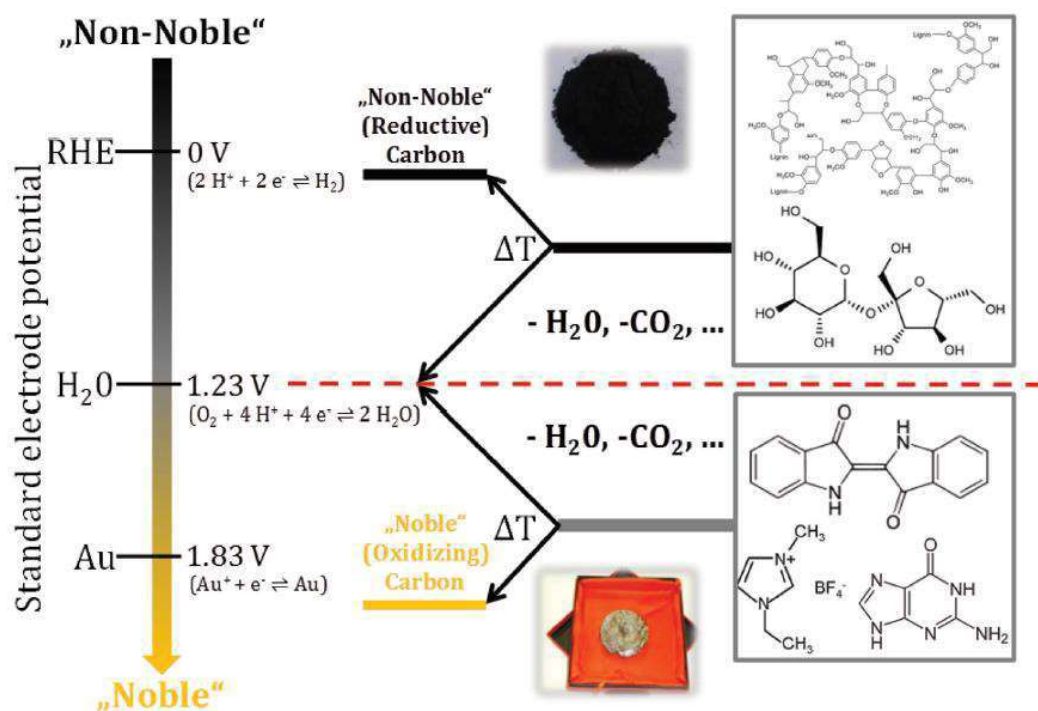


Figure 1.2. Strategies for the synthesis of noble carbons.^[10]

Alongside with the tuning of chemical and electronic properties of carbons, further options became available by structural tuning, i.e. with porous and hierarchical structures. For instance, it has been shown that carbon porosity, which also has an influence on carbon materials properties, can be tuned via hard-templating, soft-templating and salt-templating, avoiding further activation steps.^[11] Another way is using supramolecular preorganization of precursors in order to create materials with varying morphologies possibly introducing porosity and hierarchical structures.^[12] The just mentioned discoveries and improvements are just a little part of effort that the scientific community supplied over the last decades in carbon chemistry. However, all these studies and discoveries in carbon chemistry have paved the way for the application of carbons in many different fields: from catalysis^[13] to selective adsorption,^[14] from supercapacitors^[15] to membranes,^[16] but also in biomedical applications such drug delivery,^[17] ^[18] optoelectronics^[19] ^[20] and sensorics.^[21] ^[22] ^[23] Besides the described bulk methods, however, strategies to obtain coatings and films made of carbon-based materials are necessary in a world where technology is controlled by nano-sized devices: in that sense for future applications, carbon-based

materials need to be engineered not only from the chemical point of view but also from the geometrical point of view. Thin films of carbon materials have been employed as conductive electrode,^[24] ^[25] membrane for reverse osmosis,^[26] electro- and photo-catalysis,^[27] electrochemical sensing,^[28] thin film transistors,^[29] ^[30] planar carbon-carbon heterojunctions, superhydrophilic and superhydrophobic coatings,^[31] photovoltaic cells,^[32] light emitting diodes (LED) and more optical and photonic devices.^[33] In these latter cases, moreover high flatness, highly homogeneous deposition (to avoid light scattering for instance) and thickness control over wide range are required. For this purpose deposition methods to achieve highly homogeneous carbon-based thin films rely mainly on bottom-up techniques as vapor deposition methods. Vapor deposition methods such as chemical vapor deposition (CVD) and physical vapor deposition (PVD) are the most commonly used ones due to their reliability, low contaminations and high control over deposition parameters. As the CVD approach is fundamental to the work presented herein, it will be described in more detail in the following. Within the next sub-chapters, will be described the properties of the two main materials classes of this thesis, i.e. g-C₃N₄ and BCN materials, elucidating their properties and applications as bulk materials. Further description about state-of-the-art in thin film technology will be given in their dedicated chapters.

1.2. Graphitic carbon nitride: preparation and properties

The semiconductor technology is a key feature of the XXI century, which relies yet mostly on metal-based materials, III-V compounds and silicon-based technology. Since the advent of graphene, it has been proposed as the most promising candidate for next generation electronics.^[34] However, the absence of electronic bandgap and the (semi-)metallic character are limiting factors to develop graphene-based switches.^[35] Different strategies to open an electronic bandgap, for instance by inducing physical deformation such as wrinkles, ripples and crumples are currently under investigation, which can potentially induce an electronic band gap even larger than 1 eV.^[36] To date, other organic semiconductors are rising and particular attention has been regarded to g-C₃N₄ for its wide bandgap.^[37]

As early as 1834 Berzelius and Liebig reported about one of the oldest synthetic polymers named “melon” a progenitor of g-C₃N₄, however, back then characterization methods were not developed enough to get closer insights into the material.^[38]

Coming to a closer past, about 30 years ago, Liu and Cohen postulated the existence of covalent solids formed between C and N with extreme hardness, and few years later Teter and Hemley defined different possible structural configurations, with the g-C₃N₄ based on tri-s-triazine group among the energetically favored.^{[39] [40]} Since then, a plethora of attempts to synthesize carbon nitride materials as well as theoretical studies have been published and g-C₃N₄ has attracted more and more attention since it provides a sustainable fully-organic semiconductor that can be thermally synthesized from cost-effective precursors. In a way it can be viewed as an extreme case of substituting carbon with heteroatoms, as described in the section 1.1.

Syntheses of g-C₃N₄ have been reported from many different precursors, mostly based on organic molecules with high-N content such as cyanamide, dicyanamide, melamine and more.^[41] The reaction of these precursors at temperatures around 550°C lead to a polymeric structure of tri-s-triazine units, crosslinked by amino groups, even though in most materials referred as g-C₃N₄-substances the framework topology is a defective, N-bridged “poly(tri-s-triazine)”.^{[41] [42]} As a matter of clarity, in this work, polymeric materials based on heptazine units will be named as g-C₃N₄.

In figure 1.3 is shown the synthetic pathway of bulk g-C₃N₄ from melamine.^[43]

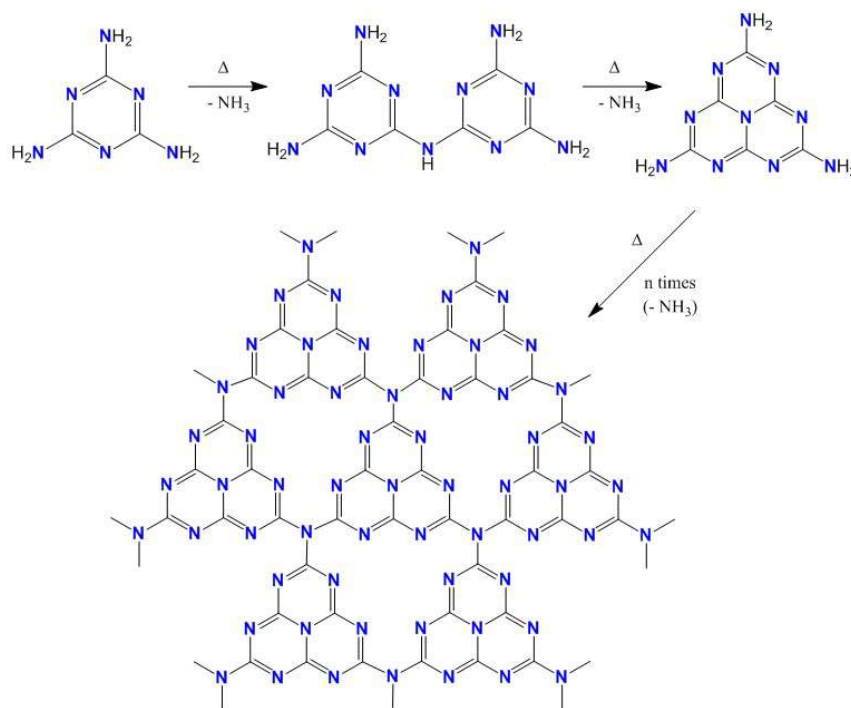


Figure 1.3. Synthetic pathway from melamine to g-C₃N₄.^[43]

The polycondensation reaction steps of melamine to g-C₃N₄ are endoergonic, driven to completion by continuously removing ammonia, leading to a material with ideal composition 3C:4N; however, incomplete condensation causes little amounts of unreacted terminal groups (amino groups) to be present.^[44] ^[42] The material is organized in graphitic-like stacked layers with interplanar distance of 0.32 nm, due to van der Waals interactions.^[45] ^[46] The latter together with the high degree of condensation and the stability of the tri-s-triazine groups are key point for the chemical and thermal stability: indeed, decomposition of g-C₃N₄ starts only slightly above 600°C with no residuals at temperature as high as 750°C, being so far among the most stable organic materials.^[45] ^[42] ^[46]

Electronic properties are, however, the most exciting part of g-C₃N₄. The highly conjugated polymeric system reveals semiconducting properties and an indirect bandgap of 2.7 eV (most commonly reported data) makes it feasible for applications with visible light.^[46] g-C₃N₄ is a metal-free n-type semiconductor, which has shown promising visible-light-response and electron-hole pair generation under visible light illumination which makes it highly interesting for photocatalysis.^[47] ^[48] Moreover, easy tunability of bandgap and band position by molecular or elemental doping is another reason why g-C₃N₄ has attracted much attention: for instance, narrowing of the bandgap has been achieved with different non-metal doping such as S, B, O and C, as reported in figure 1.4.^[47] In all cases, both valence band (VB) and conduction band (CB) have been shifted; doping could moreover induce a deeper modification in electronic properties of the material switching from n-type to p-type semiconductor as reported by Capilli et al.^[49]

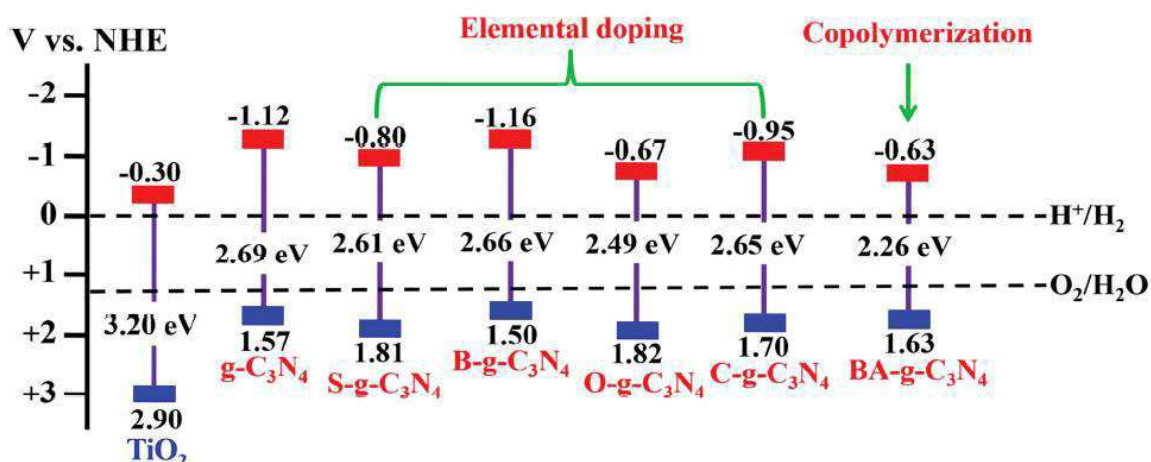


Figure 1.4. Schematic illustration of the band structure of g-C₃N₄ and doped g-C₃N₄ materials compared to TiO₂. The doping elements are placed before g-C₃N₄.^[47]

Band engineering and semiconductor properties switching from n-type to p-type are the fundamental for efficient heterojunctions and devices. Band alignment design of semiconductors is often adopted to promote exciton dissociation and separation of charges at the interface of two semiconductors, reducing charge recombination which is, however, fundamental also for semiconductor optoelectronics.^[50] Optimization of band engineering and the consequent in situ formation of a (fully organic-)heterojunction used as efficient photocatalyst for hydrogen evolution was reported by Shalom et al. obtained by introducing different amounts of barbituric acid (that provides C-doping to the material) in the precursor mixture. Schematic description of the charge separation and their use for photocatalysis is reported in figure 1.5.^[51]

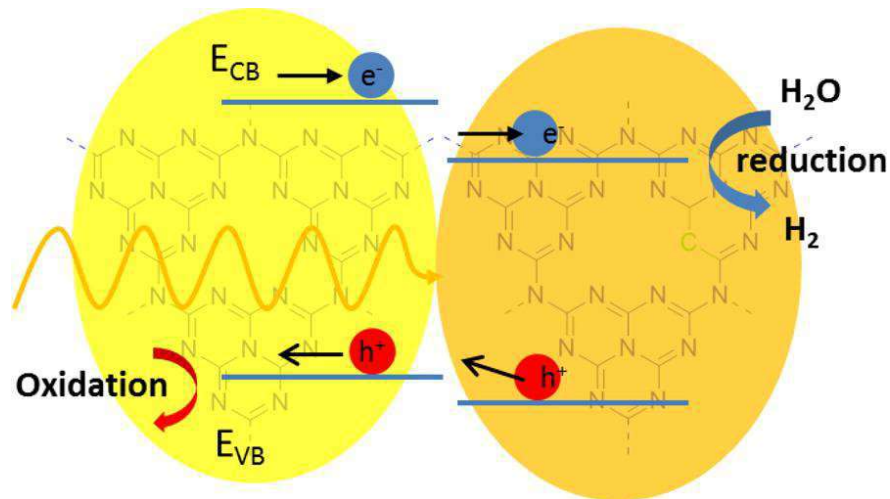


Figure 1.5. Heterojunction system proposed and the charge transfer process under light irradiation.^[51]

The elemental doping does not only allow for band engineering, but also affects material optical properties such as photoluminescence. Exemplarily, the photoluminescence of g-C₃N₄ is modified by changing the C/N ratio, as can be seen from the different colors depicted in figure 1.6, shifting to higher emission wavelength with increasing C content, from left to right.^[52]

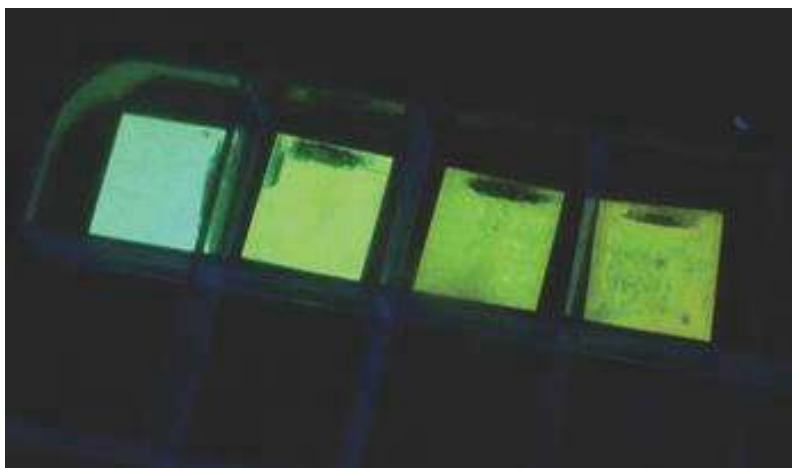


Figure 1.6. g-C₃N₄ sample with different amount of C-doping submitted to UV irradiation.^[52]

Therefore, as just shown, g-C₃N₄ is a very versatile organic semiconductor in which facile modification by non-metal doping leads to a very broad range of possible applications. It is worth to notice that g-C₃N₄ has been successfully employed for further application beyond photocatalysis, as fluorescence and electrochemical sensors,^{[53] [54] [55] [56] [57]} biomedicine,^{[58] [59]} for batteries and supercapacitors,^{[60] [61] [62] [63] [64]} as polymer initiator for gels^{[65] [66]} and solar cells,^{[67] [68] [69]} just to name a few. High incorporation of other elements, such as B in aromatic systems containing C and N lead to another class of materials, with different but as exciting properties as the g-C₃N₄ ones, i.e. BCN which is described in the following section.

1.3. Boron carbon nitride materials: preparation and properties

As mentioned in section 1.1 and 1.2, carbon-based materials can be modified by the introduction of other doping elements such as S, B, O. Starting from graphite, simultaneous introduction of B and N in a sp²-bonded graphitic layer opens a large combination of possible materials with distinct properties.^[70]

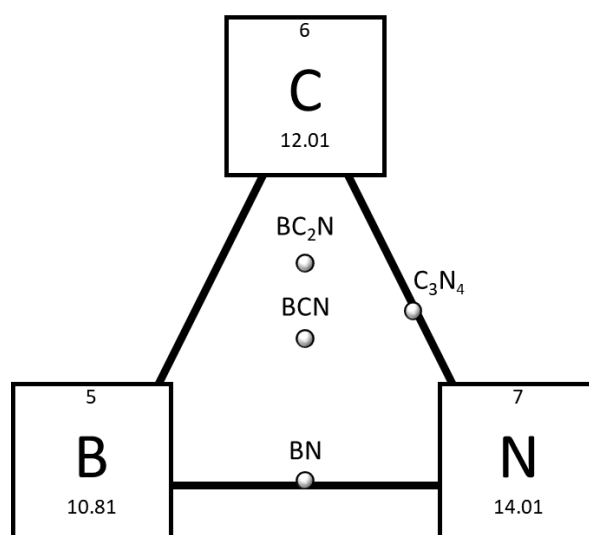


Figure 1.7. Ternary B-C-N diagram.

Taking into account the already mentioned graphene, a 0 eV band gap semiconductor, and substituting each couple of bonded C atoms with a B-N pair, hexagonal boron nitride (h-BN) is obtained, which is isomorphous to graphene but very different from a physical and chemical properties point of view. For instance, in the sometimes referred to as “white graphite” (h-BN), the electronegativity difference between B and N atoms leads to a localization of π electrons on N atoms thus creating an insulating material, with a bandgap larger than 5 eV.^{[71] [72]} Combining B, C and N could lead to different B-C-N layered configurations, since they can substitute with each other due to similar atomic parameters.^[73] The ternary B-C-N phase diagram shown in figure 4 highlights that a countless amount of possibilities can be achieved by tuning the elemental composition, from CN and BN to BC and ternary BCN compounds; in this latter case, theoretical studies show that the electronic structures and band gaps are dependent on the B/C/N composition and atomic arrangement in the material.^{[74] [75]}

To better clarify possible atomic arrangements in layered BCN materials, some possible 32-atoms unit cells are depicted in figure 1.8: it is worth to notice that already only for the BC_2N stoichiometry, there are more than 45 million theoretically possible 32-atoms unit cells (without taking into account the less possible ones containing B-B and N-N bonds).^[76] It has been recently reported, that BN and C are thermodynamically immiscible, and that they tend to separate into 2D domains of C and BN (like the second structure in figure 1.8), eventually creating an internal heterojunction with BN islands domains within the graphene lattice rather than an

homogeneous material.^[77] Theoretical studies support these results obtained by Ci et al., confirming that phase separation is favored below 3500 K and a strong preference for atomic arrangements neighboring B-N and C-C atoms while B-C, C-N, B-B or N-N bonds are disfavored.^[78] Phase segregation in BCN compounds is however still under debate in the scientific community and different reports have been published reporting BCN materials without phase segregation.^{[79] [80] [81]} Since mostly in literature there is no clear differentiation between these cases, they will generally be reported as BCN materials in this work.

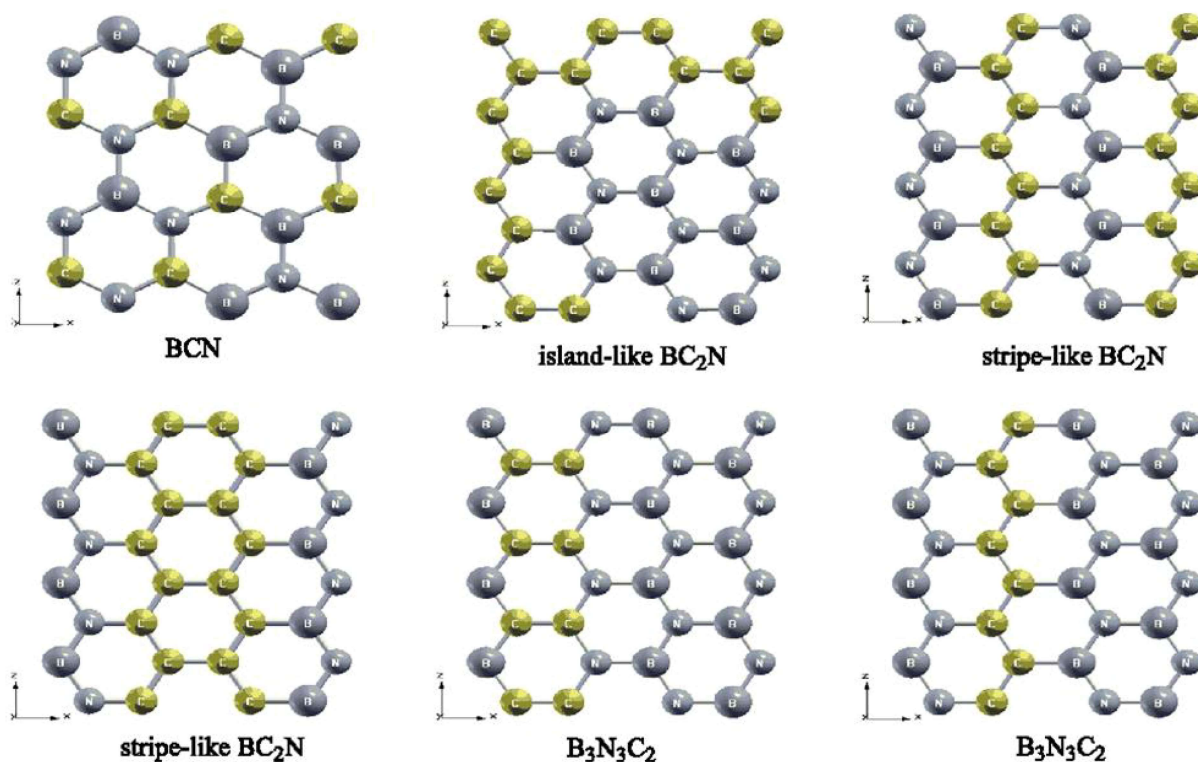


Figure 1.8. Six possible arrangement and composition for BCN layered materials.^[76]

Syntheses of bulk ternary BCN compounds have been reported from different compound: in most cases two co-precursor are used where one acts as a source of C and N elements and the second one a B source.^{[82] [83] [84]} Another possible approach is the use of single-source precursors, which has been achieved by use of B-C-N containing ionic liquid (N,N'-ethylmethylimidazolium tetracyanoborate) as reported by Fellingner et al. or complex mixtures of N-containing organic compounds, such as melamine and guanidine, with inorganic B compounds as boric acid.^{[70] [85] [86]} It has to be mentioned that due to high oxophilicity of B, it is generally very difficult from boron-oxygen containing precursor to cleave the energetically favored B–O

bond ($\sim 540 \text{ kJ mol}^{-1}$) introducing the B in a large conjugated system, which is reported to happen at temperature above 1000°C .^[70]

BCN materials have found application within different fields as hydrogen storage materials with tunable composition and specific surface area, as electrocatalysts for oxygen reduction reaction (ORR) in both alkaline and acidic media and colloidal dispersions with tunable fluorescence with possible application in biological imaging and optoelectronics, just to name a few.^{[84] [82] [85] [86]} This latter case is of particular interest, since by tuning the carbon content in the BCN (with high O content) structure, absorbance and fluorescence spectra are modified (figure 1.9), thus proving that different relative amounts of B/C/N (and O) successfully lead to modification of band gaps and optical properties of the final materials.^[84]

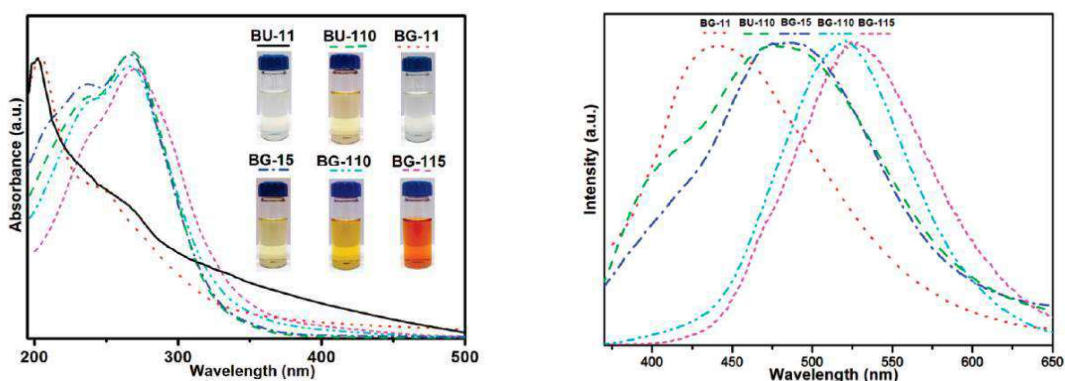


Figure 1.9. Absorbance (left) and fluorescence (right) spectra of different BCNO colloidal dispersion. Fluorescence and absorbance are tuned by changing relative composition.^[84]

As shown above, the material classes of carbon nitride and boron carbon nitride reveal many outstanding and tunable properties which can be applied in various fields including science and industry. This is, however, very likely just the tip of the iceberg, and future work will go the step toward inter- and trans-disciplinary research and applications across medicine, chemistry, physics and biology. In any case, all will have in common the need for methods to precisely tune nanostructures and morphologies. Because of this importance, the following part will focus on the CVD method as possible option for the controlled synthesis of carbon-based materials.

1.4. Chemical vapor deposition for thin film technology

In chapter 1.1 the importance of thin film deposition of carbon-based materials has been pointed out for different applications and that they can be obtained by physical

and chemical vapor deposition methods. It is nowadays difficult to define a clear border between physical and chemical deposition methods, since many techniques rely on combination of both techniques: however, as a general rule, physical methods can be ascribed to deposition methods where the film has the same composition as the source; on the other hand, in chemical vapor deposition (CVD), the composition of the film varies from the precursor one due to chemical reaction.^[87] The CVD method is of particular interest for the deposition and further implementation of carbon-based films in new generation organic devices, as for integrated electronics and lasers technology. CVD is a very powerful technique to achieve high-quality homogeneous deposition of thin films without constraints on the substrate topography, widely used for different materials from metal and oxides coatings to polymer and hybrid materials.^{[88] [89] [90] [91] [92] [93]} In order to understand what drives the film deposition in CVD processes, it is necessary to point out what are the sequential general steps occurring in the reactor from a gaseous precursor to the solid film growth, listed below and illustrated in figure 1.10:

- a. Diffusion of gaseous reactants to the reaction zone
- b. Possible gas-phase reactions that produces new reactive species and by-products (undesired)
- c. Adsorption of the reacting species on surface site and possible migration on the surface
- d. Surface chemical reaction between reactant species
- e. Desorption of volatile by-products of the reaction
- f. Diffusion of by-products away from the surface
- g. Incorporation of the condensed solid product into the growing film^{[94] [95]}

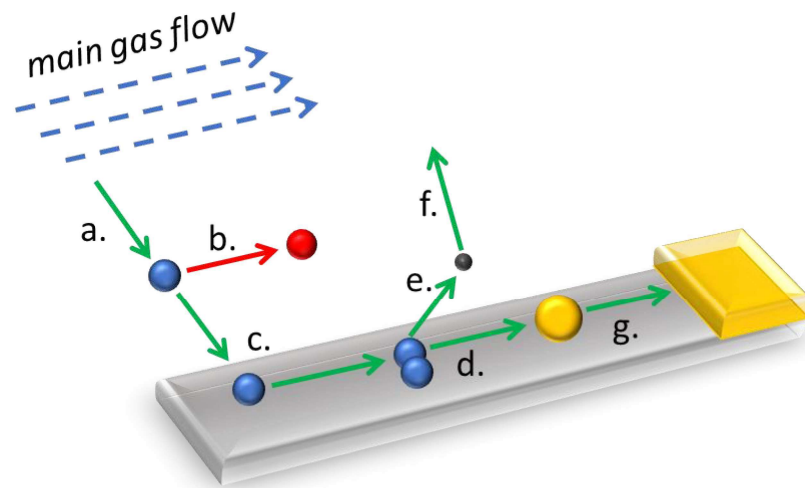


Figure 1.10. Schematic illustration of the CVD reaction steps described above (a-g).

Designing a CVD experiment requires an interdisciplinary understanding of chemical (reactions and reactions kinetic), physical (thermo- and fluido-dynamics) and engineering (mass transport phenomena and growth rate limiting steps as well as reactor design) parameters determining the deposition on the substrate.^[95] Many possible CVD configurations are nowadays on the market, such as thermal-CVD, plasma enhanced-CVD, photoenhanced-CVD and more, mostly coupled to vacuum systems for low pressure deposition. In this sense, the choice of setup is closely related to a particular film material and so is the critical point for the development. Among all the possible CVD techniques the following description of the process will focus on low pressure thermal CVD with horizontal configuration (as schematically shown as horizontal LPCVD reactor, in figure 1.11), in order to give insights of technique used in this work, from now on simply named as CVD.^[96]

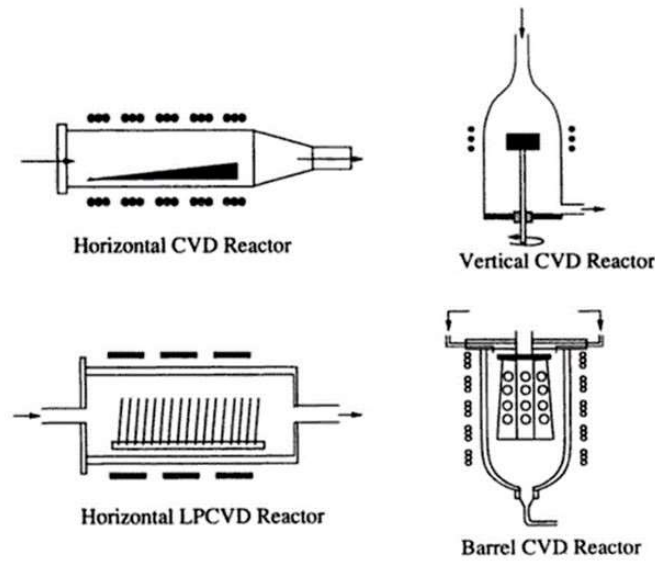


Figure 1.11. Possible CVD reactor configurations.

CVD allows achieving thin film deposition on a thickness range from single layer to few microns, by tight control of deposition parameters, temperature (T), pressure (p), gas composition and flow rates.^[94] In the following lines a brief description of the effect of these parameters on the deposition process will be given; however, a more detailed description from a physical, chemical and engineering point of view can be found in many specialistic books.^{[87] [97] [96] [94] [95]}

In steady state conditions, low pressure in CVD reactors assures to increase the free mean path and the diffusion coefficients of reactants, so improving homogeneous deposition by reducing the squared Thiele modulus (ϕ^2), defined for a general species "a" and a first order reaction as:^{[98] [97]}

$$\phi^2 = \frac{\text{"a" surface reaction rate}}{\text{"a" diffusion rate}} = \frac{L^2 k_s}{D}$$

where L is the depth length along x in the CVD reactor [m], k_s the reaction rate constant [s^{-1}] and D the diffusion constant [m^2s^{-1}]. On the one hand, to achieve high quality deposition, from an engineering point of view, reaction-controlled conditions are preferred. On the other hand it is well known that both k_s and D are T -dependent: k_s has exponential dependence to T (Arrhenius equation), whereas D in gas phase grows with $T^{3/2}$ (Chapman-Enskog model), so at high temperatures film growth can turn to be diffusion-control.^[99] However, D is inversely proportional to the pressure, thus extending the reaction-control regime even to high temperatures. For instance,

when the pressure is decreased from 760 Torr to 1 Torr the gas transfer of reactants on the surface and diffusion out of by-products are increased more than 100 times.^[100] For these reasons low pressures are nowadays the common approach to achieve high-quality film deposition. However, since CVD can be described as a tubular reactor fluid-flow condition become important as well, usually described by means of the dimensionless Reynolds number:

$$Re = \frac{\text{inertial forces}}{\text{viscous forces}} = \frac{\rho u H}{\eta}$$

where ρ is the mass density of the gas (kg/m^3), u is the flow velocity (m/s), H is the tube diameter (m) and η the viscosity ($\text{kg/m}\cdot\text{s}$). From the definition, laminar flow occurs at Re values lower than 1000, whereas above 2000 it is defined as turbulent flow. It is worth to underline that, in steady state conditions, Re is independent of the p .^[97] ^[94] In CVD reactors laminar flow (low Re) is preferred to achieve good reproducibility and process control. Gas-flow conditions affect the deposition by the resistance offered to mass transfer at the surface of the target substrate, defined as boundary layer (δ), which grows radially from the edges to the center of the target substrate (axial position respect to the edges, x) and decreases with increasing of Re (figure 1.12).^[94]

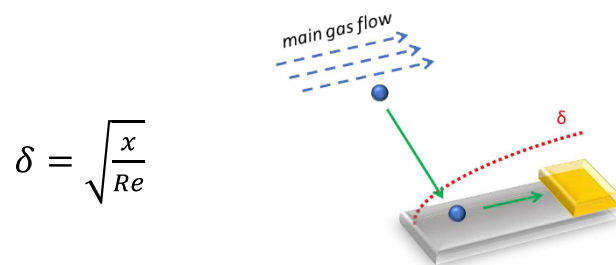


Figure 1.12. Equation and schematic depiction of the boundary layer (δ).

Engineering parameters are extremely important since they give a direct insights for optimal performance of CVD setup; however, it is very difficult to optimize all the above mentioned conditions in practical experiments, but as a general rule low pressures and low gas flows are important for homogeneous deposition, as well as keep the temperature as low as allowed by reaction thermodynamics and kinetics.

1.5. Optical properties of materials

Solid materials are commonly classified into three categories defined as metal (or conductors), semiconductor and insulator. An insulator is a material which presents an energetic gap between the valence band (VB, i.e. the energetically highest completely filled level according to Pauli principle) and conduction band (CB, i.e. the next highest band unoccupied with electrons).^[101] On the other hand, materials in which VB and CB overlap and thus no bandgap (BG) is present, are called conductors.^[102] Semiconductors fall in between, since a BG between VB and CB is present like in insulators but typically the BG energy is of the order of the photon energy of visible light or less (figure 1.13 (a)).^[101] Conductors, semiconductors and insulator can be also distinguished from their characteristic optical properties: insulators and semiconductors are optically transparent at energies below their BG energy, whereas metals are not.^[101] The Fermi level defines the energy level (possibly fictitious) where at a given temperature there is a 50% probability that such state is occupied by an electron, is of particular interest especially for semiconductor materials. If this level lies in the middle between VB and CB the semiconductor is defined as intrinsic, whereas n-type semiconductors and p-type semiconductors are defined when Fermi level energy is closer to the CB (higher electron density) or to the VB (higher hole density) respectively, schematically shown in figure 1.13 (b).^[103] Detailed description of band structures in solid materials is out of the scope of this work, but can be found in many specialistic books.^{[101] [103]}

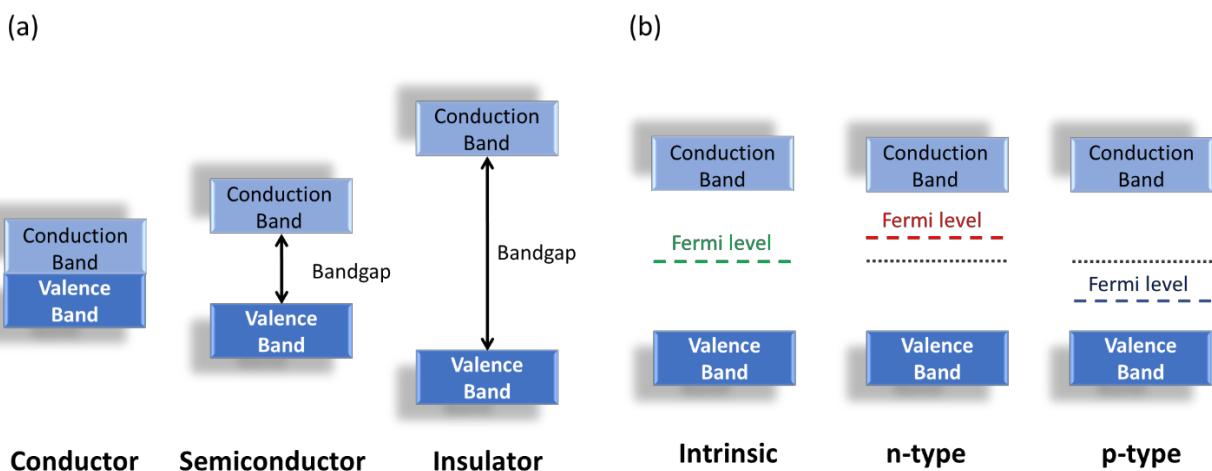


Figure 1.13. (a) Classes of materials; (b) classes of semiconductors according to the position of the Fermi level.

As mentioned above, semiconductors have BG energies that are the order of photon energy of visible light or less. In a simplified description, when a photon with higher energy than the BG interact with a material it may trigger the promotion of an electron from the VB to the CB, leaving a positive charge (hole) in the VB so creating an electron-hole pair. Electron-hole pairs have limited lifetime in a material and they can eventually recombine, with the electron returning into the hole of the VB. If this recombination occurs with photon emission, the process is called photoluminescence (PL). It is worth to point out that the emitted photons can also be reabsorbed by the material and further emitted by other decay process, as long as the photon energy is sufficient for a further transition (if there is any).^[101] The photon absorption depends on the absorption coefficient (α) which is defined as the power removed from the incident beam per unit volume per unit flux of electromagnetic energy.^[104] In absorption/transmittance measurements the light intensity (I) passing through a sample of thickness (z) decreases respect to the incident beam intensity (I_0) where the absorption coefficient increases, as described by the following equation, known as Lambert law:

$$I = I_0 e^{-\alpha z} \text{ with } T = \frac{I}{I_0}; A = -\text{Log}(T)$$

where T is the transmittance and A the absorbance, both dimensionless numbers.^[105] The absorption coefficient is however proportional to the imaginary part of the complex refractive index, which is a function of wavelength (λ), commonly denoted as extinction coefficient (k) (ω is the angular frequency):^{[106] [107]}

$$\alpha = \frac{2\omega k}{c} = \frac{4\pi k}{\lambda}$$

The complex refractive index (N) is usually written as the sum of its real (n) and imaginary parts (k) which are called the optical constant of the solid material:^[106]

$$N = n + ik$$

The real part is a dimensionless number named the refractive index and it is defined as the ratio between the speed of light in vacuum (c) and the speed of light in a medium (v):^[108]

$$n = \frac{c}{v}$$

The complex refractive index of a material is of paramount importance especially in thin film technology for optics and photonics since it correlates light-matter interactions with physical observables. Above it was already described the light-matter interactions in terms of transmittance and absorbance. However, another physical observable related to the complex refractive index is the reflectance (R), which at normal incidence for a non-absorbing material with thickness much larger than the wavelength and interfaces exposed to air, it becomes:

$$R = \frac{(n - 1)^2}{n^2 + 1}$$

where R is a dimensionless number lower or equal to unity.^[105] It is worth to remember that the sum of light intensities incident on a material absorbed, transmitted, reflected (and eventually scattered) is equal to unity and each fraction interaction depends on the optical constants (and eventually morphology) of the solid material.^{[106] [105]}

Eventually, the complex refractive index is of paramount importance for design optical and optoelectronic devices. The opportunity to tune it within organic materials offers a wide field in research and can promote development of new generation organic devices with outstanding properties, as it will be shown in the following chapters.

Chapter II

2. Graphitic carbon nitride thin films

This chapter will focus on the synthesis and characterization of graphitic carbon nitride (g-C₃N₄) thin films with an overview on the synthesis attempts already reported in literature and as a main focus the deposition method developed during the present work by CVD. Structural, composition and optical characterization will be shown with different possible application for this material in optics and beyond.

2.1. Background and state of the art

As summarized in chapter 1, g-C₃N₄ has attracted much attention in the scientific community due to its unique properties, especially related to bandgap (BG), valence band (VB) and conduction band (CB) position which makes it an appropriate semiconductor especially for photocatalysis. For example, thin films of g-C₃N₄ have been tested with promising results in electrocatalysis, photoelectrochemical cells (PEC), light emitting diodes (LEDs) and solar cells, membranes for ionic transport, actuators but also for biomedical applications.^{[1] [2] [3] [4]} However, the processing of g-C₃N₄ thin films is still difficult because of the cross-linked nature of the polymer (since the monomeric unit - in red in figure 2.1 - is trifunctional) and the dispersive forces (usually named π - π stacking) between g-C₃N₄ layers make it insoluble as well as hardly exfoliable and dispersible in common solvents. As a consequence, g-C₃N₄ up to now could not be processed as thin film via common methods for polymers as spin coating, spray coating and doctor blade.^{[5] [6] [7] [8] [9]}

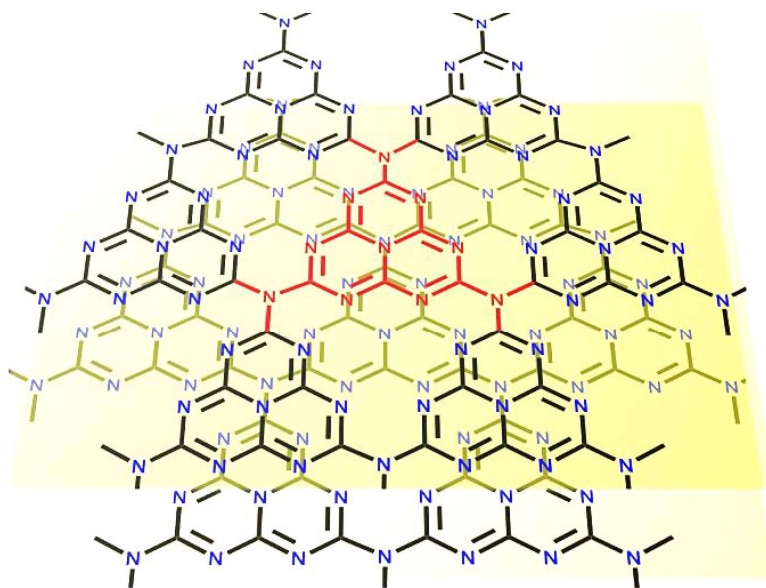


Figure 2.1. Structure of $g\text{-C}_3\text{N}_4$; in red the heptazinic monomeric unit is highlighted.

Very recently, different research groups have tried approaches to achieve $g\text{-C}_3\text{N}_4$ films on different substrates; however, in many cases, only poor-quality deposition has been achieved. Eventually, a simple and reproducible method to achieve high quality thin film with tunable thickness is still needed, to finally implement $g\text{-C}_3\text{N}_4$ thin films in optical devices.

Attempts to synthesize $g\text{-C}_3\text{N}_4$ thin films can be classified into two different categories: top-down and bottom-up approaches. Top-down methods requires various steps, often time and resource consuming, and in most cases only achieves poor substrate coverage and substrate-film contact.^[10] In this category, the Wang group recently reported on $g\text{-C}_3\text{N}_4$ dispersion prepared from cyanamide at 550°C and further treating under reflux with a strong oxidizing acid (HNO_3) at 80°C for 3 hours, which led to stable colloidal dispersion of $g\text{-C}_3\text{N}_4$ with average particle size about 310 nm. The thin films were then prepared via dip/disperse-coating and further annealing at 350°C in order to fully remove the acid and improve the poor contact of the film with the substrates surface. The film obtained showed improved performances in PEC compared to similar attempts, with about 7 times more photocurrent density respect to traditional $g\text{-C}_3\text{N}_4$ film electrodes.^[8] In our group, Kumru et al. presented a different approach to achieve stable colloidal dispersion of $g\text{-C}_3\text{N}_4$ and phenyl-doped $g\text{-C}_3\text{N}_4$ via sonication in 4-methyl-5-vinylthiazole (vTA) and visible light-triggered surface polymerization of the vTA moieties on the $g\text{-C}_3\text{N}_4$ particles.^[11] The as-modified material was then re-dispersed in chloroform, spray-

coated on a glass substrate and dried in vacuum. The authors showed also that such dispersion with very high aspect ratio (1.2-1.3 nm thick times 20-40 nm wide) can be used also as ink for inkjet printing, with possible future applications as lumiphores in ultramicroscopy and electron buffer layers in perovskite solar cells. The surface modification led to an unexpected long time stability of the dispersion in polar organic solvents and the film obtained are highly photoluminescent, with increased absorbance and PL-lifetime but lower PL internal quantum yield.^[11] In both cases, it is clear that high quality dispersion has been achieved; however, many different time-consuming steps and uses of toxic compounds are still required. Moreover, the achieved films are not homogeneous on a large scale, since only small particles are deposited without interconnection which is likely to negatively affect performances for applications in optics and optoelectronics.

Some examples of pioneering work on g-C₃N₄ films with bottom-up approaches have been proposed in literature. One of the first successful attempts have been reported in 2015 and described as “a combination of CVD and microcontact printing techniques”; the authors used anodic aluminum oxide membrane as a porous template and dipped it in cyanamide solutions to fill the pores with the g-C₃N₄ precursor (figure 2.2 (a)).^[12] The porous membrane, which in this way acts as a tank of cyanamide, was subsequently sandwiched between two substrates (glass or FTO) and heated up at 550°C for 4 hours under N₂. The obtained films, that were deposited on the glass side of the sandwich, showed micro-clusters on the side contacted with the membrane, whereas, the side grown at the surface of glass were flat and homogenous. More importantly, it has been shown that uniform deposition over large surfaces has been achieved, the film thickness was increased by increasing the amount of cyanamide in the solution and thicker films were even possible to be peeled-off the substrate, after dipping the samples in water. Yet, ultrathin film grown on FTO revealed the highest photocurrent density for pure g-C₃N₄ in photoelectrochemical (PEC) applications, 30 times higher than a later attempt to grow g-C₃N₄ thin films via electrophoretic deposition on FTO, enhancing one more time that better performances are achieved with a bottom-up respect to top-down deposition.^[12] ^[13] The positive results obtained previously for photoelectrodes by microcontact printing further pushed the performances improvement with different bottom-up approaches. Slightly later, Xie et al. reported on a chemical wet approach based on solvothermal method using melamine and

cyanuric chloride dispersion in acetonitrile to directly deposit on FTO-coated glass (figure 2.2 (b)).^[10] The FTO was directly placed in the autoclave with the dispersion and heated at 180°C for 24 hours. After cooling down, the conductive substrate was removed, washed and placed at 520°C for 1 hour. On the one hand, with this wet and multistep method photocurrent density was still about 9 times lower than the microcontact printing method, but, on the other hand, it was shown that this value was still about 18 times higher than for thin films derived via typical top-down approach from spin-casted dispersion. The better performances were confirmed also by electrochemical impedance spectroscopy, in which the authors attributed the difference between the methods to better contact between substrate and film in bottom-up approach than for top-down ones.^[10] By comparing the two bottom-up methods presented so far, the solvothermal one led to larger grains and lower performances, suggesting that vapor-based methods could provide better film quality in terms of homogeneity, performances and substrate-film adhesion (for instance, also for heterojunction preparation this is extremely important).^[11] Another liquid-based approach was proposed by Xu et al. in which they successfully deposited $\text{g-C}_3\text{N}_4$ on different substrates by burying them into a 1:1 mixture of cyanuric acid and 2,4-diamino-6-phenyl-1,3,5-triazine (CMP) (even C-doped with different amounts of barbituric acid) and heating at 550°C (figure 2.2 (c)).^[14] They have shown that CMP at 352°C undergoes liquefaction and this would allow more intimate film-substrate contact; a 500 nm thick film was then implemented as electron acceptor into organic solar cells and under solar simulator illumination showing an open-circuit voltage of about 1 eV. Despite the positive and very stimulating results, the films show a highly porous structure, which increases light scattering, a characteristic that can be detrimental for many applications especially in optics and optoelectronics, with lower limit for homogeneous deposition around 200 nm.^[14] ^[15] This approach inspired further works, leading to achieve very high current densities in PEC (up to 10 times higher than with microcontact printing) for water splitting devices. In this latter case, 20 combinations of precursors have been analyzed and only in one case a compact homogeneous film was achieved (a further step to remove large aggregates was necessary).^[16] Another bottom-up approach is the use of solid-state direct-growth of carbon nitride on solid substrates. Shalom et al. have grown thin films from 1:1 mixture of melamine and cyanuric acid by putting a thin layer of the precursor mixture between two substrates which is then heated at 550°C under N_2 flow

(figure 2.2 (d)).^[17] Very different morphologies have been found on different substrates, showing the important effect of the substrate on the film growth reflected also in the optical properties with different fluorescence and absorbance spectra for different substrate (after flushing with the surface to remove large aggregates).^[17] A further interesting solid-precursor-based approach was proposed by his group, in which they used a precursor paste of melamine and barbituric acid in ethylene glycol, which was spread over a solid substrate by razor blading and calcined at 550°C. Contrary to previous methods, this tool would allow a certain control over thickness (in the μm range) and provide an easier way to build up planar heterojunctions.^[18]

The last part of this overview on synthetic methods for g-C₃N₄ thin films will be focused on vapor-based methods, which have shown to be the most promising methods to achieve highly homogeneous g-C₃N₄ thin films. Thermal vapor condensation (TVC) was one of the first vapor methods reported, just few years ago. To achieve film deposition, Bian et al. used melamine as convenient precursor, since it sublimates at temperature around 300°C, to fill a crucible; between the powdery precursor and the lid a clean substrate was put and heated up to 500-600°C (figure 2.2 (e)).^[19] Upon heating above the sublimation point of melamine, the melamine vapor condensed on the surface of the substrate eventually creating, at higher temperature, the g-C₃N₄ network. They showed also how different substrates affect the film morphology comparing glass (very rough surface) with the smoother films on fused silica and ITO, as well as different precursors (dicyandiamide, thiourea, and urea). However, between all precursors the most uniform films were obtained from melamine. The prepared film on FTO showed the highest photocurrent density, possibly due to higher homogeneity and intimate contact to the substrate. ^[19] A follow-up work showed that by introducing 2,6-diaminopyridine as co-precursor with melamine, photocurrent density can be improved four more times respect to the bare g-C₃N₄ film, due to structural sp² C doping in the film structure.^[20] This approach further stimulates research in this direction since quality of films was quite highly improved. Arazoe et al. reported a method, named vapor deposition polymerization, to produce free-standing g-C₃N₄ thin films from guanidinium carbonate. Moreover, as in previous cases also in this case the amount of material and the heating time were the parameters that allowed for the control of the film thickness. The authors claimed that deposition occurs via thermal vaporization of melemium carbonate, which deposits on the substrate and further polymerizes to g-C₃N₄. The films were applied

as light- and humidity-driven thin film actuator, showing that light and humidity causes wrapping of the thin film. [3] [21] Based on the knowledge of previous methods, in this work melamine is used as precursor in a CVD setup in order to create high-quality g-C₃N₄ thin films with tunable thickness.

In the following picture (figure 2.2), are schematically represented the bottom-up methods just described, before the introduction of the new method developed during this work by means of CVD.

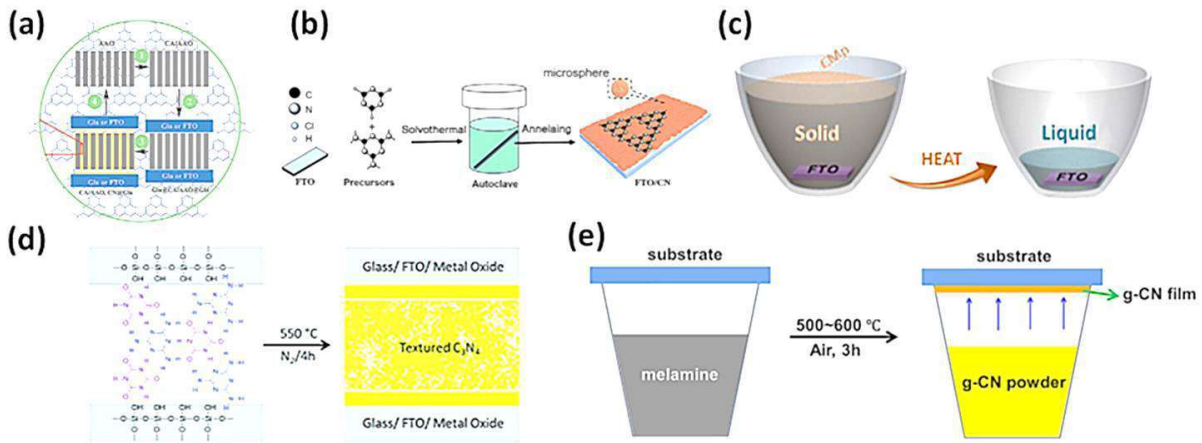


Figure 2.2. Methods for preparation of g-C₃N₄ films: (a) microcontact printing, (b) solvothermal, (c) liquid-based direct growth, (d) solid-based direct growth, (e) thermal vapor condensation method.^[1]

2.2. Chemical vapor deposition of g-C₃N₄ from melamine precursor

As reported above, vapor-based methods seem to give best results in terms of film quality, thickness tunability and homogeneity which are extremely important especially in fields like optics and optoelectronics. However, current methods still only result in films of low quality and control over processes remains limited.

In order to overcome these problems and carry carbon-based semiconductors to the next level, different methods have to be applied. Therefore, varying approaches have been taken into consideration and eventually a setup known to give high quality thin films widely exploited for inorganic materials, i.e. the CVD, has been chosen as possible target solution. It is a well-known method to achieve high-quality and homogeneous thin films over large surfaces, even for cross-linked organic networks where the lack of solubility becomes a problem with common solvent-based methods such as spin coating, spray coating or inkjet printing. Moreover it allows the control of deposition over a very wide range of thicknesses, from micrometer-sized to few-nm with very low defects and impurities.^[22] CVD is a powerful method for the deposition

of thin films, however, the complexity of the method requires prior verification before making decision on the setup.

Based on the knowledge of previous methods, melamine was chosen as a convenient solid non-hazardous precursor since it sublimates around 300°C and at 550°C it polymerizes to g-C₃N₄, as previously reported.^[1] The possibility to create high-quality g-C₃N₄ thin films with tunable thickness was first exploited by vapor deposition polymerization, schematically shown in figure 2.3 (a), (b).^[2] This method is used as a proof-of-concept to test the feasibility of a method with the CVD setup, since both are vapor-based methods for thin film deposition. The test setup consists of a test tube, which serves as the tubular reactor similar to the CVD setup, in which at the bottom is placed the melamine precursor and at the top a target substrate (glass, quartz, silicon and more). The test tube-reactor is then capped with an aluminum lid (with holes) and placed in a furnace. In order to create sufficient amount of precursor vapors, a two steps heating ramp was used. In the first step, the test tube is heated to 300°C and kept for 30 minutes, to let melamine sublimate. Subsequently the temperature is further increased to 550°C to achieve the polymerization of melamine to g-C₃N₄ on the target substrate. Furthermore, it was possible to tune the thickness in the range between 140 and 1000 nm by increasing the precursor amount from 0.2 to 2.0 g.^[2] As shown in figure 2.3 (c), (d), (f) and (g), the proof-of-concept setup with test tube, serving as analogous of the CVD setup, indeed allows obtaining thin films which reveal the characteristic features of g-C₃N₄. In particular, figure 2.3 (f) and (g) show the typical diffraction pattern of highly organized g-C₃N₄ structures containing C and N elements involved in a conjugated structure, as depicted by the EELS spectrum in figure 2.3 (d).

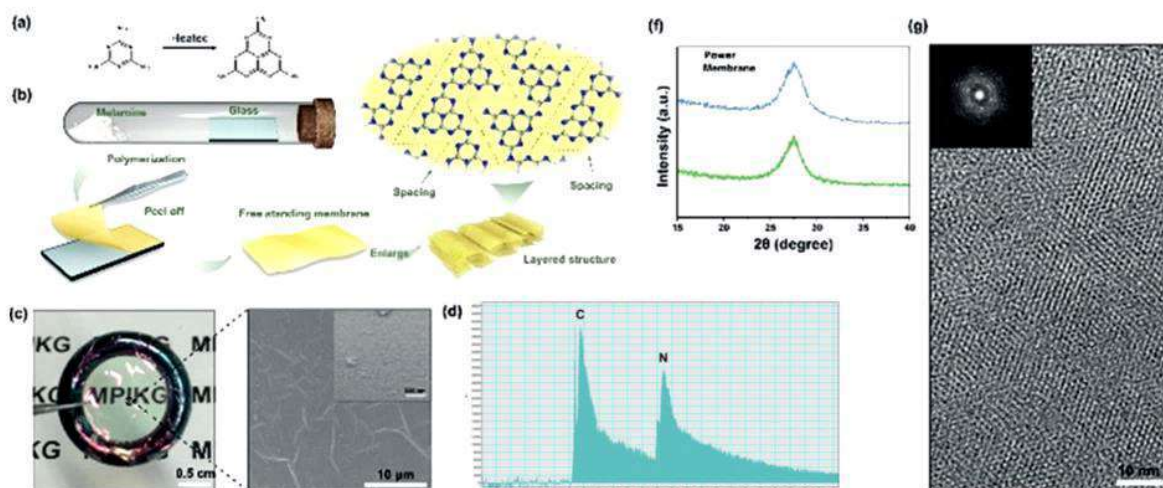


Figure 2.3. (a), (b) Proof-of-concept test tube method used for the deposition of g-C₃N₄ film from melamine precursor. (c) Free-standing g-C₃N₄ thin film and SEM image, (d) EELS spectrum, (e) XRD diffraction pattern, (f) TEM image and FTT (insert) of the g-C₃N₄ thin films prepared by the test tube method.^[2]

The successful results obtained by this proof-of-concept setup confirmed melamine to be a suitable precursor for vapor-based deposition approach and therefore allowing for the purchase of the CVD machine.

In this work, for the deposition g-C₃N₄ thin film, a thermal and low-pressure CVD setup was chosen (PlanarGROW 3S, from PlanarTech in figure 2.4). Briefly, the setup consists of 3 mass flow controllers up to 500 sccm connected to synthetic air, N₂ and Ar that can be pre-heated up to 100°C. The reaction chamber is a quartz tubular reactor (3 inches diameter) with two ovens that allow control of the temperature separately, up to 1000°C. The two ovens are the fundamental part of the reactor, the first one which will be named “upstream” is used to sublime the precursor, whereas the second one “downstream”, where are placed the target substrates on which deposition/polymerization will eventually occur. As a general approach during this work, the upstream temperature is lower than the downstream one, so that the evolved gas is eventually polymerized at higher temperature on the substrate surface. The reaction tube is connected to a dry pump by two valves to carefully control the pressure inside the reactor. A liquid N₂ trap, is placed beforehand to avoid possible corrosive by-products to enter the pump. Pressure inside the reactor, under flow conditions, is monitored by two manometers in the range 10-1000 Torr.



Figure 2.4. CVD setup PlanarGROW 3S, from PlanarTech, used in this work.

As described above, the chosen setup allows a strict control of many different deposition parameters, also very challenging when it comes to find the right combination to achieve high quality films.

Contrary to most of the approaches proposed so far for carbon-based materials thin film deposition using CVD, which includes the use toxic or possibly explosive gases, in this work it was decided to use non-hazardous solid state precursors.^{[23] [24]} Melamine was chosen as convenient precursor, since it sublimates at relatively low temperatures (around 300°C, as shown in TGA in figure S1) and at higher temperature it polymerizes into g-C₃N₄. The precursor is heated at a rate of 10°C/min to 300°C, to avoid fast sublimation which can create turbulence in the reactor, possibly affecting homogeneity of the final thin film (sublimation rate of melamine in this condition is 0.66%/min determined by derived thermogravimetry (DTG) in figure S1). Low values of pressure (10 Torr) and carrier gas flow rate (50 sccm, standard cubic centimeters per minute) are chosen, to have a reaction-controlled regime and reduce the turbulence in the reactor, as introduced in chapter 1.4. If not otherwise stated, the carrier gas is N₂; moreover, before each thin film synthesis, the reactor is flushed (for 10 minutes) with the carrier gas to remove

possible gaseous contaminants. As already mentioned, melamine polymerizes to $g\text{-C}_3\text{N}_4$ at 550°C , defining then the temperature of the second CVD oven. It is important to point out that to achieve deposition, downstream oven has to reach the final temperature (550°C) before the upstream oven starts the heating program: in fact, if ovens start heating together only poor quality, or even no film deposition is obtained. Since the reactor is larger than the test tube, the amount of material has to be increased respect to the proof-of-concept experiments. Moreover, the melamine precursor needs to be kept at 300°C until full sublimation is achieved to control thickness simply by the amount of precursor introduced in the CVD reactor. For optical characterization $g\text{-C}_3\text{N}_4$ films were deposited on silicon and fused silica substrates, however, film deposition has been successfully achieved also on Cu, glass slides, FTO, carbon paper and aluminum oxide, confirming thus the robustness of the methodology presented.

Two different CVD methods have been used, which growth profiles are depicted in figure 2.5 (a) (CN-1) and (b) (CN-2); the difference between the two methods is the downstream time, e.g. the time at which the substrates are kept at 550°C which are 90 and 330 minutes respectively. Thin films of $g\text{-C}_3\text{N}_4$ have been prepared by the two methods using 5 and 10 g of melamine to evaluate the possible differences between the two methods, in terms of thin film thickness, for instance.

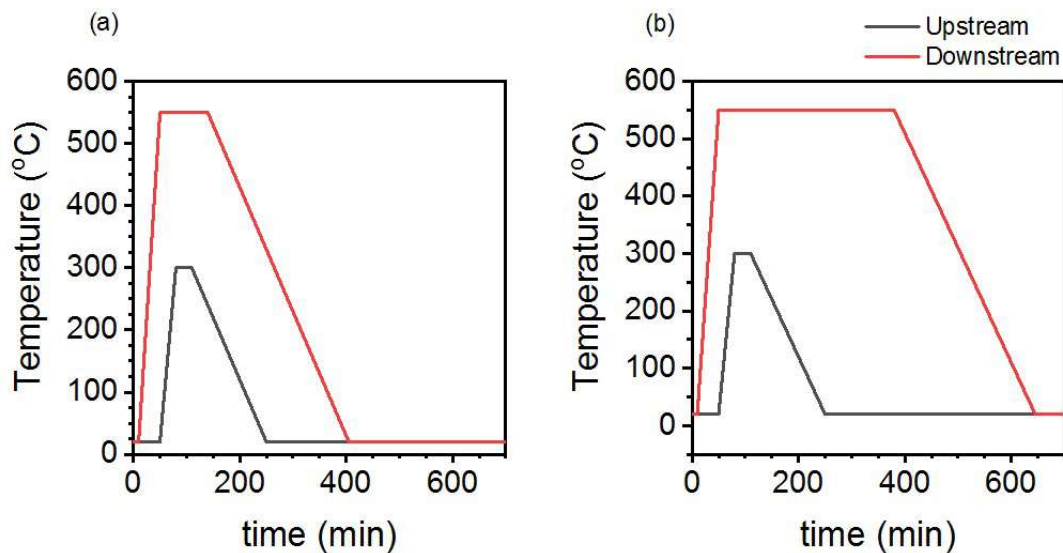


Figure 2.5. Growth profiles used for $g\text{-C}_3\text{N}_4$ thin films deposition: (a) CN-1, (b) CN-2.

Table 2.1. Summary of the samples presented in this chapter.

Sample	Melamine amount (g)	Upstream temperature (°C)	Upstream time (min)	Downstream Temperature (°C)	Downstream time (min)
CN-1a	5	300	30	550	90
CN-1b	10	300	30	550	90
CN-2a	5	300	30	550	330
CN-2b	10	300	30	550	330

Thin film deposition has been successfully obtained, as shown in figure 2.6 (a-c). In figure 4 (a) and (b), are shown the thin film samples CN-1a and CN-1b deposited on fused silica substrates. The different colors suggest that thin films with different thickness have been obtained. The bright color of the sample in figure 4 (b), it is possibly due to light interference, which suggests that this film has higher thickness respect to the one in figure 4 (a). In figure 4 (c), it is shown a large area free-standing sample (CN-1b), which has been peeled off from a glass substrate. The free-standing thin film was eventually obtained by soaking the prepared film in water for 48 hours and removed from the substrate with a spatula. The possibility to obtain large free-standing films is interesting, since it allows to move the thin films on different substrates or to use them as a single layer material. The latter is of particular interest for instance for membrane separation in liquids, where the solid substrate is usually undesirable. It is worth to point out, that below an approximate thickness of 100-150 nm it seems to be not possible to obtain large free-standing areas, possibly due to the strong interactions created during the deposition of the film (possibly even covalent) or low permeation of water below the film.

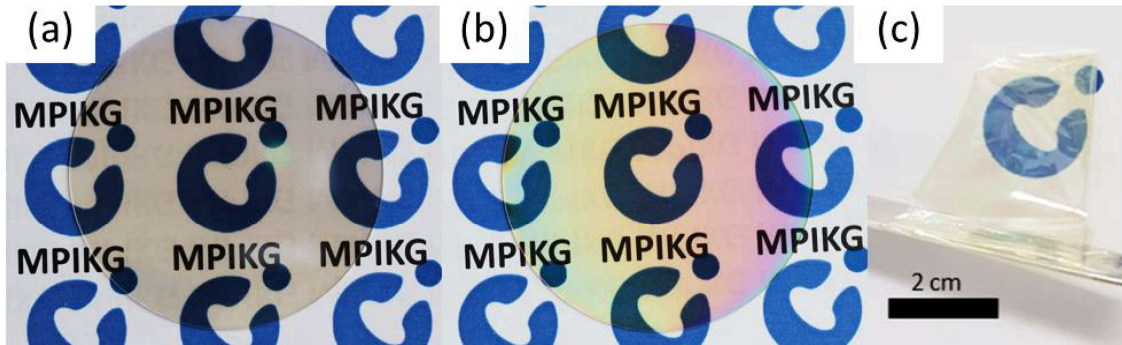


Figure 2.6. (a) CN-1a sample and (b) CN-1b sample on 2'' fused silica slide; (c) large area free-standing CN-1b sample.

The thin films have been inspected by scanning electron microscopy (SEM) to investigate the homogeneity of deposition on the substrates. In figure 2.7, are shown representative images of the thin films deposited on fused silica ((a) and (b)) and silicon ((c) and (d)) substrates. Figures 2.7 (a) and 2.7 (c), show very high homogeneity and defect-free surface of the deposited film: the homogeneity is so high, that is even difficult to say if the film is present or not (even on curved areas, as the edge of the fused silica wafer as shown in figure S2). The presence of the film is shown at the cut-edges, in figure 2.7 ((b) and (d)) (highlighted by arrows), where some defects occur in the film due to breakdown of the substrate. In both images, the films look very thin and well adhered to the substrate surface. The intimate contact with the substrate surface is an important characteristic, as previously mentioned in chapter 2.1, e.g. for planar heterojunctions. Thin film deposition has been successfully achieved also on other substrates, as for examples glass slides and carbon paper as shown in figure S3. The high homogeneity and flatness are confirmed also by atomic force microscopy (AFM), depicted in figure S4 (a) and (b). The analyses on the CN-1a (figure S4 (a)) and CN-1b (figure S4 (b)) thin film deposited on quartz substrates reveal very low roughness, comprised between 1 and 1.5 nm, without defects over large areas ($100 \mu\text{m}^2$). The surface roughness is an important parameter especially in optical applications, since samples with high surface roughness can give rise to undesired scattering effects, which can be detrimental for applications like lenses. In this case, the surface roughness is very low and similar to the surface roughness of the bare fused silica substrate (figure S4 (c)).

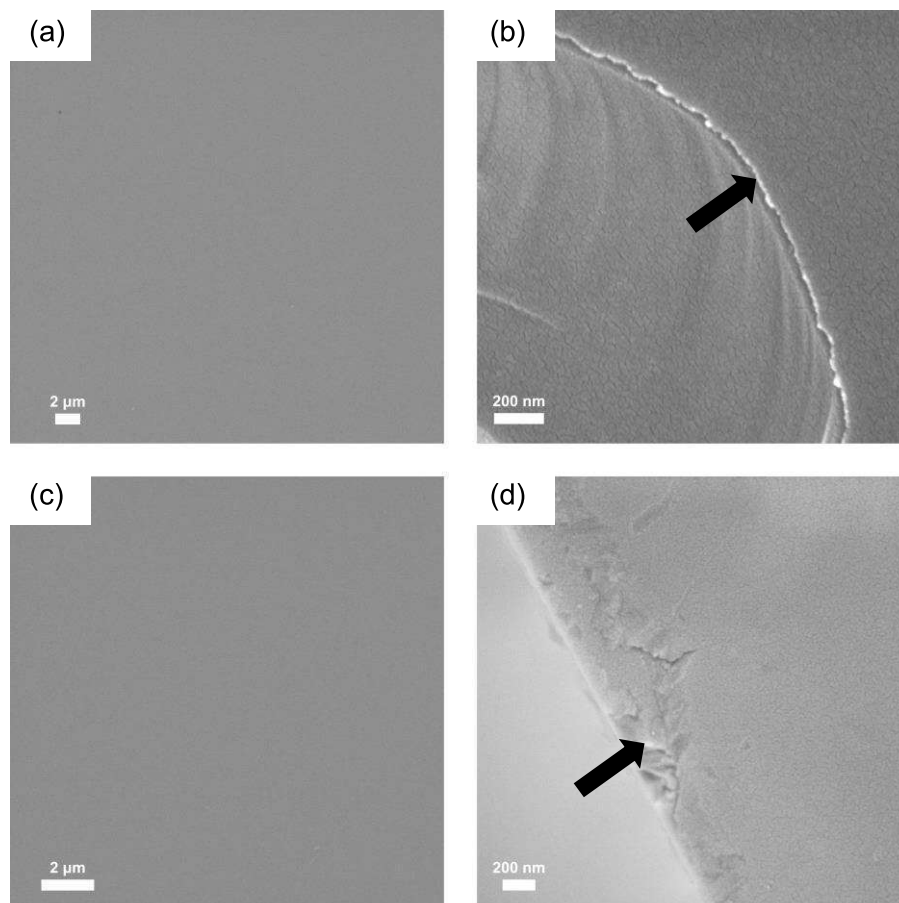


Figure 2.7. (a) and (b) CN-1a sample deposited on silicon substrate. (c) and (d) CN-1a sample on quartz substrate. Images (a) and (c) reveal the high homogeneity of the sample.

The as-deposited film are very homogeneous compared to previous attempts, however, further characterization are necessary to prove that C and N atoms are organized in the tri-s-triazine polymeric structure.^{[20] [1]} Energy Dispersive X-ray Analysis (EDX) mapping, in figure 2.8, shows that C and N elements are homogeneously contained in the CN-1a thin film, as it can be seen in the red and green elemental mapping for C and N respectively. The yellow map depicts the elemental mapping of Si, which is representative for the fused silica substrate of the sample. The Si map shows higher intensity at the cut-edge defect, where the film has been removed, like a negative of the previous C and N mapping images. However, a little signal of C and N is also recorded from the area where the film was removed, which confirms that very intimate contact between substrate and film is obtained with this deposition method. Similar results are shown for the CN-1a sample on silicon substrate, in figure S5.

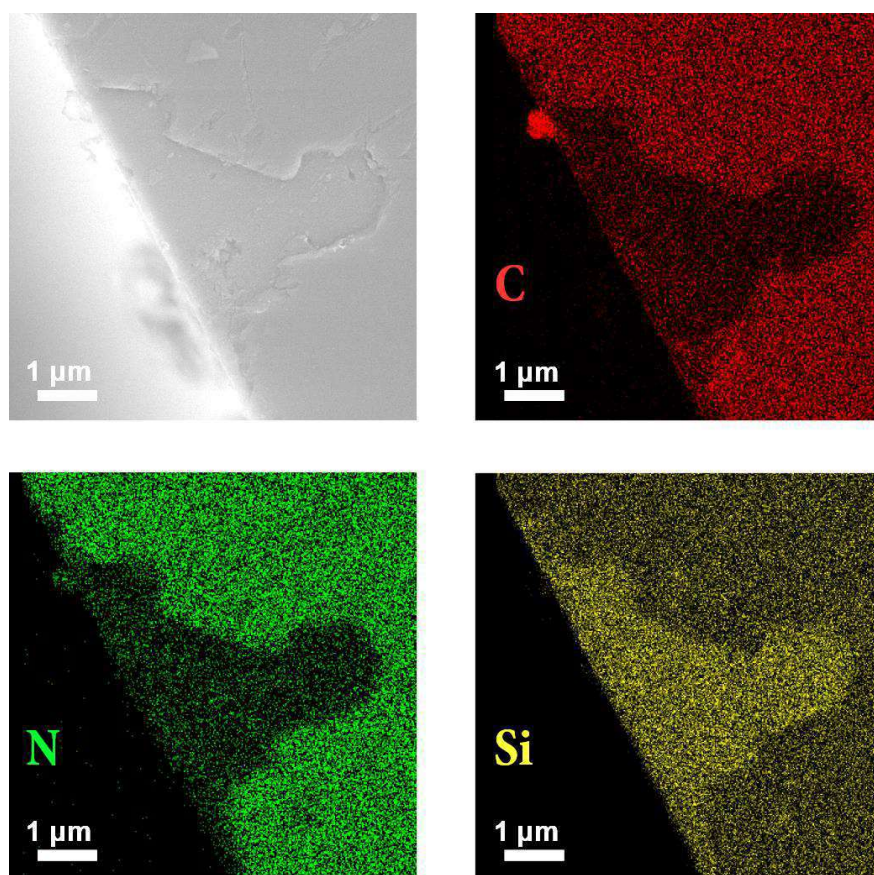


Figure 2.8. C (in red), N (in green) and Si (in yellow) EDX maps of sample CN-1a.

Deeper insights into structural and elemental properties were obtained for both CN-1a (figure 2.9 (a) and (b)) and CN-2a (figure S6 (a) and (b)) films, by means of transmission electron microscopy (TEM) and X-ray diffraction (XRD) analysis. In figure 2.9 (a) and S6 (a), the TEM images shows that the samples material has a layered structure, typical of graphitic-like materials. The presence of 2D layer stacks can be deduced by the grey shades at the material edges, emphasized in figure 2.9 (a) and S6 (a) by arrows. At lower magnifications (figures 2.9 (b) and S6 (b)), highly organized structures with preferential orientation are depicted, as confirmed by fast Fourier transform (FFT) pattern. Briefly, FFT pattern is mathematical transformation of the images, from a space domain (in this case) into a reciprocal space, which points out repetitive patterns. In ideal cases, for highly crystalline materials, the transformation leads to points in the pattern, symmetric with respect to the center, which can be related to the lattice structure.^[25] In these cases, a clear FFT pattern is obtained from the images, that reveals a periodic distance of 0.33 nm, which is in good agreement with the average interlayer distance reported for g-C₃N₄ materials in literature.^[26] [12] Further confirmation is obtained from XRD analysis obtained on

peeled-off samples, directly transferred on the XRD sample holder and dried at 60°C for 5 hours. This step was necessary, since by direct measurement of such thin and flat samples, the XRD signal was not possible to be detected. This is possibly attributed to the high signal of the substrates or the high degree of orientation of the material along the substrate plane that hinders the collection of the scattered X-rays by the detector arm. However, the peeling method led to successful analysis. The diffraction patterns are reported in figure 2.9 (c) and S6 (c), showing a peak signal in both cases at 27.3°, confirming what just presented by TEM analysis, that the material has a periodical distance of 0.33 nm which can be attributed to interlayer stacking of graphitic planes ((002) plane) of g-C₃N₄.^[2]

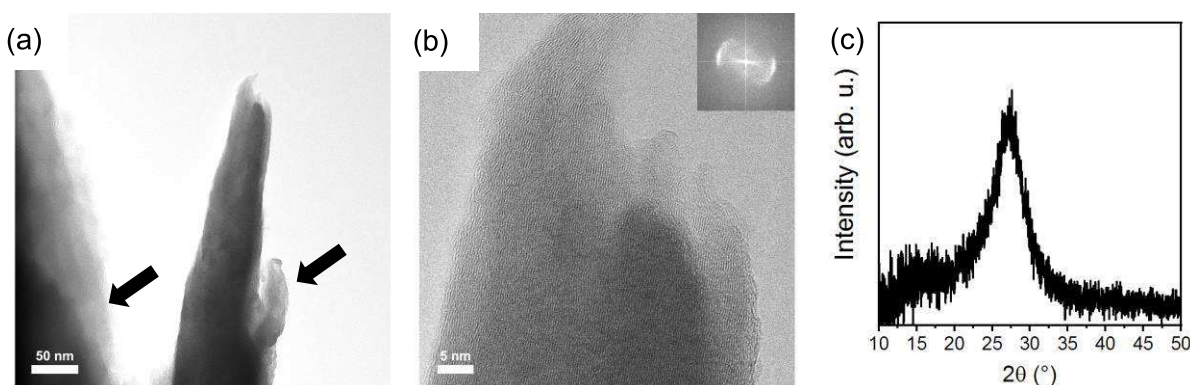


Figure 2.9. (a) and (b) TEM images of CN-1a sample (insert FFT pattern obtained from the image); (c) XRD diffraction spectrum of the peeled sample.

Elemental composition and chemical arrangement have been characterized by Fourier-transform infrared spectroscopy (FTIR) on free-standing thin films, electron energy loss spectroscopy (EELS) and X-ray photoelectron spectroscopy (XPS), shown in figure 2.10 (a), (b) and 2.11, respectively. For comparison, FTIR and Raman spectroscopy have been reported in figure S7 (a) and (b) respectively, on silicon substrate. In these latter cases, the only information that can be obtained are that FTIR film spectrum of the CN-1 and CN-2 samples are quite different from the bare silicon substrate; however, for the thicker samples CN-1b and 2b, at wavenumbers below 1500 cm⁻¹ show fingerprint vibrations of g-C₃N₄ and, inter alia, at 810 cm⁻¹ the characteristic peak of heptazine skeleton appears (figure S7 (a)).^[21] On the other hand, Raman spectra show only a slight effect of fluorescence coming from the film, however, as expected no bands, except for the ones of the substrates, are detected. FTIR spectra (figure 2.10 (a)) of free-standing CN-1b (in red) and

CN-2b (in black) samples, however, give rise to very similar spectra with further information about vibrational modes of thin films samples. At high wavenumbers vibrations attributed to terminal groups approximately at 3200 cm^{-1} for $-\text{NH}_2$ and the small peak of $-\text{C}\equiv\text{N}$ groups at 2180 cm^{-1} appears due to the deposition on soda lime glass, whereas the peak occurring at about 2350 cm^{-1} is the antisymmetric stretch band of adsorbed CO_2 on the surface.^{[21] [27] [28] [29] [30]} In the range $1620\text{--}900\text{ cm}^{-1}$, typical vibration modes originated from C-N heterocycles in the heptazine-based framework are clearly present, as well as the characteristic breathing-mode peak of the heptazine group at 810 cm^{-1} .^{[27] [20] [28]} It is worth to point out, that no carbonyl or $-\text{OH}$ vibration modes are detected, as expected, since the synthesis is performed at very low pressures and with N_2 as carrier gas. The absence of O contamination is further confirmed by EELS spectra, which K-edge lies at about 532 eV (figure 2.10 (b)). The EELS spectra, in the range $250\text{--}600\text{ eV}$, reveal for both CN-1a (in red) and CN-2a (in black), very prominent π^* peaks both for C (at 288 eV) and N (at 400 eV) K-edges, in all cases higher than the respective σ^* peak, suggesting that a very high conjugation degree is obtained all over the structure.^[31] Relative C/N ratio gives in both cases a value close to 0.9. However, it is worth to point out that the composition obtained from EELS analysis at normal incidence is only qualitative since the integration of the spectrum intensity, and thus the calculated composition, depend on the collection angle of the detector.^[32]

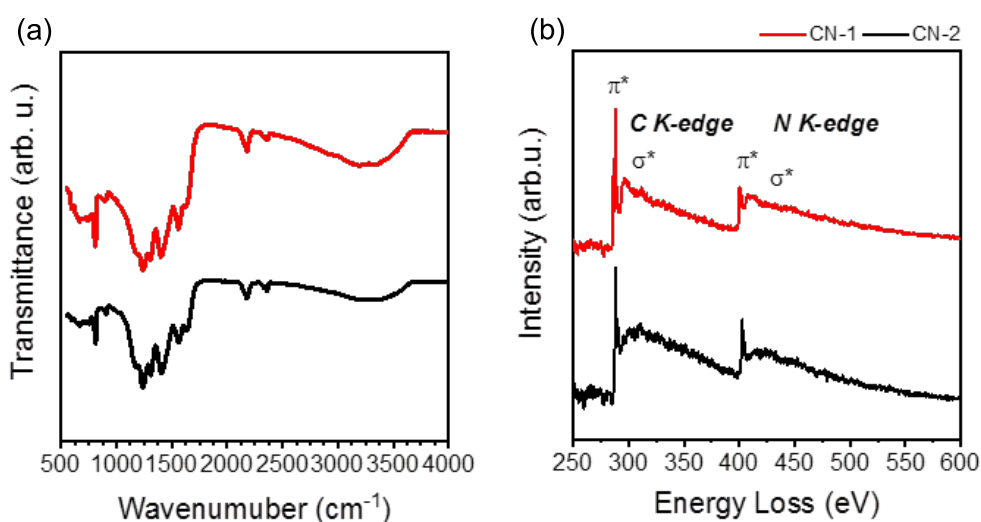


Figure 2.10. (a) FTIR spectra of CN-1b (in red) and CN-2b (in black) free-standing samples; (b) EELS spectra of CN-1a (in red) and CN-2a (in black).

In order to finally confirm the structure, XPS analysis on CN-1a sample was performed, on silicon substrate. The spectrum overview, in figure S8, shows the presence of O, C and N peaks. However, as previously reported by Hellgren et al., when CN materials are exposed to air, O concentration increases due to surface adsorption of O-containing species, which are barely seen in samples analyzed in high vacuum conditions.^[33] Carbon and nitrogen peaks in figure 2.11 (a) and (b), were further analyzed to define the chemical environment of the elements in the material and finally prove that the structure resembles the one of g-C₃N₄ widely reported for bulk materials. Deconvolution of C peak (figure 2.11 (a)) give rise to three different peaks at 284.6, 286.4 and 288.3 eV. The first one is attributed to adventitious carbon (surface contaminations), i.e. adsorbed hydrocarbons.^[33] ^[34] The two following peaks, are indeed related to the g-C₃N₄ structure, where the small peak at 286.4 eV (pink) is attributed to triazinic carbon bonded to hydrogenated amino groups, i.e. the terminal groups of the polymer, whereas at 288.3 eV is attributed to N=C—(N)₂, the sp² C of the heptazine ring.^[34] ^[33] The heptazinic C peak is very intense, confirming though the high conjugation achieved in the material, as already shown above by the EELS spectra. N peak deconvolution, in figure 2.11 (b), shows the typical heptazinic nitrogen components, with very high intensity at 398.2 eV for pyridinic N (in blue) and at 400.1 eV central N bounded to three C atoms (in orange), confirming the succesfull formation of the heptazinic structure.^[34] ^[35] At higher energies, 401.3 eV the lower intensity peak of terminal group is present; as a matter of clarity, the deconvoluted peaks are reported in color code and highlighted, with circles of on the respective unit, on the monomer of g-C₃N₄, depicted in figure 2.11 (c).^[34] Moreover, no C-O or N-O peaks could be attributed in the XPS deconvolution confirming that no O is present within the g-C₃N₄ structure. The C/N ratio obtained by XPS analysis is 0.71, very close to the ideal 0.75, slightly higher than previous reports 0.70, for bulk g-C₃N₄ obtained from melamine precursor.^[34] It is worth to point out, that the beam in XPS analysis has a spot size of some mm with a penetration depth of about 4-10 nm, which in case of bulk materials is attributed to the composition of material surface. However, for very thin films as such, the penetration depth of XPS rays allows for an analysis of the average composition film over large areas (ca. 1 mm²).^[34] Indeed, the composition has been further confirmed by elemental analysis which gives an average C/N molar ratio of 0.74, with a very

low H content (around 2%) which can be partly attributed to water adsorbed on the surface.

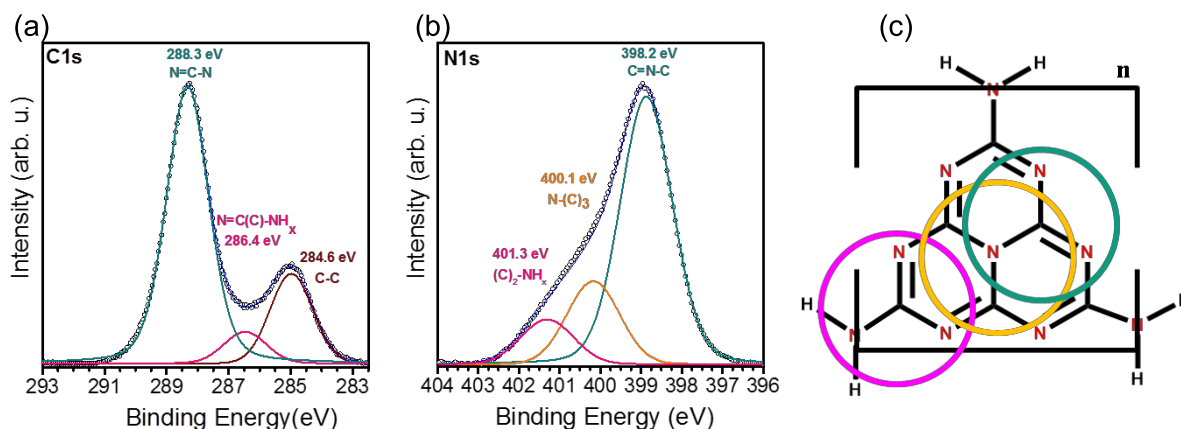


Figure 2.11. Deconvoluted XPS C1s (a) and N1s (b) peaks; (c) molecular environments attributed to the deconvoluted peaks.

In this section, a method that provides a step forward in the preparation of g-C₃N₄ thin films has been proposed, compared to previous attempts, especially in terms of high homogeneity of deposition and flatness over different substrates. The g-C₃N₄ thin film deposition has been achieved by simply using melamine as non-hazardous solid precursors. The decision to use such non-hazardous precursors has advantages mainly regarding easy-handling and safety when compared to explosive or toxic gases, widely used for carbon-based thin film materials, obtained by CVD method.^[36] Moreover, this technique provides a scalable and tunable concept that can potentially be even applied in industries, bringing this widely appreciated organic semiconductor possibly to large scale production, for new generation organic optoelectronic devices and more. The structure of the material has been proved by mean of different techniques and different scales with results highly reproducible with previous reports on the g-C₃N₄ bulk materials.

The high quality of g-C₃N₄ films achieved makes them feasible for applications in optics and optoelectronics. The following part of the chapter will be about the optical properties of the presented thin films and further conclusion and possible outlooks for the applications in optics and beyond.

2.3. Optical properties of g-C₃N₄ thin films

Optical properties of bulk g-C₃N₄ have been widely reported especially for applications in photocatalysis with visible light. The ability to create excitons, possibly

with long lifetime, by visible light excitation, as well as the convenient bandgap position, has attracted much interest recently in this research field.^[26] However, the optical properties are of paramount importance also for application in solar cells, where high extinction coefficient for active materials are required, and light management, where especially high refractive index materials attract much interest, as for instance planar waveguides, nanoantennas, photonic crystals and optical sensors.^{[37] [38] [39] [40]}

Bulk and thin film g-C₃N₄ are well-known for their typical yellowish appearance, due to absorption edge which lies in the visible spectrum of wavelengths, typically between 400 and 450 nm. ^{[41] [42] [43]} However, transmittance spectra (as well as absorbance and reflectance spectra) of thin films strongly depend on the film thickness, which causes the different appearance shown in figure 2.6.^[12] Transmittance and reflectance measurements (figure 2.12 (a-d), solid lines are samples spectra, dotted lines the substrate spectra for reference) were performed at normal incidence on transparent substrate (fused silica); these characterizations can provide useful insights both on absorbed wavelengths and thin film thickness comparison between similar samples. Some considerations on film thicknesses can be done directly from transmittance and reflectance spectra, assuming that the optical constants are the same in all the samples, which is a reasonable condition, since no differences were detected within the previous characterization. As reported in chapter 1, Lambert-Beer law describes the intensity of light transmitted through a sample is a function of sample thickness, which suggests that CN-2a sample (figure 2.12 (a)) is the thinnest among all the samples and indeed, it looks completely transparent in the figure. The spectrum shows a very sharp transmittance minimum at about 305 nm and very high transmittance in the visible range, close to the transmittance of the bare substrate, whereas reflectance spectrum (in red) is very low with a maximum at 335 nm, which confirms the very low thickness of the sample. In figure 2.12 (b) the CN-1a sample transmittance decreases especially in the UV range, where it even reaches zero transmittance in the UV range with a long tail in the visible range, specular with the reflectance. In this case it is important to point out that the long tail observed in the visible range has not to be attributed to BG shrinkage but to light reflected by the sample surfaces. The reflectance and absorbance spectra are perfectly mirrored, out of the absorbing range, showing the high quality of the sample and homogeneity of the samples. The samples prepared

from 10 g of melamine, i.e. CN-2b and CN-1b, respectively in figure 2.12 (c) and (d), show a completely different behavior. The transmittance in the UV is very low up to 400 nm. In the visible range the samples show fringes due to light interference, perfectly mirrored between transmittance and reflectance, which are the cause of the color of the samples, like in figures 2.12 (c) and (d). Interference fringes occur due to multiple reflections at the interfaces air-film, film-substrate, substrate-film and finally film-air. Let us consider a simpler condition in which a single free-standing film surrounded by air interacts with an impinging radiation, schematically represented in figure 2.12 (f): at each interface light will be partially transmitted and partially reflected back; the back reflected light can further be re-reflected or transmitted from the first interface, by this contributing to the transmitted or reflected light, respectively.^[44] This process generates an infinite number of components contributing to reflected and transmitted light, where the collected spectra are simply the result of these processes. Interference fringes are periodic oscillations due to this periodic modulation of transmitted and reflected light when interacts with media, as can be seen in everyday life in soap bubbles or oil layers on water. However, condition for thin film interference requires that film thickness is much lower than light coherence length:

$$d \ll \frac{\lambda^2}{2\pi\Delta\lambda}$$

where d is the film thickness (nm), λ is the wavelength (nm) and $\Delta\lambda$ the spectral bandwidth (nm).^[45] Moreover, the interference extrema in transmittance and reflectance are tightly related to thickness and refractive index, which then can provide useful insights in the present case; assuming constant and similar refractive indices for samples CN-2b and CN-1b (figure 2.12 (c) and (d)), at normal incidence, the thickness will be:

$$d = \frac{m}{4\nu_j n_j} = \frac{m\lambda_j}{4n_j}$$

where m is an integer (the interference order, $m=0, 1, 2, \dots$ even for constructive interference, uneven for destructive) ν_j is the light wavenumber (cm^{-1}), λ_j the wavelength (nm) and n_j the refractive index of the film.^{[45] [46]} However, since the interference order is usually unknown, the distance between two (or more) maxima

(in reflectance, which corresponds to minima in transmittance) or minima can be conveniently used:

$$d = \frac{\Delta j}{4 \left((v_{j+\Delta j} n_{j+\Delta j} - v_j n_j) \right)}$$

where $v_{(j+\Delta j)}$ and v_j are the light wavenumber (cm^{-1}) and the respective refractive indices $n_{(j+\Delta j)}$ and n_j , which then takes into account the dispersion of the refractive index function with the wavenumber, making the fringes possibly not equidistant across the spectrum.^[45] These simple equations provide a powerful method, based on simple reflectance and transmittance measurements, to deduce the thickness ranking between similar samples, fundamental for thin film technology. In the presented sample then it comes straightforward then that d increases as follows CN-1b > CN-2b > CN-1a > CN-2a.

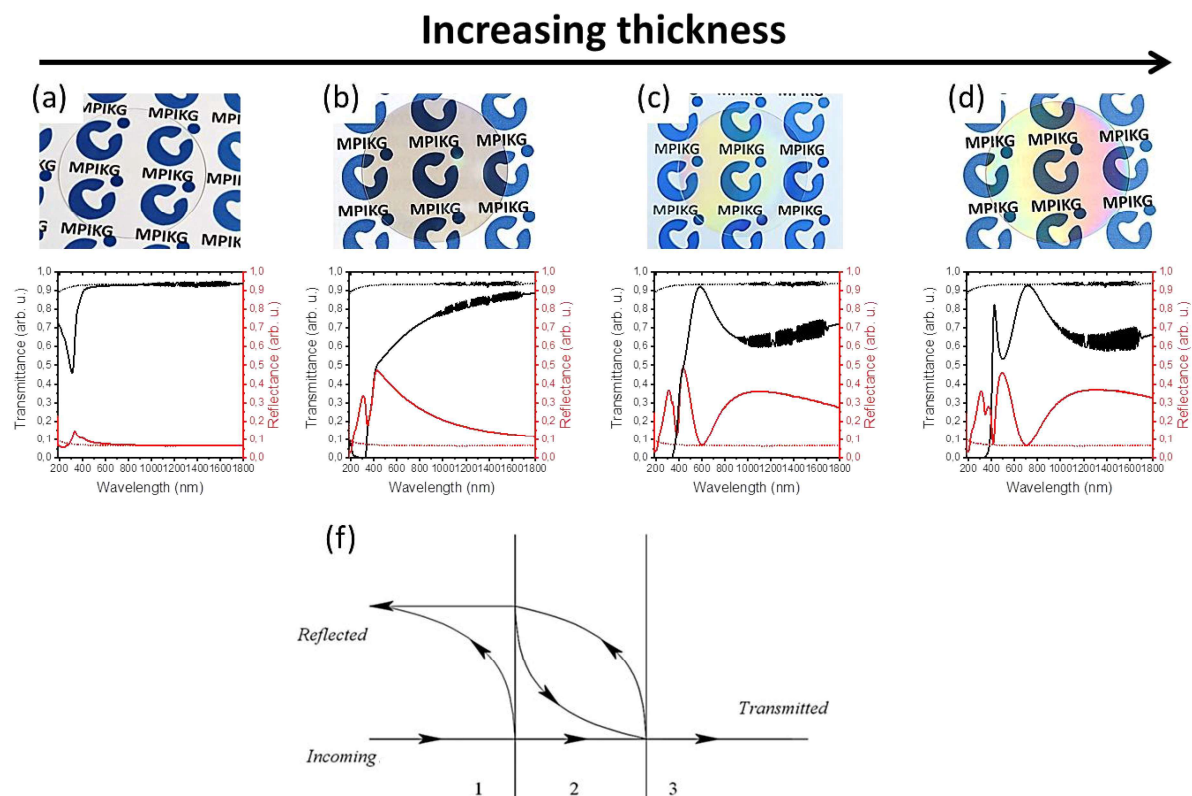


Figure 2.12. Transmittance and reflectance spectra of samples CN-2a (a), CN-1a (b), CN-2b (c), CN-1b (d) deposited on fused silica and relative pictures; (f) scheme of reflections occurring at the interfaces of thin films.^[44]

This conclusion can also be derived from reflectance measurements of samples deposited on silicon substrates (in figure S9 (a-d)). Moreover, the just proposed

thickness ranking leads to two different important conclusions: first, increasing the precursor amount successfully results in an increased film thickness and second, longer downstream times lead to thinner films. The first conclusion was already successfully proven via VDP method in a previous work, whereas the second one might seem a bit counterintuitive.^[2] In the CVD condition presented, the precursor is fully sublimed in the upstream oven to then form the g-C₃N₄ polymeric thin film in the downstream oven. This means that over time the partial pressure of melamine changes in the reactor, modifying the thermodynamic equilibrium conditions. When the partial pressure of melamine decreases down to zero (reactant starvation condition), the decreasing film thickness is assumed to be due to backward reactions on the surface as a result of equilibrium displacement, which was already observed in other cases for starved reactors.^[47] Furthermore, reaction intermediates (as tri-s-triazine units) released from the surface are possibly carried away by the nitrogen carrier gas, leading to a thinning of the g-C₃N₄ films.

From intensities of transmittance fringes maxima and minima, the spectra suggest that the material should have a high refractive index in the visible range, as proposed in a previous work by Swanepoel.^{[48] [49]} For this reason, variable angle spectroscopic ellipsometry (VASE) measurements were done for the samples, at different angles (60-65-70°) in the range 5-0.5 eV (250-2500 nm). Spectroscopic ellipsometry is an important method for analyzing optical properties of thin films. Briefly, a circularly polarized light beam interacts with the sample, which causes a modification of the light polarization according to the Fresnel formulae, and partially reflected into the detector arm, where the resulting elliptical polarization of light is analyzed in terms of amplitude ratio and phase difference.^{[50] [51]} The detected response is related to optical constants and thickness of sample, but can also be correlated to absorption coefficient, optical anisotropy, crystallinity, porosity and other material properties.^[52] ^[53] After a sample is measured, a model is constructed to describe it, in terms of thickness and optical constants and compared with experimental data. The best match between model and experimental data is usually achieved through regression until minimum error is reached.^[50] The data modelling for all the sample converged to the refractive index (n) and extinction coefficient (k) function reported in figure 2.13 (a) (extended up to 2500 nm in figure S10), in black and red line respectively. It is well known that g-C₃N₄ absorbs in the UV range and indeed up to 400 nm the extinction coefficient is high with a maximum of 1.97 at 301 nm, which is very high

compared to other conjugated polymers. The high extinction coefficient was very recently investigated by Vezie et al. and attributed to high polymer chain stiffness.^[54] High k values make this polymeric semiconductor possibly interesting for future applications in solar cells.^{[55] [56]} The refractive index (in black) shows an extremely high value, to the best of my knowledge, the highest ever recorded intrinsic n for a polymeric material at these wavelengths, with values of 2.52 at 500 nm and 2.32 at 1000 nm.^{[57] [58] [59] [60]} Moreover, at 500 nm, where it is already transparent ($k < 0.001$), the g-C₃N₄ thin film shows the highest real refractive index (n) for an organic material, even higher than the diamond which is known to have the highest n in the visible range for non-absorbing organic materials, at the same wavelength shows a value of 2.43.^[61] As mentioned in chapter 1, the refractive index is the most important parameter for application of thin films in optical devices. High values of the refractive index allows, for instance, to make optical devices, like lenses, smaller, or to achieve better light confinement, by decreasing the angle for total internal reflection and higher dielectric contrast in photonic crystals with common polymeric materials, where usually the refractive index is lower than 1.8.^[40]

The source of such extremely high refractive index can be attributed to tri-s-triazine groups that constitute the g-C₃N₄ structure and its high density. Indeed, the refractive index of polymers can be defined by the Lorentz-Lorenz equation, which defines it as a function of density (ρ), molecular weight (M_w), linear molecular polarizability (α_m) all referred to the repeating unit, or in a compact way can be reported as a ratio of molar refraction ($[R]$) and molecular volume (V_m) of the polymer repeating unit:^{[62] [60]}

$$\frac{n^2 - 1}{n^2 + 2} = \frac{4\pi \alpha_m \rho N_A}{3 M_w} = \frac{[R]}{V_m}$$

where N_A is the Avogadro number. Solving the equation for n :

$$n = \sqrt{\frac{1 + 8\pi\alpha_m\rho N_A/3M_w}{1 - 4\pi\alpha_m\rho N_A/3M_w}} = \sqrt{\frac{1 + 2[R]/V_m}{1 - [R]/V_m}}$$

Polarizability for tri-s-triazine group has been calculated by Zheng et al. and reported to be 15.6 Å³ (20.1 Å³ for triamino-tri-s-triazine), which are high values if compared for instance to benzene ring (10 Å³) and the high density, due to closely packed sheet structure, has been also reported for g-C₃N₄ film by vapor deposition polymerization to be 1.8 g cm⁻³.^{[3] [63]} All of this supports the extremely high g-C₃N₄

refractive index and furthermore, the high [R] values of the $-C=N-C-$ group (4.10, tabulated) within a polyaromatic structure, respect for instance to $-C=C-$ bond (1.73, tabulated), confirms once more that large amount of $-C=N-C-$ bonds could enhance the refractive index in polymers, as previously shown by Ueda and his group.^[58] Optical dispersion is another key parameter to measure the n variation over a wide spectral range and is defined by the Abbe number (v_D). Abbe number is often calculated in the visible range, by the refractive indices at the Fraunhofer D-, F- and C- spectral lines (589.3 486.1 and 656.3 nm respectively):

$$v_D = \frac{n_D - 1}{n_F - n_C} = \frac{6n_D}{(n_D + 2)(n_D - 1)} \frac{[R]}{[\Delta R]}$$

with $[\Delta R]$ defined as the molar dispersion.^[60] The dispersion of the refractive index is however high, resulting in low v_D (9.5) compared to diamond (55.3), but close to TiO_2 (rutile, 9.9), a widely used inorganic material in photonic application with similar refractive index (2.57).^{[64] [65]} VASE measurements allows to determinate also the thickness of the as-prepared thin film, reported in table 1. The data confirm once more what already concluded from transmittance and reflectance measurements: increasing the amount of precursor lead to thicker films and longer downstream times effectively lower the thickness. Moreover the table data suggests that films on silicon substrate are in all cases thinner that the same film prepared on quartz substrate. This can be explained in terms of different wettability and roughness of the substrate surfaces, and reported in figure S11 (a-d). The results shows that silicon surface is flatter respect to quartz and has a lower contact angle (respect to water at room temperature) so higher wettability, suggesting that thicker film can be obtained on substrates with larger roughness and lower surface energies, at the same deposition conditions. Differences between back and front deposition on quartz are attributed to the orientation of the substrate in the CVD setup, since one surface directly faces the precursor stream while the other one doesn't. Moreover, since the extinction coefficient has been defined in the considered spectral range, it can be easily derived also the absorption coefficient (α) curve (figure S12) to obtain the Tauc plot shown, at the bandgap edge, in figure 2.13 (b). The Tauc plot is a common experimental method to define the HOMO-LUMO gap, which is based on graphical extrapolation from:

$$(\alpha hf)^{\frac{1}{x}} = A(hf - E_g)$$

where h is the Planck constant, f the photon frequency, A a proportionality constant and E_g the BG energy. The exponent x is defined according to the nature of electronic transition and equal to 0.5 for direct allowed transition and 2 for indirect allowed transition.^[66] It has been widely reported that g-C₃N₄ possesses an indirect BG, so the exponent 2 was chosen for the Tauc plot.^{[10] [28] [67]} The value of the BG energy was found by interpolation of the curve edge in the linear range, at ordinate 0, which gives a value of 2.88 eV (431 nm). This value is larger compared to values previously reported for the bulk g-C₃N₄ (2.7 eV), however this difference between bulk and thin film of the same material, was already observed by Kammler et al. for an inorganic system and was attributed to Burstein–Moss shift.^{[26] [67] [68]} It is worth to remind, that this last consideration could be valid if a pure material is considered, however, synthetic methods reported for g-C₃N₄ include mostly reactions in furnaces, air-contacted or with oxygen-containing precursor. The included oxygen can therefore act as a doping atom or defect and vacancies in the structure, that can lead to BG shrinkage.^{[69] [70]}

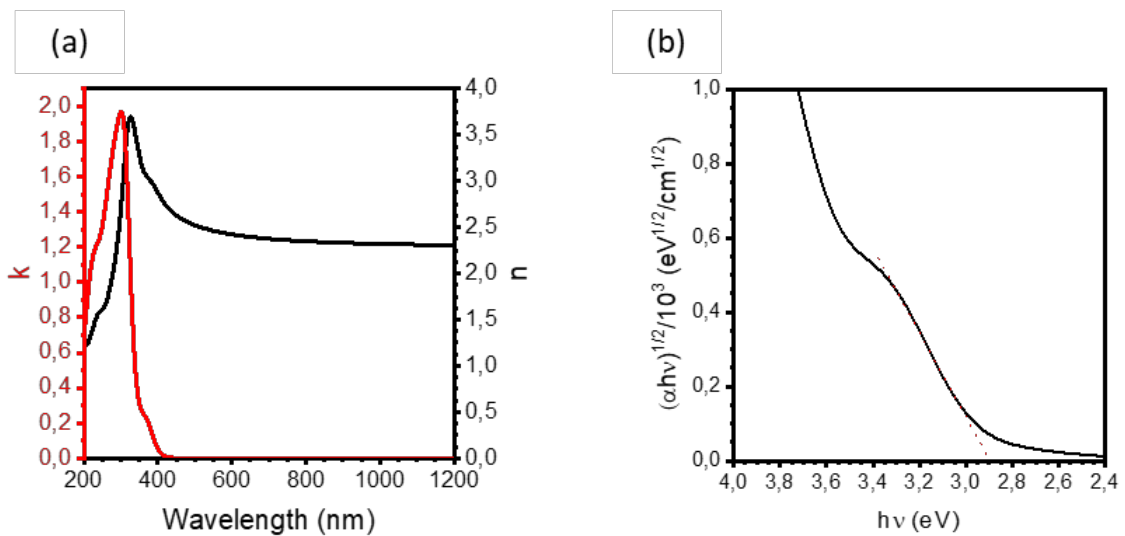


Figure 2.13. (a) Optical functions of g-C₃N₄ thin films: refractive index (black line), extinction coefficient (red line). (b) Tauc plot (in black) and tangent line (red dotted line) to determinate the bandgap.

Table 2.2. Thickness of g-C₃N₄ thin films calculated by ellipsometry. Between brackets is reported the thickness of the film on the back-side of fused silica substrate.

Sample	Precursor mass (g)	Substrate	Thickness (nm)
CN-1a	5	Silicon	13.6
	5	Fused silica	37.9 [32.7]
CN-1b	10	Silicon	112.0
	10	Fused silica	129.7 [129.0]
CN-2a	5	Silicon	3.4
	5	Fused silica	5.0 [1.0]
CN-2b	10	Silicon	89
	10	Fused silica	127.6 [126.5]

Ultraviolet photoelectron spectroscopy (UPS, figure S13) spectrum was investigated to define the HOMO-LUMO bands position of the material, schematically reported in figure 2.14, respect to vacuum energy (left axis) and to SHE (standard hydrogen electrode, right axis). The Fermi level energy (E_F) was found to be at -4.36 eV (respect to vacuum) slightly above the SHE standard potential (-4.44 eV=0 V).^{[71] [72]} The VB was defined by the tangent intersection at the edge of the VB signal and the background signal (1.64 eV) leading to VB position at -6.0 eV. The bandgap energy was previously defined via ellipsometric measurements; thus, the CB position has been simply derived (-3.12 eV). Compared to previous results the VB position shows very similar energy values, whereas the CB energy decreases (on the negative scale), causing the BG broadening, which means that more energy for the electronic transition.^{[70] [73] [67]} Shrinkage of the BG only due to CB shift was already observed by Yu et al. by increasing the C/N ratio of the bulk material: however they didn't attribute it to a doping effect but to defect states arising within the BG due to cyano groups and N-vacancies.^[70] Since the E_F lies slightly closer to the CB rather than the VB, the material behaves like an n-type semiconductor, in good agreement with previous reports on g-C₃N₄ materials.^{[13] [10]}

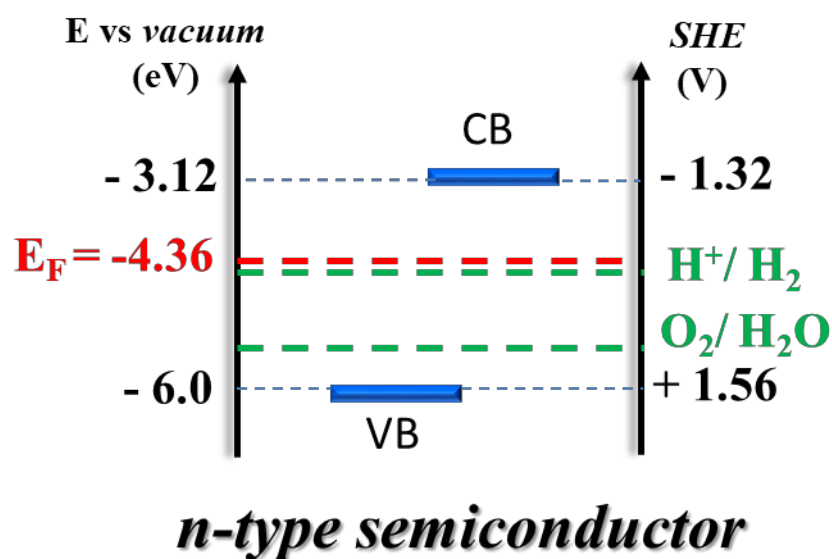


Figure 2.14. Band structure calculated for g-C₃N₄ thin films, referred to vacuum scale (left) and standard hydrogen electrode (SHE, right).

Photoluminescence (PL) is another optical key parameter, since as previously introduced, g-C₃N₄ is able to emit light under appropriate photon energy stimulus. PL give important information about the emitted photons, however, it is important to define for which wavelength PL process occurs, that can strongly differ from absorbance/transmittance spectra due to internal non-radiative processes, self-quenching, intersystem crossing and more (electronic levels and possible transitions are usually described by the Jablonski diagram reported in many physics books).^[74] Excitation spectra are recorded by setting the PL maximum wavelength and irradiate the sample at shorter wavelengths; the spectrum represents then the intensity of fluorescence recorded by the detector at each scanned wavelengths. The contour plot, reported in figure 2.15 (a), is a 3D plot of recorded excitation spectra, over the range 250-450 nm for PL wavelengths from 400-600 nm (for clarity single PL at 375 nm excitation and excitation spectra at 466 nm PL are reported on the respective axes). The contour plot depicted for the sample CN-1b on quartz reveals a single PL emission maximum (466 nm), as mostly reported for g-C₃N₄ in bulk, with two main maxima excitation intensities at 275 and 375 nm. ^[67] Moreover, the external quantum yield is 0.8 % and internal quantum yield 1.1% at 370 nm. Other sample spectra are shown in figure S14 in which similar maxima spectral positions can be seen, except for sample CN-2a. In this case a significant PL blue shift maximum (446 nm) and very different excitation spectrum shape and maxima (282 and 311 nm) are present. This

is possibly attributed to the extreme low thickness of CN-2a sample (5 nm), which could affect the optical properties of the material, as observed in other conjugated polymer thin films; in this case, the optical difference is possibly due to a reduced amount of layer stacks or lower conjugation between tri-s-triazine units along the sheet.^{[75] [76] [43]} Further studies would be necessary to understand the PL mechanism, that is still under debate in the scientific community. PL lifetimes have been determined, for CN-1b (figure 2.15 (b)) and CN-2b (figure S15), by time-correlated single photon counting (TCSPC) with 405 nm wavelength excitation, of high interest especially for photocatalytic applications. The spectra show very similar intensities and shape, where strongly non-exponential decays, suggest a broad fluorescence lifetime distribution. Similar non-exponential curves have been already observed for other conjugated polymers, as well as for g-C₃N₄ and possibly attributed to transport of the excitation via resonant energy transfer or excitons hopping.^[77] To define the lifetimes and their distribution a three-exponential-decay function was used to fit the curves:

$$I(t) = \sum_{i=1}^n A_i e^{-\frac{t}{\tau_i}}$$

where $I(t)$ is the intensity recorded as a function of time, A_i the amplitude of the single components and τ_i the fluorescence lifetimes; the average lifetime $\langle \tau \rangle$ has been calculated averaged on the amplitudes.^[78] The fitting parameters are reported in table 2.3 (and table S1 for CN-2b). The shorter lifetimes agree with previous measurements reported on bulk materials, usually around 2 and 10 ns. ^{[27] [77]} However, a third very long lifetime arises from the measurement at 61.4 ns. A longer fluorescence time means a longer time before radiative recombination of charges in the material. Therefore, it can be explained with very long conjugation present in the samples, which would confirm the high intensity peak seen in EELS and the large of sp² C and N content in XPS spectra. Moreover, Merschjann et al. reported a direct correlation between average PL lifetime and interplanar stacking in g-C₃N₄, which would be in agreement with the interplanar stacking of 0.33 nm previously shown, and support their theory on exciton hopping along the graphitic structure.^[79]

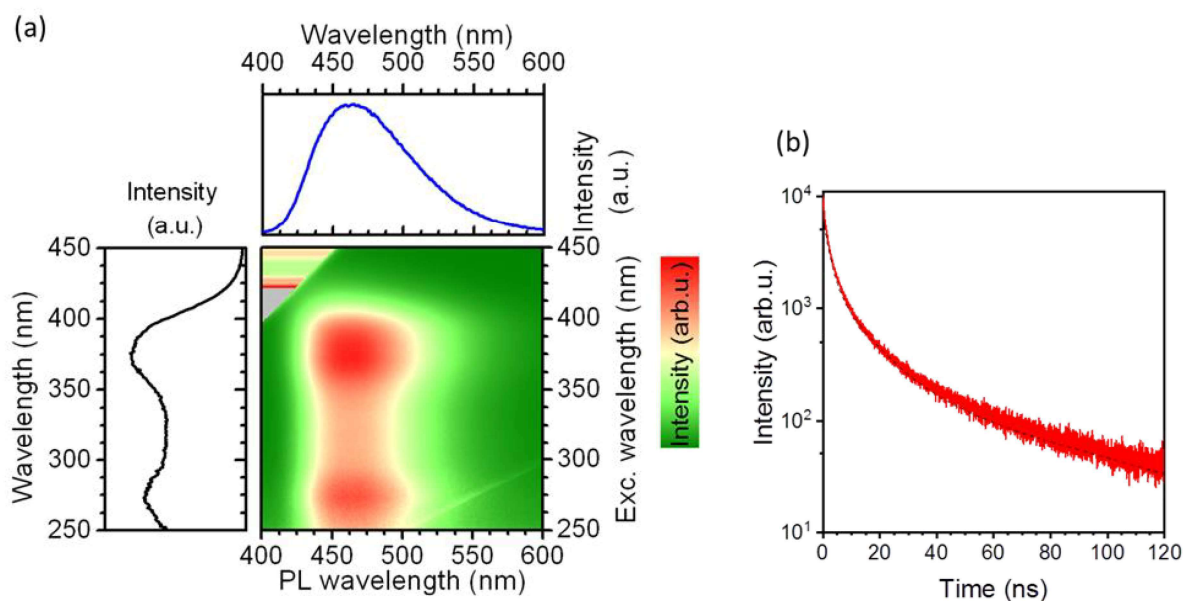


Figure 2.15. Contour plot of excitation versus photoluminescence of sample CN-1b (a), intensity is indicated in color scale from green to red; on the axes are shown representative spectra for photoluminescence (in blue) and excitation (in black); (b) fluorescence lifetime measured with 405 nm wavelength excitation (red line) and fitted lifetime function (black dashed line).

Table 2.3. Fitting parameters of fluorescence lifetime (figure 2.15 (b)) of sample CN-1b.

A_1 (counts)	τ_1 (ns)	A_2 (counts)	τ_2 (ns)	A_3 (counts)	τ_3 (ns)	$\langle \tau \rangle$ (ns)
235.96	61.40	1585.7	11.37	4624	2.08	6.54

Conjugated polymers in many cases have shown intersystem crossing, from singlet excited state to triplet excited states, by means of light excitation. Triplet states occur when the singlet exciton, instead of recombining via PL, undergoes intersystem crossing and the spin becomes parallel with the electron in HOMO level.^[80] The radiative recombination in this case is forbidden due to spin selection rules, however partially allowed if a perturbation like spin-orbit or vibrational coupling occurs.^[80] Figure 2.16 (a) shows the PL (red line) and phosphorescence (PH, black line) spectra recorded with excitation at 370 nm, in the range 400-600 nm for the sample CN-1b (slight differences from previous PL measurements can be attributed to different setup used for the phosphorescence characterization). The PH has been recorded in all cases with an extremely large impulse-detection delay of 10 ms, to avoid any possible effect of delayed PL.^[41] The spectra shape appears quite similar, with a depletion of intensity in PH spectrum at about 500 nm. The peak maxima of PL and PH coincide in the spectra (470 nm), suggesting a very low singlet-triplet energy gap,

with possibly high rate of intersystem crossing.^{[41] [80]} To further investigate the spectral dependence of PH, measurements were done with light excitation at 350 nm (green line) and 390 nm (blue line) (yellow line is the intensity collected from the excitation) and compared to the one at 370 nm (black line), in figure 2.16 (b). No significant differences, in terms of spectral shape and peak maxima, can be seen between the spectra, however, further confirms that PH effect is present in the samples. This effect is extremely important since it confirms that there is a complex mixture of excitonic processes happening in the material. Moreover, it can offer further perspectives in light harvesting for photocatalytic processes based on triplet exciton generation and energy transfer, which to date has been seldom exploited, as well as for applications in photonic devices and bio-imaging.^{[41] [81] [82]}

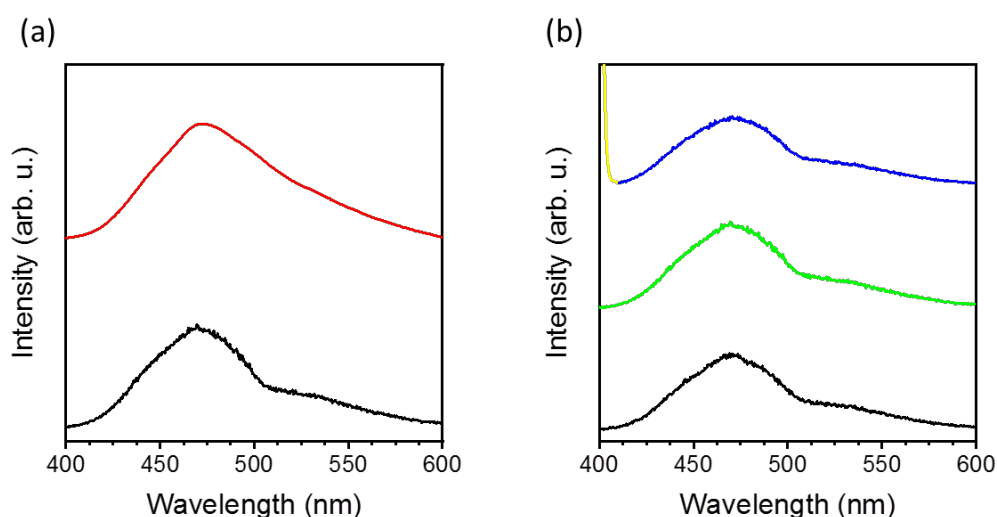


Figure 2.16. (a) Photoluminescence (red line) and phosphorescence (black line) spectra of CN-1b sample; (b) phosphorescence spectra with different excitation wavelength: 350 nm (green line), 370 nm (black line) and 390 nm (blue line, yellow line is the spectral edge of the 390 nm excitation).

2.4. Summary of chapter 2 and perspectives

In this chapter, first a new method for the synthesis of g-C₃N₄ via chemical vapor deposition from melamine as convenient precursor was presented. Melamine is a convenient precursor since sublimation can be efficiently achieved at relatively low temperatures (around 300°C) and, as widely reported in literature for bulk syntheses, is among the common precursors listed for the synthesis of g-C₃N₄ at 550°C. The same method proposed can be possibly applied for syntheses of g-C₃N₄ from different solid precursor, as for instance cyanamide, dicyandiamide, urea and more, making it very appealing as a standard method for g-C₃N₄ high-quality thin films. In a

broader view, this method can pave the way for the synthesis of wide range of carbon-based thin films from solid precursor sources, to further promote their application and replace widely used inorganic semiconductor, improving sustainability and possibly efficiencies. Moreover, the CVD technique allows to overcome the requirement of surface flatness of common techniques for thin films deposition, such as spin coating and spray coating, shown by coating of g-C₃N₄ onto the quartz flowers in figure 2.15 (a, bare quartz, b, coated with g-C₃N₄ and c, sample under UV light). Besides curved substrates, even deposition on solid powders is possible. This is shown, for example, for TiO₂ in figure 13 (d bare TiO₂ powder, e coated with g-C₃N₄), which, for instance, allows for creating bulk heterojunctions or composite materials, broadening even more the range of application interest from catalysis to electrochemistry and photonics.

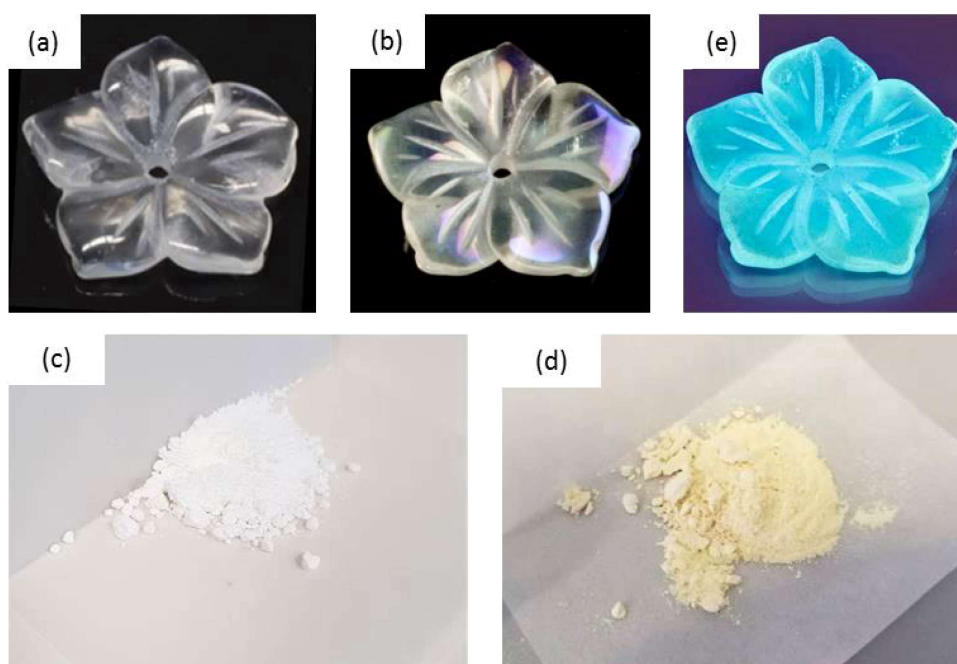


Figure 2.17. Above: flower-shaped quartz glass (a), coated with g-C₃N₄ (b) and irradiated with UV light (c). Below: TiO₂ powder (c) and after CVD coating with g-C₃N₄ (d).

As shown in the first part of this chapter, vapor-based methods provide better film quality and surface adhesion compared to liquid- and solid-based methods. This method gives further improvement since it allows accurate control of the deposition parameters for better thickness control and higher surface flatness, at the same time limiting undesired reactions, as oxygen inclusion, for a strict control of the material properties. Opposed to classic CVD methods, the herein presented synthesis has

advantages in terms of safety, avoiding storage and uses of toxic gas streams, simpler modifications of film properties, by chemical modification of the solid precursor, but keeping the typical high quality of samples which can be interesting both for research purposes but also industrial applications.

The extremely high refractive index and the PL properties of the g-C₃N₄ films are of high interest for photonic devices and photonic crystals. Photonic crystal are composite materials in which the periodic modulation of the refractive index along 1, 2 or 3 dimension lead to the creation of a photonic BG where the light with the same energy is not allowed to travel through and thus scattered.^[40] The higher is the refractive index mismatch between the components the higher is the reflectance, at other conditions fixed.^[40] As previously shown by Jiang group, highly ordered colloidal photonic crystal with tunable optical properties can be assembled from silica nanoparticles.^[83] As shown in figure 2.17, via CVD it is possible to coat very different surfaces and possibly deposit g-C₃N₄ within a colloidal structure to obtain very high refractive index contrast (2.52-2.32 for g-C₃N₄ versus ca. 1.5 silica) for laser and sensing applications.

The high interest for materials with high refractive index especially for developing highly efficient nanodevices, as nanoresonators based on Mie resonance, has been reported by Baranov et al. very recently.^[84] Thin film of g-C₃N₄ can meet for their “quest for materials”, not only for the high refractive index obtained as well for the simple fabrication method and the possibility of patterning currently under investigation in our group.

Preliminary tests in PEC on samples deposited on FTO substrates have already shown promising results by periodically switch of light illumination, at constant potential and intensity, the electrical resistance switches accordingly (figure S16 (a-d)). In all cases, the resistance under 465 nm light irradiation was reduced and restored when light was turned off. However, no redox reaction was achieved in a reference system (1M KCl 7*10⁻⁴ M K₃Fe(CN)₆ in water) possibly due to the mismatch between radiation energy and BG which would not allow enough high excitons density for the reaction (figure S16 e). Further studies will be necessary to improve the performances.

Another possible application which would further benefit from g-C₃N₄ thin film is microfluidic reactors. Photocatalytic properties have been widely exploited over the last years, however, microfluidic reactors can suffer from particles dispersion, that

can cause reactor clogging or inhomogeneous distribution of catalyst along the reactor. CVD deposition would allow highly homogeneous deposition on the reactor, so making the reactor pipes itself the catalyst, homogeneously distributed, avoiding clogging or flow drops along the full-reactor length.

BG and PL tuning by mean of different precursors, such as oxamide, benzoguanamine and more, is successfully already under investigation in our group, to improve efficiencies for different applications such as solar cells. The possibility to shrink the BG over the visible range, with possibly high extinction coefficient previously shown in this work, the high stability and low toxicity of g-C₃N₄ materials makes them possible candidates to replace widely used perovskites as active materials in solar cells applications.

The wide range of possible future applications, coupled with a robust method for high quality thin film deposition will open up new options, for a material that has already attracted much attention, so far. Moreover, CVD is a widely used method in industry, which will facilitate the proposed method to be used for implementation of g-C₃N₄ thin film in daily technological devices.

Chapter III

3. Boron Carbon Nitride Thin Films

This chapter will be dedicated to boron-carbon-nitride (BCN) ternary systems as thin films. In the first part will be given an overview of synthetic methods and applications reported so far. In the second part, the CVD synthetic methods developed during this work will be presented with chemical composition and structural properties. The last part of the chapter will be focused on the optical properties at different synthesis temperature and precursor composition.

3.1. Background and state of the art

In the previous chapter, the introduction of N into a graphitic structure (g-C₃N₄), was shown to result in very different material properties, compared to an all C-material. The introduction of a third element, here B, is known to further change the properties. On the extreme end of high B and N content would be hexagonal boron nitride (h-BN) which is a wide bandgap (up to 5.9 eV) insulator material, with a structure isomorphous to graphene.^{[1] [2]} Mixing the properties of this two seemingly very different materials, but with similar lattice parameters and structure, is expected to provide very different properties according to relative composition and atomic arrangements in the lattice.^{[1] [3]} Substitution of C atoms in a graphene sheet with B and N has been reported by theoretical studies and confirmed experimentally to be effective for widening the graphene bandgap leading to p-type and n-type semiconducting properties, respectively.^[3] Many attempts have been reported on the synthesis of BCN materials via different methods, mainly focusing on ion beam assisted, pulsed laser deposition, radio frequency (RF) /direct current (DC) sputtering and CVD deposition techniques, with single source precursor or different B, C, N containing precursors.^[4] Deposition of BCN film by ion beam assisted sputtering from B, C and BC₄ targets has been reported with further introduction of N₂ gas as a N source.^{[5] [6]} In these cases the technique allowed to tune the composition which correlates to different hardnesses (up to 28 GPa), probably correlated to a large amount of sp³ bondings. Moreover the as-prepared films showed high roughness which hinders their applications in optics and optoelectronics. Similar mechanical properties have been reported also for BCN films obtained by pulsed laser deposition

from BC_4 targets, with tunable bandgap size which was attributed to the relative composition and structure. Also in this case, the authors highlighted the poor surface quality and attributed it to the deposition method, which caused the formation of droplets all over the surface.^{[7] [8] [9]} Among the physical deposition methods, RF and DC sputtering techniques have attracted more interest due to the homogeneity, great adhesion and uniformity of the films.^[10] In order to prepare BCN thin films, single or double solid precursor targets containing B, C and N are used, commonly BC_4 , BN, graphite and BCN. Many of these studies were focused on mechanical properties of BCN films as hard, good wear resistance and low friction coatings.^{[11] [12] [13]} In most of the cases, the final film is reported to be rather amorphous and a mixture of sp^3 and sp^2 bonds between the different atoms, with only a little amount of material being accountable for 2D sp^2 BCN, probably due to the large amount of defects related to the synthetic method.^{[13] [10]} The physical methods used for BCN so far, seem to lead mainly to disordered mixtures of sp^3 and sp^2 bonds without the possibility to tightly control chemical structure and morphologies. Chemical methods have been more extensively used to synthesize BCN thin films with different elemental ratio, since this method can provide better control over the material properties and morphology. One of the first attempts to synthesize BCN thin films by chemical methods was reported by Kaner et al. back in 1987. They used a mixture of three gaseous precursors, i.e. boron trichloride, acetylene and ammonia in the temperature range of 400-700°C. They found that B, C and N were successfully incorporated in the final material structure, showing different XPS spectra from a mixture of graphite and BN, proving in that way that all the elements were effectively incorporated into the material.^[14] Later on, inspired by synthetic methods of graphene, Ci et al. used a thermal catalytic method to deposit BCN thin film on a Cu substrate from methane and ammonia-borane as gaseous co-precursors at 900-1000°C. Controlling the experimental parameters, as flow rate and temperature, they were able to tune the C content tuning the optical and electronic properties. The bandgap size was lowered from 5.7 to 1.5 eV with increasing amount of C. However, the BCN they reported was not homogeneous along the sheet: the nanostructure showed an inhomogeneous distribution of BN and graphene domains, which was attributed to the low solid solubility between the two materials, leading to phase separation as can be seen in TEM picture and model they proposed in figure 3.1.^[3] Also different single source precursors such as alkyl-boranes and alkyl-borazines have been investigated as

convenient precursors for CVD processes in presence of methane, ammonia or hydrogen flow, on different substrates.^{[2] [15] [16]} Leardini et al. used methylamine borane, a white crystalline solid with low boiling point, in a tubular quartz reactor to deposit BCN thin films on Cu substrates at 1000°C.^[16] This material was also constituted by a mixture of C and BN phases with distinct optical bandgap at 5.7 and 1.7 eV attributed respectively to BN and size quantized graphite domains.^[16] The phase separation between C and BN was reported also by other groups under similar conditions.^[1] Very recently, a single source precursor named bis-BN cyclohexane was used to deposit BCN thin films by ion-beam induced heating of the iridium substrate in ultra-high vacuum chamber. Theoretical modelling and experimental evidences suggested that the material obtained in these conditions is constituted of B₂C₂N₂ and B₃N₃ rings in the graphitic sheet with homogeneous stoichiometry, even if by theoretical calculations this structure is not the thermodynamically favored one.^[17]

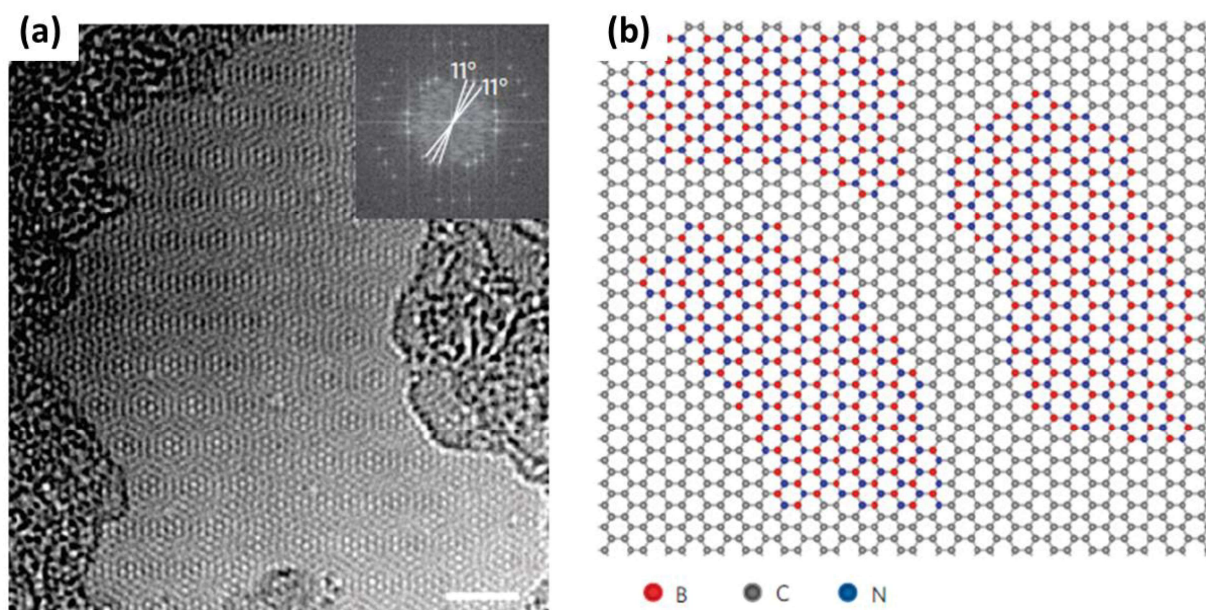


Figure 3.1. TEM image (a) and schematic structure (b) of BCN material with phase separation. Scale bar 2 nm.^[3]

As mentioned in the previous chapter, g-C₃N₄ thin films have a bandgap of 3.06 eV and we have already successfully developed methods to lower it, by doping with different monomers and co-monomers, in order to make use of it in the visible range. However, a variety of applications, such as highly reflective coatings, LED encapsulants and more require a wider bandgap. This leads to the challenge to develop a method to widen the bandgap for carbon-nitrogen-based thin film

materials, in order to make them highly transparent all over the visible range. BCN thin films can meet this criterion, as previously reported, but methods to develop homogenous thin films without phase segregation are still lacking. A wide variety of theoretical calculation have exploited the possible structures and relative stability of ternary compounds leading generally to the conclusion that phase segregation or stripe-like structures are the most stable among the considered ones.^{[18] [19]} Different possible atomic morphologies and compositions were reported to give rise to very different properties, from metallic to insulators, with a wide range of bandgaps.^{[19] [20] [21]} Moreover, Sun et al. have focused on the calculation of dielectric functions of different BCN materials, suggesting that BCN is a good candidate material with graphitic-like structure, very high refractive index (close 2.5) and high transparency in the visible region.^[21]

In the following chapter, a method for the synthesis of BCN thin films based on CVD from a solid-state single source precursor will be presented. The goal is to achieve high-quality BCN thin films within a conjugated organic system, with high transparency in the visible range and high refractive index, so that the material can find use as highly reflective coating for structural colors or encapsulant for LEDs. Elemental and structural characterization of the thin films will be given to prove the high quality of the deposition and the elemental composition at different temperatures. Furthermore, the optical properties of the thin films as transmittance, reflectance, refractive index and fluorescence will be presented.

3.2. Chemical vapor deposition of BCN thin films from melamine-boric acid adduct precursor

Chemical deposition methods can provide better quality and control over the synthetic parameter and have been widely used for deposition of organic and inorganic films, from SiO₂ and MoS₂ to graphene and diamond.^{[22] [23] [24]} For these reasons, the same setup already presented in the previous chapter was used to deposit ternary BCN thin films on various substrates. To deposit g-C₃N₄ thin films, melamine was chosen as a single source precursor for C and N since it is a chemical non-hazardous commodity that can conveniently be sublimated at relatively low temperatures. Melamine, like urea and other organic N-containing compounds, has been widely used to create supramolecular polymeric structures, due to its ability to create strong hydrogen bonds with H-bond acceptors.^{[25] [26]} Moreover, melamine was

reported to be able to create a 1:2 adduct with boric acid by hydrogen bonding in which both molecules act as donor and acceptor, named melamine diborate.^[27] Boric acid can be regarded as one of the most common and convenient B derivatives that can be used to synthesize B-containing compounds, with extremely low toxicity (lethal dose on rats 3450-4080 mg/kg, for comparison NaCl has lethal dose on rats of 3000 mg/kg upon ingestion).^[28] The melamine-boric acid adduct can presumably be considered as a possible non-hazardous, solid, single-source precursor for BCN thin films. Although using the boric acid as precursor, which contains the strong B-O bond is counterintuitive, in the following it will be shown that by this approach the B-O bond is eventually cleaved to form less stable B-N and B-C bonds.

The melamine-boric acid has been prepared with two different melamine-boric acid ratios in order to prove that it can be used as effective precursor for BCN thin film deposition. In a typical reaction 1.26 g of melamine (10 mmol) and 1.24 g (20 mmol) of boric acid have been placed in a vessel with 4 and 6 ml of deionized water, respectively. The dispersions were heated up to 95-100°C and stirred until boric acid was completely dissolved. Then, the warm boric acid solution was added directly into the melamine dispersion promptly forming a white tough solid precipitate (figure 3.2). The prepared mixture has been further heated for 30 minutes and kept overnight at 40°C in vacuum oven to further dry. The second melamine- boric acid ratio has been prepared following the same steps, however, the mass of boric acid and the water volume to dissolve it were only half the amount (0.62 g, 10 mmol in 3 ml of deionized water). In this chapter, nomenclature will be referred to the precursor composition according to the molar ratio of melamine and boric acid used for the preparation: i.e., this last one will be named 1:1 where the previous is 1:2. These two ratios were both chosen in order to evaluate if any of them would lead to the thin film deposition of a ternary BCN compound and if this allows for the control of the elemental composition of these three elements in the film.

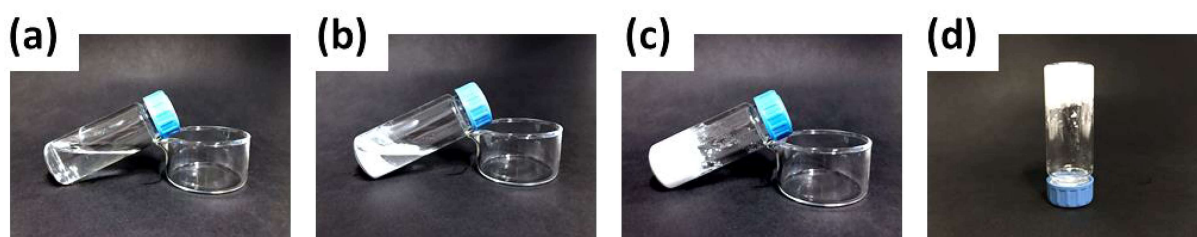


Figure 3.2. Preparation steps of melamine diborate precursor: boric acid solution (a), melamine dispersion in water (b) and the melamine diborate precipitate (c, d).

The as-prepared precursors were analyzed by FTIR in order to prove that the precursors are different from the solid mixture of the single components (figure s17). FTIR spectra of melamine borate prepared from different melamine and boric acid ratios show new vibrational peaks at low wavenumbers (below 1600 cm^{-1}) and broadened absorption from 3500 to 2500 cm^{-1} attributed to large amount of hydrogen bonds within the supramolecular structure. Moreover, FTIR spectra are very similar between the two compositions and to previous reports.^[29] To evaluate the feasibility of these single-source precursors for thin film deposition of BCN, decomposition of the melamine-boric acid precursors has been analyzed via TGA-DTG, shown in figure 3.3 for (a) the 1:1 and (b) the 1:2 precursors. In both cases, contrary to previous observations for melamine, the melamine- boric acid complex cannot be fully sublimed as about 20% of the initial mass is still present even at 1000°C . Eventually, in order to use them for deposition of BCN thin films it is necessary to develop a suitable deposition heating profile. Both TGAs show a sharp decrease of mass that occurs below 200°C which was previously attributed to boric acid dehydration. Indeed the mass loss at this temperature is larger for the sample 1:2.^[29] The 1:1 sample shows a large mass decrease at around 300°C , which is attributed to non-complexed melamine which sublimes in this temperature range, does not occur for the 1:2 sample, confirming that the melamine diborate complex has been successfully obtained. A third main mass loss appears in the range from 450 to 650°C , which suggests that at these temperatures the melamine-boric acid precursors decompose. This is the temperature range which is interesting for deposition of B-C-N containing films: large mass losses of about 25% and 35% occur for the 1:1 and 1:2 ratios, respectively, which indicates that in this range the solid precursor is condensing releasing by-products containing B-C-N elements. These by-products can be eventually adsorbed and further polymerized on a target surface, acting then as the real precursors for the thin film deposition. Previous reports suggest that in this case the melamine-boric acid adduct starts decomposing at 500°C releasing CO_2 and cyanamide as by products possibly leading to the formation of B-N bonds.^[29] Differently to the deposition of $\text{g-C}_3\text{N}_4$, the deposition method used in this case exploits the gaseous products obtained by the thermal decomposition of the precursors that are eventually polymerized on the substrate surface, creating the thin film, and leaving back a solid residue, as schematically shown in figure 3.3 (c).

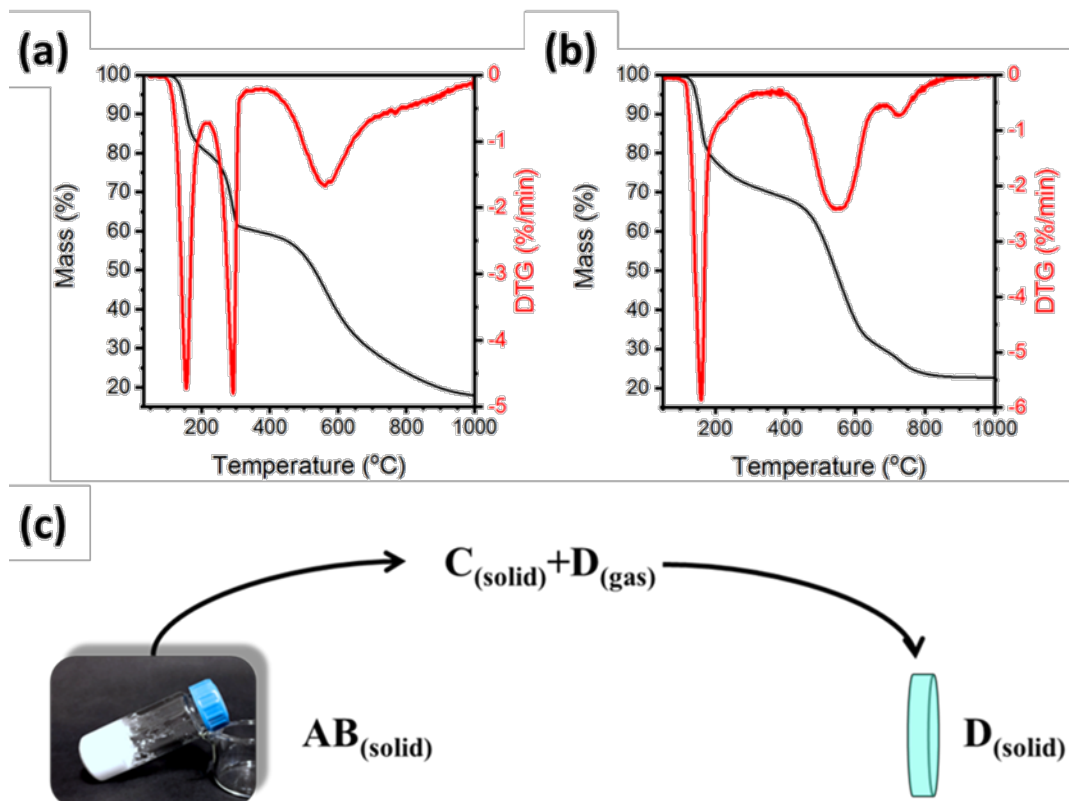


Figure 3.3. TGA (black line) and DTG (red line) of the 1:1 (a) and the 1:2 (b) precursors. Schematic representation of the thin film deposition process described (c).

To prove that the melamine-boric acid precursor is feasible for BCN deposition via CVD, as previously done for the g-C₃N₄ thin film, it was successfully tested by the proof-of-concept method using the test tube in a muffle furnace. This method has many limitations, especially regarding the single temperature control and maximum temperature which depends on the substrate and on test tube stability (usually below 600°C). The absence of vacuum can lead to high contaminations and eventually low homogeneity of the deposited films, as shown in figure S18 (a), (b). However, the presence of the B, C and N elements was proven via XPS as reported in the spectra overview in figure S18 (c). In this way, it has been possible to prove that the chosen precursors can be used for CVD deposition, possibly leading to different BCN compositions.

By the experience developed for the deposition of high-quality g-C₃N₄ shown in chapter 2, pressure and carrier gas flow conditions were not modified. The heating rate and upstream temperature were both increased: in the first case, the sublimation of not fully complexed melamine in the 1:1 precursor may lead to the formation of a film with gradient composition, so it was increased up to 17°C/min; in the second

case, the TGAs show that the decomposition temperature of 1:1 and 1:2 precursors was in the range 450-650°C. Therefore, 500° and 550°C upstream temperatures were chosen with downstream temperatures in the range of 550-800°C in order to polymerize the gaseous decomposition products at higher temperatures. A summary of the sample conditions is reported in table 3.1. After each deposition, the precursor residue was collected and weighted to estimate the amount of gases produced which could be deposited eventually. As expected, longer times and higher upstream oven temperature decreased the amount of solid residue.

Table 3.1. Summary of the CVD conditions for BCN deposition for the 1:1 and 1:2 precursors.

Molar ratio	Sample number	Precursor amount (g)	Upstream temperature (°C)	Upstream time (min)	Downstream Temperature (°C)	Downstream time (min)	Residual amount (%)
1:1	I	5	500	30	550	90	44%
	II	10					39%
	III	5	500	120	550	180	35%
	IV	10					37%
	V	5	550	30	600	90	34%
	VI	10					35%
	VII	5	550	30	800	90	38%
	VIII	10					35%
1:2	IX	7	500	30	550	90	66%
	X	14					58%
	XI	7	500	120	550	180	56%
	XII	14					53%
	XIII	7	550	30	600	90	51%
	XIV	14					49%
	XV	7	550	30	800	90	50%
	XVI	14					49%

As in the previous chapter, homogeneity and flatness of the deposited films were analyzed by SEM and AFM and reported for two representative samples in figure s19 (a-d). In both cases, the surface appears very homogeneous and defect-free even on a large scale; the SEM comparison with films prepared by the test tube method clearly shows that the CVD method allows for better film quality and more homogeneous deposition which is very important for applications in optics and optoelectronics. AFM analysis of CVD thin films shows very low roughness ($R_q = 1.0$ and 0.9 nm), very similar to the quartz substrate itself (1.0 nm). Composition and morphology at the nanoscale was investigated by TEM and EELS (figure 3.4 (a-d)). TEM images of thin films from different precursor ratio (1:1 figure 3.4 (a), 1:2 figure 3.4 (b)) but the same temperature conditions show that similar average film composition may lead to very different morphologies. In figure 3.4 (a), the sample

deposited from the 1:1 precursor show an amorphous character, possibly with layered structure as suggested in figure S20 (a). In figure 3.4 (b) the deposition from the 1:2 precursor leads to thin films with very organized structure. Highly diffracting crystalline pattern with periodicity 0.33 nm suggests that a graphitic structure occurs in the material: the periodic distance can be attributed to interlayer stackings typical for graphitic materials like graphite and h-BN.^[30] The presence of layered stacks is derived from the edges shown at lower magnifications (figure S20 (b)). It is worth to point out that in both cases, no phase separation could be detected, different from many previous reports on BCN materials. In figure 3.4 (c), the EELS spectrum of the sample in figure 3.4 (b) (sample IX) is shown, with the element K-edges labeled which is also very representative for the other samples. The three visible edges depicted at 194, 287 and 399 eV correspond to characteristic K-shell ionization edges of B, C and N respectively. The bands of each element can be well resolved and show in these cases a first sharp peak corresponding to $1s-\pi^*$ antibonding orbital, followed by a wider $1s-\sigma^*$ antibonding orbital.^[3] The O K-edge is present at around 535 eV, however, in this case only the $1s-\sigma^*$ edge is present. Analysis of EELS spectrum leads to different important conclusion: first of all, B, C and N elements are all present in the synthesized material, with very sharp and intense π^* transitions typical for delocalized π -electron systems; secondly, the spectrum reveals a very well-defined structure with very long sp^2 -hybridization structure for B, C and N elements; lastly, the O K-edge is present, in some samples, however, in all cases the very different spectral shape and the absence of well-defined $1s-\pi^*$ antibonding orbit, can be attributed to the presence of oxygen as edge-defect, thus not involved in the BCN conjugated structure.^[31] Previous results from Fellingner et al. for the synthesis of BCN at 1400°C from N,N'-ethylmethyylimidazolium tetracyanoborate ionic liquid show a much shorter extent of conjugation compared to the present work, where the synthetic temperature used is even 850°C lower.^[31] Similar comments are also valid for the CVD synthesis of BCN reported by Ci et al., where the B, C, N peak positions are quite different (185, 276 and 393 eV for B, C and N respectively) suggesting a very different electronic environment with respect to the present case.^[3] ^[32] A large blue-shift between the K-edges of the BCN thin films prepared (B, 194 eV; C, 287 eV; N, 399 eV) and previous reported BCN with phase separation (B, 185 eV; C, 276 eV; N, 393 eV) is present for all the constituting elements. The large shift, in eV, is attributed to a very different oxidation state of the elements between the two cases

and, therefore, C/BN phase separation is unlikely to occur.^[33] Moreover, the large blue-shift reveals that the system is highly electron deficient and thus very stable against oxidation, i.e. a possible candidate noble material, as will be shown in more detail in the next section of this chapter.^[34]

Compositions of the different films have been calculated by EELS and are schematically reported in the ternary phase diagram in figure 3.4 (d). It is worth to remember that, as mentioned in chapter 2, the compositions depicted in the ternary phase diagram have been obtained by EELS analysis and thus is only qualitative. However, it can be seen that the BCN relative composition doesn't significantly change between the 1:1 and the 1:2 precursor composition (with all the other conditions fixed). Increasing the synthesis temperature to 800°C (point XVI) a significant depletion of C is shown, as expected. Indeed, at very high temperature (above 1000°C), it is expected that the C content could be further reduced, thus leading to BN materials, as previously reported by other authors.^{[29] [35]}

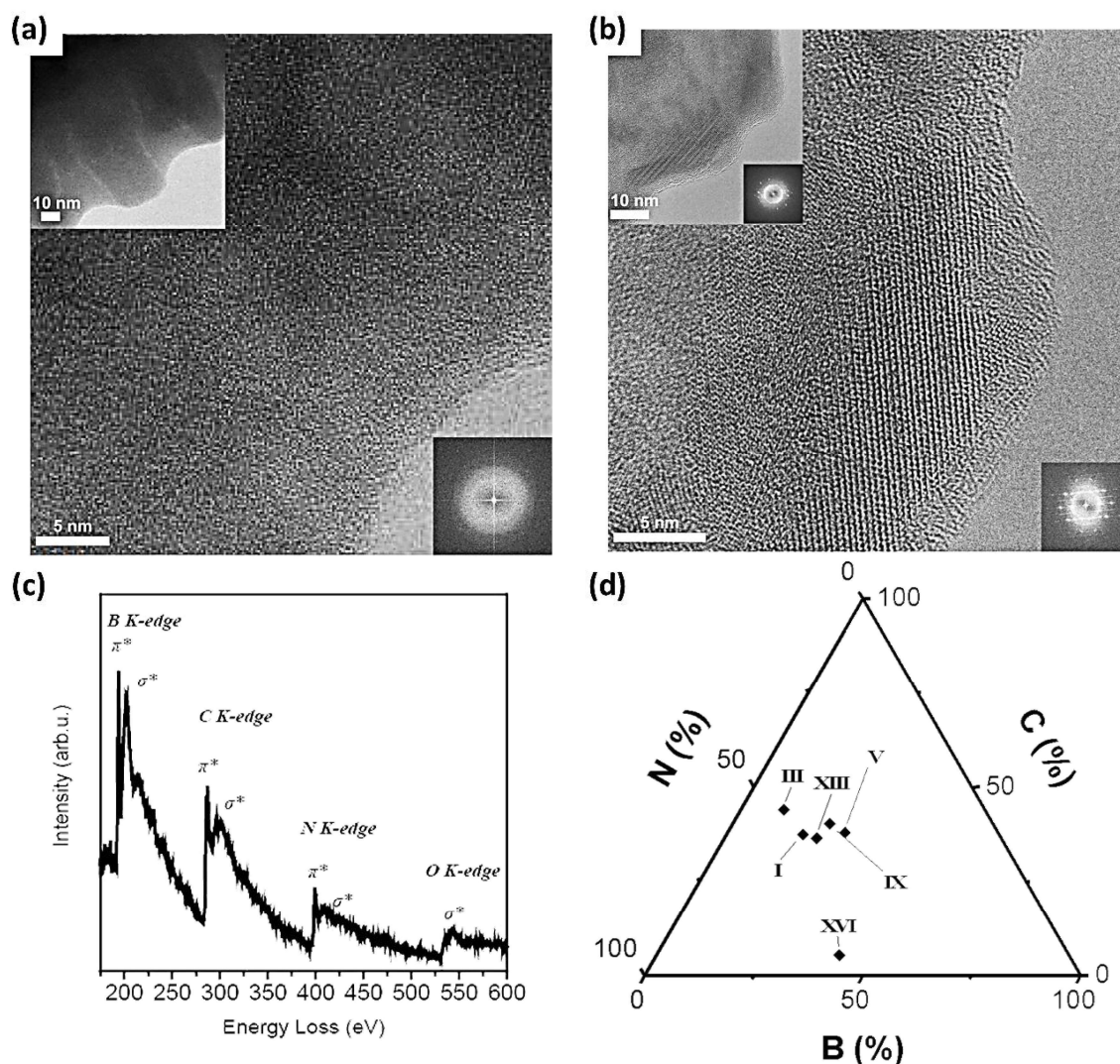


Figure 3.4. TEM and FFT pattern images of samples I (a) and IX (b). Representative EELS spectrum of BCN thin films (c). Ternary phase diagram with relative composition of some samples calculated from EELS spectra (d).

The prepared samples on silicon substrate have been characterized by Raman and FTIR spectroscopy. Raman spectra recorded are for all samples overlapping with the one recorded for the bare substrate so not providing any possible further information, as reported for two representative samples in figure S21 (a). FTIR spectroscopy (figure S21 (b)) reveals a strongly different spectrum for the bare substrate compared to the reported samples, especially in the region below 2000 cm^{-1} suggesting that deposition successfully occurred. However, it is not possible to determinate any specific vibrational mode, probably due to the extremely low thickness of the prepared samples. In order to get deeper insights, XPS analysis was performed (on sample IX), and the data are depicted in figure 3.5 (a-c) for B, C and N peaks, respectively. The spectrum overview (figure S22) shows also the presence of Si and

O peaks, attributed once more to the very low thickness of the sample. The relative chemical composition $BC_{2.4}N_{3.3}$ has been calculated from the XPS spectra, confirming that significant relative amounts of B are successfully present in the thin film. Moreover, the chemical composition is in contrast with phase separation: indeed, if phase C/BN separation would occur, it would be expected almost the same relative atomic composition for B and N. However, in the present case, almost one B atom is present each three N atoms and, for this reason, in contrast with the phase separation. The B1s spectrum (figure 3.5 (a)) was deconvoluted into two components centered at 189.2 eV and 190.5 eV and attributed to sp^2 B-C-N and B-N respectively, as previously attributed by other groups.^[35] The deconvoluted peaks lie in the range of sp^2 conjugated B, confirming though the high sp^2 conjugation achieved, in good agreement with the EELS analysis previously shown (figure 3.4 (c)). Moreover, the peak usually attributed to B-O bonds (192-192.6 eV) cannot be detected, confirming that despite the high oxophilicity of B, the presented method allows for creating less stable B-C and B-N bonds in a BCN aromatic structure, at even lower temperatures compared to previous attempts.^{[35] [31] [36]} The deconvolution of the C1s peak (figure 3.5 (b)) shows a strong preference of C to bond with heteroatoms with respect to homoatoms, supporting once more the absence of the C/BN phase separation (283.1 eV C-B, 284.6 eV C-C and 286.7 eV C-N). In the N1s spectrum (figure 3.5 (c)) the two components were further attributed to sp^2 B-N-C (397.5 eV) and C-N (398.6 eV) environments within the structure.^{[3] [35]} From XPS spectra it can be concluded, that the film is composed of different B-N, B-C and C-N environment included in the BCN sp^2 system, without evidences for phase separation. Surprisingly, the analysis of the XPS spectra reveals that a significant amounts of less stable B-C bonds with respect to the favored B-N ones are formed, in contrast to what usually reported.^[3] XPS and EELS analyses are in good agreement, confirming that the method successfully provides the deposition of BCN thin films where the B, C and N elements are present in a homogeneous and highly conjugated phase.

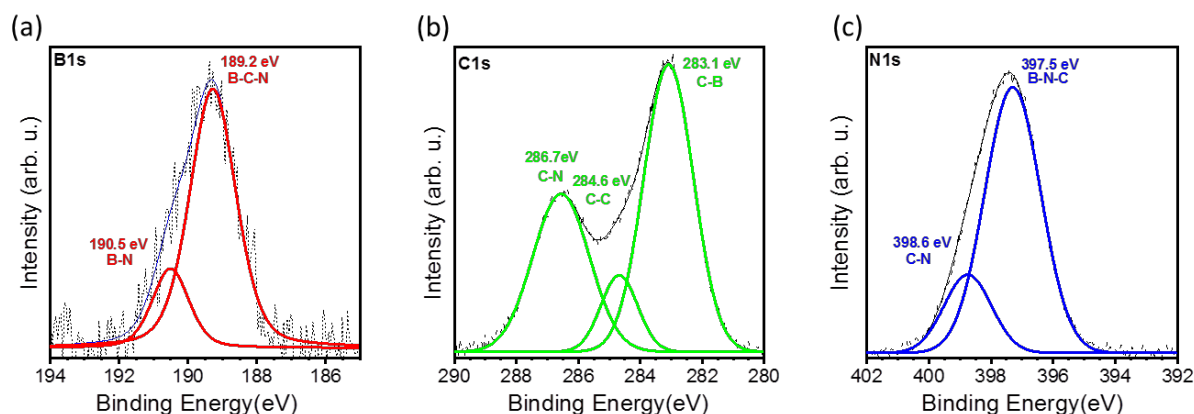


Figure 3.5. Deconvoluted XPS peaks of B1s (a), C1s (b) and N1s (c) of sample IX.

This first part was dedicated to show the CVD synthetic method used for BCN high quality thin films from solid state, non-hazardous, common precursors (melamine and boric acid). The following part of this chapter will be dedicated to optical properties of the prepared BCN thin films for possible applications in optics, transparent thin film transistors, electrochemistry and beyond.

3.3. Optical properties of BCN thin films

Optical properties of BCN materials have been reported only little since it is still under debate in the academic community whether the material forms a homogenous compound or if phase separation occurs. Moreover, relative elemental composition and morphology have a strong influence on the material properties, such as bandgap, VB and CB levels, conductivity and more.^{[37] [17]} BCN thin films are expected to possess a wider bandgap than $g\text{-C}_3\text{N}_4$, due to increased electron localization, whereas maintaining high refractive index, which is fundamental for many applications in optics, such as optical fibers, lenses, reflective coatings and encapsulants for light-emitting diodes.^[38]

Transmittance spectra were collected on quartz substrates at normal incidence in order to evaluate the effect of precursor composition ratio, mass, time and temperature. Representative comparisons between transmittance spectra are shown in figure 3.6 (a-d). The comparison between optical properties of samples prepared with the same temperature but with different precursor composition is of particular interest to evaluate the tunability of optical properties and film thickness. As already shown by TEM and EELS, samples prepared at the same temperature and different precursor ratio have very different morphologies with, however, only a little difference

in elemental composition. In figure 3.6 (a) (extended up to 1800 nm in figure S23), are shown the spectra of sample I and IX, compared to the thinnest thin film sample of g-C₃N₄ (CN-2a, presented in chapter 2), respectively in blue, green and red (the dotted black line is the bare quartz substrate), which have been synthesized at 550°C (downstream temperature). The comparison between these samples is of interest to show that the transmittance of BCN thin films is successfully blue-shifted with respect to the g-C₃N₄ one. The g-C₃N₄ thin film shows an intense peak minimum at 310 nm, which was attributed by Bian et al. to the π - π^* transition in g-C₃N₄.^[39] Transmittance spectra of samples I and IX, obtained from the 1:1 and the 1:2 precursor, respectively, show that the minimum blue-shifts with increasing the amount of boric acid in the solid precursor to 299 nm for the 1:1 (blue line) and 208 nm for the 1:2 (green line). This confirms the possibility to tune the optical properties of BCN by simply modifying the precursor composition. Moreover, both BCN samples show very high transmittance in the visible range and near infrared (figure S23), mostly overlapping with the quartz transmittance, confirming that the method proposed is effective to deposit films being highly transparent over a broad spectral range. However, it can be anticipated that the bandgaps of the two samples (figure 3.6 (d) and 3.7 (c), (d)) are similar and therefore the spectral difference is attributed to the different chemical and morphological arrangement in the samples, as previously shown by TEM images (figure 3.4 (a), (b)).

The opportunity to tune the film thicknesses was evaluated also for BCN films with a similar approach used in the previous chapter for g-C₃N₄. Sample IX, in figure 3.6 (b), was prepared by heating for 90 minutes longer the precursor (sample XI) and with double amount of precursor (sample X) under the same conditions. The peak intensity and shape reveal that increasing the amount of precursor does not lead to thicker sample, since the transmittance increases. This effect has been observed very clearly also in other samples in figure S24, where very different spectra have been recorded by simply doubling the precursor amount. Surprisingly, larger amount of precursor seem to mostly lead to film deposition of different materials; the exact reason is still under investigation. Longer synthesis heating times seem to be effective to increase the film thickness, as shown in figure 3.6 (b), where samples IX (green line) and XI (red line) keep the same spectral shape and lower transmittance intensity for the second one. Conversely to the case of g-C₃N₄, longer heating times

seem to provide films with larger thickness, possibly because the solid precursor releases slowly the film synthons, allowing in this way thickness control.

Figure 3.6 (c) (extended up to 1800 nm in figure S25 (a)) and S25 (b) show the spectral change of transmittance for samples prepared at different temperatures, prepared from the 1:2 and the 1:1 precursor ratio, respectively. Increasing the synthesis temperature, the transmittance minimum peak shifts towards lower wavelength from 299 nm in sample I to 194 nm in sample VII, suggesting a progressive shift of the absorption peak from 550 to 800°C possibly attributed to reduced C content in the BCN structure (figure S25 (b)). In a similar way, samples prepared from 1:2 ratio precursor (figure 3.6 (c)), the transmittance minimum shifts from 208 to 194 nm, at 550 and 800°C respectively. However, in samples IX (green line) and XIII (red line) minima occurs in both cases at 208 nm, but with different spectral shape. This proves that optical properties can be further tuned also by means of temperature, as well as by the initial ratio of melamine and boric acid in the solid precursor. Another important parameter that defines the optical properties of the prepared films is the bandgap. To evaluate bandgap energy and shift with temperature and precursor composition transmittance spectra have been converted to absorbance spectra, since:

$$A = -\log \frac{T}{T_{ref}}$$

where T is the transmittance of the considered sample and T_{ref} is the transmittance of the bare substrate.^[40] The calculated absorbance spectra of the considered samples were then plotted by the method proposed by Tauc et al., assuming in all cases indirect allowed transitions (figure S26 (a) and (b)).^{[41] [42]} The calculated bandgap are summarized as a function of synthesis temperature in figure 3.6 (d) (black dots 1:1 ratio, red dots 1:2) and compared to the one of g-C₃N₄ (blue dot). The presence of boric acid in the solid precursor leads in all cases to a bandgap increase, compared to g-C₃N₄, i.e. is blue-shifted in the UV spectral range. At a downstream temperature of 550°C, the calculated bandgap energy increases from g-C₃N₄ (3.06 eV) to BCN 1:1 and 1:2 (3.50 and 3.53 eV respectively), whereas BCN synthesis time seems to not sensibly affect the bandgap energy (3.52 sample XI and 3.51 eV sample III), confirming once more that the synthesis time does not significantly affect the material properties. Increasing the temperature in both cases the bandgap widens as

expected to 3.65 eV, 4.72 eV at 600°C for the 1:2 and the 1:1 precursor ratio, respectively. However, the bandgap shrinks again when the temperature is increased to 800°C to 4.50 eV from 1:1 precursor, whereas for the 1:2 ratio it further increases to 4.57 eV. In the case of the 1:2 precursor ratio, the bandgap size increases with the synthesis temperature. Moreover, in all presented cases, the BCNs bandgap energies lie between the ones of g-C₃N₄ (3.06 eV) and h-BN (5.69 eV) suggesting very different structures between these two extremes with high tunability of optical properties that can be achieved by simply changing precursor ratio and/or synthesis temperature.

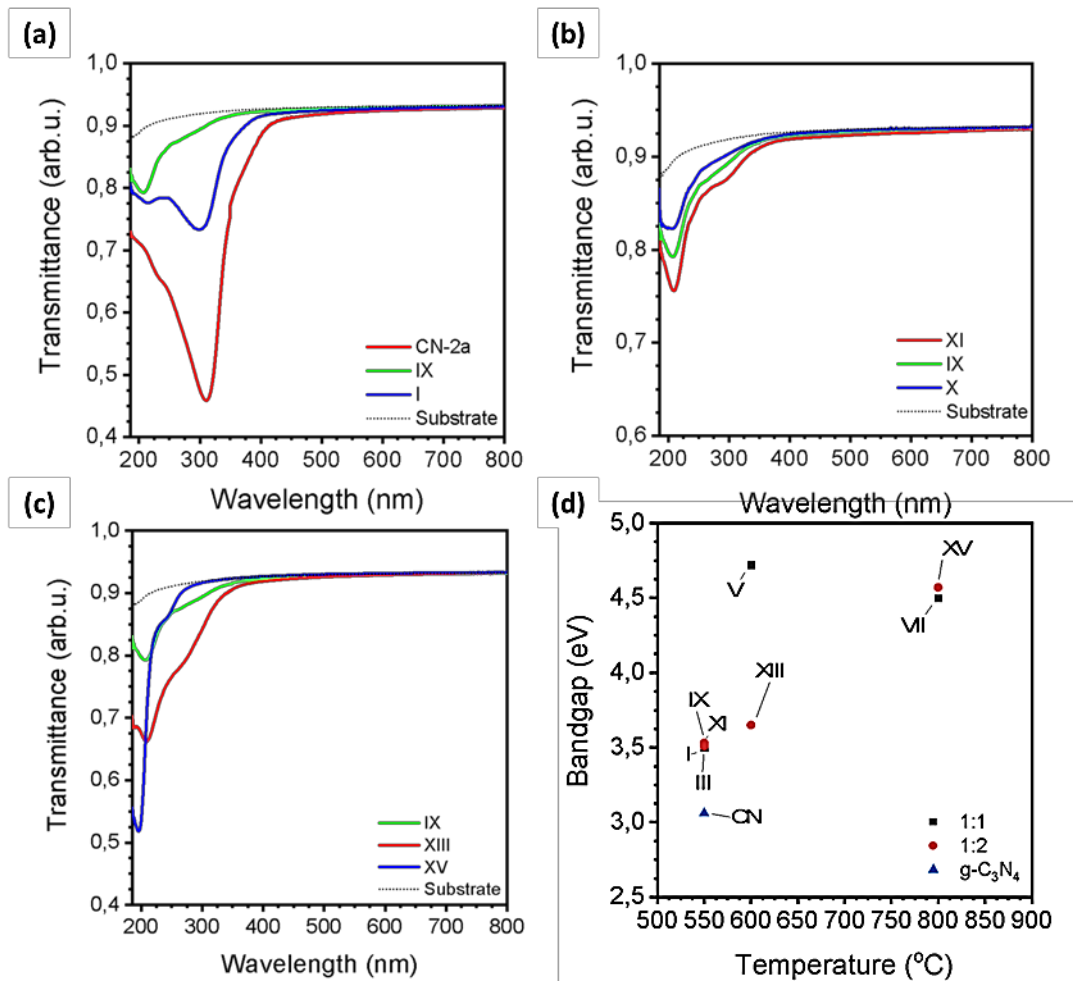


Figure 3.6. Transmittance spectra of some g-C₃N₄ and BCN samples (a), (b) and (c). Calculated bandgaps for BCN thin films deposited at different temperatures (d).

Further insights on the optical properties of the BCN thin films have been obtained by ellipsometry (figure 3.7 (a-d)). In figure 3.7 (a) and (b), the spectra of the optical parameters, refractive index (black line) and extinction coefficient (black line) are shown, obtained by modelling the data of samples I, III (figure 3.7 (a)) and IX, XI

(figure 3.7 (b)) in the range 187-1000 nm (extended to 2500 nm in figure S27 (a) and (b)). The optical functions of the BCN thin films show a very different behavior between different precursor ratios. In figure 3.7 (a), BCN thin films deposited from the 1:1 melamine-boric acid ratio precursor, shows optical functions close to the one presented in the previous chapter for g-C₃N₄. The extinction coefficient has a maximum of 1.71 at 276 nm, blue-shifted and slightly less intense with respect to the one obtained for g-C₃N₄ thin films. Moreover, the refractive index function is also slightly lowered, although being very high compared to polymer thin films.^[43] Although the refractive index slightly decreases to 2.40 at 500 nm and 2.22 at 1000 nm, the Abbe number increases to 11, which makes this thin film material more interesting for lenses application. The optical functions obtained for the samples I and III allow for the determination of the bandgap energy from the Tauc plot (figure 3.7 (d)). Assuming an indirect bandgap, the energy found for the HOMO-LUMO transition from ellipsometric measurements is 3.56 eV, very close to the one obtained from the elaboration of transmittance spectra. The small difference (0.06-0.05 eV) confirms that the calculation from the transmittance spectra allows for bandgap calculation with good approximation by means of a simple setup, i.e. the UV-VIS spectrometer. Similar conclusions can be derived for samples IX and XI, deposited from 1:2 melamine-boric acid ratio precursor at 550°C. In figure 3.7 (b), the optical functions show high extinction coefficient values (in red), however decreased in maximum intensity (1.48) and shifted towards even lower wavelength (200 nm) with respect to the sample prepared from the 1:1 precursor ratio. This is in good agreement with the blue-shift already shown for the transmittance measurements in figure 3.6 (a). The refractive index function shows similar values with the one shown in figure 3.7 (a): the refractive index at 500 nm is 2.32 and 2.24 at 1000 nm. The different shape of the refractive index function, with well-defined peaks, is typical of crystalline materials in the case of sample IX (figure 3.7 (b)) rather than the one with a single broad maximum (figure 3.7 (a), sample I), which is typically reported for amorphous materials.^[44] ^[45] This is in very good agreement with the morphology depicted in TEM images of the samples IX, which shows a crystalline structure (figure 3.4 (b)), and I, an amorphous one (figure 3.4 (a)). The other difference between the two samples relies in the optical dispersion, e.g. the inverse of the Abbe number. The presented samples obtained from 1:2 precursors show a lower dispersion, as confirmed by the

Abbe number, which increases more than 2 times (25.6), making this material even more interesting for application in lenses.

The thickness of the samples, obtained by ellipsometric measurements, is listed in table 3.2. The prepared samples have very low thicknesses, in all cases lower than 2 nm. Once more, the thickness scale derived from transmittance measurements is confirmed by ellipsometry: the samples prepared with longer heating times (III and XI) have larger thickness. In the case of sample III on fused silica substrate, the thickness values of the front films III and I are the same. However, the lower transmittance of sample III is confirmed by the larger film thickness deposited on the back. Since the transmittance measurements consider the light intensity reduced that crossed the sample section, the sum of the film thicknesses is the parameter that has to be considered. Therefore, it is in good agreement with figure 3.6 (b). Interestingly, films grown for shorter times are thicker on fused silica and thinner on silicon, whereas increasing the synthesis time the behavior is inverted. Possibly the difference is attributed to the high surface flatness of silicon (already shown in the previous chapter) which can hinder the deposition of the first layer. Once the first layer is created, the film thickness can grow at higher rates than on fused silica. Although the refractive index modelled are very high, further studies will be necessary to increase the thickness to further confirm the results obtained.

The modeled values of the optical functions show very high refractive indices, close to the one shown before for g-C₃N₄. However, high refractive index values are accompanied by a strong blue shift of the bandgap, which makes these materials highly interesting for optical applications, such as lenses and reflective coatings.^[46] Moreover, it can find applications as encapsulant for LEDs, increasing the light extraction efficiency, and transparent windows coatings, to reflect near-IR, to reduce cooling system expenses especially in states that near the equator.^[43]

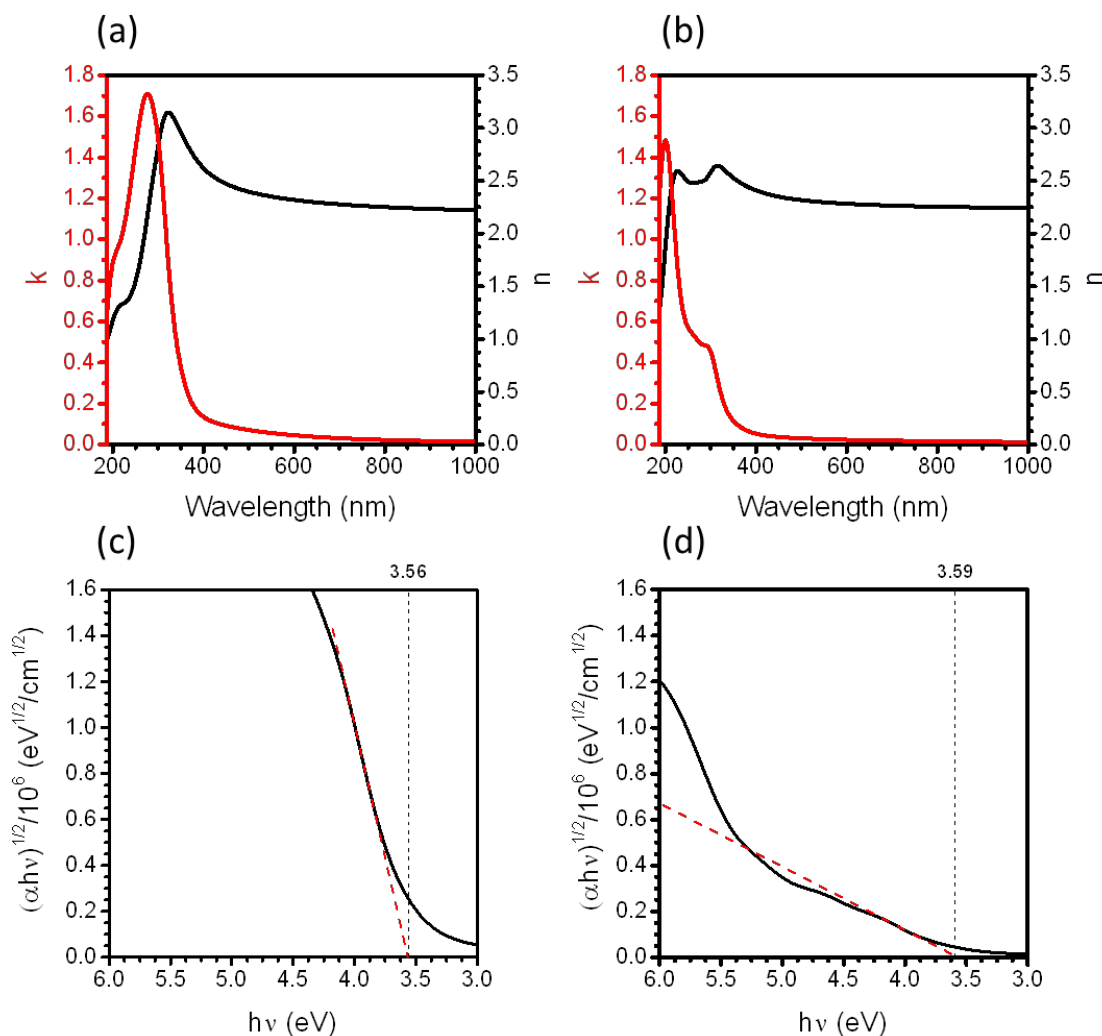


Figure 3.7. Optical functions modeled for samples I, III (a) and IX, XI (b). Tauc plots and bandgaps for samples I, III (c) and IX, XI (d).

Table 3.2. Thickness of BCN thin films calculated by ellipsometry. Between brackets is reported the thickness of the film on the backside of fused silica substrate.

Sample	Thickness on silicon (nm)	Thickness on fused silica (nm)
I	1.0	1.1 [0.5]
III	1.5	1.1 [0.8]
IX	0.4	0.6 [0.25]
XI	1.9	0.7 [0.4]

The HOMO-LUMO gap and band positions were evaluated for sample IX by UPS (figure S28) and compared to the band structure obtained in chapter 2 for g-C₃N₄ and for h-BN calculated by Pierucci et al.^[47] As previously shown, the bandgap energy lies in between g-C₃N₄ (2.88 eV) and h-BN (5.69 - 6.0 eV), however, the band structure can give more insights into the material properties.^{[3] [47]} On the one hand,

g-C₃N₄ has a small bandgap compared to h-BN with Fermi level (E_F) being closer to the CB, typical of n-type semiconductors; on the other hand, in h-BN the Fermi level lies closer to VB with higher CB and lower VB respectively (in vacuum scale). In the BCN the VB lies close to the BN, whereas the CB is closer to the g-C₃N₄. It shows that the introduction of B provides a shift towards more negative values of both VB and CB with the Fermi level lying closer to CB as in g-C₃N₄. If it can be assumed that BCN is a semiconductor, as previously reported, and supported for the present case by the high sp^2 conjugation depicted by EELS and XPS measurements, this material shows n-type semiconducting properties.^[1] This can be explained by the high N content in the material, that exceeds the B one, as confirmed by XPS characterization.^[31] The highly positive value (in terms of NHE) of the VB suggests that BCN synthesized by this method show indeed noble properties (as well as g-C₃N₄ does), a concept that has been very recently described in detail for carbon-based materials by Antonietti and Oschatz.^[48] The highly conjugated system, the stabilizing influence by significant amounts of heteroatoms like B and N, as well as the high polar character, due to the electronegativity difference between the constituting elements, provides an unusually high stability to the material. Furthermore, carbon-based materials with noble properties form at comparably low temperatures due to thermodynamic stability, as in this case where the synthesis temperature (550 °C) is hundreds degrees lower compared to previous reports for this class of materials.^[31] Very positive VB values (around 2 V vs NHE) for BCN materials were already reported, with lower bandgap (2.08-2.72 eV) but synthesized at relatively high temperature (1250 °C).^[49] ^[50] Energy band levels reported in figure 3.8 finally proves that the exploited synthetic methods for thin films via CVD is not only a method for synthesis of high quality C-based materials, but furthermore, by the appropriate choice of precursors and conditions, it is effective to deposit carbon-based materials with noble properties, i.e. with high resistance against oxidation.^[48] ^[51]

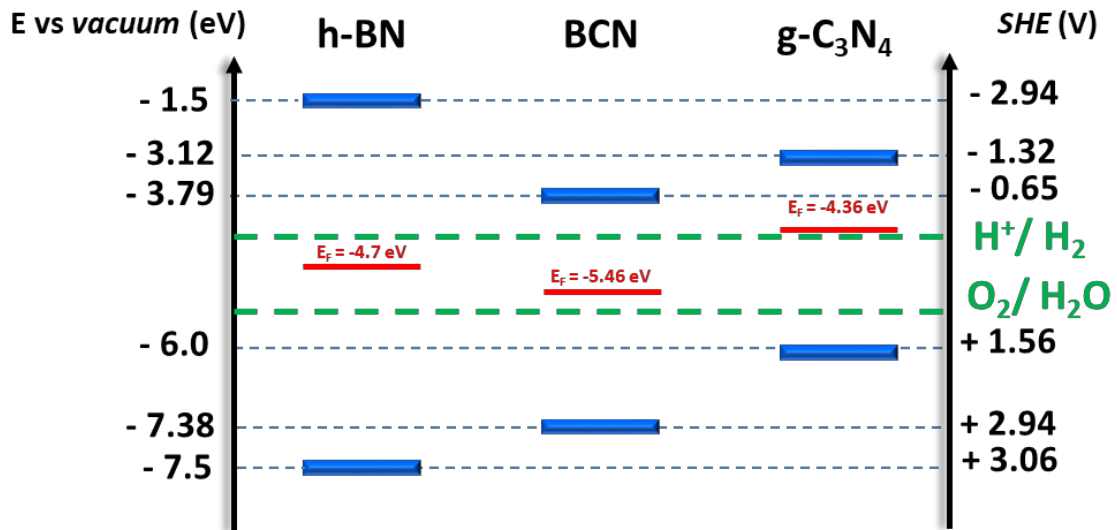


Figure 3.8. Band structure calculated for BCN and g-C₃N₄ thin films compared to h-BN, referred to vacuum scale (left) and standard hydrogen electrode (SHE, right).^[47]

Photoluminescence properties have also been analyzed, however just few of the prepared samples have shown distinct PL spectra possibly due to a very low emission intensity from very thin samples. However, among them the samples II, IV (figure S29) and VI (in figure 3.9 (a)) have shown a blue-shifted fluorescence compared to g-C₃N₄ with maxima at 426, 408 and 394 nm, respectively. The possibility to shift the fluorescence towards lower wavelengths, with respect to g-C₃N₄, is of high interest in optical and optoelectronic devices like LEDs and lasers, opening the possibility to cover a wide range of photoluminescence wavelengths along the visible range with carbon-based materials. The PL spectra have been summarized in the CIE (International Commission on Illumination) 1931 color space shown in figure 3.9 (b), a plane diagram in which the points are specified as chromaticity coordinates (y,x) and represent the chromaticities of color stimuli.^[52] It clearly shows that the fluorescence color shifts towards blue-violet respect to g-C₃N₄ and confirmed by the picture inset with flower-shaped quartz which was used as target substrate. Under visible light the quartz looks completely transparent confirming what was already observed by transmittance spectra (in figure S24, sample VI), whereas under UV illumination a violet color emission can be seen even by naked eyes.

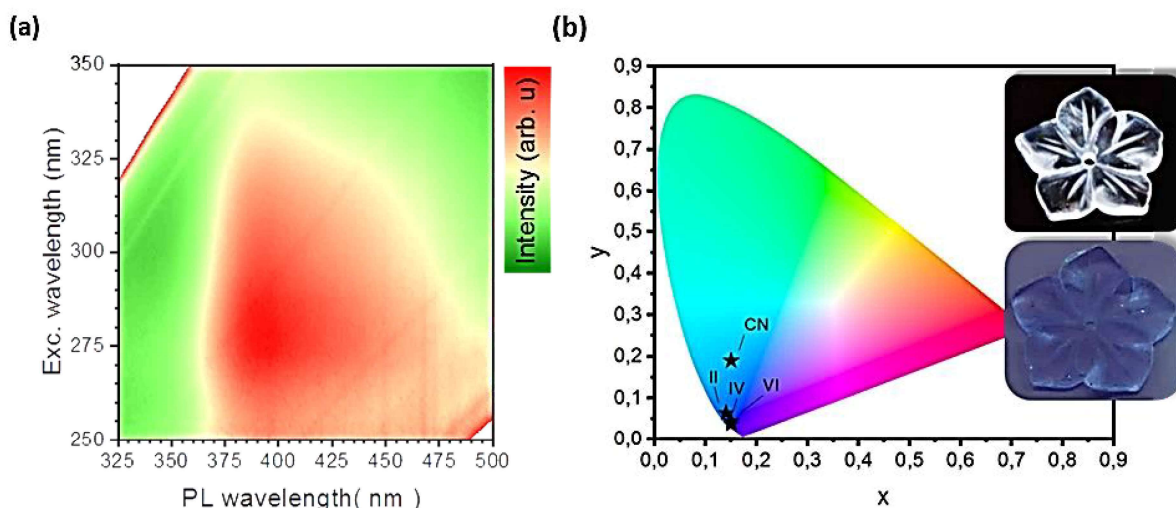


Figure 3.9. (a) Contour plot of excitation versus photoluminescence of sample VI, intensity is indicated in color scale from green to red; (b) CIE 1931 color space with points referred to BCN fluorescence color.

3.4. Summary of chapter 3 and perspectives

In this chapter, another material class for the synthesis of C-based thin film materials via chemical vapor deposition was presented. Differently from the method presented in chapter 2, this one was proven to allow for the deposition of ternary thin films containing B, C and N. Melamine diborate was chosen as non-hazardous single-source precursor, which differently from melamine, doesn't sublime. However, the decomposition of the precursor successfully leads to deposition of BCN thin films at relatively low temperatures (550-800°C). In addition to the previous one, this method allows for deposition of an even broader range of C-based materials, since the problem of non-sublimating precursor was overcome and thin film deposition of BCN thin films was successfully achieved. Moreover, it has been shown that the proper choice of precursors allows for deposition of carbon-based materials with noble properties, i.e. with high resistance against oxidation. These carbon-based thin film materials, as g-C₃N₄ and BCN, have shown very high values of refractive index, in all cases above 2, indicating that such materials have high potential for still largely unexplored applications in optics and photonics.

The addition of B has successfully led to larger bandgap sizes, providing high transparency to the thin films in the visible range. This provides a further step for the tunability of C-based materials, which allows covering a wide range of bandgaps and photoluminescence, along the visible and UV spectral ranges. The high transparency

in the visible range is of high interest for applications such as LEDs encapsulant, in which the light extraction efficiency highly increases reducing the refractive index mismatch between the encapsulant and the active material. High refractive index materials with large bandgaps can be applied, for instance, also to windows to partially reflect near infrared irradiation which causes heating in tropical areas. For instance, the “Singapore code of practice 13”, states that the indoor temperature should be maintained between 22.5 and 25.5°C, where outdoor temperature hovers between 23 and 32°C.^{[53] [54]} This obviously requires large expenses in electricity for cooling systems, which could remarkably be reduced by applying a thin layer of transparent material with high refractive index and high resistance towards oxidation, without affecting the high transparency of glass. The wide range of possibilities to tune BCN thin film properties, such as bandgap and composition, shown by this method is of high interest not only in the field of optics and optoelectronics. The absence of constraints on substrate shape, as curved surface and bulk materials as shown in the previous chapter, allows for preparation of ternary BCN-based heterojunctions.

In this chapter it has been shown that the developed CVD method allow for high quality BCN thin films deposition from very common precursors, such as melamine and boric acid. The tunability in terms of optical and electronic properties allow for wide range of future applications in optics, optoelectronics and beyond. Together with g-C₃N₄, BCN materials are very good candidates to replace widely used inorganic semiconductors for a new generation of more sustainable technologies.

Chapter IV

4. Low temperature carbon

This last chapter will be dedicated to the synthesis of carbon materials at low temperatures (200°C). The synthesis pathways are all based on carbon suboxide, a gaseous highly reactive cumulene with chemical formula C_3O_2 , as a precursor made from malonic acid and a dehydrating agent. The possibility to synthesize carbon materials from highly reactive gaseous precursors at low temperatures is not only of high interest for bulk carbon-based materials applications, but also for thin film technology.

4.1. Low temperature carbon from carbon suboxide precursor

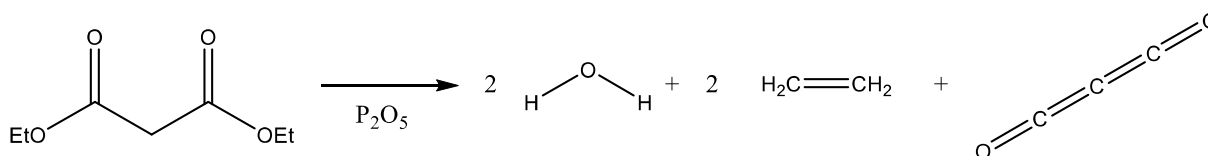
As mentioned in chapter 1, carbon materials have attracted much attention during the last decades due to their wide range of applications, such as catalysis to electronics. The possibility to replace widely used inorganic materials with organic ones is still an open challenge for material scientists. The advantages of carbon-based materials lie in the possibility to tune electronic properties, morphology and composition which leads to countless different materials with highly diversified properties. However, many challenges still need to be address in carbon science and among them, the following are of particular importance:

- Control over material properties (composition, structure, function)
- Complexity of processing (number of steps, including precursor availability and post-processing)
- Resources consumption (energy, water and time)

In the following chapter, an alternative approach towards synthesis of carbon materials at low temperatures via carbon suboxide synthesis will be presented. Carbon suboxide is a highly reactive cumulene which polymerizes to a material named “red carbon”, as it will be presented below. The structure of red carbon is still under debate in the scientific community; however, it has been widely accepted that even at temperatures lower than 200°C, it undergoes further reaction releasing CO

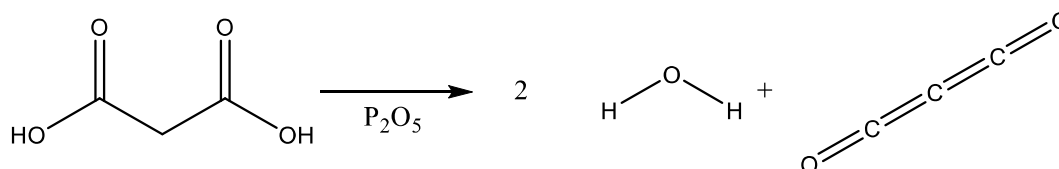
and CO₂. However, the product obtained from the polymer decomposition was not systematically investigated, so far, and will be presented later in this chapter.

First reports on higher carbon oxides date back to Brodie in 1873, when he exposed carbon monoxide to an electric current and reported on the formation of CO₂ and a red-brown film deposition on the reactor walls. Further analysis these films led to the conclusion that the compounds were oxides of carbon possibly belonging to a series, analogous to the series of hydrocarbons, which he named “oxycarbons”.^[1] ^[2] This report has inspired further research by Diels and Wolf, who in 1906, were able to isolate and characterize carbon suboxide (C₃O₂) obtained from the dehydration of diethyl malonate by large excess of P₂O₅ at 300°C.^[3] The reaction was reported as follows:^[2] ^[3]



Scheme 4.1. Dehydration of diethyl malonate with P₂O₅.

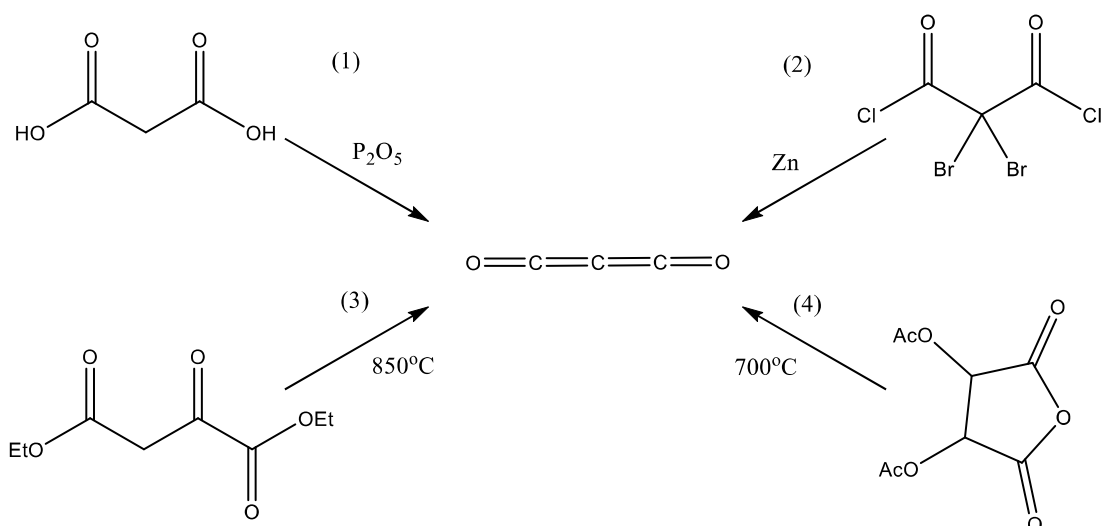
The following years, Diels and others published another similar and more productive synthesis from malonic acid in large excess of P₂O₅ at 140-160°C, which is nowadays still a widely used method for C₃O₂ preparation:^[4] ^[5]



Scheme 4.2. Dehydration of malonic acid with P₂O₅.

Carbon suboxide is a linear molecule with very different physico-chemical properties from CO and CO₂. At room temperature it is gas that condenses at 6.8°C and solidifies at -107/-112.5°C.^[6] From the chemical point of view, it behaves like a bisketene and it can be considered as double dehydrated malonic acid rather than an oxide of carbon.^[2] ^[7] It has been reported that C₃O₂ has high solubility in the majority of organic solvents whereas in presence of water, alcohols and other nucleophiles it reacts to form malonic acid, malonates and correspondent derivatives.^[7] The tendency towards these addition reactions are due to the high unsaturated character and alternating charge distribution, where the central C has a slightly higher negative charge than O, thus being more nucleophilic, whereas the other two C are partially

positive charged, i.e. the sites available for nucleophilic attack.^[7] Carbon suboxide has attracted much interest especially in the field of organic chemistry because of its high reactivity which makes it a feasible building block for heterocyclic compounds.^[7] Different organic chemical reactions have been exploited and possible reaction mechanisms are shown in literature which are, however, out of the scope of this work.^[6] ^[7] For this reason, different other methods to prepare C₃O₂ have been explored (scheme 4.3) and can be divided into two groups: the first one, based on malonic acid (1) and its derivatives (2) in which the carbon skeleton is kept during the process, and a second one, which involves high temperature degradation of β-dicarbonyl compounds as diethyl oxaloacetate (3) and diacetyltartaric anhydride (4).^[6] ^[7]



Scheme 4.3. Methods to prepare carbon suboxide.^[7]

Among all the synthetic methods, the one proposed by Diels (1) present several advantages. First of all, it requires much lower temperatures with respect to the synthesis from β-dicarbonyl compounds and thus it simplifies the synthesis, avoiding the use of special setups. Secondly, acyl halides as 2,2-dibromomalonoyl dichloride (2) are toxic and possibly explosive when in contact with water, which requires the use of air-free setups (i.e. glove box) for the synthesis. Moreover, they lead to halogen-containing by-products which are highly toxic for the environment.

Carbon suboxide is reported to undergo polymerization reactions where the polymeric product is often referred as to “red carbon” or “red coal” for its dark red appearance, or simply poly(carbonsuboxide).^[2] ^[7] ^[8] The polymer structure has been investigated and many reports agree that it contains an α-pyrionic skeleton (possibly

also with γ -pyronic units) (figure 4.1).^{[7] [8] [9]} However, the polymeric structure is still under debate in the scientific community.^{[7] [8] [9]} Because of the high monomer reactivity the polymerization occurs conveniently even at room temperature and can be started by nucleophilic, electrophilic, radical initiators and possibly even without initiators.^{[9] [8]} The red carbon is insoluble in most of the organic solvents and only partially soluble in water, with extended π system and high reactivity towards basic compounds like NH_3 due to its pyronic structure.^{[8] [9]}

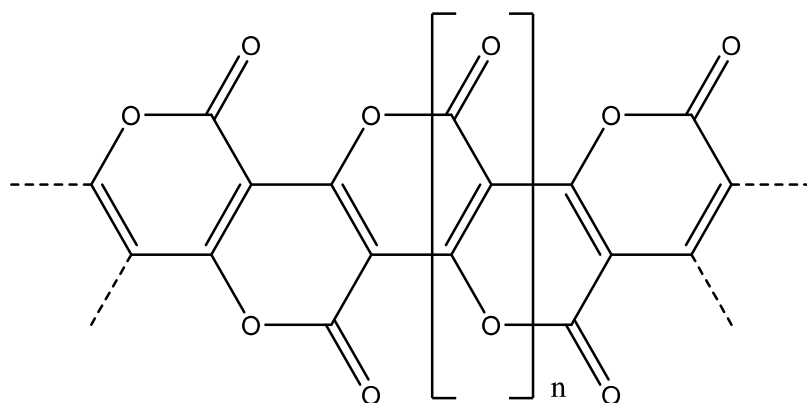


Figure 4.1. Structure of red carbon.^[8]

The polymer structure is constituted only of C and O elements in a conjugated structure that explains the strong color. Interestingly, as previously mentioned, when the polymer is heated up, it releases CO and CO₂, even at very low temperature (below 200°C), as reported by different authors.^{[2] [9] [10]} If it can be assumed that the polymer composition is C₃O₂, a release of CO₂ per monomeric unit could possibly lead to (pure) carbon materials. The opportunity to obtain carbon materials at very mild temperatures and from very common precursors is one of the challenges mentioned at the beginning of this chapter. Moreover, the preparation steps would allow for the control of the final product through the common approaches of polymer chemistry (chemical modifications, copolymerization, different initiators and more). Since the synthesis proceeds via intermediate gaseous carbon suboxide, this can be further applied to thin film technologies, particularly interesting especially for deposition on substrates with low thermal stability. Moreover, the synthetic method proposed by Diels suggests the possibility to obtain other heterocumulenes by heating molecules with convenient structures, in presence of P₂O₅ as strong dehydrating agent.

4.2. Low temperature carbon synthesis from C₃O₂ method

Carbon suboxide is a heterocumulene constituted by three carbon atoms and two oxygens with four cumulative double bonds, which makes it highly reactive. The high reactivity requires a very clean synthetic environment and high vacuum, to avoid side reactions with other gases, for instance, water moisture. For these reasons to prepare the carbon suboxide a Schlenk line distillation system was chosen. In a typical synthesis 3 g of malonic acid were mixed with 5-fold excess of dry P₂O₅ in a 250 ml flask. Since P₂O₅ is very hygroscopic the flask containing the solid mixture has to be plugged quickly to the distillation system. The reaction was done at low pressure (10⁻³ mbar), heating up the solid mixture at 160°C and collecting the carbon suboxide in liquid nitrogen, below its melting point. During the reaction the solid mixture becomes progressively red to dark brown, suggesting that C₃O₂ is formed and partially polymerized directly on the P₂O₅ surface.^{[2] [11]} After the reaction-distillation was finished, it can be seen that the collection flask walls were covered with a white deposit (figure 4.2 (a)). Subsequently, the stopcock was locked and the product stored overnight at -18°C in a sealed box to let the C₃O₂ melt. After about 18 hours the liquid was turning slightly yellow-reddish (figure 4.2(b)); then it was left for further react at room temperature for 6-8 more hours at room temperature, until a dark red-brown sticky material was obtained (figure 4.2 (c)). The dark red-brown color of the product (figure 4.2 (c)) resembles the typical color widely reported for poly(carbon suboxide).^{[9] [12]} Surprisingly, it was observed that when the product was heated up under very mild conditions (200°C) it suddenly turned to a black and powdery material (figure 4.2 (d)).

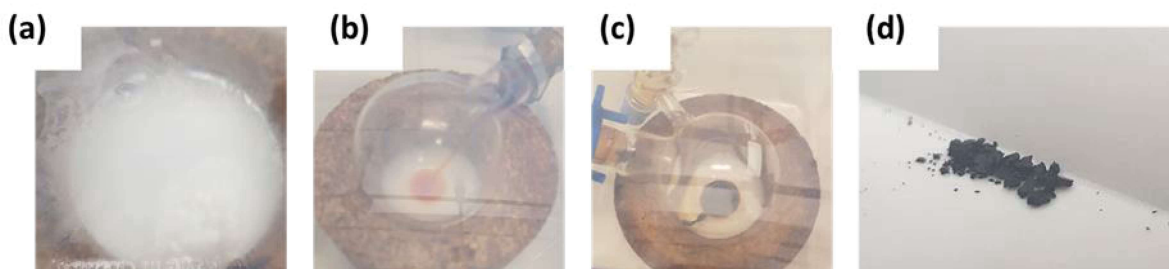


Figure 4.2. (a-d) Timeline of LTC preparation.

For this reason, the prepared product was analyzed by TGA-MS (mass spectrometry) to better understand the decomposition process at low temperatures (figure 4.3 (a) and (b)). In figure 4.3 (a) are shown the TGA and DTG of the product at 2.5°C/min

heating rate in N_2 , that show a main mass decrease at temperatures lower than 200°C . The residual mass at 200°C decreases down to 35%, suggesting that the main reaction steps occur below this temperature. The 65% mass decrease at 200°C of the red carbon suggests that, per each mole of the monomeric units C_3O_2 , which molecular mass is 68 g mol^{-1} , the mass loss would correspond to 44 g, e.g. the mass of a mole of CO_2 . This means that for each molecule of C_3O_2 if a CO_2 unit is removed a C_2 , i.e. a carbon residue, is left. At higher temperatures the material mass slowly decreases further, however, without any evident reaction step, up to 1000°C where the residual mass is about 8%. Mass spectrometry has been used to analyze the gaseous fragments released during the thermal decomposition (figure 4.3 (b)). The main fragments are detected at m/z (mass/charge) 12, 16, 44 and 26 and are attributed to C^+ , O^+ , CO_2^+ and $C_2H_2^+$ respectively. As expected, water signal ($m/z=18$) is extremely low, as well as the one of OH^+ ($m/z=17$) which can be related to the presence of hydroxy- groups as in carboxylic acids or alcohols. This is in good agreement with what previously reported by Carofiglio et al., i.e. that the thermal decomposition of carbon suboxide polymer at low temperatures releases CO_2 as majoritary product.^{[10] [9]} This suggests once more that the product obtained resembles the red carbon polymer expected. The presence of the $C_2H_2^+$ groups is attributed to the presence of ketene during the preparation of C_3O_2 , or to reaction with air moisture before the analysis.

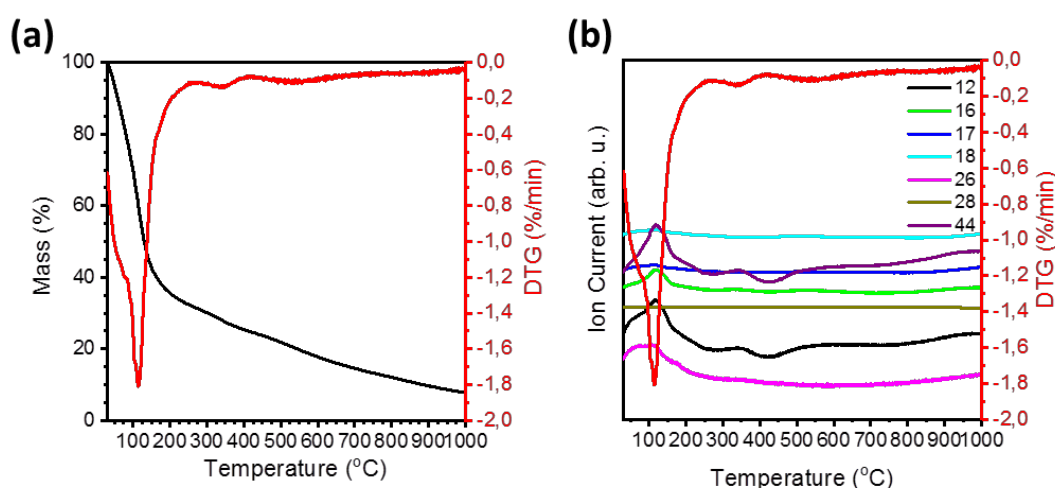


Figure 4.3. TGA, DTG (a) and DTG-MS (b) of red carbon.

4.2.1. Preparation of low temperature carbon

The as-prepared product was confirmed to further react at temperatures below 200°C releasing CO₂ as main by-product. This opens the possibility that the final product is a carbonaceous material with high carbon content. To prepare the low temperature carbon (LTC), the red carbon product was collected from the flask and placed in a crucible. The collected sample was heated up to 200°C for 5 hours under N₂ flow with a 10°C/min heating rate. The final black product was then collected and analyzed. SEM analysis reveals that the solid material is probably constituted of a layered structure as can be deduced in figure 4.4 (a-c) at different magnifications.^[13] TEM images (figure 4.4 (d-f)) show sharp edges of the material where the different grey shades further reveals that the material is made out of layer stacks, possibly organized in a graphitic-like fashion. However, no ordered pattern has been observed even at very high magnifications (figure 4.4 (f)), that suggests that the structure of the LTC resembles the one of amorphous carbon materials.^[14]

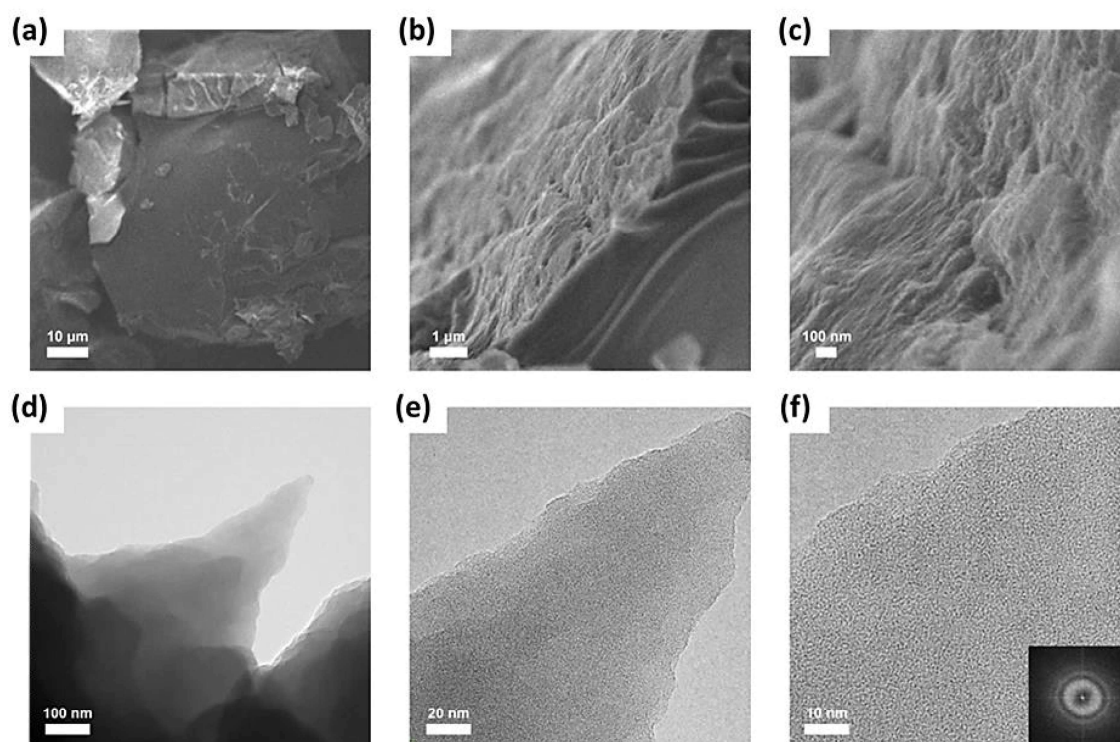


Figure 4.4. SEM images of the LTC (a-c); TEM images of the LTC (d-f).

The obtained material was further characterized by FT-IR, Raman spectroscopy and XRD to get further insights into the material properties and structure. Figure 4.5 (a) shows the FT-IR spectrum of the carbon material prepared at 200°C, with main absorption bands below 1900 cm⁻¹. This indicates that the LTC has only low portions

of –OH and –CH_x, suggesting though a very low hydrogen content.^{[12] [8]} Although it is difficult to draw conclusions on the sample structure from the FTIR spectra, some characteristic peaks can be attributed to particular vibrations. In this absorption range, the first intense peak at 1735 cm⁻¹ of C=O groups is followed by a wide absorption band between 1620 and 1300 cm⁻¹ attributed to sp² hybridized C within an aromatic structure, possibly containing O; last at 798 cm⁻¹ is attributed to C=C bending, as previously reported.^{[15] [16] [17] [18]} Raman spectrum, in figure 4.5 (b), shows the typical D and G bands of carbon materials at 1346 and 1591 cm⁻¹ respectively with relative intensity I(D)/I(G) close to unity (1.02). This confirms the presence of sp² hybridized C in a defective carbon matrix, where the defects are likely to be related to vacancies, edges and corrugation in the material.^{[19] [20]} Moreover the G band peak is shifted respect to the graphite one, widely reported at 1580 cm⁻¹, which is attributed to the presence of oxygen as observed by Kudin et al. in graphene oxide-like materials, where single double bond alternation occurred in Scholz Bohem-like model with larger sp² C areas.^[20] It is worth to notice that similar spectra were also obtained by Seiler et al. upon water swelling of oxidized graphite.^[21] The overtone 2D-band and D+G peak are also present, although with very low intensity, at 2671 and 2860 cm⁻¹ respectively which can be related to the formation of few layers of graphite.^[19] The XRD diffractogram (figure 4.5 (c)) shows very characteristic features of the material at 2θ values of 18.1, 19.1, 24.5 and 32.8 indicated as I, II, III and IV, respectively. The depicted diffraction peaks can be related to repetitive patterns occurring in the material structure using the Bragg's law:^[22]

$$d = \frac{n\lambda}{2\sin\theta}$$

where d is the characteristic distance (nm), n is an integer, λ the X-ray wavelength (nm) and θ the angle of diffraction. Assuming n=1 (i.e. the observed diffraction peaks are first order diffractions) the peaks correspond to distances of 0.49 (I), 0.46 (II), 0.36 (III) and 0.27 (IV) nm, respectively. The peak corresponding to 0.36 nm is attributed to interlayer distance between graphitic-like planes. On the one hand, in graphite oxide interplanar distance is much larger, around 0.7-0.8 nm, and diffraction peak would occur at 2θ values of around 10°, excluding thus the presence of graphite oxide.^{[23] [18] [24]} However, interlayer spacing for graphite is widely reported at values of 0.34 nm, just slightly smaller than the one observed in the LTC sample.^{[22] [24] [25]}

Similar values have been recorded also for reduced graphite oxide, suggesting though that this distance could be attributed to more loosely spaced graphitic planes than in graphite; in the case of thermal reduction of graphite oxide, the larger distance between graphitic planes was attributed to partial exfoliation between the graphitic planes, due to evolution of CO and CO₂.^{[18] [23]} The diffraction pattern shows, however, that the four peaks are sharper and well resolved when compared to reduced graphite oxide materials.^{[26] [27]} This reveals that the LTC structure is better organized and possibly to a larger extent with respect to reduced graphene oxide. The comparison between the diffraction patterns of the LTC and the one of the red carbon (figure S30), suggests that possibly the structure of the red carbon precursor is partially transferred to the LTC after the thermal treatment at 200°C, i.e. a topotactic transformation occurred. Moreover, the position of the peaks I, II and IV resembles also the diffraction peaks of the [100], [101] and [110] planes observed by Khvostikova et al. in exfoliated graphite samples.^[13] However, further investigation would be necessary to assign the diffraction peaks and define the LTC structure.

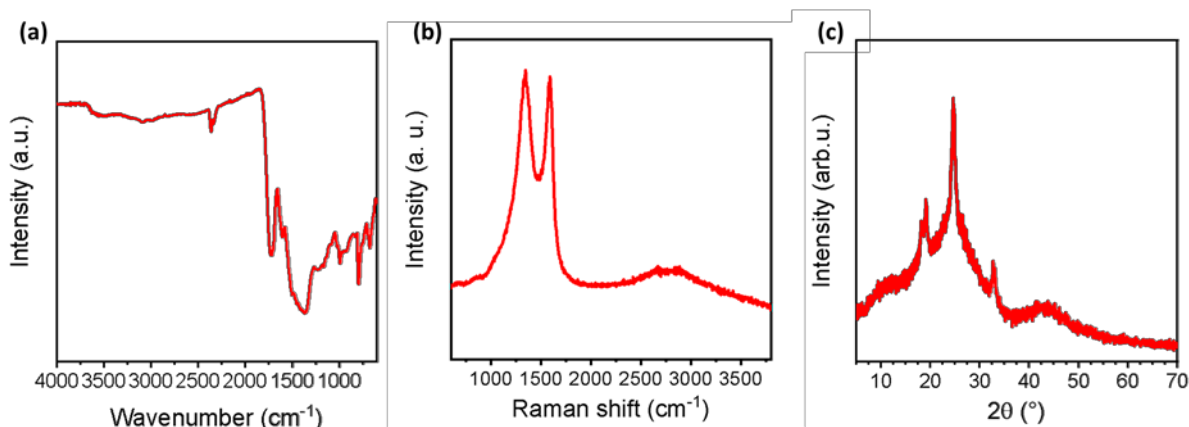


Figure 4.5. FTIR (a) and Raman (b) spectra of the LTC. XRD diffractogram of LTC (c).

Elemental composition and chemical arrangement in the LTC was analyzed by elemental analysis (EA), EDX, EELS, XPS and ¹³C MAS NMR. Elemental composition obtained is shown in table 4.1, obtained by EA, EDX, XPS and EELS. As previously mentioned in chapter 2, EELS composition is not quantitative since it has been recorded only at normal incidence. EA shows a rather high O content, with C/O ratio of only 2.3; furthermore, H (ca. 2.5% wt) signal was present. The presence of H is in contrast with FTIR (figure 4.5 (a)) since, as mentioned above, no –OH and –CH_x peaks are evident: therefore, the hydrogen content can be mostly attributed to adsorbed water. The adsorbed water decreases also the C/O ratio, explaining the

lower C/O ratio in comparison to XPS and EDX quantifications. EDX and XPS analysis are recorded in vacuum, and indeed in both cases the C/O ratio is increased, although still different. As expected, the O content is larger in XPS measurements than in EDX. This is possibly related to higher O content on the surface of the LTC carbon, e.g. O-containing terminal groups, compared to the bulk of the material, since XPS has much lower penetration depth with respect to the EDX.^[28] From the calculated EDX C/O ratio, it can be assumed that about three molecules of CO₂ are successfully removed each four C₃O₂ monomer units by the thermal treatment of the red carbon at 200°C. However, in all cases the composition show that no P is present in the final material. This confirms that the synthetic method does not introduce any P impurity, which could lead to the formation of organophosphates.^[29] XPS and ¹³C NMR analysis can give further insights on the chemical arrangements. The C1s spectrum of LTC, in figure 4.6 (a), shows three different components that correspond to as many C-containing functional groups: sp² C=C (284.8 eV) corresponding to non-oxygenated aromatic ring, at 286.6 eV is attributed to sp³ C-C and the last deconvoluted peak (288.9 eV) is attributed to carbon bounded to O (C-O or C=O).^{[30] [31] [26]} Large differences between binding energies of C 1s sp² and sp³ (1.7±0.3 eV) were previously reported by other authors and confirmed by XPS C1s peaks of diamond (higher binding energies) and pure graphite (lower binding energies), taken as references.^{[26] [27] [30] [31]} From the C1s peaks deconvolution and assignments, the overall sp² C composition is above 68%, suggesting then that the majority of C is involved in a conjugated structure. Moreover, the O 1s peak (figure 4.6 (b)) shows only a single chemical environment for O, which is then in good agreement with the above discussion. The peak at 532.4 eV is thus attributed to -C-O or -C=O.^{[26] [32] [33]} The ¹³C solid state NMR, in figure 4.6 (c), is in good agreement with the XPS analysis. At lower chemical shifts (15 ppm), sp³ C band is identified and the presence of C-O bonds is shown by the peak at 97 ppm.^[34] The latter was very recently investigated in detail by Gao et al. in reduced graphite oxide samples, and attributed to lactol -O-C=O groups, possibly with pyrone configuration, which is an expected residue from the decomposition of red carbon (figure 4.1).^[27] At 154 ppm, the last intense peak is attributed thus to sp² C in the LTC, which results shifted with respect to graphitic carbon materials, possibly for the deshielding effect of oxygen-containing groups that lead to lower fields resonance.^{[27] [35] [36]} The shoulder at 178 ppm and the broad peak at 204 ppm, with

much lower intensity with respect to the previous, are possibly attributed to carbonyl-containing groups and a spinning side band, respectively.^{[37] [38]} It is worth to point out that ^{13}C MAS NMR was made after several attempts to dissolve the LTC for liquid NMR in different deuterated solvents as d-THF, d-DMSO, d-DMF, D_2O ; however, in all cases no signals were detected, as exemplarily depicted in figure S31, for LTC dispersed in D_2O and d-DMF. The absence of signals, and thus confirmation of the LTC insolubility, is supported by the Tyndall effect depicted in figure 4.6 (d), for LTC dispersed in DMF at room temperature. EELS spectrum, in figure 4.6 (e), shows the K-edges of C and O elements. The C K-edge at 286 eV shows the typical π^* peak of conjugated carbon materials, followed by σ^* features at 296 eV. Therefore, this confirms that the material is conjugated to a large extent; moreover, the shape of the C K-edge can be used as qualitative tool to define similarities with other C-based materials and C-allotropes. By comparison with the literature widely reported on carbon materials, the shape is different from graphite and diamond, resembling more the spectra reported for amorphous carbon materials, glassy carbon and reduced graphene oxide.^{[31] [39] [40] [41] [42]} In general, the comparison of EELS spectrum is in good agreement with previous characterization, confirming that the material contains a mixture of sp^2/sp^3 hybridized C. The oxygen peak appears very low, however, it shows both a very small π^* peak, at 530 eV, followed by the σ^* one. It is very difficult to draw any conclusion on the oxygen peak since very seldomly it is discussed in literature.

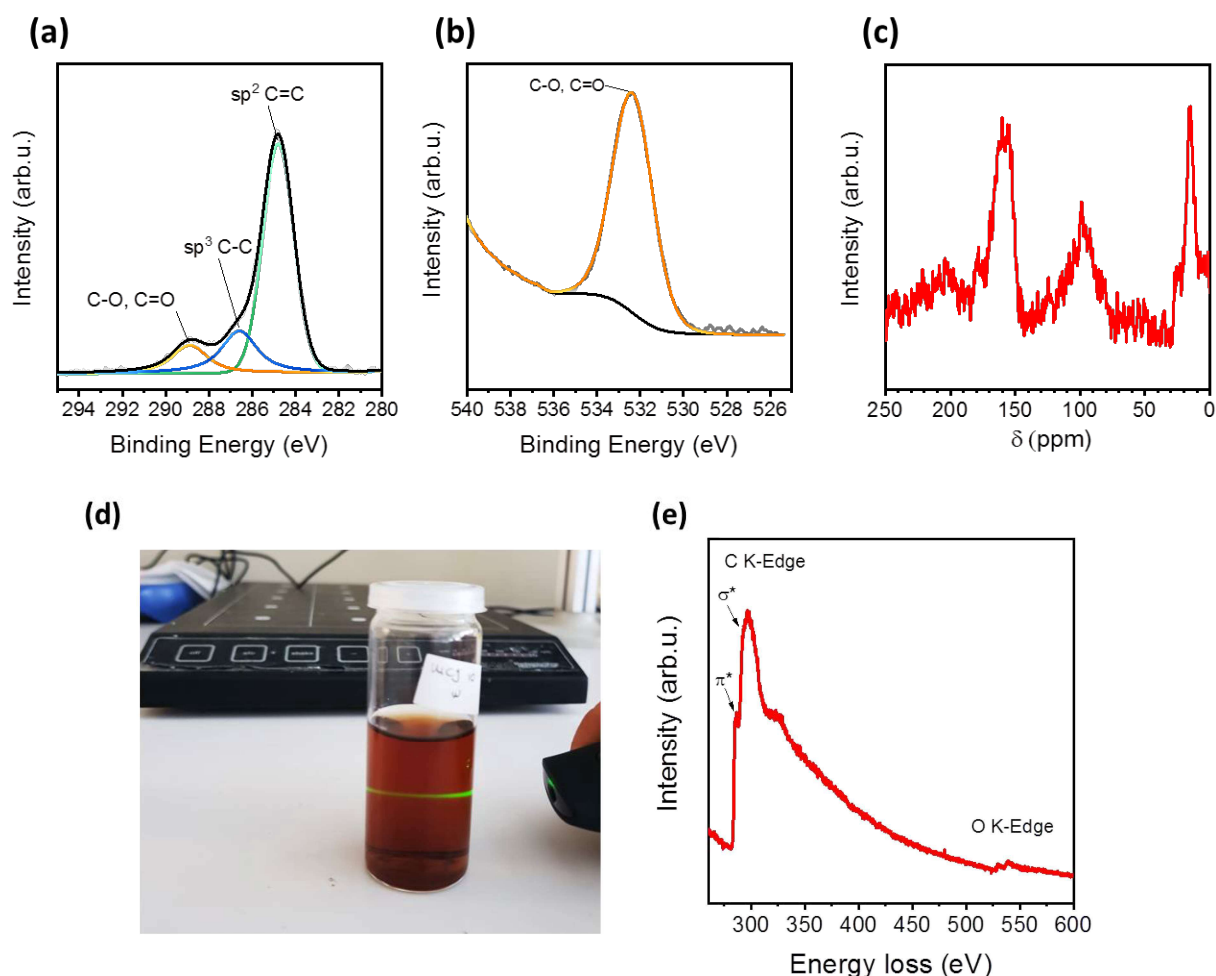


Figure 4.6. Deconvoluted XPS C1s (a) and O1s (b) peaks, ^{13}C MAS NMR spectrum (c), Tyndall effect (d) and EELS spectrum (e) of the LTC.

Table 4.1. Average elemental composition of LTC obtained by different characterization methods.

	C (%at)	O (%at)	C/O	N (%at)	P (%at)
EA	53.9	23.3	2.3	-	-
EDX	79.0	21.0	3.8	-	-
XPS	73.5	26.5	2.8	-	-
EELS	85.6	13.3	6.4	(1.1)	-

To evaluate the stability properties of the LTC prepared, TGA in N_2 and synthetic air environments were performed, as shown by the black lines in figure 4.7 (a) and (b), respectively. In both cases, a mass decrease of about 3% at temperature below $100^\circ C$ is attributed to removal of adsorbed water.^[43] The decomposition of the LTC starts in both cases, at temperatures around $300^\circ C$ into two main steps: the first one, shown by the DTG minima (red curve) in the two graphs, appears in both cases at ca. $350^\circ C$, which is possibly accompanied by ring opening and further oxygen

removal; however, as expected, the residual mass is 10% lower in synthetic air at 350°C. The second one, quite different between the two cases, occurs at 500°C in synthetic air, and 535°C in N₂. Moreover, the residual mass at 1000°C, is about 43% in N₂ and only 3% in synthetic air, as expected from carbon-based materials.^[26]

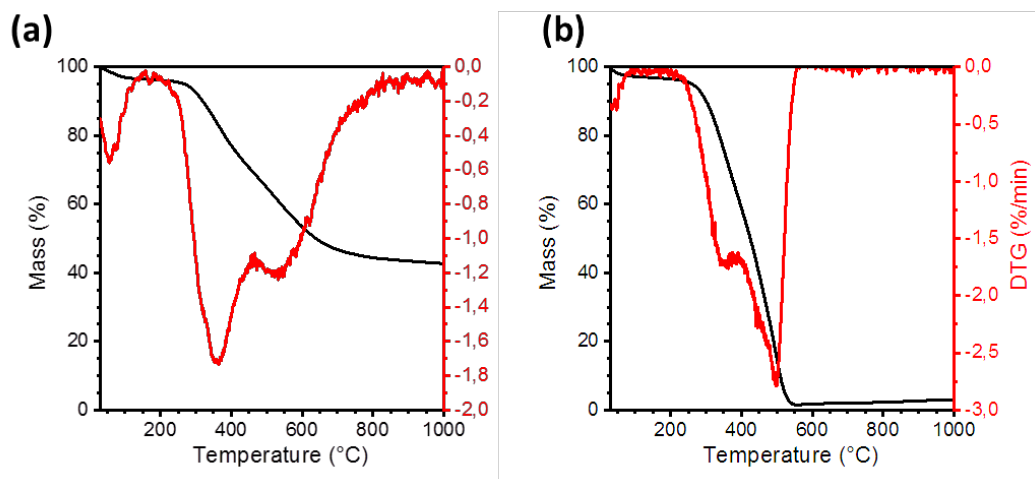


Figure 4.7. TGA (black line) and DTG (red line) of the LTC in N₂ (a) and synthetic air (b).

The optical properties were evaluated by diffuse reflectance spectroscopy, in order to evaluate if a bandgap in the visible range is present. Figure S32 shows the absorption spectrum in the visible range. The absorption spectrum shows a broad absorbance all over the visible light range, with a steep decrease for the intensity between 700 and 850 nm, in good agreement with the black colour shown in figure 4.2 (d). The range of the absorbance spectrum does not reveal a bandgap in the visible range, so in case there is any, it lies above the spectrometer range, i.e. 850 nm. Further characterization with wider spectral range setup will be necessary to verify the possible bandgap and thus the bands position for future applications of LTC, as for instance in catalysis and for heterojunction-based devices.

In this chapter, an alternative method has been introduced for the synthesis of bulk LTC based on carbon suboxide. Preliminary characterization have shown that the material shows the typical features of carbon materials, i.e. high carbon content and sp² conjugation. However, further studies would be necessary to define the structure and electronic properties and thus the future applications of this LTC material. In the following section it will be described the preliminary attempts to synthesize the LTC as a thin film by the test tube method and first trials to implement it in the CVD setup.

4.2.2. Thin films deposition of low temperature carbon

The proof-of-concept method for the preparation of g-C₃N₄ and BCN thin films using a solid precursor in a test tube previously shown in chapters 2 and 3, was also used in this case in order to evaluate the possibility to deposit LTC thin films on solid substrates. Also in the present case, thin film deposition was successfully achieved by using a solid mixture of P₂O₅ and malonic acid at 160°C for 30 minutes. Preliminary results of such thin films have shown that the deposited films have different absorbance spectrum with respect to the bulk material (figure 4.8 (a), black line) and intense red fluorescence (red line), with a bandgap of 1.97 eV (figure S33), and thus lying in the visible range. The prepared thin films show high C content (above 80 at% in EDX) as revealed by EDX mapping at the thin film edge (figure 4.8 (b-e)). The film edge on a glass slide is clearly present on the right side of figure 4.8 (b); the C, O and Si EDX elemental maps, respectively in figure 4.8 (c), (d) and (e), show that C is only present in the film area, whereas O and Si outside of it, since they are the main components of glass slides. On the nanoscale (figures 4.8 (g, h)), the film shows highly organized areas with crystalline patterns (figure 4.8 (h)) embedded in an amorphous matrix. The EELS spectrum in figure 4.8 (i), confirms the LTC thin film has a high C content, with the π^* edge indicating that the C is involved in a conjugated structure. Furthermore, the film was dispersed in THF and dried on XRD sample holder for XRD measurements. Several sharp peaks have been obtained (figure 4.8 (f)), which suggests the presence of a very organized structure over a large extent. However, no explanation has been found yet to describe such pattern. Moreover, these thin films have been exposed to different amines, that caused deep absorbance and fluorescence blue-shift, due to possible reaction, as exemplarily shown in figure S34 for the film exposed to ammonia solution. The sensing properties have been preliminarily tested also with other volatile amines as ethylamine and aniline, and in all cases color change occurred (figures S35 (a-d)).

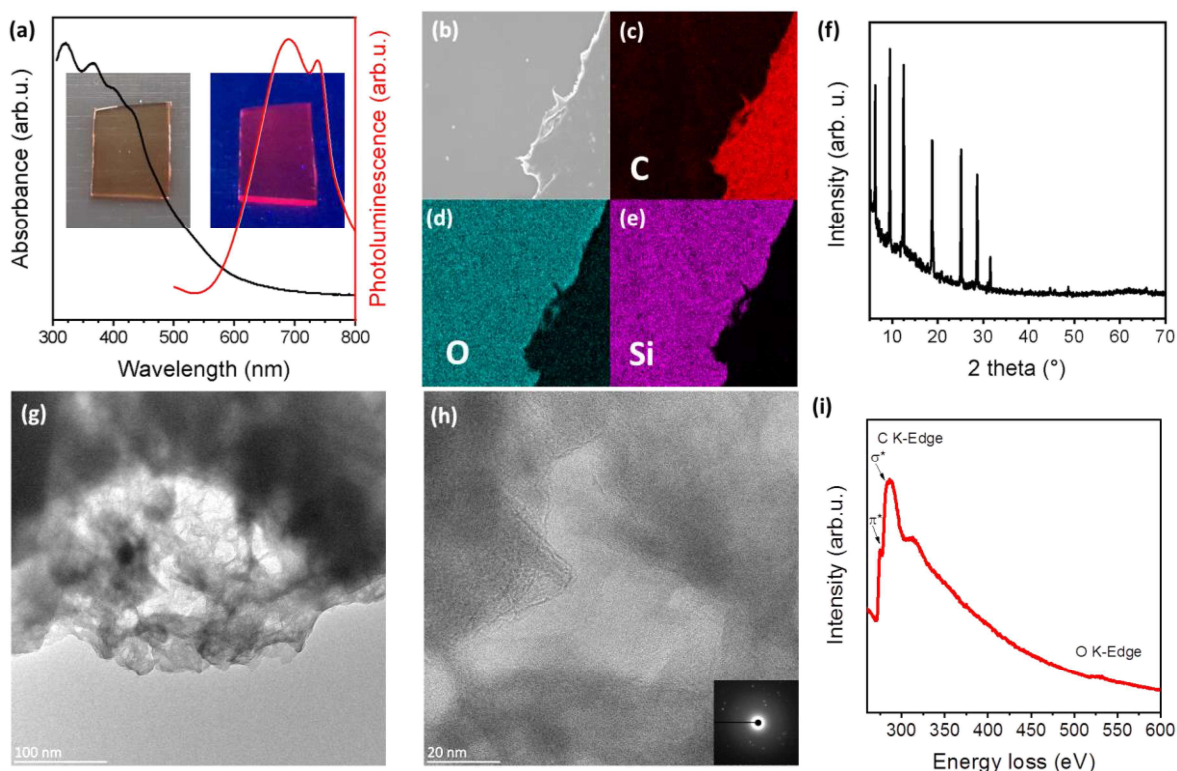


Figure 4.8. Absorbance (black line) and fluorescence spectra (red line), with insert picture of the LTC thin film under ambient light and UV irradiation (a); SEM image (b) and EDX maps of C (c), O (d) and Si (e) of the LTC thin film; XRD diffractogram (f), TEM images (g-h) and EELS spectrum of the LTC thin film.

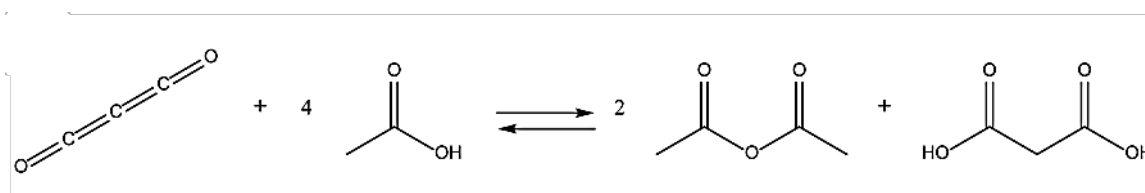
Eventually, first trials for the synthesis of LTC thin films were conducted also in the more advanced CVD setup. Thin film deposition has been successfully obtained also by means of CVD, as depicted in figure S36 on glass substrates. The thin film coating deposited by CVD has a brown color appearance, similar to the one obtained by the test tube method and a similar absorbance spectrum.

The test tube method was successfully exploited for the deposition of the LTC material which has the typical characteristic of carbon-based semiconductor materials, i.e. high carbon content and fluorescence. The different properties of the LTC thin film compared to the LTC as bulk material are attributed to a different kinetic mechanism of polymerization of the C_3O_2 precursor. Indeed, the polymerization obtained from gas-phase deposition leads to a highly ordered material with respect to the bulk reaction, as shown by the XRD diffraction pattern (figure 4.8 (f)). Moreover, the different kinetic polymerization mechanism can be also affected by the substrate (soda lime glass), which possibly acts as a reaction catalyst improving the high structural organization of the LTC thin film. Furthermore, the deposition has been

successfully implemented in the CVD setup, however, this is yet at an early but promising stage and we are currently studying the properties of the films deposited by CVD, for future applications in optics and catalysis.

4.3. Low temperature carbon from malonic acid acetic anhydride precursors

In the previous section, have been described methods for preparation of LTC both as bulk and thin films materials, from common and commercially available solid precursors, here P_2O_5 and malonic acid. The very high interest to produce carbon materials at very low temperature and the widespread possible applications, ranging from catalysis and electrochemistry to optics and optoelectronics, pushed us to find alternative synthetic methods. Moreover, phosphates are well-known eutrophication agents, which have been recently banned also from detergent, due to ecological effects. Thus, the challenge to obtain LTC materials by means of only organic precursor, required to find an available organic dehydrating agent, such as carboxylic anhydrides. Among the organic anhydrides, acetic anhydride is a widely used organic precursor, widely used Hoffmann synthesis of acetylsalicylic acid. Diels and Lalin, in 1908, reported among the possible equilibrium reaction of C_3O_2 with acetic acid one leading to acetic anhydride and malonic acid products (scheme 4.3).^[44]



Scheme 4.3. Reaction of carbon suboxide with acetic acid.

The reaction was not taken into account, since no malonic acid was found in the product.^[44] However, almost 80 years later, Connors and Ifan, proved that the inverse reaction led to carbon suboxide, that they successfully isolated and analyzed.^[45]

Carbon suboxide was prepared by dissolving malonic acid in acetic anhydride. The solution was then heated to $150^\circ C$ to distill C_3O_2 in a flask containing cold anhydrous diethyl ether.^[45] For these reasons, acetic anhydride was chosen as possible substitute of P_2O_5 and a simpler method based only on organic precursor was developed.

4.3.1. Synthesis of low temperature carbon from acetic anhydride and malonic acid precursors

Malonic acid and acetic anhydride were mixed in 1:1 molar ratio in a glass vessel and, as depicted in figure 4.9 (a), malonic acid is insoluble in acetic anhydride. The 1:1 molar ratio was chosen as standard method, since it gave higher final product yield; however, also 1:2 malonic acid-acetic anhydride molar ratio has been tested with similar results. The 1:1 malonic acid-acetic anhydride mixture was placed at 90°C for 4 hours with lid to avoid carbon suboxide to leave the reaction vessel. After 1 hour at 90°C, the dispersion turned into a homogeneous solution with orange-red coloration possibly due to the formation of carbon suboxide was possibly present in the vessel (figure 4.9 (b)). After 4 hours the solution in the vessel had an intense red coloration (figure 4.9 (c)). The fluid was then placed into a capped crucible and heated up to 200°C for 5 hours under N₂. The LTC final product (figure 4.9 (d)) was then collected and analyzed. It is worth to notice, that when the separate single compounds were submitted to the same thermal treatment, only little amount of white solid from malonic acid was recovered (figure S37), since acetic anhydride boils at 140°C and malonic acid melts at 137°C. Eventually, the black product after heating at 200°C malonic acid and acetic anhydride is due to their reaction.

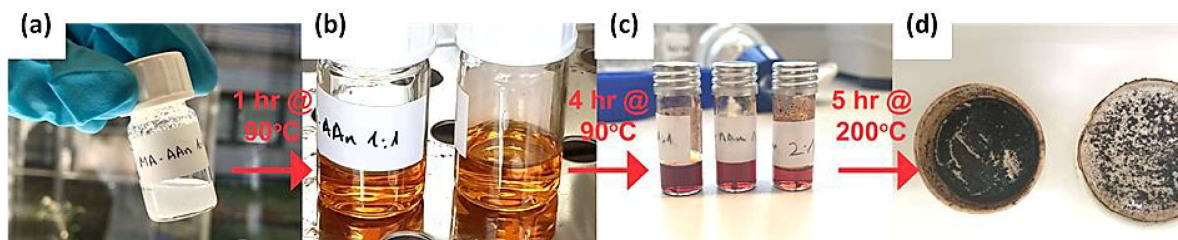


Figure 4.9. (a-d) Timeline of LTC preparation from malonic acid and acetic anhydride.

The decomposition of the 90°C red solution was analyzed by TGA-MS in N₂, in figure S38. As in the previous case, synthesis from P₂O₅ and malonic acid, the decomposition occurs mostly below 200°C, with a residual mass of about 15% at 1000°C. However, in the present case, also the m/z fragments at 41, 42, 43, 45 and 60 were detected, together with the signals attributed to CO₂ (m/z =44 and 22). The m/z masses 41, 42 and 43 were attributed to H_nCCO (with n=1, 2, 3), 45 to COOH and 60 to acetic acid.

The black product was then characterized by the same methods used for LTC from P₂O₅ and malonic acid precursors. Many of the characterization results, such as

FTIR, Raman, ^{13}C MAS NMR, XRD, diffuse reflectance spectrometry and TGA in nitrogen shown in figure 4.10 (a-d) and S39 (a) and (b), respectively, lead to similar conclusion with respect to the ones already described in the previous section. Moreover, the C/O ratio is very similar between the two methods, as shown in table 4.2, except for the XPS analysis. Eventually, the similar results obtained suggest that the two materials are very similar.

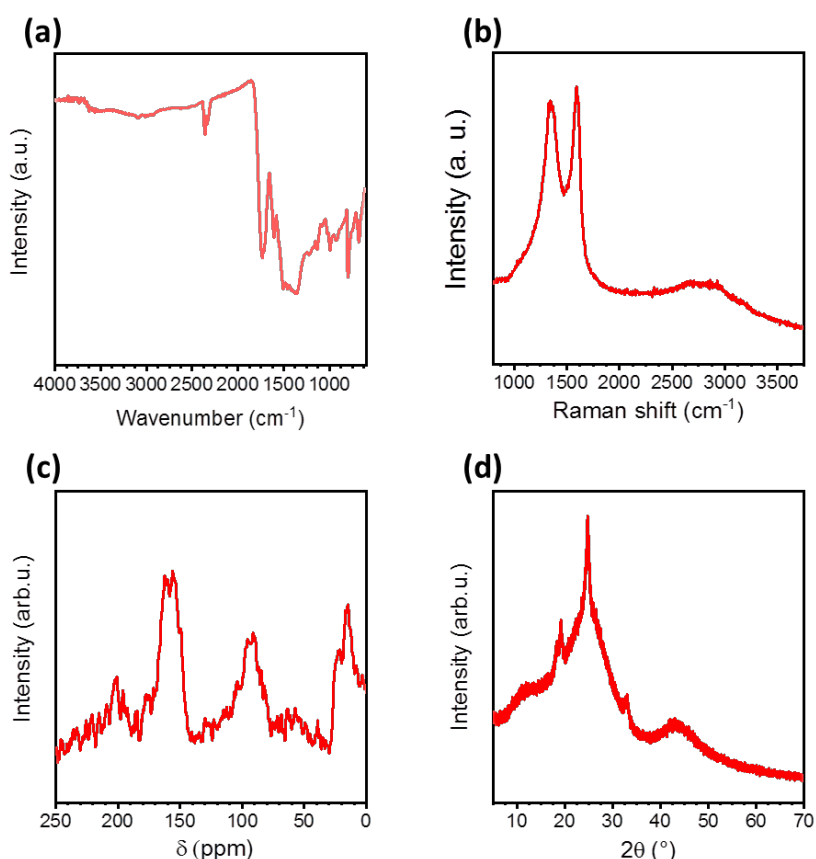


Figure 4.10. FTIR (a), Raman (b), ^{13}C MAS NMR spectra and XRD diffractogram of the LTC prepared from malonic acid and acetic anhydride.

Table 4.2. Average elemental composition of the LTC prepared by malonic acid and acetic anhydride calculated by different methods.

	C (%at)	O (%at)	C/O	N (%at)	P (%at)
EA	48.5	26.2	1.9	-	-
EDX	78.7	21.3	3.7	-	-
XPS	66.1	33.9	1.9	-	-

However, SEM and TEM reveal some differences in morphology between the products obtained with the two methods. In figure 4.11 (a-d) are shown the SEM

images of the LTC, where the material shows a layered porous structure, which resembles the ones previously reported for porous graphitic carbon materials. [45]

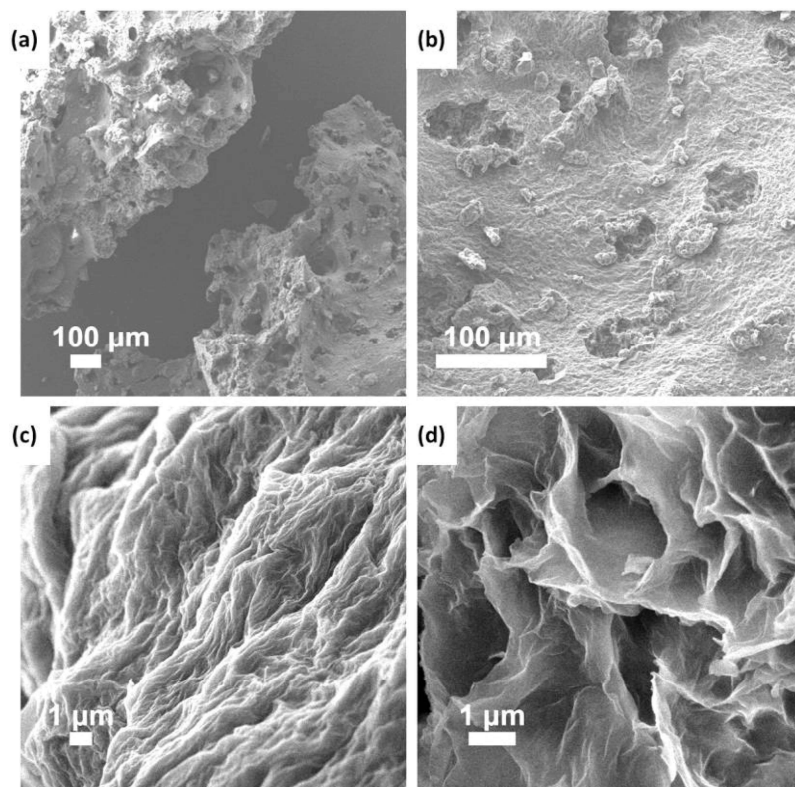


Figure 4.11. SEM pictures of LTC from malonic acid and acetic anhydride at different magnifications (a-d).

At higher magnifications, the LTC shows two different morphologies depicted in the figure 4.12. In figure 4.12 (a), (b) the sample shows an essentially amorphous structure; however, as highlighted in figure 4.12 (b), some nanostructures, with repetitive distances of about 0.35 nm are present (figure 4.12 (c)). However, the sample shows also darker nanoparticles, as in figure 4.12 (d). The sample looks amorphous overall, as shown by the FFT insert, however, a deeper look into the particles (figure 4.12 (e)) show that they are highly organized and confirmed by the FFT pattern. The highly defined spots, obtained by the FFT of the image reveals periodical distances of 0.12 and 0.21 nm, which, could be the [110] and [100] in-plane diffraction of graphite.^[46] Moreover, the dark field TEM image shows that many nanocrystalline structures are embedded in an amorphous matrix. In this area the EELS spectrum shows that these particles are mostly composed of C, with a pronounced π^* peak at 285 eV, meaning that a conjugated system is present. However, it was not possible to find any correlation for it with other EELS spectra in literature.

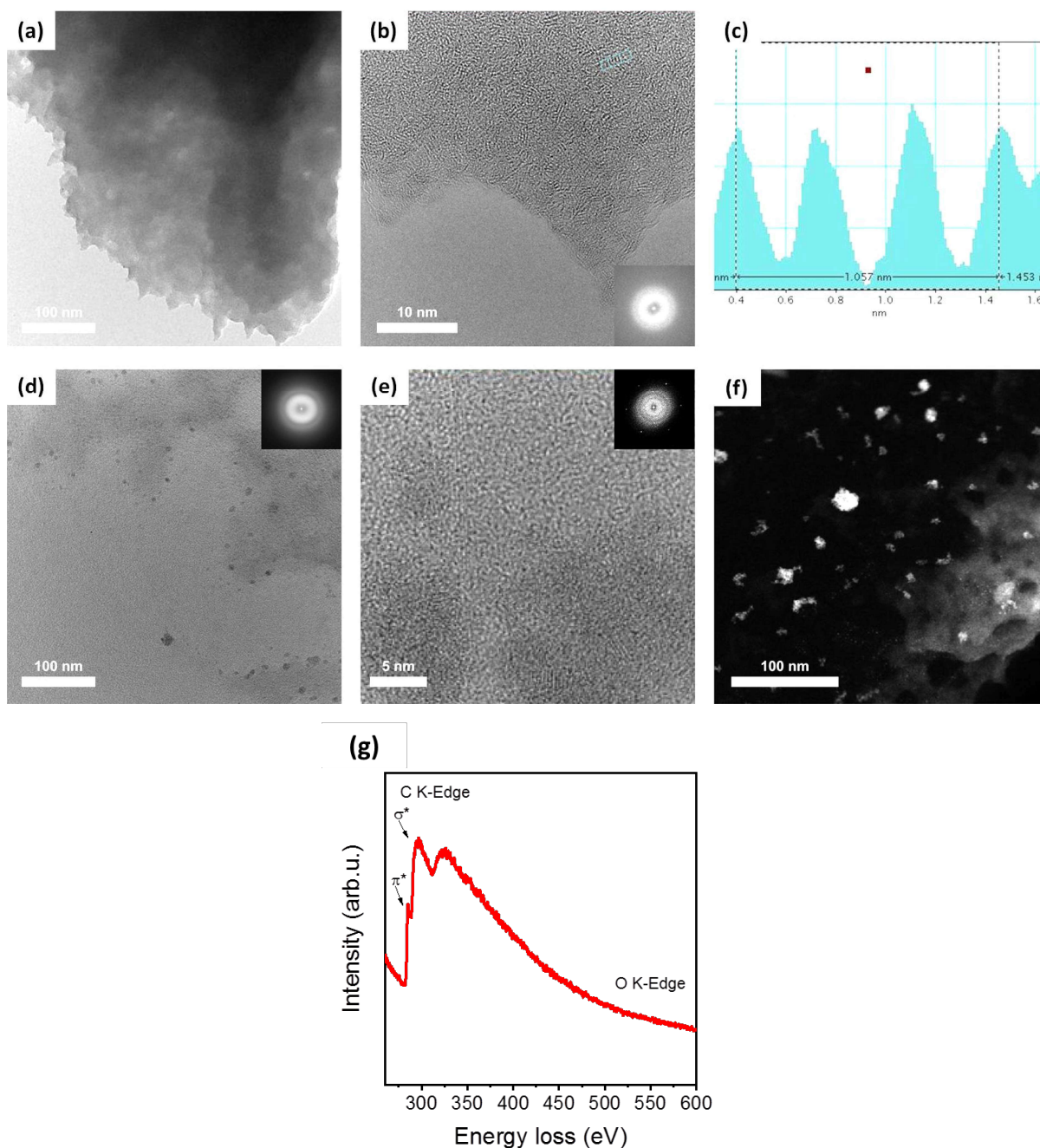


Figure 4.12. TEM images of the LTC prepared from malonic acid and acetic anhydride (a, b, d and e). Peak to peak distance of nanostructures (c) referred to figure (b). Dark field TEM image (f) which highlights the presence of nanosized crystalline structures. EELS spectrum of the nanocrystals (g).

XPS deconvoluted spectra of C1s and O1s are shown in figure 4.13 (a) and (b), respectively. Differently from the LTC introduced in section 4.2.1, in this case, C1s peak has been deconvoluted into 4 peaks at 284.6, 287.0, 288.6 and 291.4 eV. The first peak is attributed to sp^2 C=C bonds and the relative $\pi-\pi^*$ shake-up satellite at 291.4 eV.^{[33] [47]} The other two peaks were attributed to carbon bonded to O and, in particular, C-O (287.0 eV) and O-C=O (288.6 eV).^{[33] [38] [48]} O1s peak was

deconvoluted into two peaks, at 531.7 and 533.6 eV attributed respectively to C=O and C-O, in good agreement with previous characterizations (figure 4.13 (b)).^[33]

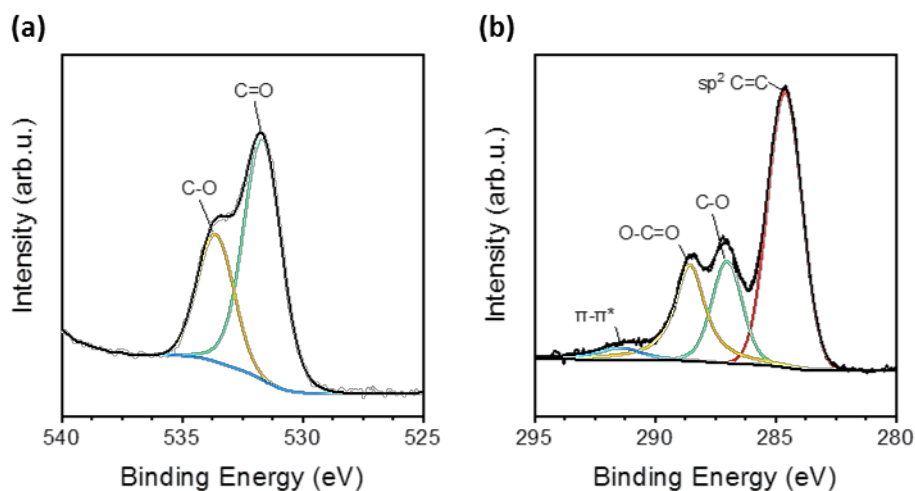


Figure 4.13. Deconvoluted XPS C1s (a) and O1s (b) peaks of the LTC prepared from malonic acid and acetic anhydride.

In conclusion, this alternative method for the synthesis of LTC from acetic anhydride and malonic acid has revealed some differences with the previous one based on P_2O_5 and malonic acid. The method has been highly simplified, avoiding the use of a Schlenk line setup and liquid nitrogen to collect the carbon suboxide, since the reaction can be conducted in a glass vessel at atmospheric pressure. Although chemical composition, XRD, FTIR, Raman, ^{13}C MAS NMR characterizations are very similar, different morphologies have been found by means of SEM and TEM. The latter, in particular, showed the presence of two characteristic structures, the first amorphous, and the second composed of nanocrystal with an FFT pattern that resembles the one of graphite. Eventually, the presented synthesis is a very simple method to obtain LTC at $200^\circ C$ without the use of special setup and large amounts of P_2O_5 . As for the case of the LTC prepared from malonic acid and P_2O_5 , also in this case, further characterization will be necessary to better understand properties and possible future applications of this LTC material, e.g. in catalysis and electrochemistry.

4.4. Summary of chapter 4 and perspectives

In this last chapter, we presented a different approach towards the synthesis of carbon at low temperature. The first method relies on the use of a solid mixture of a

strong dehydrating agent (P_2O_5) and malonic acid to produce carbon suboxide (C_3O_2). The latter is a highly reactive molecule that readily polymerizes into red carbon (or red coal) which name is related to its deep red color. The red carbon, under very mild temperature conditions ($200^\circ C$) further reacts releasing mainly CO_2 , as by-product a leaving a carbonaceous black material. The obtained product reveals typical features of carbon materials, such as high C content, conjugation along the structure and very characteristic diffraction pattern. Eventually, the presented method can be described as an innovative approach towards the synthesis of carbon at very low temperature. Moreover, it has many advantages since it allows for the control of final product properties and composition as the common approaches of polymer chemistry during the preparation steps (chemical modifications, copolymerization, different initiators and more) can be applied. Preliminary tests have shown that it is possible to produce thin films from P_2O_5 /malonic acid solid mixture, via, both the test tube proof-of-concept method and in the CVD setup. The preparation of C-based thin films at such low temperature is of high interest in optics and optoelectronics, for instance to create C-based planar heterojunctions and deposition over sensitive substrates. Indeed, in many cases, C-based thin films decompose at high temperatures, thus the deposition of a carbon-based bilayer, can be detrimental for the film below. However, further characterization will be necessary to define the properties of the bulk and thin film materials and the possible applications, for example in catalysis, electrochemistry, optics and optoelectronics.

The last part of this chapter was dedicated to an alternative approach towards the synthesis of bulk LTC, by means of malonic acid and acetic anhydride, a liquid organic dehydrating agent. This method allows for a simpler LTC synthesis, since it doesn't require the use of a Schlenk line, liquid nitrogen to collect C_3O_2 and the solid mixture with P_2O_5 . The reaction is conducted in a glass vessel where the two organic compounds are mixed. By heating the vessel at $90^\circ C$ the dispersion turns into a liquid deep red solution; by further heating up to $200^\circ C$, it left a black carbonaceous residue. The material was then collected and analyzed, revealing many common characteristic with the previous one. Eventually, the method was successfully employed to obtain LTC from simple organic precursor, without the need of special setups, like the Schlenk line and liquid nitrogen. Moreover, this method has the same advantages of the previous one allowing for the option of composition and properties tuning during the preparation steps.

The preparation of LTC materials is in general of high interest, with milder and more controlled conditions, allowing for a better control of the final material properties. Moreover, the general approach which makes use of a strong dehydrating agent to create highly reactive synthons is a possible strategy for the future syntheses of C-based materials.

Chapter V

5. Conclusion, final remarks and perspectives

This work addresses the challenge to develop carbon-based thin films with suitable properties for new generation devices. The aim is to replace widely used inorganic materials with organic ones, in order to overcome the fundamental limits of widely used materials such as silicon, arsenic and rare earths. Chemical vapor deposition was chosen as appropriate method for the deposition of thin films since it is widely known method, both in research and industry, and it allows for tight control over the deposition conditions and eventually material properties. The general approach towards the synthesis of carbon-based thin film materials is schematically shown in figure 5.1. The starting point is always a solid precursor (or a mixture of two precursors), which can be used for the synthesis of a target bulk material, and with suitable properties for thin film deposition by CVD, i.e. sublimation. In order to preliminary test the possibility to use a precursor for chemical vapor deposition of thin film, a reference test method was developed by means of a test tube in a muffle furnace. This simple method was used since it allows for the possibility to reproduce similar conditions to those in the chemical vapor deposition setup. Eventually, the synthesis is then scaled up to the CVD setup to deposit high quality thin films over large surfaces with better control over the deposition parameters.

After a thorough review of scientific literature on C-based materials to describe the general properties, a deeper focus on the properties of the two particular binary and ternary systems, g-C₃N₄ and BCN, as bulk materials was given in **chapter 1**.

In **chapter 2**, it was first illustrated the state-of-the-art of g-C₃N₄ thin films and the different approaches used so far for g-C₃N₄ thin film deposition. The great interest behind the deposition of g-C₃N₄ materials was clearly highlighted by the large number of attempts proposed up to date. Indeed, the insolubility of g-C₃N₄ requires the development of different methods for the deposition of thin film from the ones used for common polymeric materials, such as spin coating and spray coating. However, before the present work, the deposition of thin films of g-C₃N₄ was suffering from the poor homogeneity and low control over the deposition parameters, that are

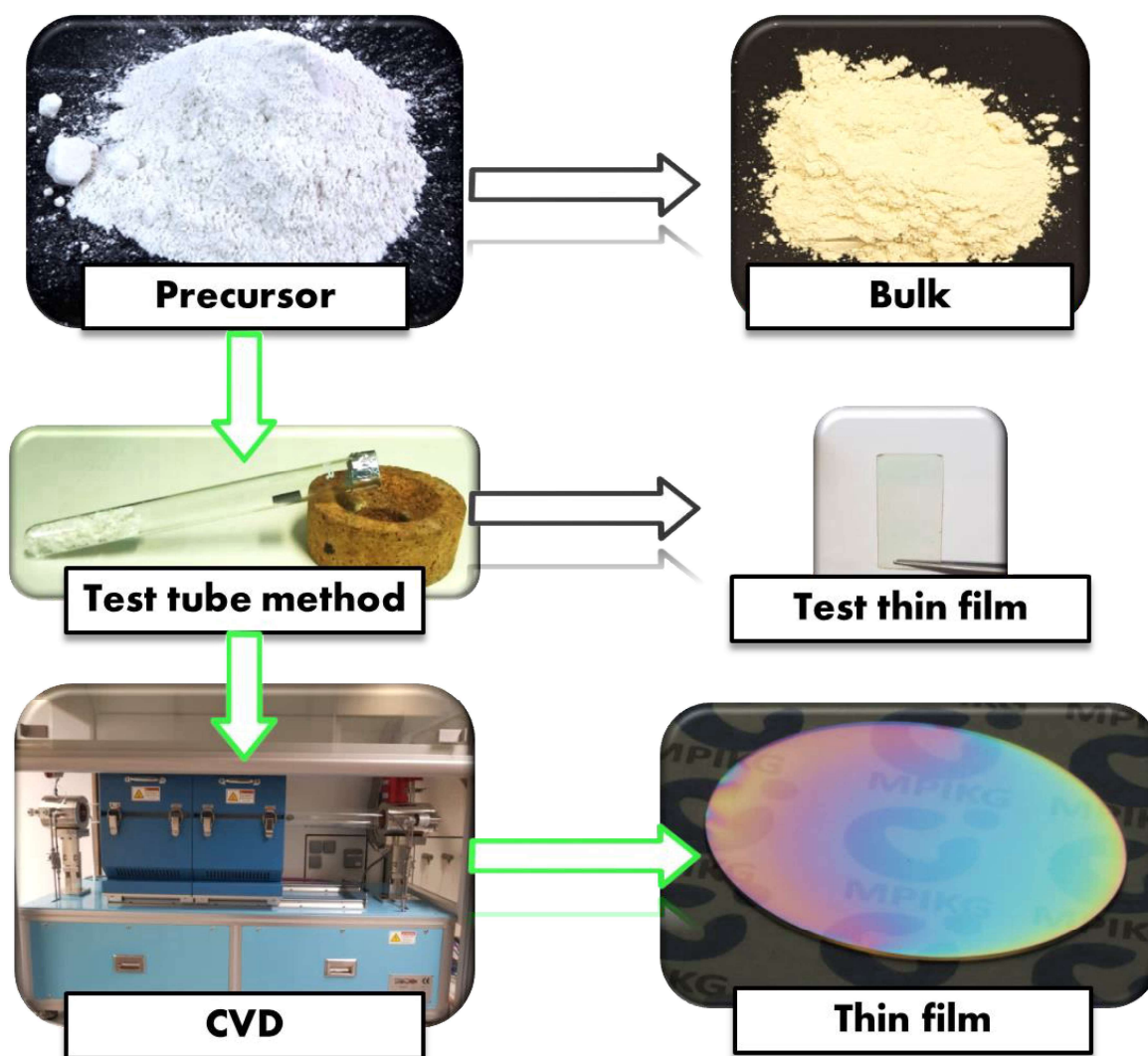


Figure 5.1. General approach towards the synthesis of carbon-based thin films used during this work.

detrimental for optical and optoelectronic applications. Among the possible solid precursors for $g\text{-C}_3\text{N}_4$, melamine was chosen as an appropriate single-source precursor for thin films deposition, since it sublimates at relatively low temperature (about 300°C). The possibility to deposit $g\text{-C}_3\text{N}_4$ thin films was successfully tested with the test tube method. Furthermore, with this method it was shown the possibility to tune the film thickness by different amount of melamine precursors. Therefore, the method was implemented in the CVD setup, where by properly choosing the deposition conditions, high quality thin films of $g\text{-C}_3\text{N}_4$ were successfully deposited over a wide range of solid substrates, from flat surfaces to fibers, curved objects and powders. It was shown that by controlling the precursor amount and the deposition time, it was possible to control the thickness within a wide range, from 3.5 to 130 nm. The $g\text{-C}_3\text{N}_4$ thin films were characterized in terms of structural and optical properties,

depicting also the band structure. For the optical properties of the g-C₃N₄ thin films it was found to have, to the best of knowledge, the highest intrinsic refractive index for a polymeric material, reported so far. The refractive index reaches value of 2.52 at 500 nm, which is even higher than the diamond (2.43) at the same wavelength. The refractive index is the property of main interest when it comes to light management and thus is of high interest for optical applications, like photonic crystals. Moreover, the possibility to tune the electronic properties and to achieve deposition on very different substrates opens a widespread range of opportunities for future applications beyond optics, e.g. for catalysis and electrochemistry. Eventually, the chemical vapor deposition is also a widely used technique in industry and thus this method could be also a starting point for the industrial production of g-C₃N₄ thin films.

Chapter 3 aimed at the deposition of ternary BCN thin film materials. As in chapter 2, it was first given an overview of the state-of-the-art methods for such thin film deposition proposed so far in literature. For the deposition of BCN thin films, melamine diborate was chosen as single source solid precursor which was prepared from melamine and boric acid. The goal was to deposit ternary BCN thin film which possibly have wider bandgap, i.e. high transparency in the visible range, with respect to the g-C₃N₄ thin films while maintaining a very high refractive index. At first, the feasibility of the synthesis was tested successfully with the test tube in order to confirm that all the three elements were successfully present in the thin film prepared. Then, the synthesis was scaled up in the CVD setup. In contrast to the deposition of g-C₃N₄, the melamine diborate doesn't sublime, thus a different approach was required. In this case, the precursor was decomposed at relatively high temperatures to create gaseous precursor synthons which were eventually polymerized at the substrate surface at higher temperatures. Also in this case the method developed was successful for the deposition of BCN thin film materials. It was shown that by changing the melamine to boric acid ratio in the precursor or the temperature conditions in the CVD it was possible to tune the optical properties of the materials. However, in this case, only little thickness tunability has been achieved, and obtained by increasing the preparation time in the CVD. With respect to the optical properties, also BCN thin films showed very high refractive indices, just slightly lower than the g-C₃N₄, and very high transparency in the visible range. The analysis of the band structures confirmed that in both cases the precursor and the methods chosen to deposit of C-based thin film materials led to very low valence band and thus noble

properties, i.e. high stability with respect to oxidation. The methods described for thin film deposition using a CVD setup, open the possibility to deposit a very wide range of C-based material thin films from non-hazardous solid precursors, without the necessity of using flows of toxic gases. This is of paramount importance since it allows for the deposition of thin film materials with outstanding properties and large tunability in terms of thickness as well as optical and electronic properties, for applications in optics optoelectronics and beyond, while synthesis conditions and precursors can be kept rather sustainable compared to current methods.

The last chapter, **chapter 4**, was focused on the synthesis of carbon materials at low temperature. To achieve the goal, carbon suboxide was firstly prepared from P_2O_5 and malonic acid, to then serve as precursor. Carbon suboxide is a highly reactive cumulene which readily polymerizes into a polymer with pyronic structure, named red carbon. The red carbon was reported to decompose even at low temperatures releasing CO_2 as main byproduct, possibly leaving a carbonaceous solid product. C_3O_2 was prepared in moisture-free distillation system connected to a Schlenk line, to avoid possible side reactions. The distillation product was collected at liquid nitrogen temperature and let react in the collection flask until a deep red coloration occurred. Subsequently, the red product was heated to $200^\circ C$ leaving a black residue that was further analyzed. The characterizations showed that the material reveals features that resemble the one of carbon materials, as for instance high C content and π -conjugation. For these reason it has been described as an innovative method to obtain low temperature carbon (LTC) materials. The method presented bears several advantages beyond the very low temperature used, since it allows to control the synthesis steps which leads to the option to tune the final product properties and composition through the common approaches of polymer chemistry during the preparation steps (chemical modifications, copolymerization, different initiators and more). Also, C_3O_2 allows for a gas phase reaction, thus, preliminary tests have been conducted with the test tube method and in first trials with the CVD. This is yet at an early stage, however, thin films have been successfully deposited and further characterizations are ongoing at present time to better understand the properties and possible applications in optics and optoelectronics. The last part of chapter 4 was dedicated to an alternative method for the preparation of LTC, by replacing solid P_2O_5 with acetic anhydride as dehydrating agent. The use acetic

anhydride, which is a liquid organic compound, highly simplifies the preparation of LTC, since it does not require the use of complex setups, like in the previous case. The reaction can simply be conducted in a glass vessel or crucible and the same final temperature. The product obtained from the malonic acid/acetic anhydride system revealed many similarities to the one obtained from malonic acid/ P_2O_5 . However, some differences, with special regards to morphology, have been identified and discussed. The presented method bears the same advantages as the one from malonic acid/ P_2O_5 in terms of temperature and reaction control, but, moreover it is highly simplified and without the necessity to dispose large amounts of P_2O_5 . Eventually, this is a valuable method for the preparation of LTC, from fully organic and common precursors. Therefore, the following steps will require to get more insights into the properties of these materials possibly introducing heteroatoms in the structure for future applications, e.g. in catalysis and electrochemistry.

The challenge to replace the wide use of inorganic materials in thin film devices has been addressed successfully for the initial steps during this work, with the hope to give useful insights to future developments in this direction.

Appendix

A. Materials

All materials were used as purchased unless noted otherwise. Melamine (99%, Sigma Aldrich), boric acid (99.99%, Alfa Aesar), malonic acid (99%, Alfa Aesar), phosphorus pentoxide (99%, Sigma Aldrich), acetic anhydride (>99%, Sigma Aldrich), N,N-dimethylformamide-d7 (>99.5%, Sigma Aldrich), tetrahydrofuran-d8 (>99.5%, Sigma Aldrich), deuterium oxide (99.9%, Sigma Aldrich), dimethyl sulfoxide-d6 (99.8%, Sigma Aldrich). Substrates: fused silica wafers (2 inches diameter, thickness 500 ± 25 μm , 2 side polished, MicroChemicals), silicon wafer (2 inches diameter, thickness 400 ± 25 μm , 1 side polished, (111), with native silicon oxide, MicroChemicals).

B. Synthesis procedures

Chapter 2

Synthesis of g-C₃N₄ thin films (test tube method)

In a typical recipe, 1 g of melamine was placed at the bottom of an 18 cm test tube (18 mm diameter). A glass slide (1 cm x 2.5 cm) was afterwards inserted at the top of the test tube and placed at about 3 cm from the top. Then, the test tube was capped with an aluminum foil lid with holes and placed horizontally into a muffle furnace. Under N₂ flow the temperature was increased to 300°C at 10°C/min and kept for 30 minutes and then the temperature was further increased to 550°C at 2.5°C/min and kept for 4 hours. After the deposition program was finished, it was let cool down naturally and the sample was collected when it reached room temperature.

Synthesis of g-C₃N₄ thin films (CVD method for sample CN-1a)

In typical deposition experiment, a 2" fused silica and a 2" silicon wafers were thoroughly rinsed with water, acetone, ethanol and isopropanol and dried with compressed air. After drying, they were placed on a wafer vertical holder at about 1 cm distance from other. The vertical holder was then placed in the CVD machine in the middle of the downstream oven. Then, 5 g of melamine in a glass boat were

placed at the center of the upstream oven. The CVD machine was then locked and slowly reduced the pressure inside the reactor below 10 Torr. Afterwards, the previously prepared recipe was run. In the first step, the pressure was increased to 10 Torr with a pre-heated (100°C), N₂ flow for 10 minutes. Subsequently, the downstream oven temperature was raised to 550°C in 40 minutes and kept at this temperature for 90 minutes. After the downstream oven reached the final temperature, the upstream oven temperature was increased to 300°C at 10°C/min and kept for 30 minutes. After the deposition program was finished, the CVD setup was let cool down naturally and the samples collected when the system reached the room temperature.

The other samples presented were prepared following the same procedure, changing, as mentioned in chapter 2, the melamine mass (from 5 g to 10 g) and/or the downstream time (from 90 to 330 minutes).

For the deposition g-C₃N₄ thin film, a PlanarGROW 3S from PlanarTech thermal and low-pressure CVD setup was used (in figure 2.4). The setup consists of 3 mass flow controllers up to 500 sccm connected to synthetic air, N₂ and Ar that can be pre-heated up to 100°C. The reaction chamber is a quartz tubular reactor (3 inches diameter) with two ovens that allow control of the temperature separately, up to 1000°C. Pressure inside the reactor, under flow conditions, is monitored by two manometers in the range 10-1000 Torr.

Chapter 3

Synthesis of the melamine-boric acid adduct (1:1)

1.26 g of melamine and 0.62 g of boric acid were placed into two different glass vessels with 4 and 3 ml of deionized water, respectively. The two vessels were placed in an oil bath pre-heated at 95-100°C and stirred, until boric acid completely dissolved. When the boric acid was completely dissolved, this solution was added the warm melamine dispersion, which promptly created a white solid precipitate. The precipitated was further dried for 30-40 minutes in the oil bath and then let it further dry in a vacuum oven at 40°C, overnight.

Synthesis of the melamine-boric acid adduct (1:2)

1.26 g of melamine and 1.24 g of boric acid were placed into two different glass vessels with 4 and 6 ml of deionized water, respectively. The two vessels were placed in an oil bath pre-heated at 95-100°C and stirred, until boric acid completely dissolved. When the boric acid was completely dissolved, this solution was added the warm melamine dispersion, which promptly created a white solid precipitate. The precipitated was further dried for 30-40 minutes in the oil bath and then let it further dry in a vacuum oven at 40°C, overnight.

Synthesis of BCN thin films from 1:1 melamine-boric acid adduct (test tube method)

In a typical recipe, 1.8 g of melamine-boric acid adduct (1:1) was placed at the bottom of an 18 cm test tube (18 mm diameter). A glass slide (1 cm x 2.5 cm) was afterwards inserted at the top of the test tube and placed at about 3 cm from the top. Then, the test tube was capped with an aluminum foil lid with holes and placed horizontally into a muffle furnace. Under N₂ flow the temperature was increased to 300°C at 10°C/min and kept for 30 minutes and then the temperature was further increased to 550°C at 2.5°C/min and kept for 4 hours. After the deposition program was finished, it was let cool down naturally and the sample was collected when it reached room temperature.

Synthesis of BCN thin films from 1:2 melamine-boric acid adduct (test tube method)

In a typical recipe, 2.4 g of melamine-boric acid adduct (1:2) was placed at the bottom of an 18 cm test tube (18 mm diameter). A glass slide (1 cm x 2.5 cm) was afterwards inserted at the top of the test tube and placed at about 3 cm from the top. Then, the test tube was capped with an aluminum foil lid with holes and placed horizontally into a muffle furnace. Under N₂ flow the temperature was increased to 300°C at 10°C/min and kept for 30 minutes and then the temperature was further increased to 550°C at 2.5 °C/min and kept for 4 hours. After the deposition program was finished, it was let cool down naturally and the sample was collected when it reached room temperature.

Synthesis of BCN thin films (BCN sample I)

In typical deposition experiment, a 2" fused silica and a 2" silicon wafers were thoroughly rinsed with water, acetone, ethanol and isopropanol and dried with compressed air. After drying, they were placed on a wafer vertical holder at about 1 cm distance from other. The vertical holder was then placed in the CVD machine in the middle of the downstream oven. Then, 5 g of 1:1 melamine-boric acid adduct in a glass boat were placed at the center of the upstream oven. The CVD machine was then locked and slowly reduced the pressure inside the reactor below 10 Torr. Afterwards, the previously prepared recipe was run. In the first step, the pressure was increased to 10 Torr with a pre-heated (100°C), N₂ flow for 10 minutes. Subsequently, the downstream oven temperature was raised to 550°C in 40 minutes and kept at this temperature for 90 minutes. After the downstream oven reached the final temperature, the upstream oven temperature was increased to 500°C at 17°C/min and kept for 30 minutes. After the deposition program was finished, the CVD setup was let cool down naturally and the samples collected when the system reached the room temperature.

For the deposition BCN thin film, a PlanarGROW 3S from PlanarTech thermal and low-pressure CVD setup was used (in figure 2.4). The setup consists of 3 mass flow controllers up to 500 sccm connected to synthetic air, N₂ and Ar that can be pre-heated up to 100°C. The reaction chamber is a quartz tubular reactor (3 inches diameter) with two ovens that allow control of the temperature separately, up to 1000°C. Pressure inside the reactor, under flow conditions, is monitored by two manometers in the range 10-1000 Torr.

The other samples presented were prepared following the same procedure, changing, as mentioned in chapter 3, the precursor mass (from 5 g to 10 g) and/or the downstream time (from 90 to 180 minutes).

Synthesis of BCN thin films (BCN sample IX)

In typical deposition experiment, a 2" fused silica and a 2" silicon wafers were thoroughly rinsed with water, acetone, ethanol and isopropanol and dried with compressed air. After drying, they were placed on a wafer vertical holder at about 1 cm distance from other. The vertical holder was then placed in the CVD machine in the middle of the downstream oven. Then, 7 g of 1:2 melamine-boric acid adduct in a glass boat were placed at the center of the upstream oven. The CVD machine was

then locked and slowly reduced the pressure inside the reactor below 10 Torr. Afterwards, the previously prepared recipe was run. In the first step, the pressure was increased to 10 Torr with a pre-heated (100°C), N₂ flow for 10 minutes. Subsequently, the downstream oven temperature was raised to 550° in 40 minutes and kept at this temperature for 90 minutes. After the downstream oven reached the final temperature, the upstream oven temperature was increased to 500°C at 17°C/min and kept for 30 minutes. After the deposition program was finished, the CVD setup was let cool down naturally and the samples collected when the system reached the room temperature.

The other samples presented were prepared following the same procedure, changing, as mentioned in chapter 3, the precursor mass (from 7 g to 14 g) and/or the downstream time (from 90 to 180 minutes).

For the deposition BCN thin film, a PlanarGROW 3S from PlanarTech thermal and low-pressure CVD setup was used (in figure 2.4). The setup consists of 3 mass flow controllers up to 500 sccm connected to synthetic air, N₂ and Ar that can be pre-heated up to 100°C. The reaction chamber is a quartz tubular reactor (3 inches diameter) with two ovens that allow control of the temperature separately, up to 1000°C. Pressure inside the reactor, under flow conditions, is monitored by two manometers in the range 10-1000 Torr.

Chapter 4

Synthesis of low temperature carbon from malonic acid and P₂O₅

In a typical recipe, 3 grams of malonic acid were mixed with 5-fold amount of P₂O₅ and placed in a 250 ml bottom round flask. The flask was connected to a Liebig condenser and a 250 ml collection flask preceded by a stopcock. The distillation system was connected to a Schlenk line and, after flushing the system for 3 times with N₂, the pressure was reduced to 10-3 mbar. Subsequently, the flask containing the precursor mixture was immersed in a pre-heated oil bath at 160°C and the collection flask in a Dewar flask with liquid nitrogen. The reaction was run for 15 minutes. Then the heating bath was removed, and collection flask locked at the stopcock to keep the collected product in vacuum. By slowly increasing the pressure in the system, the stopcock and the collection flask were removed and stored,

without releasing the vacuum, in plastic box at -18°C for 18 hours and then 6-8 more hours at room temperature until a deep red coloration occurs (the “red carbon”).

Note: the connections must be greased with special low temperature grease and hold by plastic clips in order to ensure that the system is air-excluded during the reaction. Moreover, it is strongly suggested to use the silicon oil for high temperatures (above 200°C).

The product was then collected and placed in an alumina crucible. The crucible containing the polymeric product was placed in a muffle furnace and heated at $10^{\circ}\text{C}/\text{min}$ to 200°C and kept for 5 hours, under N_2 flow. The LTC was then collected and analyzed.

Synthesis of LTC thin films (test tube method)

0.8 g of malonic acid and 4 g of P_2O_5 were mixed and placed at the bottom of an 18 cm test tube. A glass slide (1x 2.5 cm) was afterwards inserted at the top of the test tube and placed at about 3 cm from the top. Then, the test tube was capped with an aluminum foil lid with holes and placed horizontally into a muffle furnace. Under N_2 flow the temperature was increased to 160°C at $10^{\circ}\text{C}/\text{min}$ and kept for 30 minutes. After the deposition program was finished, it was let cool down naturally and the sample was collected when it reached room temperature.

Synthesis of LTC thin films (CVD method)

6 grams of malonic acid have been mixed with 5-fold amount of P_2O_5 and placed in a glass crucible in the CVD. The precursor mixture has been heated up at 160°C ($10^{\circ}/\text{min}$), at 10 Torr and 50 sccm of N_2 flow. In order to adjust to as similar condition as possible to the method used with the Schlenk line, the downstream oven was left at room temperature in order to deposit and polymerize the precursor. The substrate was left at room temperature overnight. Subsequently, the temperature of the substrate was increased to 200°C under N_2 flow and kept for 5 hours. The CVD temperature was decreased naturally to room temperature at a pressure of 10 Torr, before collecting the samples.

For the deposition LTC thin film, a PlanarGROW 3S from PlanarTech thermal and low-pressure CVD setup was used (in figure 2.4). The setup consists of 3 mass flow controllers up to 500 sccm connected to synthetic air, N_2 and Ar that can be pre-heated up to 100°C . The reaction chamber is a quartz tubular reactor (3 inches

diameter) with two ovens that allow control of the temperature separately, up to 1000°C. Pressure inside the reactor, under flow conditions, is monitored by two manometers in the range 10-1000 Torr.

Synthesis of low temperature carbon from malonic acid and acetic anhydride

In a typical recipe 1 g of malonic acid was put in 1 ml of acetic anhydride (1:1 molar ratio). The malonic acid is insoluble in acetic anhydride at room temperature. By heating up to 90°C for 4 hours the malonic acid dispersion in the acetic anhydride turns to a deep red solution. The red solution was cooled down naturally to room temperature, and transferred to an aluminum crucible. The crucible containing the red solution was then further heated up to 200°C for 5 hours at 10°C/min in a muffle furnace under N₂ flow. The black solid product has been fetched at room temperature.

C. Supporting information

Chapter 2

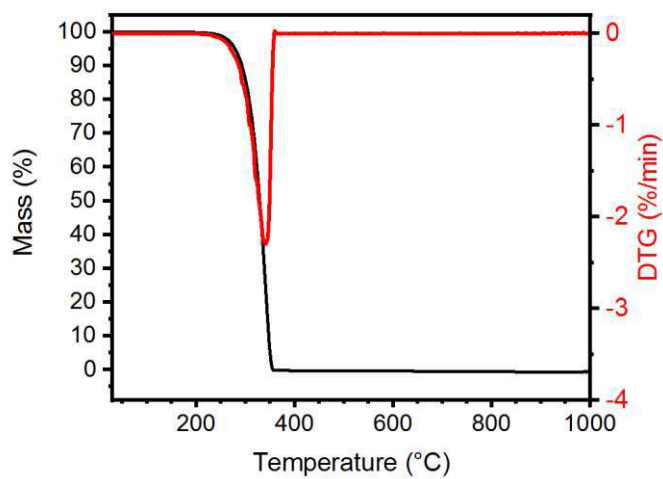


Figure S1. TGA of melamine

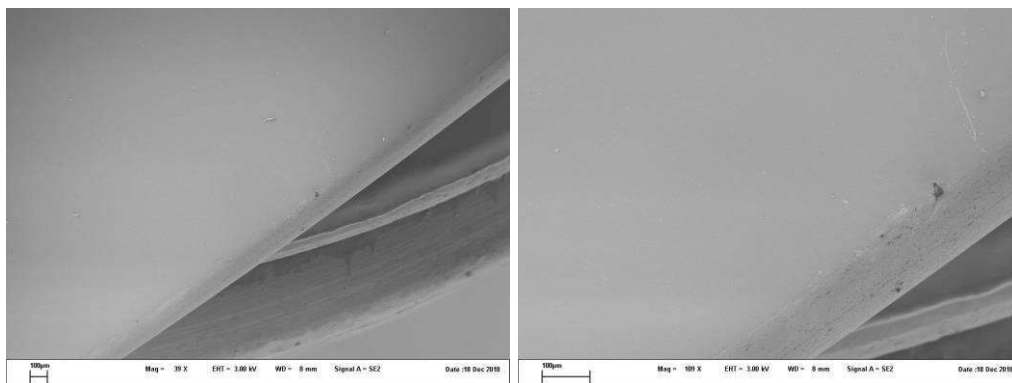


Figure S2. SEM pictures of CN-1a at the edge of the fused silica substrate.

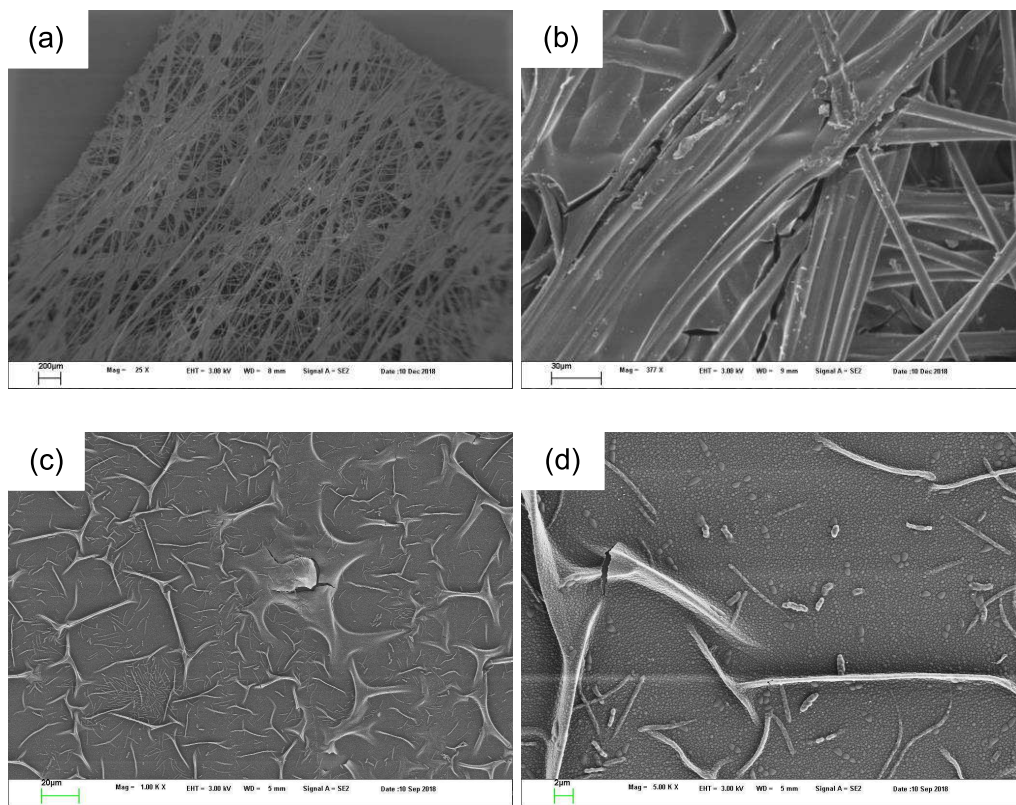


Figure S3. (a), (b) SEM pictures of g-C₃N₄ thin film deposited on carbon paper; (c), (d) SEM pictures of g-C₃N₄ thin film deposited on glass slide.

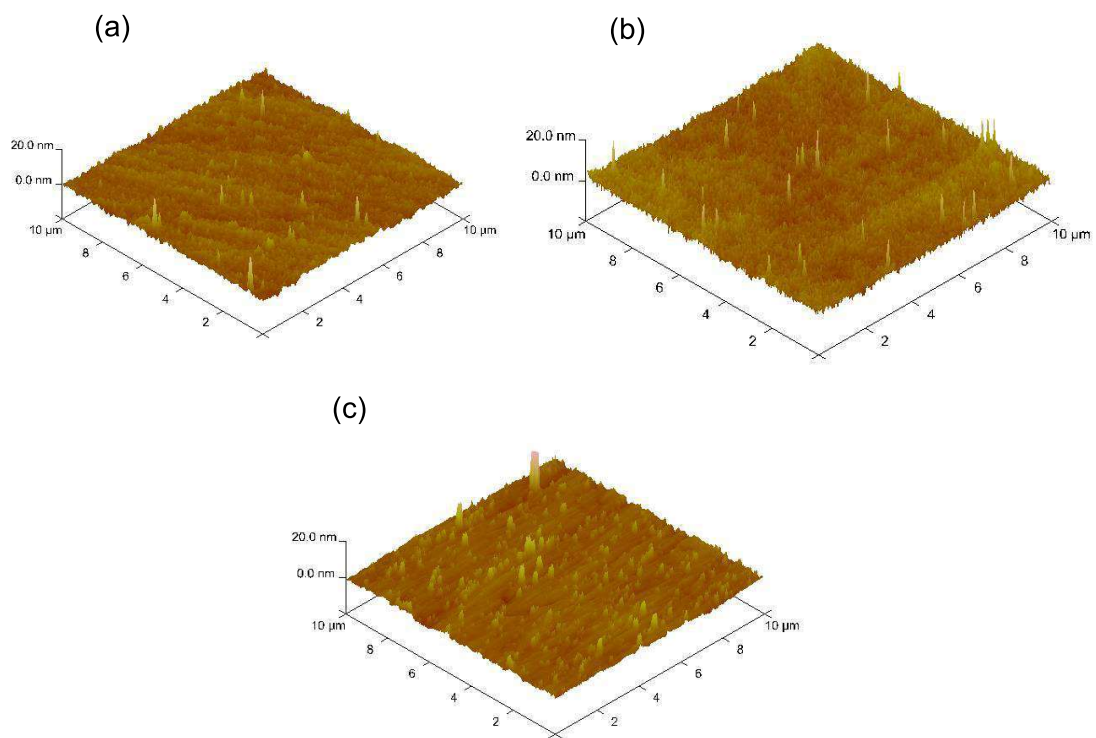


Figure S4. AFM surface images of CN-1a sample (a), CN-1b sample (b) and fused silica bare substrate (c).

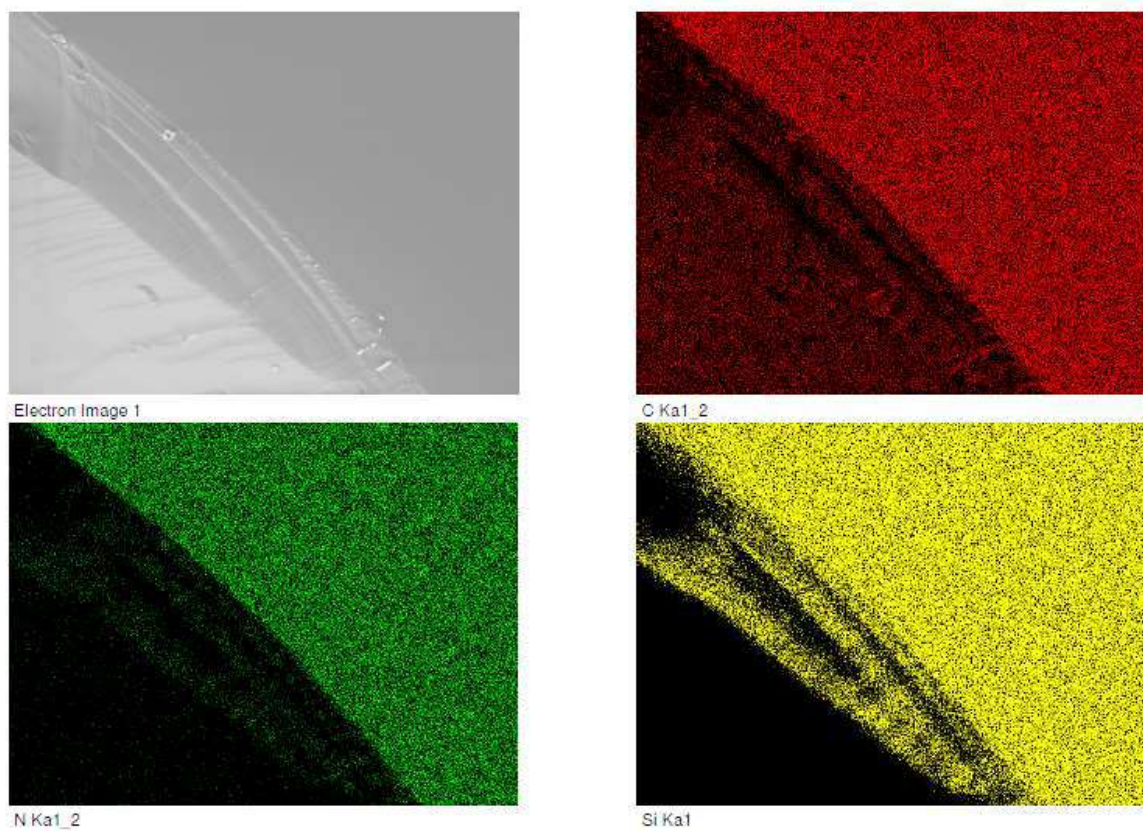


Figure S5. EDX maps of sample CN-1 on silicon substrate: C (in red), N (in green) and Si (in yellow).

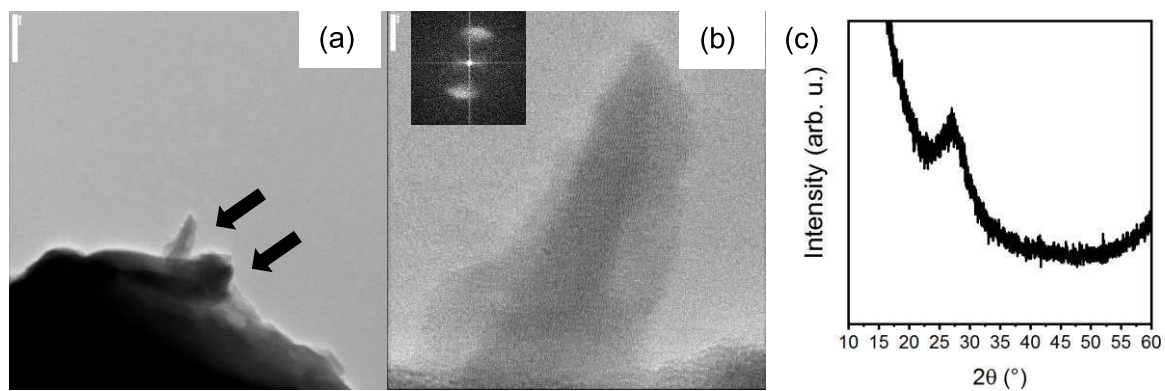


Figure S6. (a), (b) TEM images of CN-2a sample (insert FFT pattern obtained from the image); (c) XRD diffraction spectrum of the peeled sample.

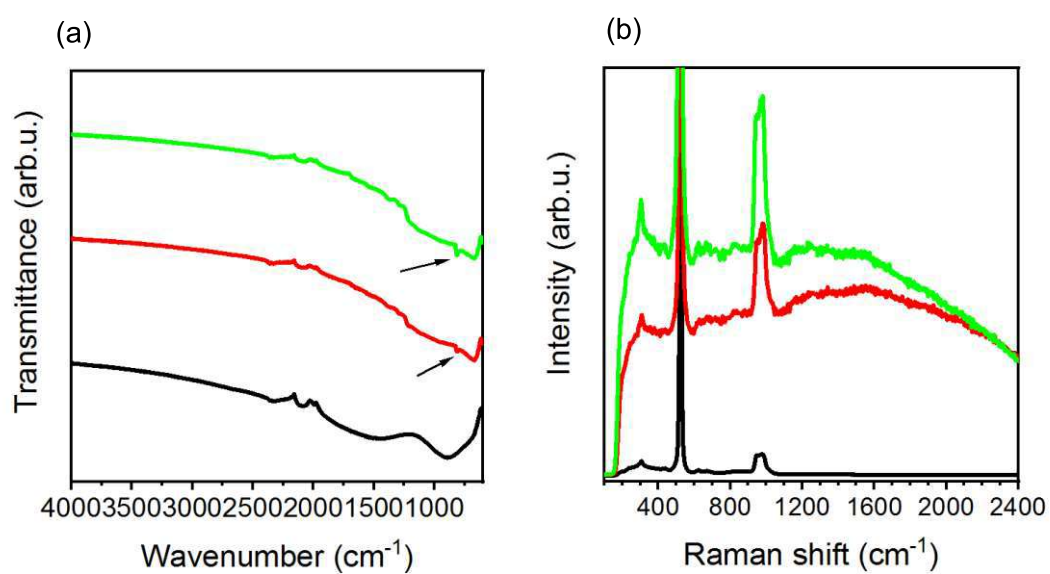


Figure S7. (a) FTIR of CN-1b (green line) CN-2b (red line) and bare silicon substrate (black line). (b) Raman spectra CN-1b (red line) CN-2b (green line) and bare silicon substrate (black line).

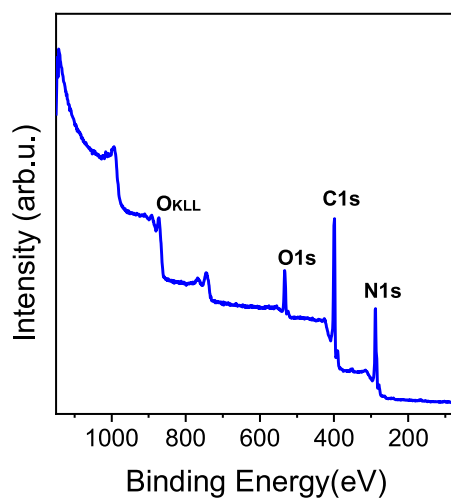


Figure S8. XPS overview of CN-1a sample.

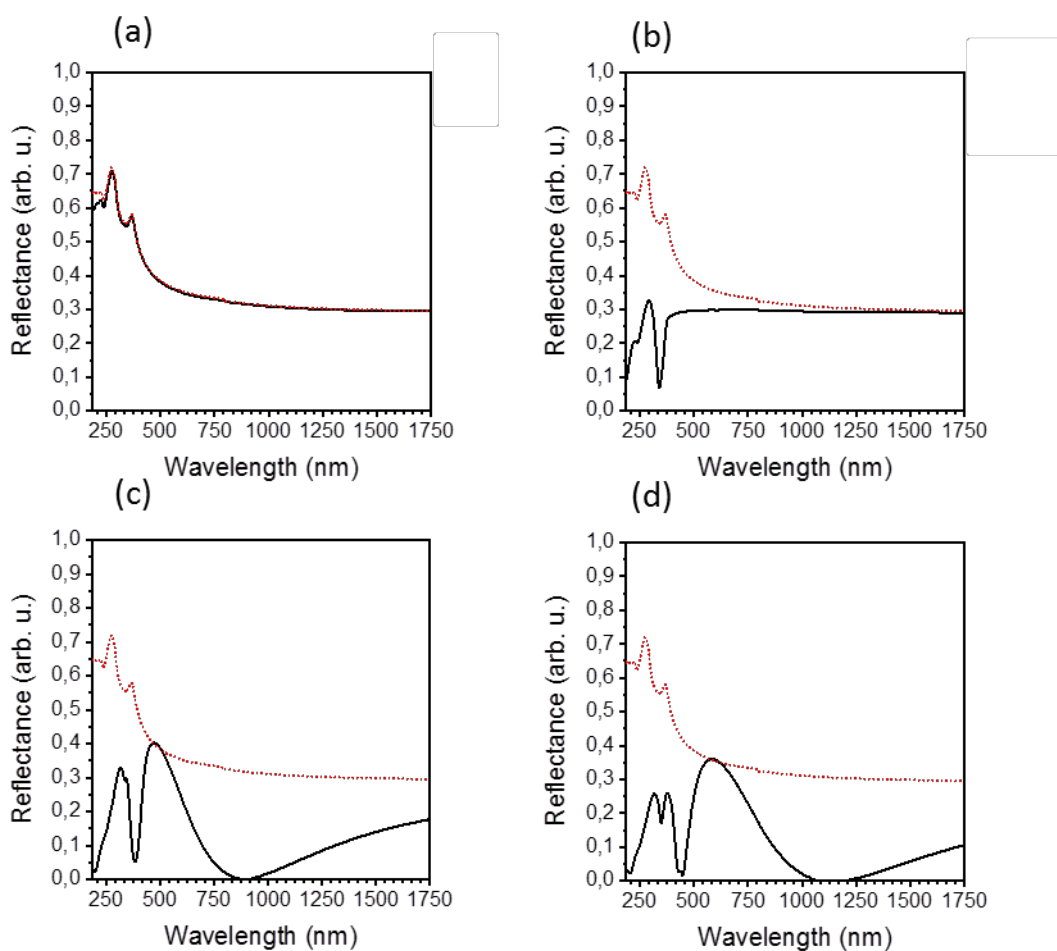


Figure S9. Reflectance spectra of CN-2a (a), CN-1a (b), CN-2b (c) and CN-1b (d) on silicon. Silicon substrate reflectance is plotted in red dotted line.

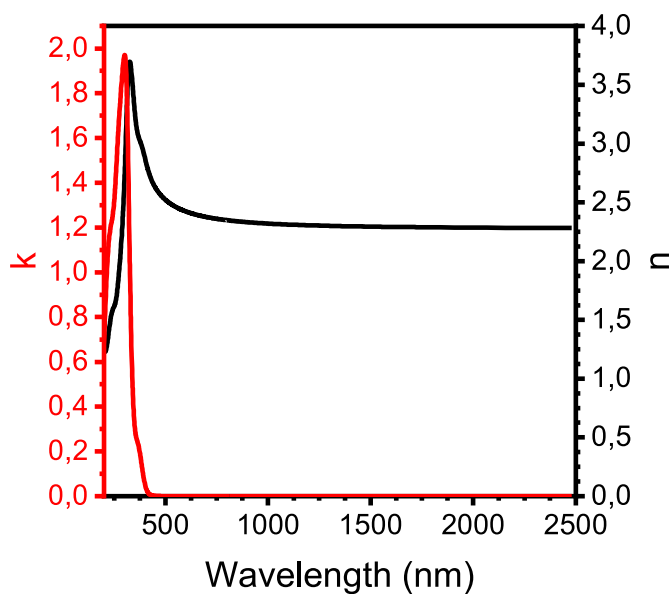


Figure S10. Optical function (n , in black) and (k , in red) of g-C3N4 extended up to 2500 nm.

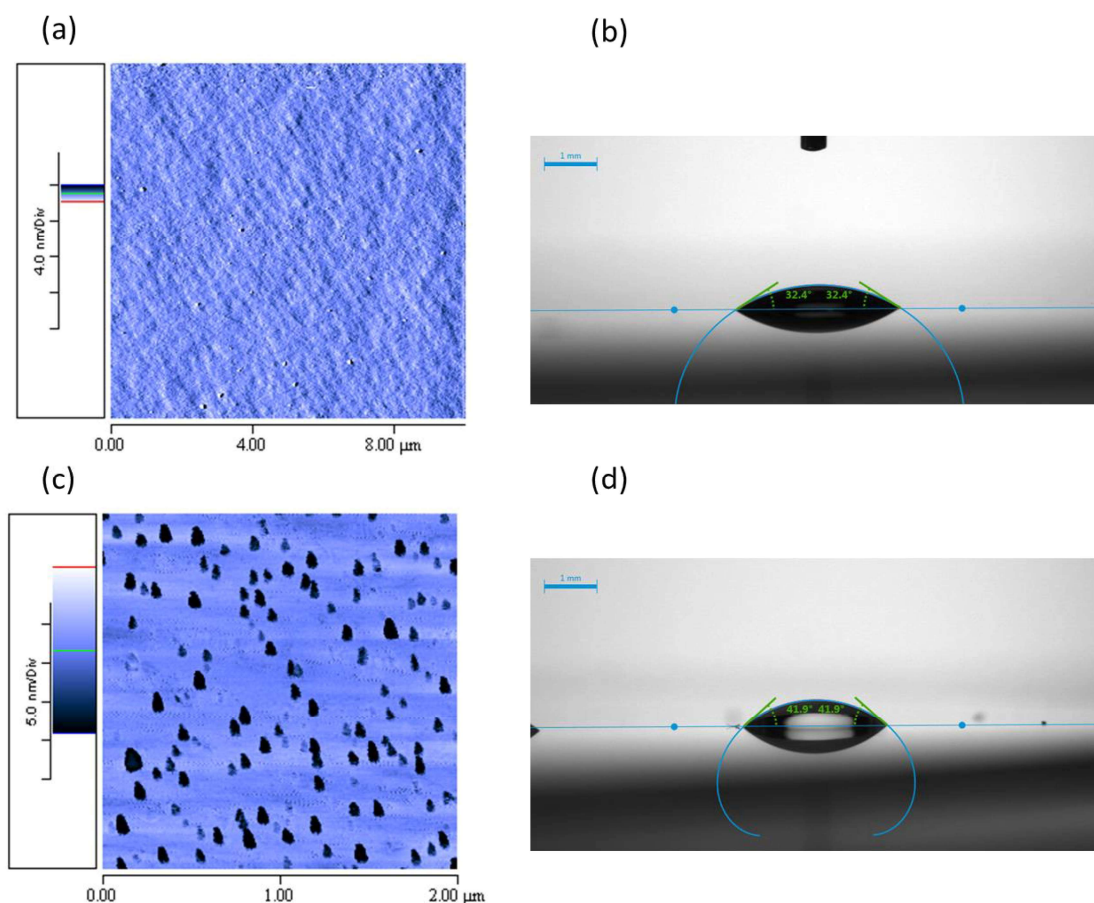


Figure S11. AFM (a) and contact angle (b) respect to water of the silicon substrate. AFM surface picture (c) and contact angle (d) respect to water of the fused silica substrate.

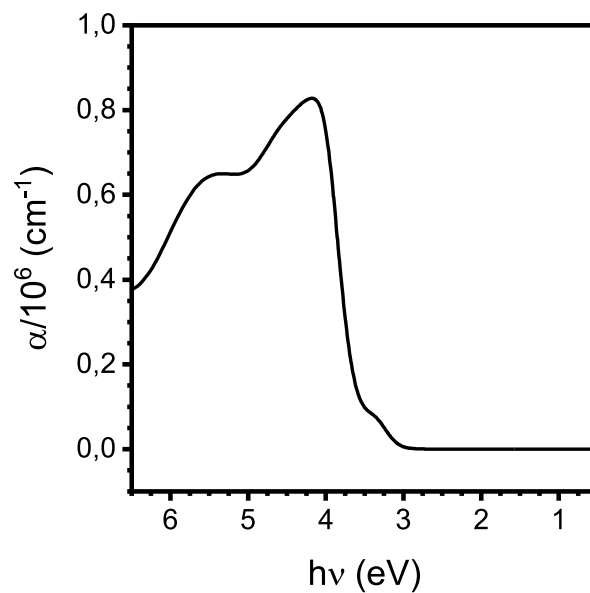


Figure S12. Absorption coefficient of g-C₃N₄ thin films.

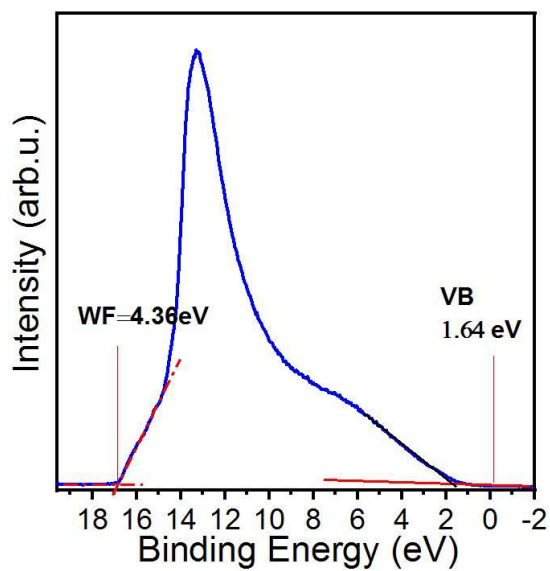


Figure S13. UPS spectrum of g-C₃N₄ thin film. Red lines show how the Fermi level and the valence band have been obtained.

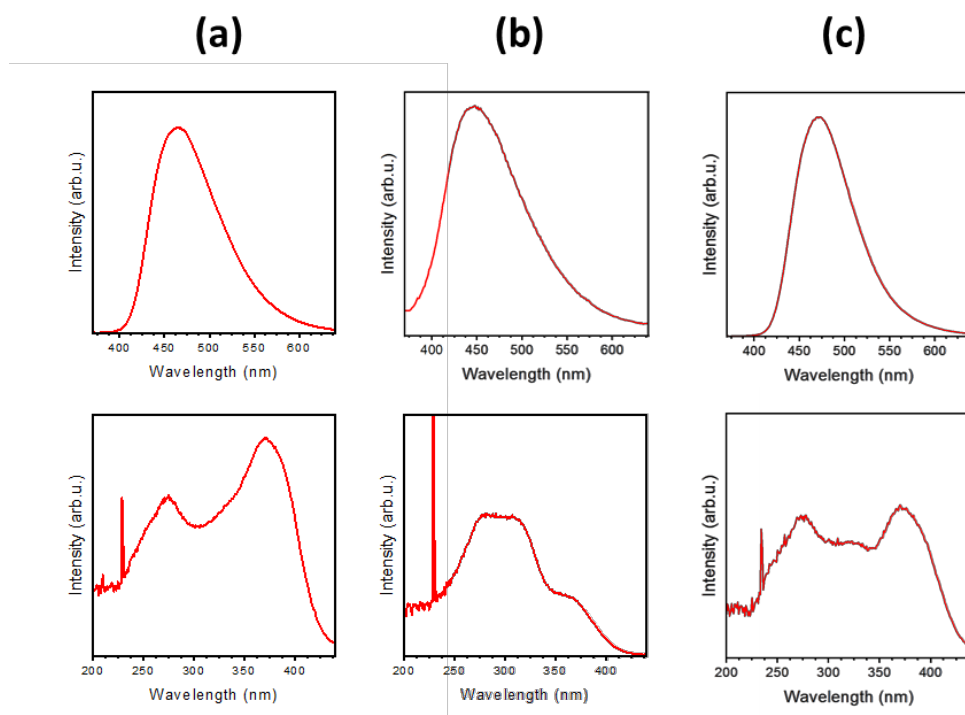


Figure S14. PL spectra (above) and excitation spectra (below) of samples CN-1a (a), CN-2a (b) and CN-2b (c)

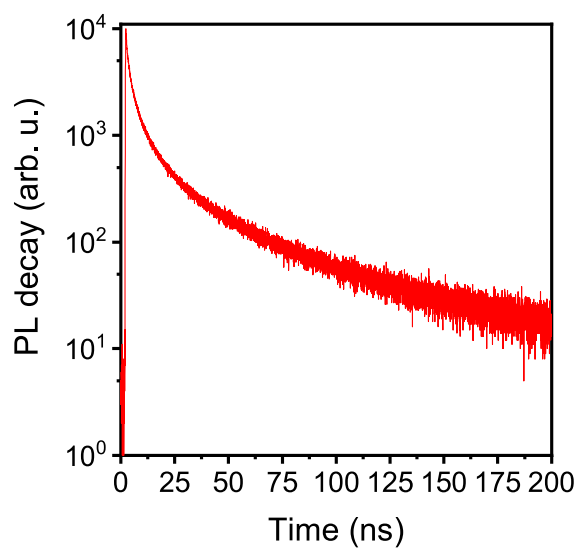


Figure S15. TCSPC of sample CN-2b.

Table S1. Fitting parameters of fluorescence lifetime for sample CN-2b

A_1 (counts)	τ_1 (ns)	A_2 (counts)	τ_2 (ns)	A_3 (counts)	τ_3 (ns)	$\langle \tau \rangle$ (ns)
215.46	69.78	1426.4	13.29	4383	2.365	7.36

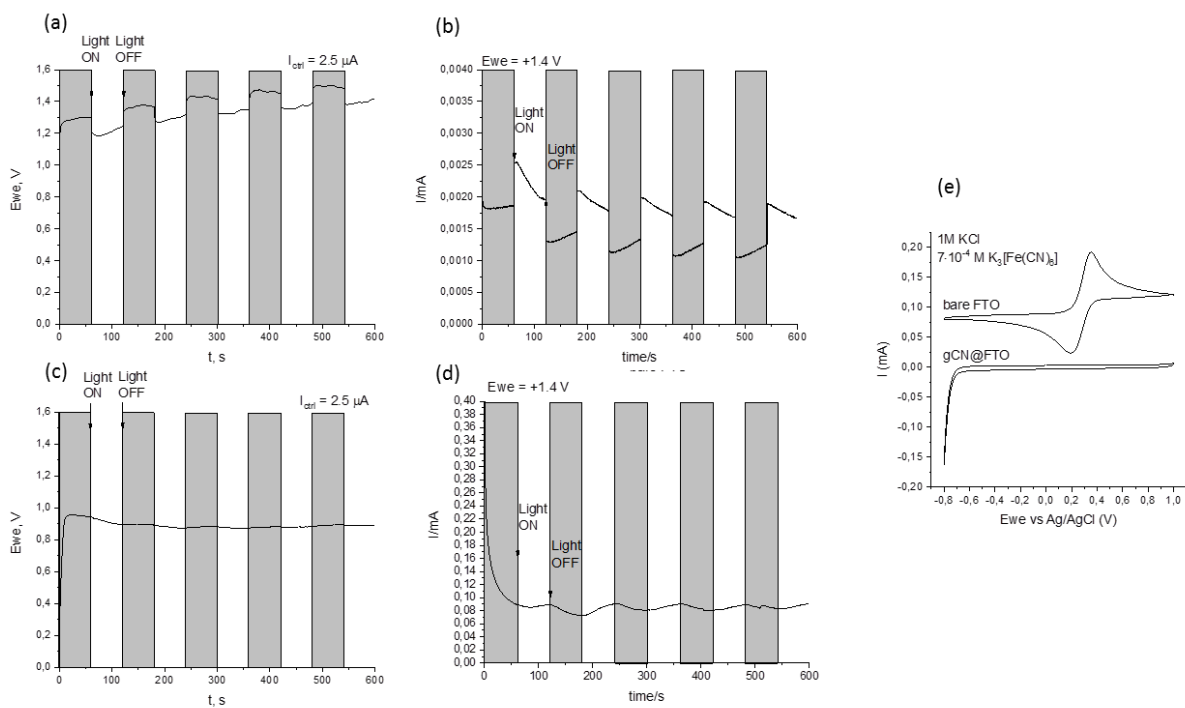


Figure S16. Electrochemical measurements of $g-C_3N_4$ thin films (a and b) respect to the FTO substrate (c and d) with ON-OFF illumination steps of 60 seconds. (e) PEC test for redox reaction in the reference system 1M KCl $7 \cdot 10^{-4} M K_3Fe(CN)_6$ in water.

Chapter 3

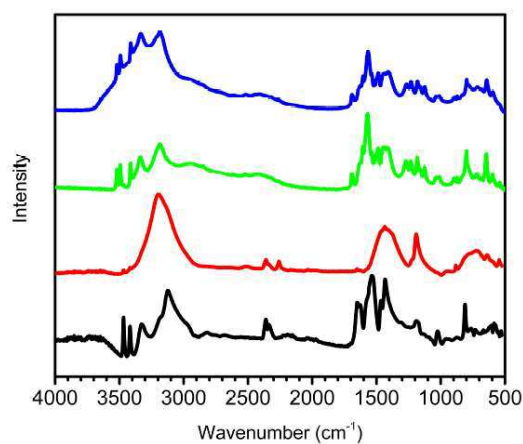


Figure S17. FTIR spectra of melamine (black line), boric acid (red line) and melamine-boric acid adduct 1:1 (green line) and 1:2 (blue line).

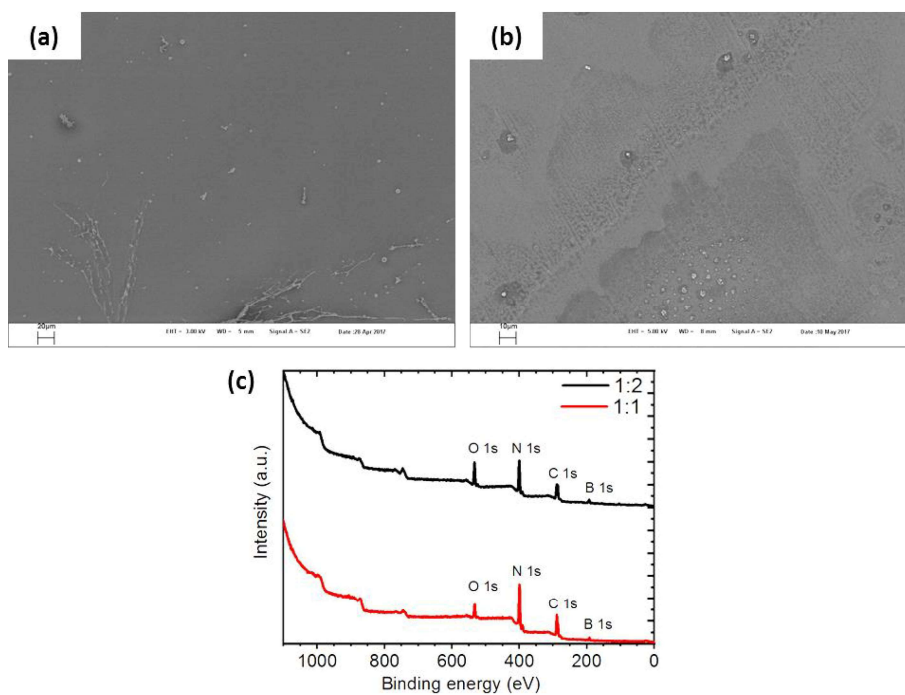


Figure S18. SEM images of BCN thin films prepared by the test tube method from 1:1 (a) and 1:2 (b) precursors. XPS overview of the B, C and N peaks, proving the presence of the three elements in the thin films (c) both from 1:1 (red line) and 1:2 (black line) precursors.

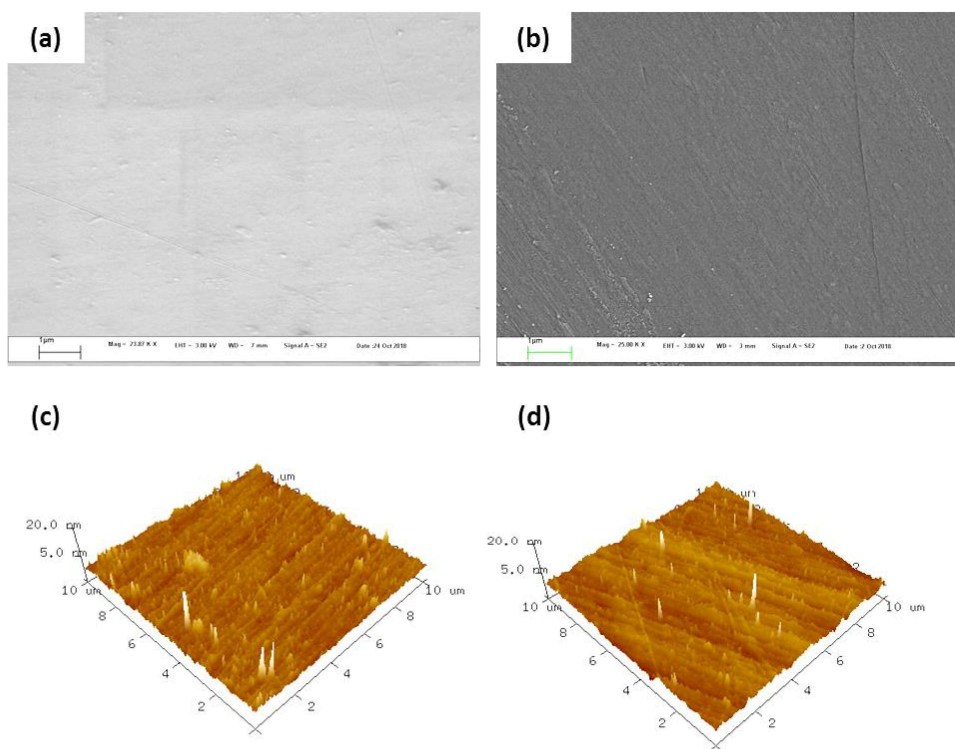


Figure S19. SEM images of BCN 1:1 (a) and 1:2 (b) thin films deposited by CVD. AFM surface images of BCN 1:1 (c) and 1:2 (d) thin films deposited by CVD.

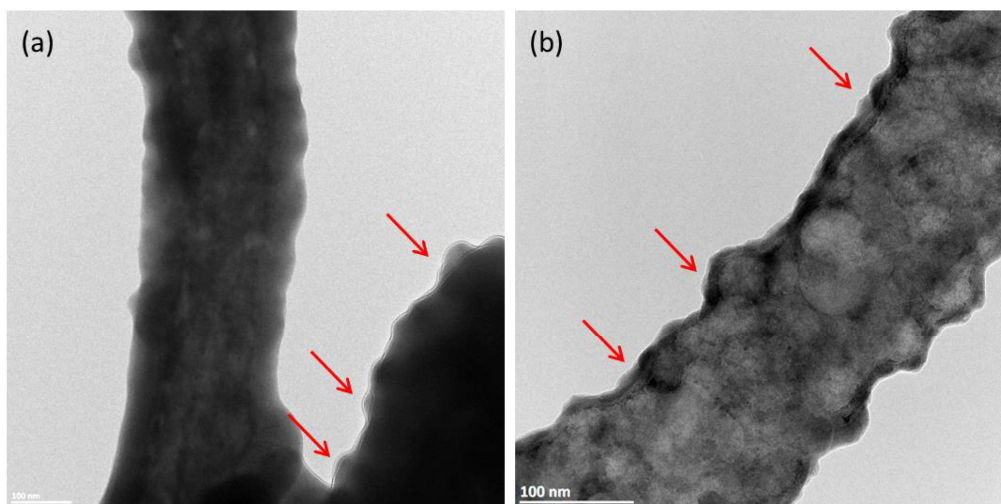


Figure S20. TEM images at low magnification of sample I (a) and IX (b). With red arrows are indicated the areas that suggest the presence of layered structure.

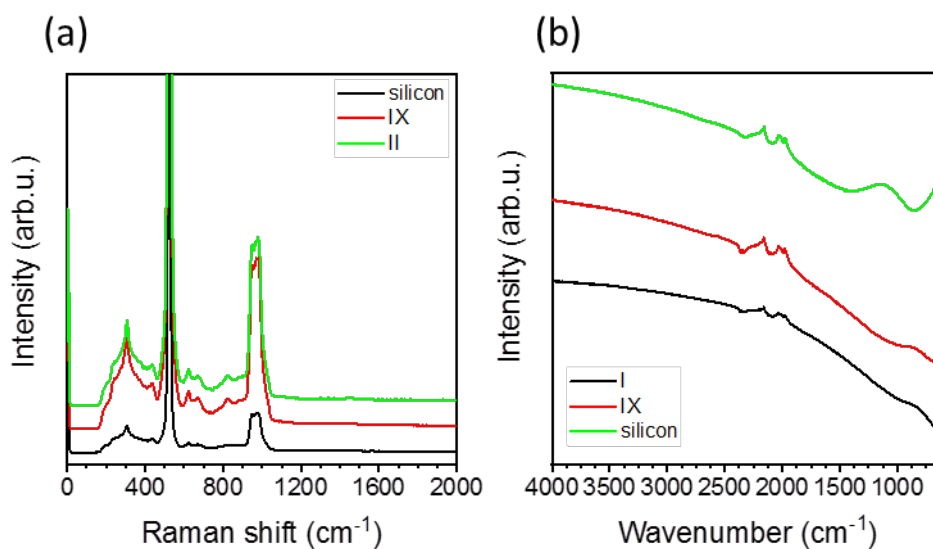


Figure S21. (a) Raman spectra of samples II (green line) and IX (red line) compared to the silicon spectrum (black line). (b) FTIR spectra of samples I (black line) and IX (red line) compared to the silicon spectrum (green line).

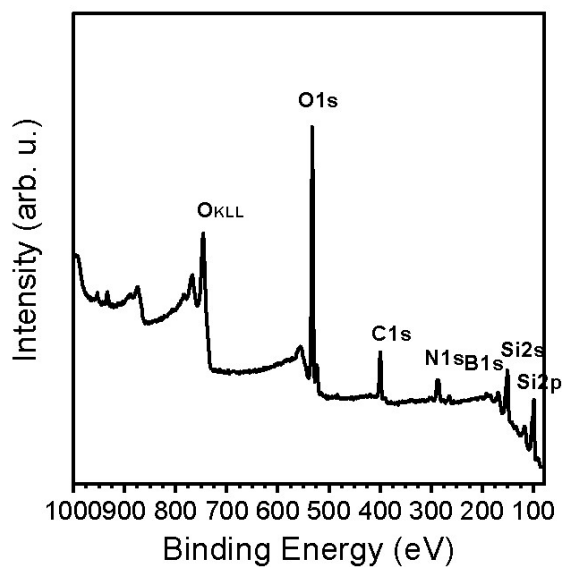


Figure S22. XPS overview of sample IX.

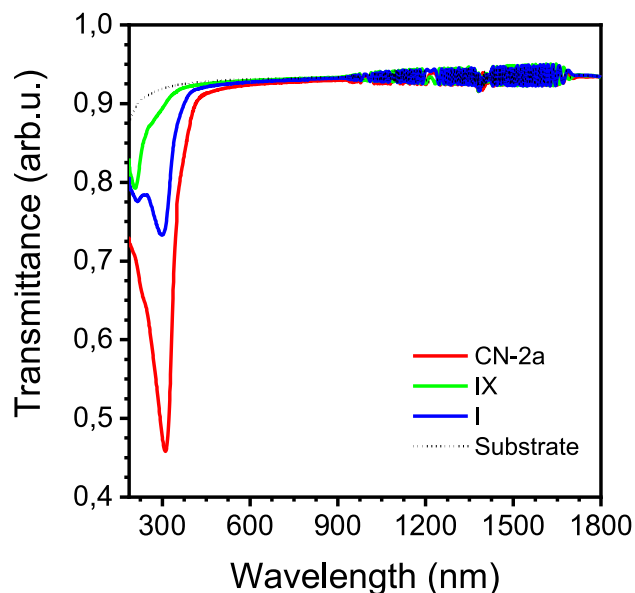


Figure S23. Transmittance spectra of sample I (blue line), IX (green line) and CN-2a (red line) extended to 1800 nm. Black dotted line is the transmittance of the quartz substrate used for the deposition.

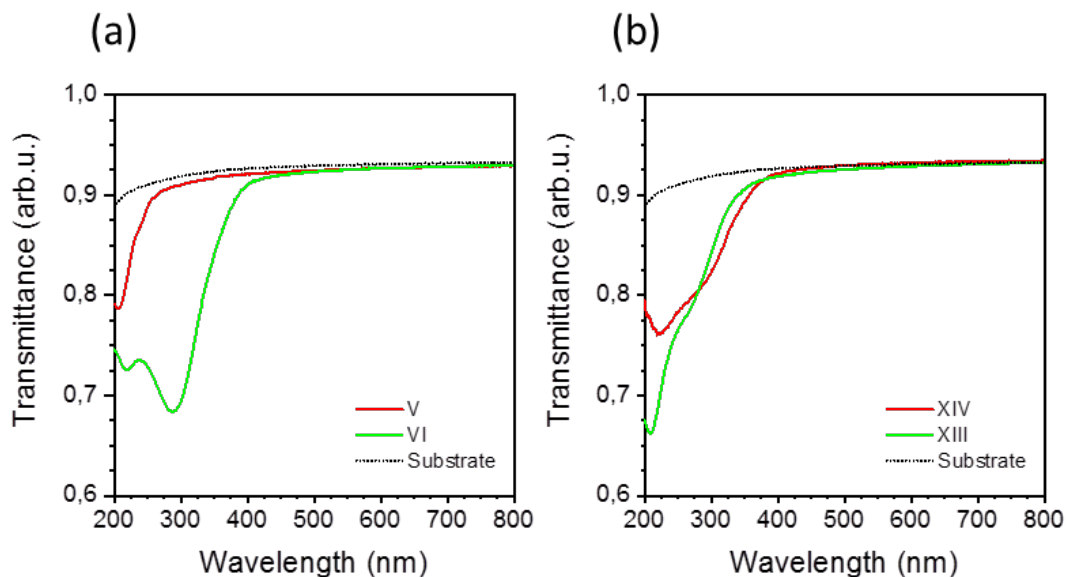


Figure S24. (a) Transmittance spectra of sample V (red line) and VI (green line). (b) Transmittance spectra of sample XIV (red line) and XIII (green line). Black dotted line is the transmittance of the quartz substrate used for the deposition.

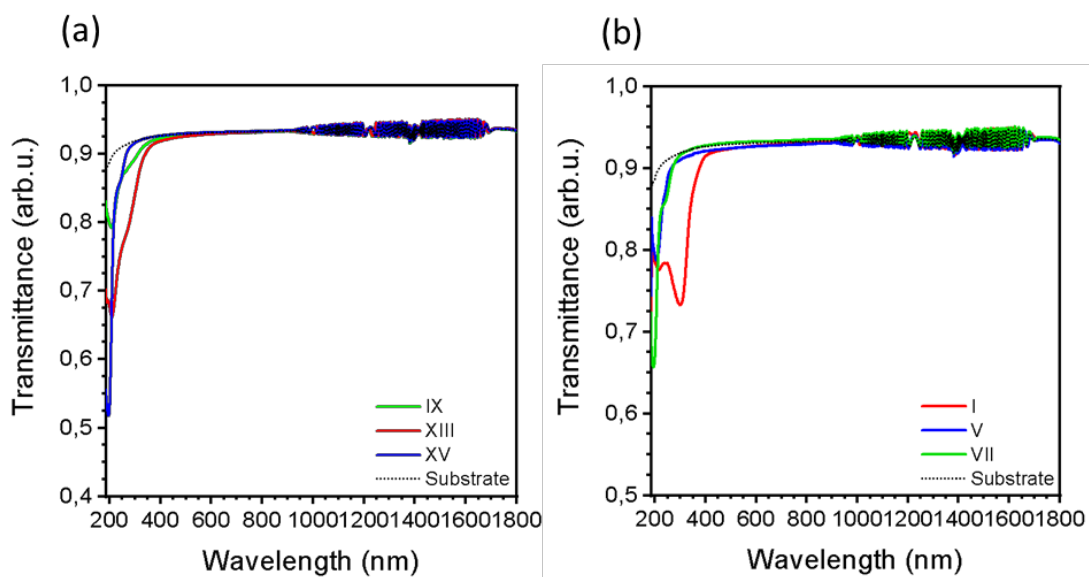


Figure S25. (a) Transmittance spectra of sample XV (blue line), IX (green line) and XIII (red line) extended to 1800 nm. (b) Transmittance spectra of sample I (red line), V (blue line) and VII (green line) extended to 1800 nm. Black dotted line is the transmittance of the quartz substrate used for the deposition.

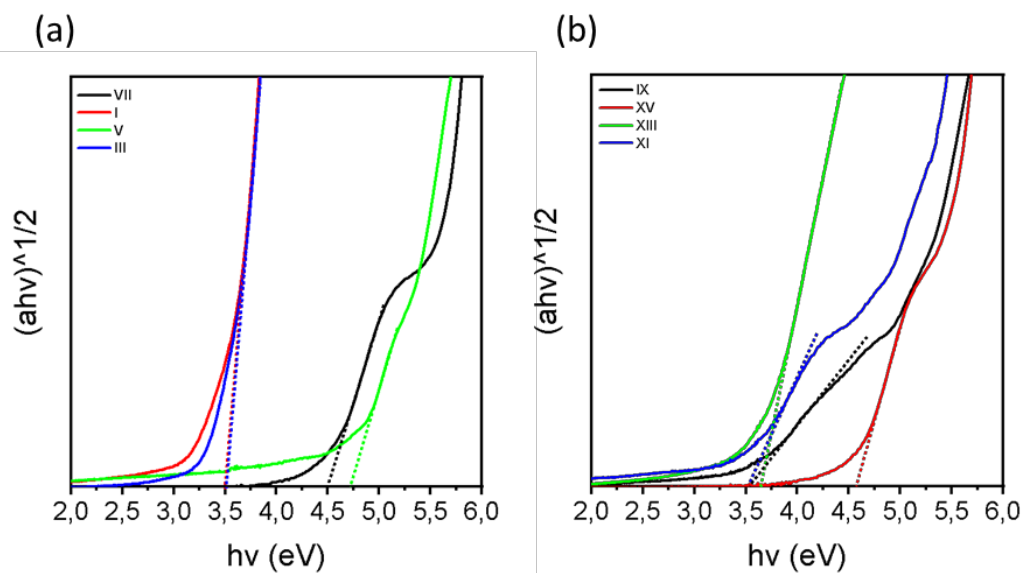


Figure S26. (a) Calculated Tauc plots of thin films prepared from 1:1 precursor: I (red line), III (blue line), V (green line) and VII (black line). (b) Calculated Tauc plots of thin films prepared from 1:2 precursor: IX (black line), XI (blue line), XIII (green line) and XV (red line).

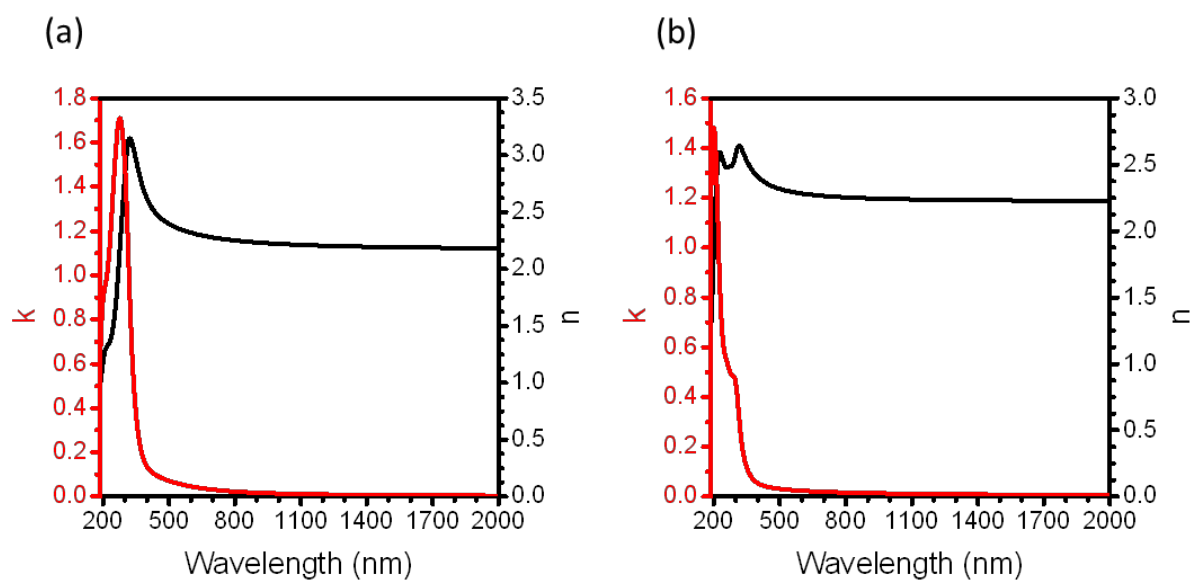


Figure S27. Optical functions n (black lines) and k (red lines) extended to 2000 nm of sample I (a) and IX (b).

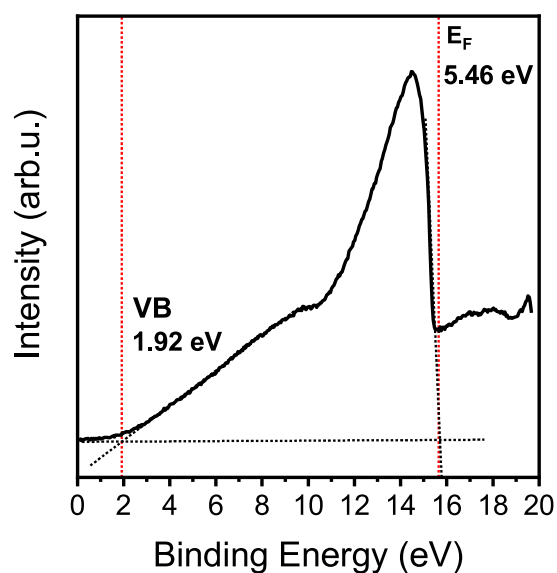


Figure S28. UPS spectrum of sample IX. Red lines show how the Fermi level and the valence band have been obtained.

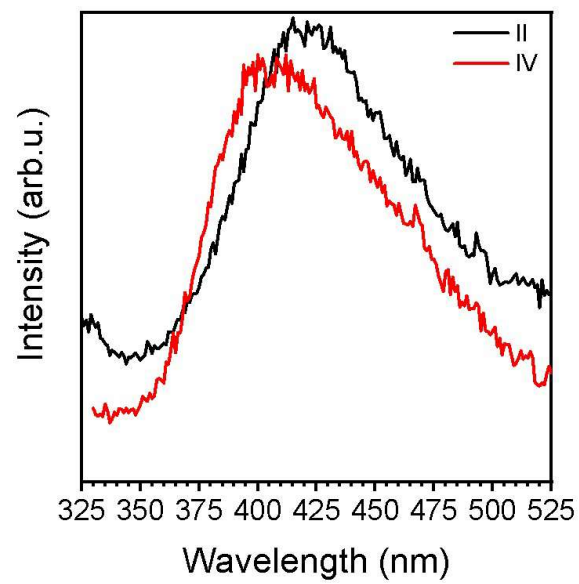


Figure S29. Fluorescence spectra of samples II (black line) and IV (red line).

Chapter 4

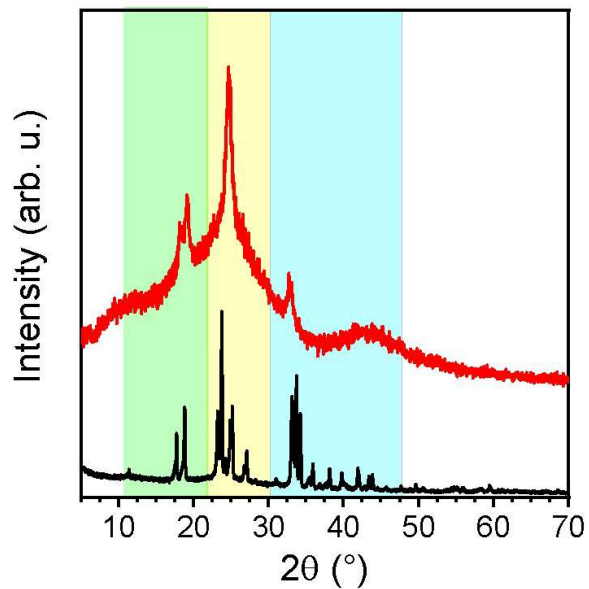


Figure S30. XRD diffraction pattern of LTC (red line) and the precursor (black line). The three areas highlights the possibility of topotactic transformation.

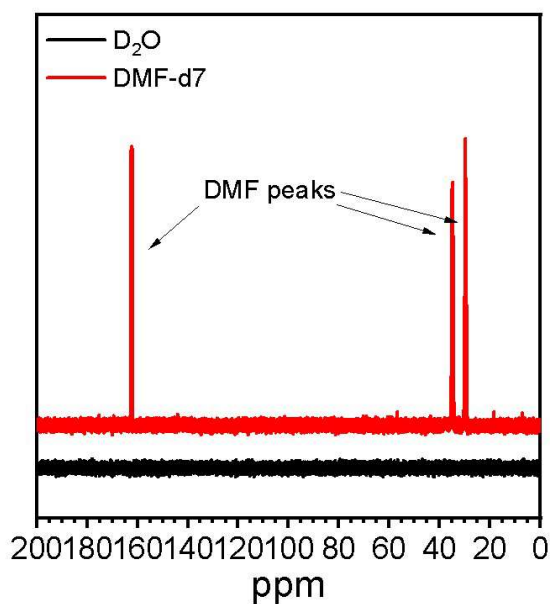


Figure S31. Liquid ¹³C of LTC in d-DMF (red line) and D₂O (black line).

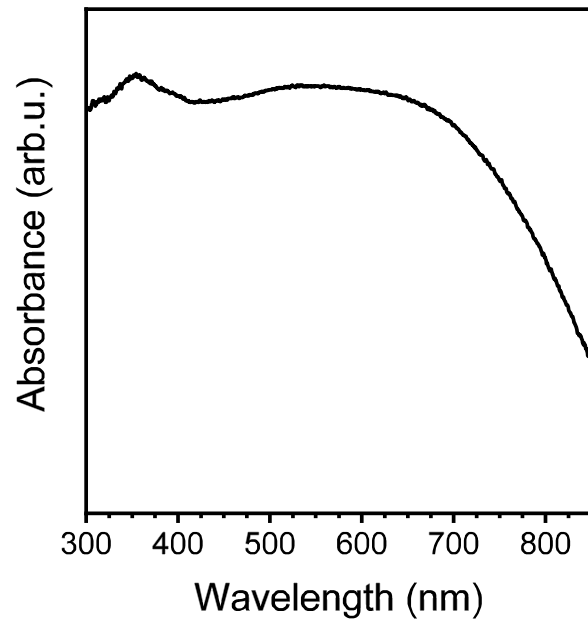


Figure S32. DRS spectrum of LTC.

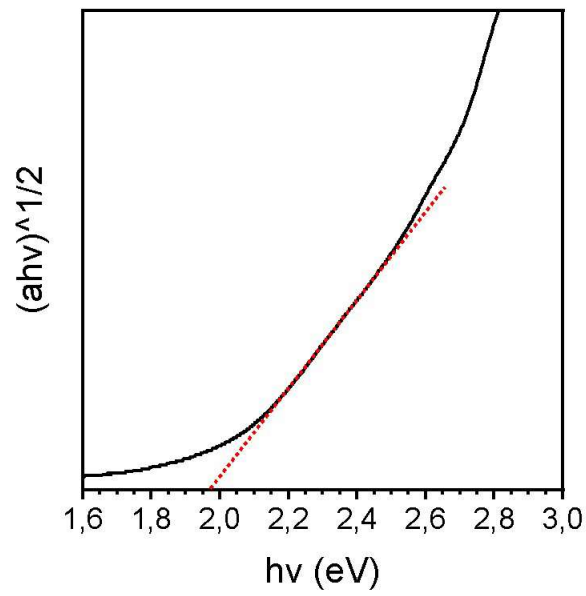


Figure S33. Tauc plot of LTC thin film prepared by the test tube method.

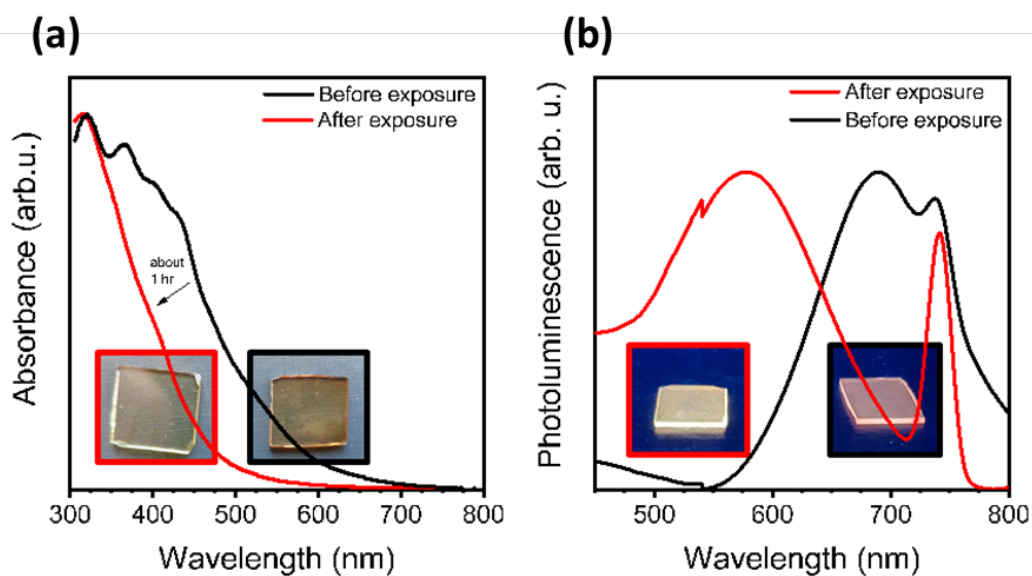


Figure S34. (a) Absorbance spectra of LTC thin films before (black line) and after (red line) being exposed to vapors of NH_3 solution, with sample pictures in insert. (b) Photoluminescence spectra of LTC thin films before (black line) and after (red line) being exposed to vapors of NH_3 solution, with sample pictures in insert.

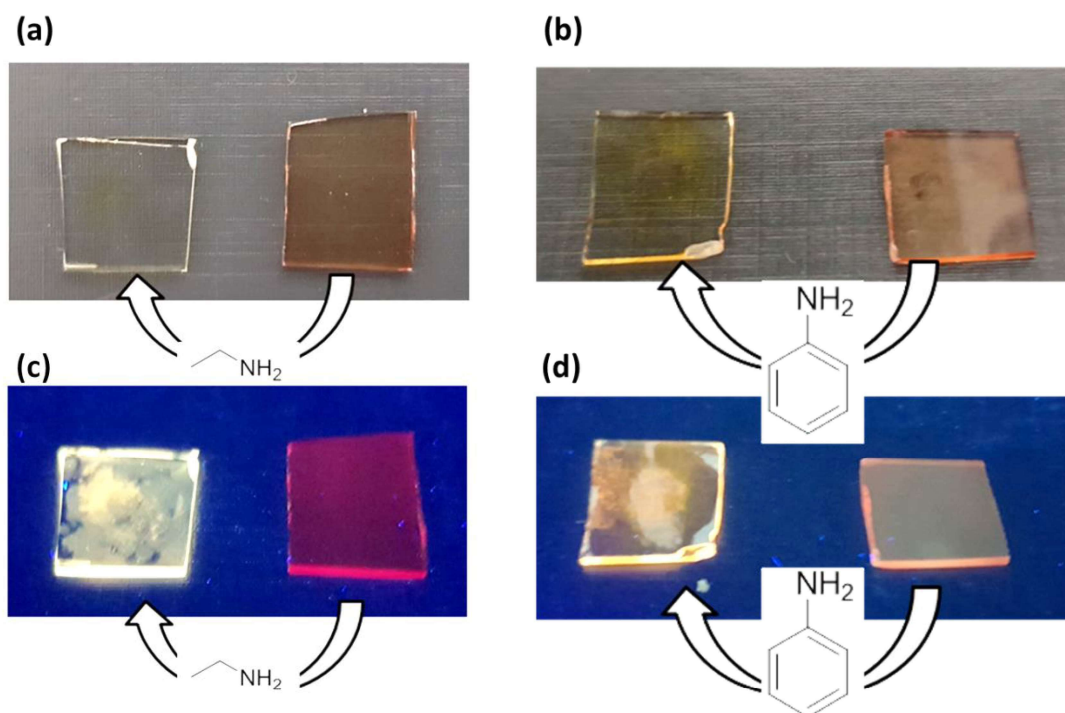


Figure S35. Pictures of LTC thin films in natural light, before and after being exposed to ethylamine (a) and aniline (b). Pictures of LTC thin films under UV light, before and after being exposed to ethylamine (c) and aniline (d).

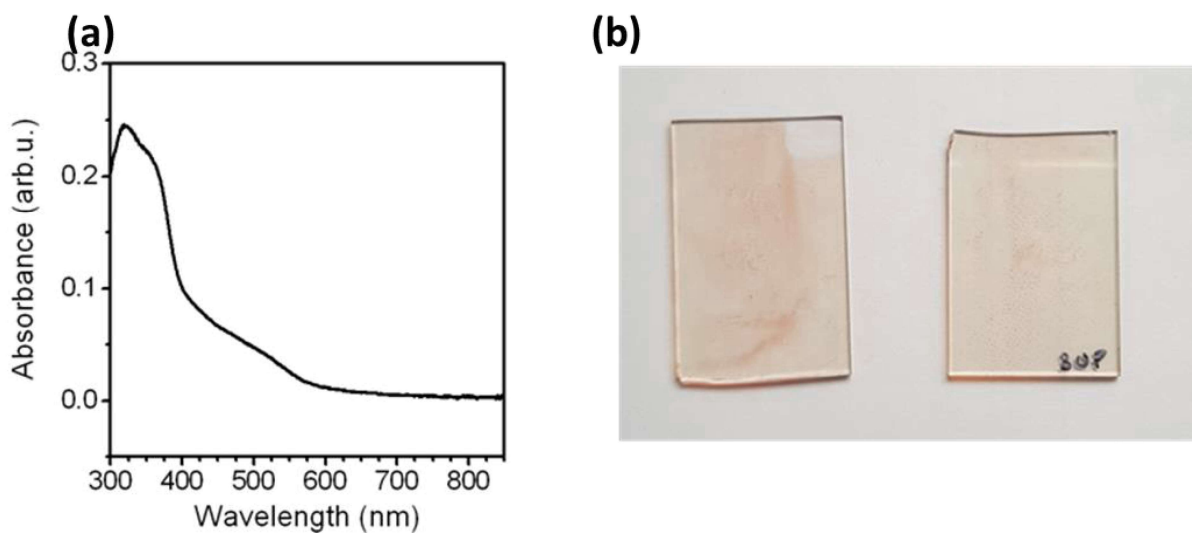


Figure S36. (a) Absorbance spectrum of the LTC thin films shown in (b), prepared by the CVD method.



Figure S37. Malonic acid recovered after thermal treatment at 200°C.

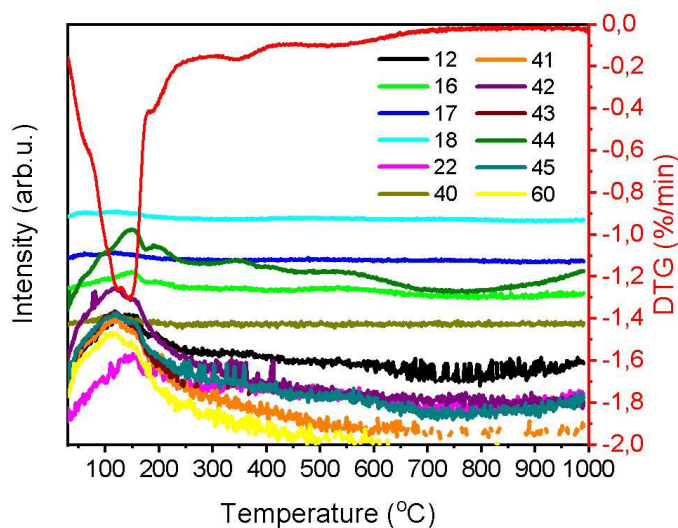


Figure S38. DTG and MS of the LTC precursor malonic acid-acetic anhydride after the thermal treatment at 90°C, i.e. the red solution in figure 4.9 (c).

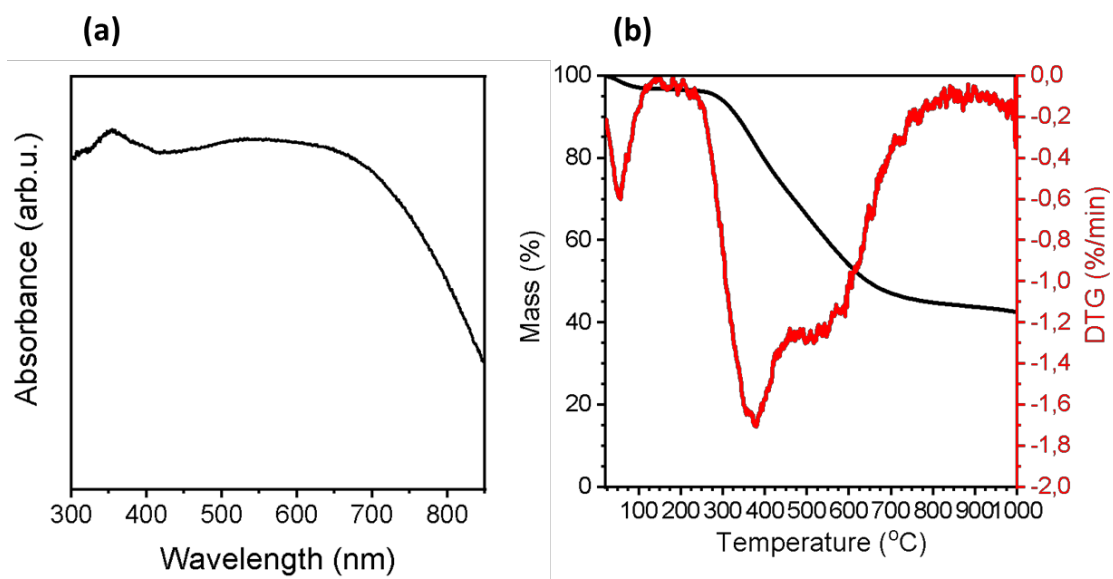


Figure S39. (a) DRS of the LTC from malonic acid-acetic anhydride precursor. (b) TGA (black line) and DTG under N₂ of the LTC from malonic acid-acetic anhydride precursor.

D. Characterization methods

Atomic Force Microscopy (AFM). The atomic force microscope was employed for the investigation of surface profiles. The images are obtained by scanning the sample surface with a sharp tip which is converted into high-resolution 3D images. The tip is a part of a flexible cantilever mounted on cylindrical piezoelectric tube that deflects according to the voltage applied, producing a precise raster of the sample surface.

AFM surface patterns were obtained Dimension 3100 Atomic Force Microscopy from Veeco Instruments.

Scanning Electron Microscopy (SEM). Scanning Electron Microscopy (SEM) is a microscopy technique allowing to image materials surface at high magnifications using the wave-particle dualism of electrons. SEM technique is particularly suitable to scan sample surface details such as topology, texture, morphology and particle size of samples.

SEM imaging was performed after Au/Pd sputtering of the non-conductive sample on carbon sample holders in a LEO 1550-Gemini system (acceleration voltage: 0.2 to 30 kV).

Energy Dispersive X-ray Spectroscopy (EDX). This spectroscopy method is suitable for the determination of elemental composition of solid samples. The sample is irradiated with an electron beam which interacts with the electrons of the inner orbitals. The electron beam excites the sample electrons and creates holes that are eventually filled by electrons from higher orbital energy while X-ray photons are emitted. The energy of the emitted photons is characteristic for each element and the number of emitted photons is correlated to the atom content.

EDX was taken on the SEM equipped with an Oxford Instruments X-MAX 80 mm² detector.

Transmission Electron Microscopy (TEM) and Electron Energy Loss Spectroscopy (EELS). The TEM technique exploits the wave-particle dualism to image objects with sizes even lower than 1 nm. The resolution is proportional to the wavelength, and thus the accelerated electrons with very short wavelength allows for detect structures that could not be detected with a visible light source. The electron

beam is focused and transmitted through a very thin section of the sample in high vacuum. The electrons are collected by the detector below the sample and the image is created as a result of the interaction between the electron beam and the sample. The inelastic scattering of the transmitted electrons causes an electron energy loss and a random deflection of their path. By using an additional electron spectrometer, the electron energy loss can be detected and used to infer the type of atoms, the elemental composition, the chemical bonding and the electronic properties of the sample.

The measurements were acquired using a Jeol JEM-ARM200F microscope, equipped with a cold field emission gun, the Gatan GIF Quantum detector and the JED-2300 Energy-dispersive X-ray detector. The used acceleration voltage was typically 80 kV.

Combustion Elemental Analysis (EA). The quantitative determination of elemental composition for non-metallic elements as C, N, H and S is obtained by the combustion of a sample in an oxygen atmosphere. The decomposition products detected are elaborated in terms of relative elemental ratios.

Elemental analysis was performed using a Vario Micro Device.

Water Contact Angle Measurement. The contact angle is measured on a flat surface from the image of a water sessile drop at the three-phase contact points which is recorded by a camera placed in front of the sample. The software estimates the right and left contact angles between the water droplet and surface, which is useful to determine the sample surface properties, such as hydrophilicity and hydrophobicity.

Water contact angle was investigated by using Krüss contact angle measuring system G10 and recorded via Krüss software.

X-ray Diffraction (XRD). X-rays are short wavelength electromagnetic radiation which can be used to analyze ordered structures of sub-micrometer sizes, i.e. crystalline structures. The sample is irradiated with a beam of monochromatic X-rays which are scattered from certain lattice planes. This is possible since the X-ray wavelength has the same magnitude of the lattice distances. In case of ordered structure, the diffraction pattern shows peaks that occur due constructive interference

from adjacent parallel planes. The position and the full width at half maximum of the peaks contain information about the lattice planes distances (Bragg's law) and the crystallite size (Scherrer equation), respectively.

XRD measurements were performed on a Bruker D8 Advance instrument using Cu-K α radiation for 2θ values between 5° and 70° with typical step scan of $0.05^\circ/\text{s}$.

Fourier Transform Infrared (FTIR) Spectroscopy. The FTIR spectroscopy is a non-destructive optical technique based on the characteristic absorption of molecules at frequencies in the mid-infrared range. The frequency absorption occurs at a characteristic resonant energy typical of vibrational and vibrational-rotational transitions of functional groups, which depend on the bond strength and atoms masses.

FTIR spectra were collected in the range $4000\text{-}500\text{ cm}^{-1}$ with a Thermo Scientific Nicolet iD5 spectrometer with an attenuated total reflection (ATR) support.

Raman Spectroscopy. The Raman spectroscopy is a complementing technique of FTIR. In this case, the sample is irradiated with a monochromatic laser source which induces a dipole moment within the molecule based on its polarizability. In contrast to FTIR, Raman spectroscopy it is based on inelastic scattering of photons which causes a change in polarization in the sample and, therefore, highly polarized groups (e.g. C-O and O-H) are weak Raman scatterers, whereas relatively neutral bonds (e.g. C-C and C=C) give rise to stronger Raman signals.

Raman spectra were taken with a confocal Raman microscope (WiTech Alpha300 R) equipped with a 532 nm green laser.

Thermogravimetric analysis (TGA) and mass spectroscopy (MS). TGA is a thermal analysis in which the mass change of a sample is recorded as a function of temperature and time. The decomposition of the material is usually done in synthetic air or inert atmosphere (N_2 or He), and commonly used heating rates $10^\circ\text{C}/\text{min}$ or $2.5^\circ\text{C}/\text{min}$. The mass change is usually a mass loss is accompanied by the evolution of gaseous by-products, which can be detected when a TGA system is coupled with a mass spectrometer. The mass spectrometer records the mass/charge ratio of gaseous ionized by-products giving further information about the decomposition process.

TGA measurements were done using a thermo microbalance TG 209 F1 Libra (Netzsch, Selb) coupled with a Thermostar Mass spectrometer (Pfeiffer Vacuum) with ionization energy of 75 eV. For TGA measurements the heating rate used was 10°C/min in N₂ or synthetic air, whereas for TGA-MS characterization it was 2.5°C/min in N₂.

Nuclear Magnetic Resonance (NMR) Spectroscopy. NMR spectroscopy is a non-destructive technique based on the excitation of NMR-active nuclei by a radio frequency when exposed to a strong magnetic field. The nuclear spin of many characteristic isotopes such as ¹H, ¹³C allows for splitting the nuclear energy levels when subjected to a strong magnetic field. The energy difference between the levels depends on the applied magnetic field and on the local molecular environment. The application of a radiofrequency pulse that can be absorbed by the nuclei causes a transition from the spin state at lower energy to the one at higher energy. When the applied radiofrequency pulse is equal to the Larmor frequency, the resonance condition is achieved and after the pulse is removed the signal is recorded. The signal, known as Free Induction Decay, is converted into a frequency domain spectrum by the Fourier transform. The NMR experiments are usually done in liquid phase, where if possible, a sample is dissolved in a deuterated solvent. However, in case the sample is insoluble, the NMR experiments can be done also in solid-state. In the latter case, the sample is spin with rotatory speed at 54.7°, which is known as magic angle with respect to the applied magnetic field.

Liquid NMR spectra were recorded by Bruker Ascend400 for ¹³C –NMR at 100.6 MHz frequency. Solid state ¹³C magic angle spinning (MAS) NMR experiments were carried out with a Bruker Avance 400 MHz spectrometer operating at 100.56 MHz at a MAS rate of 10 kHz using 4 mm MAS HX double resonance probe.

X-ray Photoelectron Spectroscopy (XPS). XPS is a non-destructive technique based on the photoelectric effect, exciting electrons from the core levels by an X-ray source. The sample is irradiated in ultra-high vacuum with X-rays (common sources Mg K α (1253.6eV) and Al K α (1486.6eV)) and, if the excitation energy is sufficient, the core electrons are ejected with a well defined kinetic energy. The measured kinetic energy thus depends on the energy of the excitation source ($h\nu$), the binding

energy of the electron (E_B) and the work function (Φ) dependent on the material and the spectrometer:

$$E_k = h\nu - E_B - \Phi$$

The electrons emitted from the inner shell of the atom are evaluated in XPS; the binding energy and the intensity of a photoelectron peak allows for identifying the chemical element, the binding motifs, the oxidation state. The areas of the peaks give information on the relative elemental composition of the sample surface, since the penetration depth is usually below 10 nm.

XPS measurements were performed using CISSY equipment with a SPECS XR 50 X-ray gun Mg K α radiation (1254.6 eV) and Combined Lens Analyzer Module (CLAM), for the samples in chapter 2 and 3. A Thermo Scientific K-Alpha⁺ X-ray Photoelectron Spectrometer with a monochromatic Al K α X-ray (1486.68 eV) source was used for samples in chapter 4.

Ultraviolet Photoelectron Spectroscopy (UPS). This spectroscopic characterization allows for the determination of the valence band energy and the workfunction of the material exploiting the photoelectric effect. The sample is irradiated with a photon beam with energy lower than 50 eV, which causes the excitation of valence band electrons with lower binding energies with respect to XPS. For this characterization a SPECS UVS 10/35 was used in an ultrahigh vacuum chamber (UHV) with He I (21.2 eV) radiation source. The detector was a CombinedLens with an analyzer module thermoVG (TLAM). The Fermi level of gold reference was used to calibrate the system.

Time-correlated single photon counting (TCSPC). The fluorescence decays lifetimes were obtained by using a 405 nm pulsed excitation using a pulse width 4 μ s and the emission dispersed with an H10 monochromator, detected using a 9816 photomultiplier (EMI) with a digital oscilloscope TDS540(Tektronix).

Photoluminescence, fluorescence (PL). Photoluminescence, or simply fluorescence, is a non-destructive analysis in which the photons emission of a sample is recorded as a function of wavelength. In this case, the photon emission of a sample is triggered usually by a lower excitation wavelength, which causes the

excitation of electrons to an electronic excited state and further recombination accompanied by light emission.

Photoluminescence spectra were recorded by Horiba FluoroMax-4 equipped with a thin film sample holder set at 60° with respect to the excitation, integration time 0.2 to 1 s and slits apertures 1. The excitation wavelength was chosen accordingly to the sample in the range 200-450 nm.

Phosphorescence (PH). Photons absorbed can trigger an emission that happens within a short time scale, known as fluorescence, or within a long time scale of minutes or even hours. The latter is called phosphorescence. The long delay in photon emission is associated with a transition from a singlet excited state to a triplet excited state before the relaxation at a ground state, and described by the Jablonsky diagram.

Phosphorescence spectra were recorded by a Jasco FP-8300 spectrofluorometer with 10 ms and 25 ms chopping time. The excitation wavelengths used are 350, 370 and 390 nm.

Diffuse Reflectance Spectroscopy (DRS). Diffuse reflectance spectroscopy is a spectroscopic technique used on powdered samples to study the effect of an impinging radiation. Contrary to reflectance measured on thin films, which reflections are described by the Fresnel equations, on powdery samples the result is combination of reflection, scattering and refraction of the impinging radiation. In particular, this method is interesting to calculate, by the Kubelka-Munk method, the bandgap of powdery materials.

DRS spectra were obtained by Shimadzu UV 2600 equipped with an integrating sphere.

Transmittance and Reflectance spectroscopy. These two methods are complementary methods to study light-matter interaction of thin films. In the first case, the light intensity crossing the sample section is recorded as a function of the radiation wavelength. When light is reflected or absorbed (or scattered) the light transmittance decreases and recorded by the spectrometer. In reflectance measurements it is measured the light reflected by an ideally flat surface. The

recorded spectra contain information about the thickness and the optical properties of the sample that can be deduced with appropriate elaboration.

Transmittance and reflectance spectra were collected with a Varian Agilent Cary 5000 UV-VIS-NIR with a double ray for intensity correction in the range 185-1800 nm and equipped with a setup for reflectance and transmittance at normal incidence. For reflectance measurements, an aluminum mirror was used as a standard reference.

Variable Angle Spectroscopic Ellipsometry (VASE). Ellipsometry is a very sensitive characterization technique which is used to determine the thickness of thin films and/or optical constants. It exploits a polarized light beam which is reflected by the sample surface at different incident angles and it detects the variation of polarization state and phase, in terms of ψ and Δ . These parameters are related to the ratio of Fresnel reflection coefficients, for p- and s- polarized light. The data are then fit to find the best model to describe the optical functions, in agreement with the experimental data. Ellipsometry is a very sensitive spectroscopic technique that can be used to determine the optical constants and thickness, but also roughness, crystallinity, porosity of thin films and optical anisotropy.

VASE measurements and elaboration were done with J.A. Woollam VASE ellipsometer in the range 250-2500 nm at 65°, 70° and 75° equipped with vertical sample stage and AutoRetarder.

E. Abbreviation list

g-C₃N₄	Graphitic carbon nitride
BCN	Boron carbon nitride
E_F	Fermi level
BG	Bandgap
VB	Valence band
CB	Conduction band
1:1	Melamine-boric acid adduct 1 to 1 molar ratio
1:2	Melamine-boric acid adduct 1 to 2 molar ratio
n	Refractive index
K	Extinction coefficient
R	Reflectance
T	Transmittance
A	Absorbance
HOMO	Highest occupied molecular orbital
LED	Light emitting diodes
CVD	Chemical vapor deposition
PVD	Physical vapor deposition
XRD	X-ray diffraction
EELS	Electron energy loss spectroscopy
TEM	Transmission electron microscopy
SEM	Scanning electron microscopy
TGA	Thermogravimetric analysis
DTG	Derivative thermogravimetry
EDX	Energy Dispersive X-ray Analysis

FFT	Fast Fourier transform
FTIR	Fourier-transform infrared spectroscopy
XPS	X-ray photoelectron spectroscopy
λ	Wavelength
VASE	Variable angle spectroscopic ellipsometry
PL	Photoluminescence
PH	Phosphorescence
TCSPC	Time-correlated single photon counting
PEC	Photoelectrochemical cell
AFM	Atomic force microscopy
BN	Boron nitride
NMR	Nuclear magnetic resonance
LUMO	Lowest unoccupied molecular orbital
NHE	Normal hydrogen electrode
CIE	International Commission on Illumination
UV	Ultraviolet
UPS	Ultraviolet photoelectron spectroscopy
LTC	Low temperature carbon
P₂O₅	Phosphorus pentoxide
MS	Mass spectrometry
m/z	mass to charge ratio
MAS	Magic angle spinning
(d-)THF	(deuterated-)tetrahydrofuran
(d-)DMF	(deuterated-)dimethylformamide
(d-)DMSO	(deuterated-)dimethyl sulfoxide

D₂O

Deuterated water

%at

Atomic percent

F. Publication list

P. Lova, P. Giusto, F. Di Stasio, G. Manfredi, G. M. Paternò, D. Cortecchia, C. Soci and D. Comoretto, *Nanoscale*, 2019.

K. Xiao, P. Giusto, L. Wen, L. Jiang and M. Antonietti, *Angewandte Chemie International Edition*, 2018, 57, 10123-10126.

P. Lova, D. Cortecchia, H. N. S. Krishnamoorthy, P. Giusto, C. Bastianini, A. Bruno, D. Comoretto and C. Soci, *ACS Photonics*, 2018, 5, 867-874.

P. Giusto, P. Lova, G. Manfredi, S. Gazzo, P. Srinivasan, S. Radice and D. Comoretto, *ACS Omega*, 2018, 3, 7517-7522.

P. Lova, C. Bastianini, P. Giusto, M. Patrini, P. Rizzo, G. Guerra, M. Iodice, C. Soci and D. Comoretto, *ACS applied materials & interfaces*, 2016, 8, 31941-31950.

Presentations

Poster

XXII AIM Italian Meeting on Macromolecules 2016, Genoa, Italy

P. Giusto, C. Bastianini, G. Manfredi, P. Lova and D. Comoretto

“Structural Colors and Polymeric Materials”

6th International Conference on Multifunctional, Hybrid and Nanomaterials 2019, Sitges, Spain

P. Giusto, J. Siena and M. Antonietti

“Carbon Nitride and Boron Carbon Nitride High Quality Thin Films for Optical Applications”

G. Acknowledgements

First of all, I would like to thank prof. Markus Antonietti for the opportunity to carry out this work under his supervision at the Max Planck Institute of Colloids and Interfaces. His direct supervision, his great ideas and enthusiasm have been an inspiration for me during this work. Besides that, I want to thank him also for the cultural and philosophical discussion over many different topics during these years. Thank you.

Moreover, I would like to give a special thanks to Regina Rothe, who really helped me a lot during these years, always being supportive and present. All the officemates, from Max and Marius, Nikki, Julya and Francesco have really made my days special and unforgettable. I would like to give a huge thanks to all the friends that were supporting me during this time at the Max Planck Institute which are the main characters of the nice memories and I will never forget. Thanks Ralf (Ralligalli), Baris (PhD), Milena, Nievesita, Chris, Alessandro (Dani), Alessandro (Vince') Cataldo, Majd (comandante), Danielito, Joao, Noah, Steffen, Enrico, Janina, Sylvain, Sasha, Stefano, Ivan(e), Shaowen, Martin, Runyu, Ipek, Tobias, Nadja, Ryan, Christene, Alex, Lukas, Voelker, Clemens, Konstantin, Jose', Jan, Karen. I hope I didn't forget any. Un ringraziamento speciale voglio farlo a Martina e Valerio, per essere stati sempre presenti nei momenti difficili e in quelli di gioia, sia in istituto che al di fuori. Grazie davvero ragazzi. This work wouldn't have been possible without the help of the super nice technicians of our department: Heike, Antje, Irina, Katharina, Rona, Reinhild, Anne, Olaf and the technical support of Michael, Heiko, Ivo and Sven. As well as the secretaries Carolin and Luisa for their help in organizing and supporting. Lastly, I would like to thank Katharina Zesch for the big support dealing with companies and handling the quotations in super short time. Thank you all!

Ovviamente tutto questo non sarebbe stato possibile senza gli amici di una vita quelli con cui sono cresciuto nella "magica" Imperia, e sareste davvero troppi da nominarvi tutti, grazie per essermi stati vicino anche essendo così lontano. Dalla memorabile compagnia del "cinema", i "Freys", la compagine di montegrappa, la compagnia di cantina "Diddi", i coinquilini a San Martino e i ragazzi di eCO₂logic, grazie a tutti. Un ringraziamento particolare va a Guenda che è un'imperiese adottata e mi ha supportato un sacco durante questi anni, soprattutto nei momenti difficili, come fanno gli amici di una vita. Gli amici incontrati nel percorso che mi hanno portato qui in particolare a Genova, dove ho passato 6 anni fantastici che mi hanno fatto crescere

e ho conosciuto persone fantastiche, dai compagni di universita' a tutti quelli con cui ho speso delle fantastiche e memorabili giornate. Un ringraziamento particolare va a Vittorio che oltre a essere stato un fantastico compagno di universita' ed un grande amico durante tutto questo periodo, e' riuscito a organizzarsi per venirmi a trovare a Berlino l'unico momento che io non c'ero. Spero che ci saranno altre occasioni. Un ringraziamento particolare tengo a farlo anche alla Prof. Patrini al Prof. Comoretto e il suo gruppo, ed in particolare Paola e Giovanni, per il supporto scientifico durante la tesi magistrale e durante il dottorato. Paola e Gio, oltre alla collaborazione siete stati ottimi amici ai quali ho spesso rotto le scatole ma siete sempre stati presenti che questo fosse legato a qualcosa di scientifico o meno, grazie di tutto.

La mia famiglia mamma, papa' e mio fratello Luca che nonostante io non sia mai a casa mi fanno sempre sentire vicino a loro e ci sono sempre nei momenti difficili e in quelli belli. Tutto quello che sono riuscito a fare lo devo a loro, che mi hanno insegnato tutto quello che so dal primo giorno che sono nato ad oggi, e sono tutt'ora dei modelli per me. Vorrei ringraziare anche tutta la famiglia zii e cugini per il loro supporto e la grande accoglienza (e le vivande) che mi riservano ogni volta che torno a casa. Un pensiero va anche ai nonni, che per diversi motivi non sono riuscito a stargli vicino nei loro ultimi giorni, che mi hanno cresciuto e insegnato tanto, grazie di tutto, so che sareste orgogliosi di me.

L'ultimo e forse piu' importante pensiero e dedicato a te che sei la mia compagna di tutti i giorni, Nina e che piu' di tutti hai dovuto sopportare i miei scleri e momenti di nervosismo, ma lo hai fatto sempre con il sorriso, grazie di tutto amore mio.

H. Declaration

Die vorliegende Dissertation entstand im Zeitraum zwischen Februar 2017 und Juni 2019 am Max Planck Institut für Kolloid und Grenzflächenforschung, unter der Betreuung von Prof. Dr. Dr. h.c. Markus Antonietti.

Hiermit erkläre ich, dass die vorliegende Arbeit selbstständig angefertigt und keine anderen als die angegebenen Hilfsmittel und Quellen verwendet wurden.

This dissertation was carried out and written between February 2017 and June 2019 at the Max Planck Institute for Colloids and Interfaces under the supervision of Prof. Dr. Dr. h.c. Markus Antonietti.

I hereby declare that this work has been done by myself and that I used only the tools and sources indicated.

Paolo Giusto,
Potsdam, June 2019

Asinus asinum fricat

(Cicero, De Amicitia)

I. Bibliography

General background and perspective

- [1] A. J. Heeger, *Angewandte Chemie International Edition* 2001, 40, 2591.

Chapter I

- [1] M. E. Weeks, *Journal of Chemical Education* 1932, 9, 4.
- [2] P. J. Harris, P. J. F. Harris, *Carbon nanotube science: synthesis, properties and applications*, Cambridge university press, 2009.
- [3] B. Yeh, W. Lim, *Nature chemical biology* 2007, 3, 521.
- [4] M. S. Dresselhaus, M. Terrones, *Proceedings of the IEEE* 2013, 101, 1522.
- [5] M. Inagaki, M. Toyoda, Y. Soneda, T. Morishita, *Carbon* 2018, 132, 104.
- [6] N. Fechner, T.-P. Fellingner, M. Antonietti, *Journal of Materials Chemistry A* 2013, 1, 14097.
- [7] H. J. Burch, J. A. Davies, E. Brown, L. Hao, S. A. Contera, N. Grobert, J. Ryan, *Applied physics letters* 2006, 89, 143110.
- [8] R. Czerw, M. Terrones, J.-C. Charlier, X. Blase, B. Foley, R. Kamalakaran, N. Grobert, H. Terrones, D. Tekleab, P. Ajayan, *Nano Letters* 2001, 1, 457.
- [9] R. Walczak, B. Kurpil, A. Savateev, T. Heil, J. Schmidt, Q. Qin, M. Antonietti, M. Oschatz, *Angewandte Chemie International Edition* 2018, 57, 10765.
- [10] M. Antonietti, M. Oschatz, *Advanced Materials* 2018, 30, 1706836.
- [11] N. Fechner, T. P. Fellingner, M. Antonietti, *Advanced Materials* 2013, 25, 75.
- [12] Z. Zhou, F. He, Y. Shen, X. Chen, Y. Yang, S. Liu, T. Mori, Y. Zhang, *Chemical Communications* 2017, 53, 2044.
- [13] M. Antonietti, N. Lopez-Salas, A. Primo, *Advanced Materials* 2018, 1805719.
- [14] M. Oschatz, M. Antonietti, *Energy Environmental Science* 2018, 11, 57.
- [15] X. Chen, R. Paul, L. Dai, *National Science Review* 2017, 4, 453.
- [16] S. Saufi, A. Ismail, *Carbon* 2004, 42, 241.
- [17] R. Cheng, Y. Xue, in *Carbon Nanomaterials for Biomedical Applications*, Springer, 2016, 31.
- [18] M. Kakran, L. Li, "Carbon nanomaterials for drug delivery", presented at Key Engineering Materials, 2012.
- [19] P. Avouris, M. Freitag, V. Perebeinos, *Nature photonics* 2008, 2, 341.
- [20] F. Yuan, S. Li, Z. Fan, X. Meng, L. Fan, S. Yang, *Nano Today* 2016, 11, 565.
- [21] N. A. Travlou, M. Seredych, E. Rodríguez-Castellón, T. J. Bandosz, *Journal of Materials Chemistry A* 2015, 3, 3821.
- [22] N. A. Travlou, M. Seredych, E. Rodríguez-Castellón, T. J. Bandosz, *Carbon* 2016, 96, 1014.
- [23] Y. Battie, O. Ducloux, P. Thobois, T. Susi, E. I. Kauppinen, A. Loiseau, *physica status solidi* 2011, 248, 2462.
- [24] R. U. R. Sagar, X. Zhang, C. Xiong, Y. Yu, *Carbon* 2014, 76, 64.
- [25] Z. Liu, B. Sun, X. Liu, J. Han, H. Ye, Y. Tu, C. Chen, T. Shi, Z. Tang, G. Liao, *Journal of Materials Chemistry A* 2018, 6, 7409.
- [26] J. Ortiz-Medina, H. Kitano, A. Morelos-Gomez, Z. Wang, T. Araki, C.-S. Kang, T. Hayashi, K. Takeuchi, T. Kawaguchi, A. Tanioka, *NPG Asia Materials* 2016, 8, e258.
- [27] C. Hu, L. Dai, *Angewandte Chemie International Edition* 2016, 55, 11736.
- [28] D. Kato, N. Sekioka, A. Ueda, R. Kurita, S. Hirono, K. Suzuki, O. Niwa, *Angewandte Chemie International Edition* 2008, 47, 6681.
- [29] H. Choi, S. H. Kim, J. Jang, *Advanced materials* 2004, 16, 732.

- [30] D. M. Sun, C. Liu, W. C. Ren, H. M. Cheng, *Advanced Electronic Materials* 2016, 2, 1600229.
- [31] S. Wang, Y. Zhu, F. Xia, J. Xi, N. Wang, L. Feng, L. Jiang, *Carbon* 2006, 9, 1848.
- [32] K. M. Krishna, Y. Nukaya, T. Soga, T. Jimbo, M. Umeno, *Solar energy materials and solar cells* 2001, 65, 163.
- [33] M. Kinoshita, M. Steiner, M. Engel, J. P. Small, A. A. Green, M. C. Hersam, R. Krupke, E. E. Mendez, P. Avouris, *Optics express* 2010, 18, 25738.
- [34] A. K. Geim, K. S. Novoselov, in *Nanoscience and Technology: A Collection of Reviews from Nature Journals*, World Scientific, 2010, 11.
- [35] G. Algara-Siller, N. Severin, S. Y. Chong, T. Björkman, R. G. Palgrave, A. Laybourn, M. Antonietti, Y. Z. Khimyak, A. V. Krasheninnikov, J. P. Rabe, *Angewandte Chemie* 2014, 126, 7580.
- [36] S. Deng, V. Berry, *Materials Today* 2016, 19, 197.
- [37] J. Zhang, X. Chen, K. Takanabe, K. Maeda, K. Domen, J. D. Epping, X. Fu, M. Antonietti, X. Wang, *Angewandte Chemie International Edition* 2010, 49, 441.
- [38] E. Kroke, M. Schwarz, *Coordination Chemistry Reviews* 2004, 248, 493.
- [39] A. Y. Liu, M. L. Cohen, *Science* 1989, 245, 841.
- [40] D. M. Teter, R. J. Hemley, *Science* 1996, 271, 53.
- [41] W.-J. Ong, L.-L. Tan, Y. H. Ng, S.-T. Yong, S.-P. Chai, *Chemical reviews* 2016, 116, 7159.
- [42] J. Liu, H. Wang, M. Antonietti, *Chemical Society Reviews* 2016, 45, 2308.
- [43] Q. Su, J. Sun, J. Wang, Z. Yang, W. Cheng, S. Zhang, *Catalysis Science & Technology* 2014, 4, 1556.
- [44] S. T. Melissen, S. N. Steinmann, T. Le Bahers, P. Sautet, *The Journal of Physical Chemistry C* 2016, 120, 24542.
- [45] A. Thomas, A. Fischer, F. Goettmann, M. Antonietti, J.-O. Müller, R. Schlögl, J. M. Carlsson, *Journal of Materials Chemistry* 2008, 18, 4893.
- [46] X. Wang, S. Blechert, M. Antonietti, *Acs Catalysis* 2012, 2, 1596.
- [47] S. Cao, J. Low, J. Yu, M. Jaroniec, *Advanced Materials* 2015, 27, 2150.
- [48] J. Fu, J. Yu, C. Jiang, B. Cheng, *Advanced Energy Materials* 2018, 8, 1701503.
- [49] G. Capilli, M. Costamagna, F. Sordello, C. Minero, *Applied Catalysis B: Environmental* 2019, 242, 121.
- [50] J. Zhang, M. Zhang, R. Q. Sun, X. Wang, *Angewandte Chemie International Edition* 2012, 51, 10145.
- [51] M. Shalom, M. Guttentag, C. Fettkenhauer, S. Inal, D. Neher, A. Llobet, M. Antonietti, *Chemistry of materials* 2014, 26, 5812.
- [52] J. Xu, M. Shalom, F. Piersimoni, M. Antonietti, D. Neher, T. J. Brenner, *Advanced Optical Materials* 2015, 3, 913.
- [53] E. Z. Lee, Y. S. Jun, W. H. Hong, A. Thomas, M. M. Jin, *Angewandte Chemie International Edition* 2010, 49, 9706.
- [54] W. Ma, D. Han, M. Zhou, H. Sun, L. Wang, X. Dong, L. Niu, *Chemical Science* 2014, 5, 3946.
- [55] C. Cheng, Y. Huang, X. Tian, B. Zheng, Y. Li, H. Yuan, D. Xiao, S. Xie, M. M. Choi, *Analytical chemistry* 2012, 84, 4754.
- [56] J. Tian, Q. Liu, A. M. Asiri, A. H. Qusti, A. O. Al-Youbi, X. Sun, *Nanoscale* 2013, 5, 11604.
- [57] A. Du, S. Sanvito, Z. Li, D. Wang, Y. Jiao, T. Liao, Q. Sun, Y. H. Ng, Z. Zhu, R. Amal, *Journal of the American Chemical Society* 2012, 134, 4393.
- [58] X. Zhang, H. Wang, H. Wang, Q. Zhang, J. Xie, Y. Tian, J. Wang, Y. Xie, *Advanced materials* 2014, 26, 4438.
- [59] L.-S. Lin, Z.-X. Cong, J. Li, K.-M. Ke, S.-S. Guo, H.-H. Yang, G.-N. Chen, *Journal of Materials Chemistry B* 2014, 2, 1031.
- [60] J. Chen, Z. Mao, L. Zhang, D. Wang, R. Xu, L. Bie, B. D. Fahlman, *ACS nano* 2017, 11, 12650.
- [61] X. Li, Y. Feng, M. Li, W. Li, H. Wei, D. Song, *Advanced Functional Materials* 2015, 25, 6858.

- [62] M. Tahir, C. Cao, N. Mahmood, F. K. Butt, A. Mahmood, F. Idrees, S. Hussain, M. Tanveer, Z. Ali, I. Aslam, *ACS applied materials interfaces* 2013, 6, 1258.
- [63] Y. Ding, Y. Tang, L. Yang, Y. Zeng, J. Yuan, T. Liu, S. Zhang, C. Liu, S. Luo, *Journal of Materials Chemistry A* 2016, 4, 14307.
- [64] Y. Luo, Y. Yan, S. Zheng, H. Xue, H. Pang, *Journal of Materials Chemistry A* 2019, 7, 901.
- [65] B. Kumru, M. Shalom, M. Antonietti, B. V. Schmidt, *Macromolecules* 2017, 50, 1862.
- [66] J. Liu, T. An, Z. Chen, Z. Wang, H. Zhou, T. Fan, D. Zhang, M. Antonietti, *Journal of Materials Chemistry A* 2017, 5, 8933.
- [67] T. R. Chetia, M. S. Ansari, M. Qureshi, *Journal of Materials Chemistry A* 2016, 4, 5528.
- [68] X. Chen, Q. Liu, Q. Wu, P. Du, J. Zhu, S. Dai, S. Yang, *Advanced Functional Materials* 2016, 26, 1719.
- [69] L. L. Jiang, Z. K. Wang, M. Li, C. C. Zhang, Q. Q. Ye, K. H. Hu, D. Z. Lu, P. F. Fang, L. S. Liao, *Advanced Functional Materials* 2018, 28, 1705875.
- [70] T.-P. Fellingner, D. S. Su, M. Engenhorst, D. Gautam, R. Schlögl, M. Antonietti, *Journal of Materials Chemistry* 2012, 22, 23996.
- [71] H. Zeng, C. Zhi, Z. Zhang, X. Wei, X. Wang, W. Guo, Y. Bando, D. Golberg, *Nano letters* 2010, 10, 5049.
- [72] O. Hod, *Journal of chemical theory computation* 2012, 8, 1360.
- [73] L. Song, Z. Liu, A. L. M. Reddy, N. T. Narayanan, J. Taha- Tijerina, J. Peng, G. Gao, J. Lou, R. Vajtai, P. M. Ajayan, *Advanced Materials* 2012, 24, 4878.
- [74] Y. Miyamoto, A. Rubio, M. L. Cohen, S. G. Louie, *Physical Review B* 1994, 50, 4976.
- [75] J. Lu, K. Zhang, X. F. Liu, H. Zhang, T. C. Sum, A. H. C. Neto, K. P. Loh, *Nature communications* 2013, 4, 2681.
- [76] S. Azevedo, R. De Paiva, *EPL* 2006, 75, 126.
- [77] L. Ci, L. Song, C. Jin, D. Jariwala, D. Wu, Y. Li, A. Srivastava, Z. Wang, K. Storr, L. Balicas, *Nature materials* 2010, 9, 430.
- [78] K. Yuge, *Physical review B* 2009, 79, 144109.
- [79] I. Caretti, R. Torres, R. Gago, A. Landa-Canovas, I. Jiménez, *Chemistry of Materials* 2010, 22, 1949.
- [80] S. Beniwal, J. Hooper, D. P. Miller, P. S. Costa, G. Chen, S.-Y. Liu, P. A. Dowben, E. C. H. Sykes, E. Zurek, A. Enders, *ACS nano* 2017, 11, 2486.
- [81] R. Y. Tay, H. Li, S. H. Tsang, M. Zhu, M. Loeblein, L. Jing, F. N. Leong, E. H. T. Teo, *Chemistry of Materials* 2016, 28, 2180.
- [82] D. Portehault, C. Giordano, C. Gervais, I. Senkovska, S. Kaskel, C. Sanchez, M. Antonietti, *Advanced Functional Materials* 2010, 20, 1827.
- [83] M. Jalaly, F. J. Gotor, M. Semnan, M. J. Sayagués, *Scientific reports* 2017, 7, 3453.
- [84] W. Lei, D. Portehault, R. Dimova, M. Antonietti, *Journal of the American Chemical Society* 2011, 133, 7121.
- [85] J. Wang, J. Hao, D. Liu, S. Qin, D. Portehault, Y. Li, Y. Chen, W. Lei, *ACS Energy Letters* 2017, 2, 306.
- [86] S. Wang, E. Iyyamperumal, A. Roy, Y. Xue, D. Yu, L. Dai, *Angewandte Chemie* 2011, 123, 11960.
- [87] K. S. K. S. S. Harsha, *Principles of vapor deposition of thin films*, Elsevier, 2005.
- [88] T. T. Kodas, M. J. Hampden-Smith, *The chemistry of metal CVD*, John Wiley & Sons, 2008.
- [89] M. Barankin, E. Gonzalez li, A. Ladwig, R. Hicks, *Solar energy materials solar cells* 2007, 91, 924.
- [90] Z. Dimitrova, D. Gogova, *Materials Research Bulletin* 2005, 40, 333.
- [91] H. Nandivada, H. Y. Chen, L. Bondarenko, J. Lahann, *Angewandte Chemie International Edition* 2006, 45, 3360.
- [92] M. R. Leyden, Y. Jiang, Y. Qi, *Journal of Materials Chemistry A* 2016, 4, 13125.
- [93] M. M. Tavakoli, L. Gu, Y. Gao, C. Reckmeier, J. He, A. L. Rogach, Y. Yao, Z. Fan, *Scientific reports* 2015, 5, 14083.
- [94] S. Sivaram, *Chemical vapor deposition: thermal and plasma deposition of electronic materials*, Springer Science & Business Media, 2013.

- [95] M. Ohring, Materials science of thin films, Elsevier, 2001.
- [96] J. L. Vossen, W. Kern, W. Kern, Thin film processes II, Vol. 2, Gulf Professional Publishing, 1991.
- [97] D. Dobkin, M. K. Zuraw, Principles of chemical vapor deposition, Springer Science & Business Media, 2003.
- [98] H. S. Fogler, Essentials of Chemical Reaction Engineering: Essenti Chemica Reactio Engi, Pearson Education, 2010.
- [99] E. L. Cussler, Diffusion: mass transfer in fluid systems, Cambridge university press, 2009.
- [100] H. O. Pierson, Handbook of chemical vapor deposition: principles, technology and applications, William Andrew, 1999.
- [101] N. Peyghambarian, S. W. Koch, A. Mysyrowicz, Introduction to Semiconductor Optics (Prentice Hall Series in Solid State Physical Electronics), Prentice Hall, 1993.
- [102] IUPAC, in Materials Chemistry Edu, International Union of Pure and Applied Chemistry.
- [103] D. K. Roy, Physics of semiconductor devices, Universities Press, 2004.
- [104] M. Dresselhaus, G. Dresselhaus, S. B. Cronin, A. G. Souza Filho, Solid State Properties, Springer, 2018.
- [105] O. Stenzel, The Physics of Thin Film Optical Spectra - An Introduction, 2005.
- [106] M. Dresselhaus, 2001.
- [107] H. A. Macleod, Thin-film optical filters, CRC press, 2010.
- [108] A. D. McNaught, A. D. McNaught, Compendium of chemical terminology, Vol. 1669, Blackwell Science Oxford, 1997.

Chapter II

- [1] J. Bian, C. Huang, R. Q. Zhang, ChemSusChem 2016, 9, 2723.
- [2] K. Xiao, P. Giusto, L. Wen, L. Jiang, M. Antonietti, Angewandte Chemie 2018, 130, 10280.
- [3] H. Arazoe, D. Miyajima, K. Akaike, F. Araoka, E. Sato, T. Hikima, M. Kawamoto, T. Aida, Nature materials 2016, 15, 1084.
- [4] W. Bing, Z. Chen, H. Sun, P. Shi, N. Gao, J. Ren, X. Qu, Nano Research 2015, 8, 1648.
- [5] C. Aspell, *Polymer science* Vol. 20, Halsted Press (John Wiley & Sons), New York 1988.
- [6] *Specialty polymers* Springer Netherlands, Glasgow : New York 1987.
- [7] E. M. Pérez, N. Martín, Chemical Society Reviews 2015, 44, 6425.
- [8] J. Zhang, M. Zhang, L. Lin, X. Wang, Angewandte Chemie International Edition 2015, 54, 6297.
- [9] B. Kumru, M. Antonietti, B. V. Schmidt, Langmuir 2017, 33, 9897.
- [10] X. Xie, X. Fan, X. Huang, T. Wang, J. He, RSC Advances 2016, 6, 9916.
- [11] B. Kumru, D. Cruz, T. Heil, B. V. Schmidt, M. Antonietti, Journal of the American Chemical Society 2018, 140, 17532.
- [12] J. Liu, H. Wang, Z. P. Chen, H. Moehwald, S. Fiechter, R. van de Krol, L. Wen, L. Jiang, M. Antonietti, Advanced Materials 2015, 27, 712.
- [13] J. Xu, M. Shalom, ACS applied materials interfaces 2016, 8, 13058.
- [14] J. Xu, T. J. Brenner, L. Chabanne, D. Neher, M. Antonietti, M. Shalom, Journal of the American Chemical Society 2014, 136, 13486.
- [15] J. Xu, M. Shalom, F. Piersimoni, M. Antonietti, D. Neher, T. J. Brenner, Advanced Optical Materials 2015, 3, 913.
- [16] Y. Fang, X. Li, X. Wang, ACS Catalysis 2018, 8, 8774.
- [17] M. Shalom, S. Gimenez, F. Schipper, I. Herraiz-Cardona, J. Bisquert, M. Antonietti, Angewandte Chemie International Edition 2014, 53, 3654.

- [18] G. Peng, L. Xing, J. Barrio, M. Volokh, M. Shalom, *Angewandte Chemie International Edition* 2018, 57, 1186.
- [19] J. Bian, Q. Li, C. Huang, J. Li, Y. Guo, M. Zaw, R.-Q. Zhang, *Nano Energy* 2015, 15, 353.
- [20] J. Bian, L. Xi, C. Huang, K. M. Lange, R. Q. Zhang, M. Shalom, *Advanced Energy Materials* 2016, 6, 1600263.
- [21] D. Miyajima, H. Arazoe, M. Kawamoto, K. Akaike, Y. Koizumi, T. Aida, 2015.
- [22] K. K. Gleason, *CVD polymers: fabrication of organic surfaces and devices*, John Wiley & Sons, 2015.
- [23] M. N. Uddin, H. Notomi, T. Kida, M. Yamazato, M. Nagano, *Thin Solid Films* 2004, 464-465, 170.
- [24] Y. M. Manawi, Ihsanullah, A. Samara, T. Al-Ansari, M. A. Atieh, 2018, 11, 822.
- [25] M. Inagaki, F. Kang, *Materials science and engineering of carbon: characterization*, Butterworth-Heinemann, 2016.
- [26] S. Cao, J. Low, J. Yu, M. Jaroniec, *Advanced Materials* 2015, 27, 2150.
- [27] P. Xia, M. Antonietti, B. Zhu, T. Heil, J. Yu, S. Cao, *Advanced Functional Materials* 2019, 1900093.
- [28] Q. Guo, Y. Zhang, J. Qiu, G. Dong, *Journal of Materials Chemistry C* 2016, 4, 6839.
- [29] G. González-Gaitano, J. R. Isasi, *The Chemical Educator* 2001, 6, 362.
- [30] L. Li, D. Cruz, A. Savateev, G. Zhang, M. Antonietti, Y. Zhao, *Applied Catalysis B: Environmental* 2018, 229, 249.
- [31] M. J. Bojdys, J. O. Müller, M. Antonietti, A. Thomas, *Chemistry—A European Journal* 2008, 14, 8177.
- [32] V. C. Angadi, C. Abhayaratne, T. Walther, *Journal of microscopy* 2016, 262, 157.
- [33] N. Hellgren, R. T. Haasch, S. Schmidt, L. Hultman, I. Petrov, *Carbon* 2016, 108, 242.
- [34] K. Akaike, K. Aoyama, S. Dekubo, A. Onishi, K. Kanai, *Chemistry of Materials* 2018, 30, 2341.
- [35] Y. Luo, J. Wang, S. Yu, Y. Cao, K. Ma, Y. Pu, W. Zou, C. Tang, F. Gao, L. Dong, *Journal of Materials Research* 2018, 33, 1268.
- [36] P. Bagla, 2018.
- [37] X. Bao, Y. Zhang, J. Wang, D. Zhu, C. Yang, Y. Li, C. Yang, J. Xu, R. Yang, *Chemistry of Materials* 2017, 29, 6766.
- [38] P. Cheben, P. J. Bock, J. H. Schmid, J. Lapointe, S. Janz, D.-X. Xu, A. Densmore, A. Delâge, B. Lamontagne, T. J. Hall, *Optics letters* 2010, 35, 2526.
- [39] A. I. Kuznetsov, A. E. Miroshnichenko, M. L. Brongersma, Y. S. Kivshar, B. Luk'yanchuk, *Science* 2016, 354, aag2472.
- [40] D. Comoretto, *Organic and hybrid photonic crystals*, Springer, 2015.
- [41] H. Wang, S. Jiang, S. Chen, X. Zhang, W. Shao, X. Sun, Z. Zhao, Q. Zhang, Y. Luo, Y. Xie, *Chemical science* 2017, 8, 4087.
- [42] G. Zhang, G. Li, Z. A. Lan, L. Lin, A. Savateev, T. Heil, S. Zafeiratos, X. Wang, M. Antonietti, *Angewandte Chemie International Edition* 2017, 56, 13445.
- [43] J. Bian, J. Li, S. Kalytchuk, Y. Wang, Q. Li, T. C. Lau, T. A. Niehaus, A. L. Rogach, R. Q. Zhang, *ChemPhysChem* 2015, 16, 954.
- [44] S. W. King, M. Milosevic, *Journal of Applied Physics* 2012, 111, 073109.
- [45] O. Stenzel, *The Physics of Thin Film Optical Spectra - An Introduction*, 2005.
- [46] G. Benno, K. Joachim, Fermilab, 2003.
- [47] S. Bose, *High temperature coatings*, Butterworth-Heinemann, 2017.
- [48] R. Swanepoel, *Journal of Physics E: Scientific Instruments* 1983, 16, 1214.
- [49] T. S. Reddy, M. S. Kumar, *RSC Advances* 2016, 6, 95680.
- [50] J. A. Woollam, 2019.
- [51] H. Bach, D. Krause, *Thin films on glass*, Springer Science & Business Media, 2013.
- [52] I. J. A. Woollam Co., *Guide to Using WVASE 32: Spectroscopic Ellipsometry Data Acquisition and Analysis Software*, J. A. Woollam Company, Incorporated, 2008.
- [53] L. A. Pettersson, L. Hultman, H. Arwin, *Applied optics* 1998, 37, 4130.
- [54] M. S. Vezie, S. Few, I. Meager, G. Pieridou, B. Dörling, R. S. Ashraf, A. R. Goñi, H. Bronstein, I. McCulloch, S. C. Hayes, *Nature materials* 2016, 15, 746.

- [55] J. Grey, *Nature materials* 2016, 15, 705.
- [56] W.-J. Ong, L.-L. Tan, Y. H. Ng, S.-T. Yong, S.-P. Chai, *Chemical reviews* 2016, 116, 7159.
- [57] S. D. Bhagat, J. Chatterjee, B. Chen, A. Stiegman, *Macromolecules* 2012, 45, 1174.
- [58] N.-H. You, T. Higashihara, Y. Oishi, S. Ando, M. Ueda, *Macromolecules* 2010, 43, 4613.
- [59] E. K. Macdonald, M. P. Shaver, *Polymer International* 2015, 64, 6.
- [60] T. Higashihara, M. Ueda, *Macromolecules* 2015, 48, 1915.
- [61] H. Phillip, E. Taft, *Physical Review* 1964, 136, A1445.
- [62] J.-g. Liu, M. Ueda, *Journal of Materials Chemistry* 2009, 19, 8907.
- [63] W. Zheng, N.-B. Wong, W.-K. Li, A. Tian, *Journal of chemical theory computation* 2006, 2, 808.
- [64] Y. Li, F. Piret, T. Léonard, B.-L. Su, *Journal of colloid interface science* 2010, 348, 43.
- [65] M. R. Weatherspoon, Y. Cai, M. Crne, M. Srinivasarao, K. H. Sandhage, *Angewandte Chemie International Edition* 2008, 47, 7921.
- [66] B. D. Viezbicke, S. Patel, B. E. Davis, D. P. Birnie III, *physica status solidi* 2015, 252, 1700.
- [67] J. Liu, H. Wang, M. Antonietti, *Chemical Society Reviews* 2016, 45, 2308.
- [68] A. Thomas, A. Fischer, F. Goettmann, M. Antonietti, J.-O. Müller, R. Schlögl, J. M. Carlsson, *Journal of Materials Chemistry* 2008, 18, 4893.
- [69] Y. Zhang, T. Mori, J. Ye, M. Antonietti, *Journal of the American Chemical Society* 2010, 132, 6294.
- [70] H. Yu, R. Shi, Y. Zhao, T. Bian, Y. Zhao, C. Zhou, G. I. Waterhouse, L. Z. Wu, C. H. Tung, T. Zhang, *Advanced Materials* 2017, 29, 1605148.
- [71] T. F. Fuller, J. N. Harb, *Electrochemical engineering*, John Wiley & Sons, 2018.
- [72] S. Trasatti, *Pure and Applied Chemistry* 1986, 58, 955.
- [73] Y. Cui, Z. Ding, P. Liu, M. Antonietti, X. Fu, X. Wang, *Physical Chemistry Chemical Physics* 2012, 14, 1455.
- [74] M. Sauer, J. Hofkens, J. Enderlein, in *Handbook of fluorescence spectroscopy and imaging: from single molecules to ensembles*, 2011, 1.
- [75] O. Mirzov, I. Scheblykin, *Physical Chemistry Chemical Physics* 2006, 8, 5569.
- [76] H. Wu, H. Xu, F. Tao, X. Su, W. Y. William, T. Li, Y. Cui, *New Journal of Chemistry* 2018, 42, 12802.
- [77] H. Zhang, A. Yu, *The Journal of Physical Chemistry C* 2014, 118, 11628.
- [78] L. M. Hirvonen, K. Suhling, *Meas. Sci. Technol* 2017, 28, 012003.
- [79] C. Merschjann, T. Tyborski, S. Orthmann, F. Yang, K. Schwarzburg, M. Lublow, M.-C. Lux-Steiner, T. Schedel-Niedrig, *Physical Review B* 2013, 87, 205204.
- [80] A. Köhler, J. Wilson, *Organic Electronics* 2003, 4, 179.
- [81] H. Wang, S. Jiang, S. Chen, D. Li, X. Zhang, W. Shao, X. Sun, J. Xie, Z. Zhao, Q. Zhang, *Advanced Materials* 2016, 28, 6940.
- [82] Y. Li, M. Gecevicius, J. Qiu, *Chemical Society Reviews* 2016, 45, 2090.
- [83] Y. Huang, J. Zhou, B. Su, L. Shi, J. Wang, S. Chen, L. Wang, J. Zi, Y. Song, L. Jiang, *Journal of the American Chemical Society* 2012, 134, 17053.
- [84] D. G. Baranov, D. A. Zuev, S. I. Lepeshov, O. V. Kotov, A. E. Krasnok, A. B. Evlyukhin, B. N. Chichkov, *Optica* 2017, 4, 814.

Chapter III

- [1] L. Song, Z. Liu, A. L. M. Reddy, N. T. Narayanan, J. Taha-Tijerina, J. Peng, G. Gao, J. Lou, R. Vajtai, P. M. Ajayan, *Advanced Materials* 2012, 24, 4878.
- [2] M. A. Mannan, Y. Baba, T. Kida, M. Nagano, I. Shimoyama, N. Hirao, H. Noguchi, *Thin Solid Films* 2011, 519, 1780.

- [3] L. Ci, L. Song, C. Jin, D. Jariwala, D. Wu, Y. Li, A. Srivastava, Z. Wang, K. Storr, L. Balicas, *Nature materials* 2010, 9, 430.
- [4] J. Xiao, C. Wang, Q. Shen, L. Zhang, *Surface and Coatings Technology* 2015, 276, 141.
- [5] E. Byon, J.-K. Kim, S. Lee, J.-H. Hah, K. Sugimoto, *Surface and Coatings Technology* 2003, 169, 340.
- [6] F. Zhou, Q. Wang, B. Yue, X. Wu, L. Zhuge, X. Cheng, *Materials Chemistry and Physics* 2013, 138, 215.
- [7] C. Wang, J. Xiao, Q. Shen, L. Zhang, *Thin Solid Films* 2016, 603, 323.
- [8] Q. Yang, C. Wang, S. Zhang, D. Zhang, Q. Shen, L. Zhang, *Surface and Coatings Technology* 2010, 204, 1863.
- [9] R. Attri, M. Sreedhara, C. Rao, *ACS Applied Electronic Materials* 2019.
- [10] M. M. Zagho, H. D. Dawoud, N. Bensalah, T. Altahtamouni, *Emergent Materials* 2018, 1.
- [11] E. Salas, R. Jimenez Rioboo, J. Sánchez-Marcos, F. Jiménez-Villacorta, A. Muñoz-Martín, J. Prieto, V. Joco, C. Prieto, *Journal of Applied Physics* 2013, 114, 213508.
- [12] D. H. Kim, E. Byon, S. Lee, J.-K. Kim, H. Ruh, *Thin Solid Films* 2004, 447, 192.
- [13] J.-K. Park, J.-H. Lee, W.-S. Lee, Y.-J. Baik, *Thin Solid Films* 2013, 549, 276.
- [14] R. Kaner, J. Kouvetakis, C. Warble, M. Sattler, N. Bartlett, *Materials research bulletin* 1987, 22, 399.
- [15] F. Leardini, E. Flores, I. J. Ferrer, J. R. Ares, C. Sánchez, P. Molina, H. P. Van Der Meulen, C. G. Navarro, G. L. Polin, F. J. Urbanos, *Nanotechnology* 2017, 29, 025603.
- [16] V. S. Sulyaeva, Y. M. Romyantsev, V. G. Kesler, M. L. Kosinova, *Thin Solid Films* 2015, 581, 59.
- [17] S. Beniwal, J. Hooper, D. P. Miller, P. S. Costa, G. Chen, S.-Y. Liu, P. A. Dowben, E. C. H. Sykes, E. Zurek, A. Enders, *ACS nano* 2017, 11, 2486.
- [18] S. Azevedo, R. De Paiva, *EPL* 2006, 75, 126.
- [19] X. Blase, J.-C. Charlier, A. De Vita, *R. Car, Applied Physics A* 1999, 68, 293.
- [20] M. S. Mazzoni, R. Nunes, S. Azevedo, H. Chacham, *Physical Review B* 2006, 73, 073108.
- [21] J. Sun, X.-F. Zhou, Y.-X. Fan, J. Chen, H.-T. Wang, X. Guo, J. He, Y. Tian, *Physical Review B* 2006, 73, 045108.
- [22] Y. H. Lee, X. Q. Zhang, W. Zhang, M. T. Chang, C. T. Lin, K. D. Chang, Y. C. Yu, J. T. W. Wang, C. S. Chang, L. J. Li, *Advanced materials* 2012, 24, 2320.
- [23] M. Ohring, *Materials science of thin films*, Elsevier, 2001.
- [24] K. Kobashi, K. Nishimura, Y. Kawate, T. Horiuchi, *Physical review B* 1988, 38, 4067.
- [25] N. Fechler, N. P. Zussblatt, R. Rothe, R. Schlögl, M. G. Willinger, B. F. Chmelka, M. Antonietti, *Advanced Materials* 2016, 28, 1287.
- [26] M. Shalom, S. Inal, C. Fettkenhauer, D. Neher, M. Antonietti, *Journal of the American Chemical Society* 2013, 135, 7118.
- [27] A. Roy, A. Choudhury, C. N. R. Rao, *Journal of molecular structure* 2002, 613, 61.
- [28] 2019.
- [29] T. Hagio, K. Kobayashi, T. Sato, *Journal of the Ceramic Society of Japan* 1994, 102, 1051.
- [30] O. Hod, *Journal of chemical theory and computation* 2012, 8, 1360.
- [31] T.-P. Fellingner, D. S. Su, M. Engenhorst, D. Gautam, R. Schlögl, M. Antonietti, *Journal of Materials Chemistry* 2012, 22, 23996.
- [32] R. F. Egerton, *Electron energy-loss spectroscopy in the electron microscope*, Springer Science & Business Media, 2011.
- [33] H. Tan, J. Verbeeck, A. Abakumov, G. Van Tendeloo, *Ultramicroscopy* 2012, 116, 24.
- [34] V. Keast, A. Scott, R. Brydson, D. Williams, J. Bruley, *Journal of microscopy* 2001, 203, 135.
- [35] M. A. Mannan, Y. Baba, N. Hirao, T. Kida, M. Nagano, H. Noguchi, *Materials Sciences and Applications* 2013, 4, 11.
- [36] B. J. Matsoso, K. Ranganathan, B. K. Mutuma, T. Lerotholi, G. Jones, N. J. Coville, *Nanotechnology* 2017, 28, 105602.

- [37] *Specialty polymers* Springer Netherlands, Glasgow : New York 1987.
- [38] T. Higashihara, M. Ueda, *Macromolecules* 2015, 48, 1915.
- [39] J. Bian, J. Li, S. Kalytchuk, Y. Wang, Q. Li, T. C. Lau, T. A. Niehaus, A. L. Rogach, R. Q. Zhang, *ChemPhysChem* 2015, 16, 954.
- [40] O. Stenzel, *The Physics of Thin Film Optical Spectra - An Introduction*, 2005.
- [41] B. D. Viezbicke, S. Patel, B. E. Davis, D. P. Birnie III, *physica status solidi* 2015, 252, 1700.
- [42] J. Tauc, R. Grigorovici, A. Vancu, *physica status solidi (b)* 1966, 15, 627.
- [43] J.-g. Liu, M. Ueda, *Journal of Materials Chemistry* 2009, 19, 8907.
- [44] A. Forouhi, I. Bloomer, *Physical review B* 1988, 38, 1865.
- [45] A. Forouhi, I. Bloomer, *Physical review B* 1986, 34, 7018.
- [46] E. K. Macdonald, M. P. Shaver, *Polymer International* 2015, 64, 6.
- [47] D. Pierucci, J. Zribi, H. Henck, J. Chaste, M. G. Silly, F. Bertran, P. Le Fevre, B. Gil, A. Summerfield, P. H. Beton, *Applied Physics Letters* 2018, 112, 253102.
- [48] M. Antonietti, M. Oschatz, *Advanced Materials* 2018, 30, 1706836.
- [49] C. Huang, C. Chen, M. Zhang, L. Lin, X. Ye, S. Lin, M. Antonietti, X. Wang, *Nature communications* 2015, 6, 7698.
- [50] M. Kibria, Z. Mi, *Journal of Materials Chemistry A* 2016, 4, 2801.
- [51] R. Walczak, B. Kurpil, A. Savateev, T. Heil, J. Schmidt, Q. Qin, M. Antonietti, M. Oschatz, *Angewandte Chemie International Edition* 2018, 57, 10765.
- [52] International Commission on Illumination, 2019.
- [53] S. Damiaty, S. Zaki, S. Wonorahardjo, N. Wong, H. Rijal, "Comfort Temperature in Air Conditioned Office Buildings: Case Study of Indonesia And Singapore", presented at *Malaysia-Japan Joint International Conference 2015 (MJJIC2015)*, 2015.
- [54] Vol. Singapore Standard, CP13, Productivity and Standard Board, Singapore, 1999.

Chapter IV

- [1] B. C. Brodie, *Proceedings of the Royal Society of London* 1873, 21, 245.
- [2] L. Reyerson, K. Kobe, *Chemical Reviews* 1930, 7, 479.
- [3] O. Diels, B. Wolf, *Berichte der deutschen chemischen Gesellschaft* 1906, 39, 689.
- [4] O. Diels, G. Meyerheim, *Berichte der deutschen chemischen Gesellschaft* 1907, 40, 355.
- [5] A. Ellern, T. Drews, K. Seppelt, *Zeitschrift für anorganische und allgemeine Chemie* 2001, 627, 73.
- [6] L. B. Dashkevich, V. Beilin, *Russian Chemical Reviews* 1967, 36, 391.
- [7] T. Kappe, E. Ziegler, *Angewandte Chemie International Edition in English* 1974, 13, 491.
- [8] J. Schmedt auf der Günne, J. Beck, W. Hoffbauer, P. Krieger-Beck, *Chemistry—A European Journal* 2005, 11, 4429.
- [9] T. Carofiglio, L. Pandolfo, G. Paiaro, *European polymer journal* 1986, 22, 491.
- [10] A. Blake, A. Hyde, *Transactions of the Faraday Society* 1964, 60, 1775.
- [11] N. L. Yang, A. Snow, H. Haubenstein, F. Bramwell, *Journal of Polymer Science: Polymer Chemistry Edition* 1978, 16, 1909.
- [12] A. Snow, H. Haubenstein, N.-L. Yang, *Macromolecules* 1978, 11, 77.
- [13] O. Khvostikova, H. Hermann, H. Wendrock, T. Gemming, J. Thomas, H. Ehrenberg, *Journal of Materials Science* 2011, 46, 2422.
- [14] L. Wang, R. Zhang, U. Jansson, N. Nedfors, *Scientific reports* 2015, 5, 11119.
- [15] T. w. Kwon, Y. K. Jeong, I. Lee, T. S. Kim, J. W. Choi, A. Coskun, *Advanced Materials* 2014, 26, 7979.
- [16] J. Robertson, *Advances in Physics* 1986, 35, 317.
- [17] S. S. Balaji, M. Sathish, *RSC Advances* 2014, 4, 52256.

- [18] I. Sengupta, S. Chakraborty, M. Talukdar, S. K. Pal, S. Chakraborty, *Journal of Materials Research* 2018, 33, 4113.
- [19] J. L. Fajardo-Díaz, F. López-Urías, E. Muñoz-Sandoval, *Scientific reports* 2018, 8, 3546.
- [20] K. N. Kudin, B. Ozbas, H. C. Schniepp, R. K. Prud'Homme, I. A. Aksay, R. Car, *Nano letters* 2008, 8, 36.
- [21] S. Seiler, C. E. Halbig, F. Grote, P. Rietsch, F. Börrnert, U. Kaiser, B. Meyer, S. Eigler, *Nature communications* 2018, 9, 836.
- [22] A. Popova, *Coke and Chemistry* 2017, 60, 361.
- [23] P. Sehrawat, S. Islam, P. Mishra, S. Ahmad, *Scientific reports* 2018, 8, 3537.
- [24] H.-K. Jeong, Y. P. Lee, R. J. Lahaye, M.-H. Park, K. H. An, I. J. Kim, C.-W. Yang, C. Y. Park, R. S. Ruoff, Y. H. Lee, *Journal of the American Chemical Society* 2008, 130, 1362.
- [25] S. Some, Y. Kim, Y. Yoon, H. Yoo, S. Lee, Y. Park, H. Lee, *Scientific reports* 2013, 3, 1929.
- [26] K. Dave, K. H. Park, M. Dhayal, *RSC Advances* 2015, 5, 95657.
- [27] W. Gao, L. B. Alemany, L. Ci, P. M. Ajayan, *Nature chemistry* 2009, 1, 403.
- [28] I. Prencipe, D. Dellasega, A. Zani, D. Rizzo, M. Passoni, *Science and technology of advanced materials* 2015, 16, 025007.
- [29] R. Bruckner, *Organic Mechanisms: Reactions, Stereochemistry and Synthesis*, Springer-Verlag Berlin, 2016.
- [30] L. Li, H. Zhang, Y. Zhang, P. K. Chu, X. Tian, L. Xia, X. Ma, *Materials Science and Engineering: B* 2002, 94, 95.
- [31] P. K. Chu, L. Li, *Materials Chemistry and Physics* 2006, 96, 253.
- [32] A. Ganguly, S. Sharma, P. Papakonstantinou, J. Hamilton, *The Journal of Physical Chemistry C* 2011, 115, 17009.
- [33] C. Hontoria-Lucas, A. López-Peinado, J. d. D. López-González, M. Rojas-Cervantes, R. Martin-Aranda, *Carbon* 1995, 33, 1585.
- [34] A. M. Ladwig, R. D. Koch, E. G. Wenski, R. F. Hicks, *Diamond and Related Materials* 2009, 18, 1129.
- [35] M. Balci, *Basic 1H-and 13C-NMR spectroscopy*, Elsevier, 2005.
- [36] A. Panich, A. Shames, N. Sergeev, *Applied Magnetic Resonance* 2013, 44, 107.
- [37] M. Mermoux, Y. Chabre, A. Rousseau, *Carbon* 1991, 29, 469.
- [38] T. Szabó, O. Berkesi, P. Forgó, K. Josepovits, Y. Sanakis, D. Petridis, I. Dékány, *Chemistry of materials* 2006, 18, 2740.
- [39] A. Tararan, A. Zobelli, A. M. Benito, W. K. Maser, O. Stéphan, *Chemistry of Materials* 2016, 28, 3741.
- [40] J. Wen, Z. Zeng, L. Yang, Q. Zeng, H. Lou, H. Sheng, D. J. Miller, W. Yang, H.-k. Mao, *Microscopy and Microanalysis* 2017, 23, 2268.
- [41] M. Hu, J. He, Z. Zhao, T. A. Strobel, W. Hu, D. Yu, H. Sun, L. Liu, Z. Li, M. Ma, *Science advances* 2017, 3, e1603213.
- [42] A. Sikora, F. Garrelie, C. Donnet, A. Loir, J. Fontaine, J. C. Sanchez-Lopez, T.-C. Rojas, *Journal of Applied Physics* 2010, 108, 113516.
- [43] S. Park, J. An, J. R. Potts, A. Velamakanni, S. Murali, R. S. Ruoff, *Carbon* 2011, 49, 3019.
- [44] O. Diels, L. Lalin, *Berichte der deutschen chemischen Gesellschaft* 1908, 41, 3426.
- [45] K. A. Connors, A. Ifan, *Journal of pharmaceutical sciences* 1987, 76, 834.
- [46] J. Y. Howe, C. J. Rawn, L. Jones, H. Ow, *Powder diffraction* 2003, 18, 150.
- [47] M. Nováček, O. Jankovský, J. Luxa, D. Sedmidubský, M. Pumera, V. Fila, M. Lhotka, K. Klímová, S. Matějková, Z. Sofer, *Journal of Materials Chemistry A* 2017, 5, 2739.
- [48] S. Stankovich, R. D. Piner, X. Chen, N. Wu, S. T. Nguyen, R. S. Ruoff, *Journal of Materials Chemistry* 2006, 16, 155.